UNIVERSITAT DE BARCELONA

An STM/FM-AFM investigation of selected organic and inorganic 2D systems on metallic surfaces

Sonia Matencio Lloberas

ADVERTIMENT. La consulta d'aquesta tesi queda condicionada a l'acceptació de les següents condicions d'ús: La difusió d'aquesta tesi per mitjà del servei TDX (**www.tdx.cat**) i a través del Dipòsit Digital de la UB (**diposit.ub.edu**) ha estat autoritzada pels titulars dels drets de propietat intel·lectual únicament per a usos privats emmarcats en activitats d'investigació i docència. No s'autoritza la seva reproducció amb finalitats de lucre ni la seva difusió i posada a disposició des d'un lloc aliè al servei TDX ni al Dipòsit Digital de la UB. No s'autoritza la presentació del seu contingut en una finestra o marc aliè a TDX o al Dipòsit Digital de la UB (framing). Aquesta reserva de drets afecta tant al resum de presentació de la tesi com als seus continguts. En la utilització o cita de parts de la tesi és obligat indicar el nom de la persona autora.

ADVERTENCIA. La consulta de esta tesis queda condicionada a la aceptación de las siguientes condiciones de uso: La difusión de esta tesis por medio del servicio TDR (**www.tdx.cat**) y a través del Repositorio Digital de la UB (**diposit.ub.edu**) ha sido autorizada por los titulares de los derechos de propiedad intelectual únicamente para usos privados enmarcados en actividades de investigación y docencia. No se autoriza su reproducción con finalidades de lucro ni su difusión y puesta a disposición desde un sitio ajeno al servicio TDR o al Repositorio Digital de la UB. No se autoriza la presentación de su contenido en una ventana o marco ajeno a TDR o al Repositorio Digital de la UB (framing). Esta reserva de derechos afecta tanto al resumen de presentación de la tesis como a sus contenidos. En la utilización o cita de partes de la tesis es obligado indicar el nombre de la persona autora.

WARNING. On having consulted this thesis you're accepting the following use conditions: Spreading this thesis by the TDX (**www.tdx.cat**) service and by the UB Digital Repository (**diposit.ub.edu**) has been authorized by the titular of the intellectual property rights only for private uses placed in investigation and teaching activities. Reproduction with lucrative aims is not authorized nor its spreading and availability from a site foreign to the TDX service or to the UB Digital Repository. Introducing its content in a window or frame foreign to the TDX service or to the UB Digital Repository is not authorized (framing). Those rights affect to the presentation summary of the thesis as well as to its contents. In the using or citation of parts of the thesis it's obliged to indicate the name of the author.

Programa de Doctorat en Nanociències

Universitat de Barcelona

An STM/FM-AFM investigation of selected organic and inorganic 2D systems on metallic surfaces

Author:

Sonia Matencio Lloberas

Supervisors:

Dr. Esther Barrena Villas

Prof. Carmen Ocal García

Institut de Ciència de Materials de Barcelona (ICMAB-CSIC)

Tutor:

Dr. Elisa Vallés Giménez

Departament Química Física, Universitat de Barcelona

Contents

Contents iii

1 Motivation 1

2 Introduction 3
- 2.1 The Molecule-Metal Interface . . . 3
- 2.2 Principles of Scanning Probe Microscopy . . . 6
  - 2.2.1 Scanning Tunneling Microscopy (STM) . . . 8
  - 2.2.2 Frequency Modulation Atomic Force Microscopy (FM-AFM) 12
    - 2.2.2.1 Relation between Δf and F_{ts} . . . 13
    - 2.2.2.2 Tunneling Current for an Oscillating Tip . . . 15
    - 2.2.2.3 Combined STM/FM-AFM . . . 16
  - 2.2.3 Tip-Sample Forces . . . 18
  - 2.2.4 Dissipation . . . 22
  - 2.2.5 Spectroscopies . . . 24

3 Experimental Setup 29
- 3.1 Description of the UHV System . . . 29
- 3.2 The STM/FM-AFM Setup . . . 32
- 3.3 Preparation of Clean Substrates . . . 35
- 3.4 Molecular Deposition of Organic Layers . . . 36

4 Oxidation of Cu(111) by Air Enriched Argon Bombardment 39
- 4.1 Introduction . . . 39
- 4.2 Description of the Cu_2O . . . 40
- 4.3 Experimental Details . . . 42
- 4.4 Structural Study of the Cu_2O/Cu(111) Surface . . . 43
  - 4.4.1 The Cu(111) Surface . . . 43
  - 4.4.2 Oxidation of Cu(111) . . . 43
  - 4.4.3 Copper Oxides: Nucleation, Structural and Stoichiometric Defects and Structural Phases . . . 47
  - 4.4.4 Theoretical models of oxide precursors configurations . . . 60
  - 4.4.5 Oxide Nanowires and the Open Honeycomb Structure . . . 62
  - 4.4.6 Copper nitride . . . 66
- 4.5 Conclusions . . . 70

4.6 Appendix 72

5 Spectroscopic Characterization of Copper Oxide 75
5.1 Introduction 75
5.2 Previous Work Function Studies 76
5.3 Experimental Details 77
5.4 Contact Potential Difference Measurements 77
5.5 Tunneling Current and Force Characterization 78
5.5.1 Resistance in Series Model 84
5.5.2 Tip-Sample Deformation 88
5.5.3 Discussion 94
5.6 Atomic "Flip-Flop" in Tunneling Current Spectroscopies 95
5.7 Conclusions 99

6 Study of PTCDA on Si(111)-7x7 and AgSi(111) Surfaces 101
6.1 Introduction 101
6.2 The PTCDA Molecule 102
6.3 Method for Kappa Imaging 106
6.4 Experimental Details 111
6.5 Characterization of the Substrates 112
6.5.1 The Si(111)-7×7 Surface 112
6.5.2 The Ag/Si(111) Surface 115
6.6 PTCDA on Si(111)–7×7 Surface 118
6.6.1 Structural Study 118
6.6.2 Imaging the Decay Constant 121
6.7 PTCDA on Ag/Si(111) Surface 124
6.7.1 Structural Study 124
6.7.2 Point Spectroscopy 132
6.7.3 Imaging the Decay Constant 135
6.8 Conclusions 137

7 Study of the Monolayer of DIP on Cu(111) 139
7.1 Introduction 139
7.2 The DIP Molecule 140
7.3 Experimental Details 142
7.4 Theoretical DIP Structures on Cu(111) 143
7.5 Experimental Study of DIP on Cu(111) 146
7.5.1 DIP Phases on Cu(111) 146
7.5.2 Stability of the Long-Range Ordered Phases 155
7.6 Electronic Study of DIP on Cu(111) 157
7.7 Conclusions 159

8 Study of ClAlPc on Au(111) 161
8.1 Introduction 161
8.2 Introductory Concepts to the Molecular System and Substrate . . . 162

8.3 Experimental Details 164
8.4 Results and Discussion 165
8.4.1 The Au(111) Surface 165
8.4.2 Monolayer and Bilayer of ClAlPc/Au(111) 166
8.4.3 Contact Potential Difference Measurements 175
8.5 Conclusions 179

9 Final Conclusions **181**

10 Resumen **185**

Abbreviations **209**

Acknowledgements **213**

Bibliography **213**

Chapter 1

Motivation

Organic/inorganic interfaces play a key role in organic electronic devices such as organic light emitting diodes (OLED), organic field effect transistors (OFET) and organic solar cells (OSC). In these interfaces crucial processes such as charge injection or extraction take place. Improving the performance of these devices has the potential to result in more efficient sources of lighting, printable electronics, and highly scalable solar energy harvesting. With this aim, a solid understanding at atomic level of the structural and electronic properties of organic/inorganic interfaces is needed.

The research presented in this thesis is based on scanning probe microscopies which are powerful techniques to probe and manipulate the electronic and structure at atomic scale. The structural and electronic properties of selected organic and inorganic 2D systems on metallic surfaces have been investigated by a combined scanning tunneling microscopy (STM) and frequency modulation atomic force microscopy (FM-AFM) in ultra-high vacuum conditions and at room temperature. The combination of these local probe techniques permits elucidating the interface structure at atomic level and disentangle electronic from topographic information.

Cuprous oxide (Cu_2O) is an intrinsic p-type semiconductor. Copper oxide ultrathin films have been suggested to be candidates for uses as low resistance electrodes, catalysts, sensing materials and semiconductor materials for solar cell transformation. But the properties of this ultrathin film may differ from the bulk properties. With the aim of increase the actual knowledge, an atomic thin film of copper oxide has been grown on Cu(111). Its structural and electronic properties have been studied and are presented in Chapters 4 and 5.

Several organic molecules have been tested on different surfaces: perylene-3,4,9,10-tetracarboxylic anhydride (PTCDA), diindenoperylene (DIP) and chloroaluminum phthalocyanine (ClAlPc). All of them are small π conjugate molecules that have been grown by molecular beam deposition. The final structure of these molecules on the surfaces is a competition between intermolecular and molecule-substrate forces. The perylene derivatives DIP and PTCDA are served as model systems for a basic understanding of organic/inorganic interfaces. In the organic/metal interface many complex processes can occur such as charge transfer, charge re-arrangement and push back effect, affecting the work function change in a non trivial way. The structural and electronic properties of the PTCDA on Si(111)7x7 and AgSi(111) have been studied and are presented in Chapter 6. The DIP on the Cu(111) surface and the ClAlPc on Au(111) are shown in Chapter 7 and Chapter 8, respectively.

Chapter 2

Introduction

In this introductory chapter, the organic-metal interfaces and the scanning probe microscopies used in this thesis are explained. The first part is dedicated to the most important aspects of the metal-organic semiconductor interfaces since they are the most studied systems along this thesis (Chapters 6, 7 and 8). A metal-inorganic semiconductor system has been also studied (Chapters 4 and 5) and the needed details are given therein. In the second part of this chapter a brief summary of the historical development and the basics of scanning tunneling microscopy and atomic force microscopy is presented. A description of the typical tip-sample forces that act in ultra-high vacuum environment and the spectroscopies used in this thesis are also described.

2.1 The Molecule-Metal Interface

There is a large number of organic molecules that can be used for the fabrication of organic electronic devices and in the study of fundamental questions concerning growth, structure, and physical properties, however small conjugated and planar molecules are of particular interest for the investigation of these issues. Their comparatively low molecular weight in combination with their stability against polymerization and thermal decomposition up to several hundred degrees allow the sublimation of these molecules under UHV conditions by organic molecular beam epitaxy (OMBE).

Depending on the nature of the forces between the molecules and the surface two different processes are distinguished, physisorption and chemisorption. Physisorption is characterized by weak van der Waals interactions where molecules are located at relatively large distances from the surface and are usually highly mobile. Chemisorption is defined by the formation of chemical bonds with the substrate and/or by the charge transfer between molecule and substrate due to the smaller adsorption distance that produces an overlap between orbitals. The borderline between physisorption and chemisorption is not clearly defined and, for example, charge transfer does not only correspond to chemisorptive processes and can also be present under physisorption [23]. However, the formation of new local directed bonds between molecules and surface is clearly attributed to chemisorption. A physisorbed molecule should preserve its chemical integrity and orbital structure upon adsorption while a chemisorbed molecule would have its structure affected by the bonding.

An important issue in a metal-organic interface concerns the energetic positions of the molecular frontier orbitals, highest occupied molecular orbital (HOMO) and lowest unoccupied molecular orbital (LUMO), with respect to the metal work function. Several experimental studies about molecules on metal surfaces pointed out that the simple Schottky-Mott rule of vacuum alignment at the interface does not completely describe this case anymore [110] as formation of an interface dipole produces a shift of the relative positions of the vacuum levels as can be observed in Figure 2.1(a). The metal work function is defined as the energy difference between the metal Fermi level (E_F) and the vacuum level (VL). The molecular ionization energy (IE) and the electron affinity (EA) are defined as the energy difference between the vacuum level and the HOMO and LUMO, respectively as can be observed in Figure 2.1(a). The formation of the interface dipole (represented in Figure 2.1(a) as Δ) causes an abrupt shift of the vacuum level at the molecule-metal interface affecting the local work function of the metal as well as the relative position of the molecular levels (HOMO and LUMO) respect to the Fermi energy level of the metal. If the interface dipole is pointing towards the molecule the local work function tends to increase while if it is pointing towards the metal surface the local work function tends to decrease. The magnitude and sign of Δ determine the hole electron injection barriers, issue of enormous importance in organic based devices.

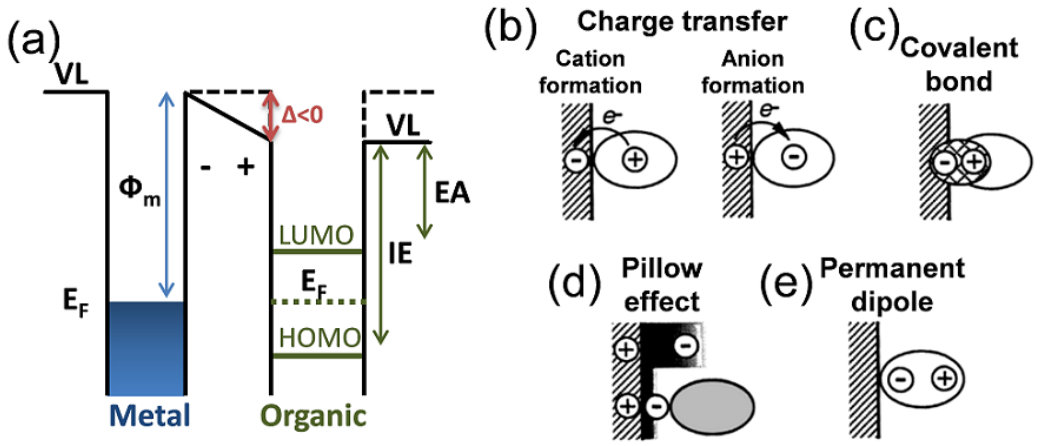

FIGURE 2.1: (a) Energy diagram of a metal-organic semiconductor interface with a dipole barrier. (b)-(e) Possible physical origins of the interface dipole: charge transfer from the molecule (cation formation) or metal (anion formation), covalent bond formation, pillow effect and permanent dipole (adapted from [110]).

Depending on the molecule-surface interaction the interface dipole can have different physical origins, some examples are represented in Figure 2.1(b)(e) [37, 110, 116, 211]. A charge transfer can occur from the molecule to the metal surface (cation formation) or from the metal to the organic molecule (anion formation) yielding a partial equilibration of the chemical potentials (Fermi levels) of the metal surface and molecule (see Figure 2.1(b)). The strength and direction of the charge transfer completely depend on the metal-organic system and are normally accompanied by a structural rearrangement at both sides of the interface. Bond formation is another chemical interaction represented in Figure 2.1(c), which will lead to a rearrangement of the electronic structure and is strongly dependent on the molecule geometry. The resultant surface states can contain mixed electronic states without any resemblance to the states of the separated molecule and substrate [28, 133].

The pillow or push back effect is associated with the compression of the metal wave function tails at the molecule-metal interface due to the Pauli repulsion and schematically represented in Figure 2.1(d). Consequently, the spilling out of the wave function and the local surface potential or work function are reduced. The metal work function drops by a substantial amount with the first monolayer of the adsorbed organic molecules, giving the appearance of an interface dipole barrier, and remains essentially constant for higher coverages. This effect is not limited to physisorbed molecules and also occurs at organic-metal interfaces with

stronger interactions. However, it is harder to differentiate between the various contributions to the interface dipoles [9, 110, 116]. Another important issue is the effect of molecules with a permanent dipole. They create an electrostatic potential and can induce a relative shift of the molecular levels with respect the metal [121, 123]. Not only polar molecules have a permanent dipole, some nonpolar molecules can undergo polar by conformational changes upon adsorption.

The total interface dipole is given by the sum of the above mentioned mechanisms: chemical interactions (charge transfer and bond formation), pillow effect and polarization effects. While the pillow effect always leads to a decrease of the local metal work function, the other two contributions can feature both directions.

The structural and electronic study of these interfaces at atomic scale is of most important in order to achieve a solid understanding to improve the performance of semiconductor devices. The complex processes that can occur at the interface make difficult to know, a priori, the final properties of the interface. This thesis is based on the structure and electronic analysis of the monolayers formed by self-assembly of selected organic and inorganic 2D systems on different metallic surfaces.

2.2 Principles of Scanning Probe Microscopy

Progress in surface science and nanotechnology have been possible due to the advance in tools that allow its study, like the scanning probe microscopy (SPM). This branch of microscopes provides topographical images of surfaces with a physical probe that scan the surface. The two first were the scanning tunneling microscopy (STM) introduced in 1981 and the atomic force microscopy (AFM) introduced in 1985. Many variations of probe based microscopies have been developed since then. The studies that are presented in this thesis have been performed by a combined STM and AFM in frequency modulation mode and under ultra-high vacuum (UHV) conditions at room temperature. Both techniques are complementary since they probe different physical entities.

Historical Introduction

In 1958, Richard Feynman invited the scientist to a new branch of research in an an entitled talk *There's Plenty of Room at the Bottom*: to see individual atoms distinctly and to arrange the atoms the way we want [60]. Around 20 years were needed to develop the tools needed for these goals, the scanning tunneling microscope and the atomic force microscopy. The STM was developed by Gerd Binnig and Heinrich Rohrer in 1981 and the AFM by Gerd Binning in 1986, both at the IBM Zürich Research Laboratory.

The STM was the first instrument that enabled the imaging of flat surfaces with atomic resolution. Only one year after its invention, STM helped to solve one of the most intriguing problems in surface science of that moment: the structure of the Si(111)-(7×7) surface. The adatom layer of the 7×7 reconstruction was imaged with STM by Binnig et al. [20]. This image, together with X-ray and electron scattering, allowed Takayanagi et al. [197] to develop the dimer-adatom-stacking fault (DAS) model for the 7×7 reconstruction. This success led to a wide acceptance of the STM capabilities in surface science and consequently, in 1986, Gerd Binnig and Heinrich Rohrer were awarded with the Nobel Prize for Physics[1].

Since then, STM has been used to image a large number of metals and semiconductors, but despite its phenomenal success a serious limitation exists. As the working principle is based on the tunneling current that flows from the tip to the sample (or vice versa), it is not possible to image insulator materials. Since the first STM experiments, it was noticed that significant forces were acting between tip and sample at the close distance needed for STM. Soon it was speculated that these forces could be put to good use in the atomic force microscope, which was invented by Binnig in 1986 [65]. The AFM is based on a tip attached to a flexible cantilever that bends under the influence of the forces acting on the tip. There are various methods for detecting the motion of the cantilever with nanometer scale accuracy. For example, the first AFM used an STM in the metallic backside of the cantilever to measure its deflection [65]. Because electrical conductivity is not needed for AFM, it can be used to image any flat surface sample. In 1995, one decade after the AFM invention, Giessibl achieved atomic resolution of the Si(111)-(7×7) surface using noncontact AFM in frequency modulation [69].

[1] together with Ernst Ruska for the development of the first electron microscope

2.2.1 Scanning Tunneling Microscopy

Scanning tunneling microscopy is based on the quantum principle of electron tunneling between two conductive electrodes, a sharp tip and the sample. In a general setup, a tip is mounted on a scanner which allows x, y and z movement with subatomic precision. A voltage difference, V_{bias}, is applied between the tip and the sample and when the tip is placed over the surface, with a tip-sample distance in the range of several angstroms, a tunneling current flows from the tip to the sample (or vice versa). The tunneling current depends exponentially with the tip-sample distance and is reduced by one order of magnitude as the distance increases by one angstrom allowing high spatial resolution.

STM can be operated principally in two modes: constant current or constant height. In constant current mode, the tunneling current is the feedback signal in a z-feedback loop. The tip scans the xy plane and the recorded z position is used to generate the topographic STM images. A schematic representations of the basic STM setup is shown in Figure 2.2(a). In the constant height mode, the tip scans the xy plane with a constant z. The recorded tunneling current at each xy point is used to generate the constant height STM image. Constant current is the most common use mode. The contrast observed in a topographic STM image is a convolution of the electronic density of states (DOS) of the sample and its topography. For the simplest situation of a metallic surface, where the local density of states is constant over the surface, the observed STM contrast is due to topographic variations.

If the applied bias voltage is positive with respect to the sample (as schematically shown in Figure 2.2(b)) the energy of the electron states of the sample is lowered. Then, electrons tunnel from occupied tip states into unoccupied sample states. On the other hand, for negative biases they tunnel from occupied sample states into unoccupied tip states. In the experimental setup used in this thesis the bias voltage is applied to the sample with the exception of Chapter 6 that was performed in another setup where the bias voltage is applied to the tip.

Tunneling Current

A tunneling current appears when electrons move through a barrier that they classically can not move though. In classical mechanics, a particle will move

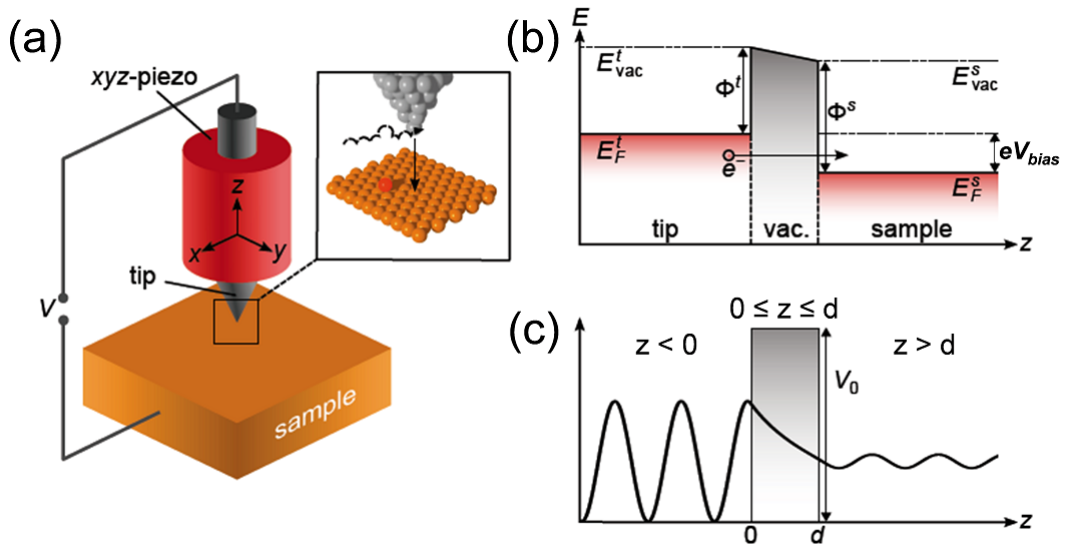

FIGURE 2.2: (a) Schematic representation of the STM where a sharp tip is mounted on a *xyz*-piezo and scanned the sample. In the inset, the tip and sample on the constant tunneling current mode are represented. (b) Schematic energy diagram of the tip-vacuum-sample system. E^t_F and E^s_F are the Fermi energies, E^t_{vac} and E^s_{vac} the vacuum levels, and ϕ_t and ϕ_s the work functions of the tip (index t) and the sample (index s), respectively. The positive bias voltage V_{bias} applied to the sample lowers the energy of the electron states in the substrate, enabling the tunneling of electrons from the tip to the sample across the vacuum barrier. (c) Real part of the particle wave function in one dimension, for the case of a rectangular tunneling barrier of width d and height V_0. The particle is traveling from left to right.

over a barrier only if it has enough energy to do it. However, in the quantum mechanical world, electrons have wavelike properties and have a little probability to move through the barrier, this is called tunnel.

In the quantum mechanics scenario, the electron is described by a wavefunction, $\psi(z)$, and satisfies the time independent Schrödinger equation:

$$H\psi(z) = -\frac{\hbar^2}{2m}\frac{d^2}{dz^2}\psi(z) + U(z)\psi(z) = E\psi(z), \tag{2.1}$$

where H is the Hamiltonian, $\hbar$ is the reduced Planck's constant, m is the electron mass, $U(z)$ is the potential energy and E represents the system energy.

The solutions of Equation 2.1 for a particle traveling from the left to the right with energy $E < V_0$, where V_0 is the barrier height, for the three regions of Figure 2.2(c) are:

$$\psi(z) = \begin{cases} A_1 e^{ikz} + A_2 e^{-ikz} & \text{for z} < 0 \\ B_1 e^{Kz} + B_2 e^{-Kz} & \text{for } 0 \leq \text{z} \leq \text{d} \\ C e^{ikz} & \text{for z} > \text{d}. \end{cases} \tag{2.2}$$

The coefficients A_1, A_2, B_1, B_2 and C are determined by requiring that the wave function is continuous. The wavenumbers k and K are given by $k = \sqrt{2mE/\hbar}$ and $K = \sqrt{2m(V_0 - E)/\hbar^2}$.

The expression of the tunneling current relies on the transmission coefficient, T, which determines the probability of the incoming particle to be transmitted across the barrier, $T = |C|^2/|A_1|^2$, and is calculated for the case of a very high tunneling barrier as:

$$T \approx \exp\left(-2\frac{\sqrt{2m(V_0 - E)}}{\hbar} d\right). \tag{2.3}$$

In Equation 2.3 it can be observed that the transmission probability decreases exponentially with increasing the barrier width, i.e. with the tip-sample distance.

For a metal-vacuum-metal tunneling junction, the tunneling barrier V_0 of a state located at the Fermi level is given by the work function ϕ of the metal (assuming both metals have an equal work function). The work function of a metal surface is defined as the minimum energy needed to remove an electron from the bulk to the vacuum level and it depends on the material and the crystallographic orientation of the surface. The upper limit of the occupied states in a metal is the Fermi level (neglecting the thermal excitation). When the applied bias is much smaller than the work function, $eV_{bias} \ll \phi$, the energy levels of all the sample states that participate in the tunneling are close to the Fermi level. The transmission coefficient can be then be expressed as:

$$T \approx \exp\left(-2\kappa d\right), \tag{2.4}$$

where $\kappa = \sqrt{2m\phi}/\hbar$ is the decay constant of a sample state near the Fermi level in the barrier region. The typical ϕ value for metals is about 5 eV, which gives a typical κ value of 11 nm^{-1}. The apparent barrier height can be calculated as:

$$\phi = \frac{\hbar^2}{8m}\left(\frac{dlnI}{dz}\right)^2 \approx 95\left(\frac{dlnI}{dz}\right)^2. \tag{2.5}$$

The above considerations are sufficient to explain the exponential distance dependence of the tunneling current, but not the electronic effects when imaging. For a quantitative description of the phenomenon of electron tunneling, a three-dimensional description is required. A three-dimensional many-body description of electron tunneling was presented in 1961 by Bardeen [11] and applied to STM in 1985 by Tersoff and Hamann to enable the interpretation of STM images [203].

In Bardeen's approach, the tip and the sample are treated as separate entities [11]. The transition probability between the unperturbed tip states and the unperturbed sample states is calculated by considering the proximity of the tip to the sample as a perturbation potential and applying time-dependent perturbation theory. The tunneling current is then given to first order by:

$$I = \frac{2\pi e}{\hbar}\sum_{t,s}\{f(E_t)[1-f(E_s+eV_{bias})] - f(E_s+eV_{bias})[1-f(E_t)]\}\times|M_{ts}|^2\delta(E_t-E_s). \tag{2.6}$$

The summation runs over the electron states in the tip (index t) and the sample (index s), with energies E_t and E_s. The Fermi function, f, describes the occupation of the states, V_{bias} is the bias voltage and E_{ts} is the transition matrix element between the electron state (χ_t) in the tip and the electron state (ψ_s) in the sample. The factor containing the Fermi functions represents the fact that tunneling can only occur from occupied to unoccupied states, and the delta function ensures that the principle of energy conservation is satisfied. In the case of low temperatures (room temperature or below) and small voltages ($\sim$ 10 mV), the last equation can be approximated by:

$$I \approx \frac{2\pi e^2 V}{\hbar}\sum_{t,s}|M_{ts}|^2\delta(E_t-E_F)\delta(E_s-E_F). \tag{2.7}$$

In this case, only electrons at the Fermi level E_F contribute to the tunneling current. Starting from Bardeen's formalism of electron tunneling, Tersoff and Hamann developed a theory that enabled the interpretation of STM images [203]

in which they assumed the tip to be locally spherical and used s-like wave functions for the tip states. By inserting this assumption into Equation 2.7, the following result for the tunneling current between the tip and the sample is obtained:

$$I = \frac{32\pi^3 e^2 V(\phi^s)^2 D_{tip}(E_F) R^2}{\hbar\kappa^4} e^{2\kappa R} \sum_s |\psi_s(r_0)|^2 \ \delta(E_s - E_F), \tag{2.8}$$

where $\kappa = \sqrt{2m\phi^s/\hbar^2}$, ϕ^s is the work function of the sample surface, $D_{tip}(E_F)$ the tip density of states at the Fermi level, r_0 and R are the center and the radius of the tip curvature. The sample local density of states (LDOS) at position r is in generally defined as $\sum_s |\psi_s(r_0)|^2 \ \delta(E_s - E_F)$. From last equation it can be extracted that the tunneling current depends on the sample local density of states (LDOS). Therefore, if the assumption of s-wave tip states can be applied, constant-current STM images show topographic maps of constant sample density of states.

2.2.2 Frequency Modulation Atomic Force Microscopy

In 1986 Binnig, Gerber and Quate developed, at Stanford University, the atomic force microscope (AFM) to measure ultrasmall forces (less than 1 μN) between a tip and the surface. They proposed to monitor the elastic deformation of a spring with the STM. Other systems were developed to measure the deflection of the cantilever: optical deflection [139], fiber interferometry [165] and piezoresistive methods [207]. The most commonly used is the optical deflector method. In AFM, the imaging signal is given by the force between the scanning probe and the sample, this gives to the AFM an important advantage from STM, it can measure any surface, electrically conductive or insulator.

In FM-AFM, the tip is rigidly mounted in a flexible prong which is driven to oscillate at or close to its resonance frequency (f_0) and constant amplitude. The tip-sample interactions produce a change in the tip oscillation frequency. The observable magnitude is the frequency shift, $\Delta f = f - f_0$. An attractive tip-sample interaction increases the resonance frequency and a repulsive tip-sample interaction decreases the resonant frequency of the tip as can be observed in Figure 2.3. In the next subsection, the connection between Δf and the tip-sample force (F_{ts}) is derived.

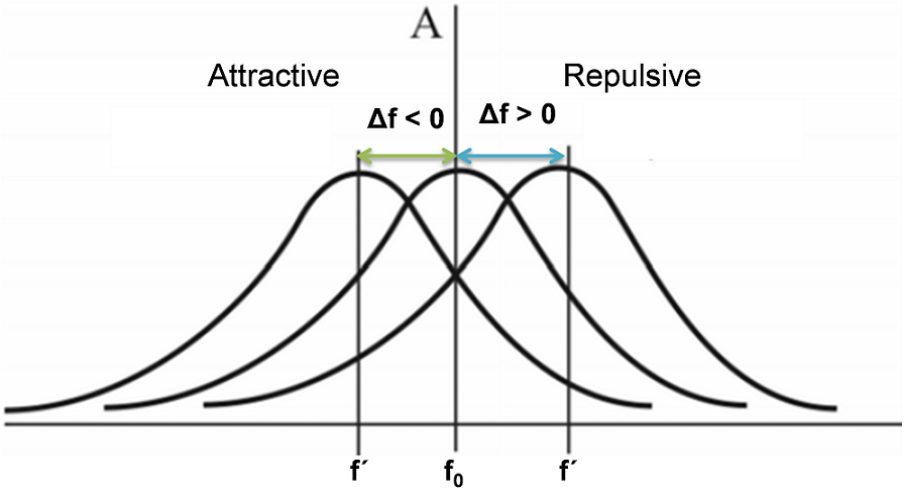

FIGURE 2.3: Frequency versus amplitude representation for a tip-sample far from the surface, $\Delta f = 0$ Hz Attractive tip-sample interaction decreases the resonance frequency of the tip ($\Delta f < 0$). Repulsive tip-sample interaction increases the resonance frequency of the tip ($\Delta f > 0$).

2.2.2.1 Relation between Δf and F_{ts}

In the very simple model of an harmonic oscillator shown in Figure 2.4, the tip is treated as an effective mass $m*$ attached to a spring of stiffness k. The movement of the free (unperturbed) oscillator is given by $q(t) = Acos(2\pi f_0 t)$, and its eigenfrequency f_0 is given by:

$$f_0 = \frac{1}{2\pi}\sqrt{\frac{k}{m*}}. \tag{2.9}$$

As an approximation, the influence of the tip-sample interaction can be described by an additional spring of stiffness k_{ts}, which corresponds to the force gradient experienced by the tip moving in the force field of the sample, $k_{ts} = -\partial F_{ts}/\partial z$ [3, 70]. For oscillation amplitudes, A, significantly smaller than the decay length of the tip-sample interaction (k_{ts}), the decay length can be assumed to be constant during the oscillation cycle. Then, the effective stiffness becomes $k' = k + k_{ts}$, as illustrated in Figure 2.4(b), and the frequency of oscillation of the cantilever becomes

$$f = \frac{1}{2\pi}\sqrt{\frac{k + k_{ts}}{m*}}. \tag{2.10}$$

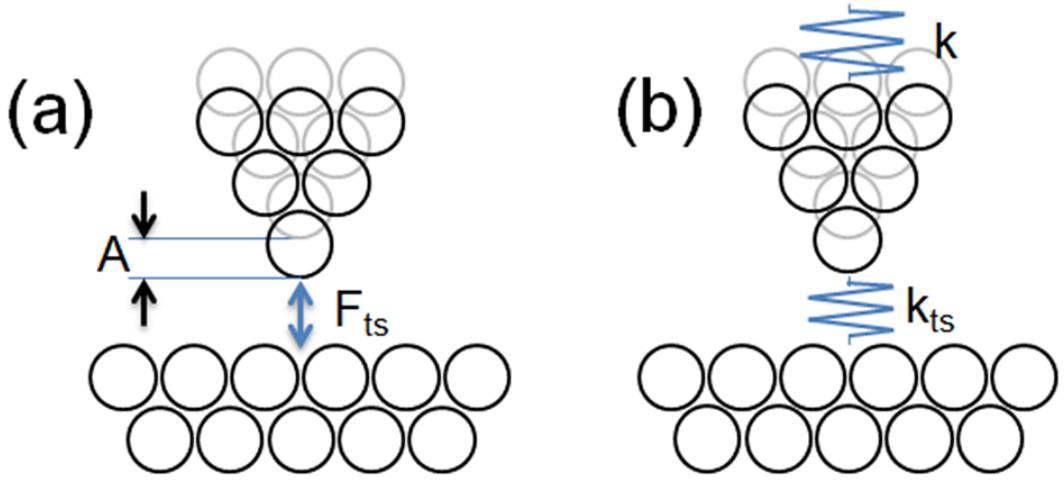

FIGURE 2.4: Schematic representation of the tip and sample in FM-AFM. The tip oscillates at its resonant frequency, f_0, with a certain amplitude, A. (a) The tip-sample interaction. (b) The tip is attached to a spring of stiffness k. The tip-sample interaction is taken into account by an additional spring of stiffness k_{ts}.

Then the movement of the tip is described by a weakly disturbed harmonic oscillator of effective stiffness k'. If the force gradient is much smaller than the stiffness of the spring, $k_{ts} \ll k$, the square root in 2.10 can be approximated to lowest order by a power series of k_{ts}/k,

$$f = f_0\sqrt{1+\frac{k_{ts}}{k}} \approx f_0\left(1+\frac{1}{2}\frac{k_{ts}}{k}\right). \tag{2.11}$$

The frequency shift, Δf, observed in FM-AFM is approximately equal to the force gradient at the position of the apex of the tip z above the surface plane. In the limit of oscillation amplitudes small compared to the decay length of the tip-sample interaction, Δf can be expressed as:

$$\Delta f \approx -\frac{f_0}{2k}\frac{\partial F_{ts}}{\partial z}. \tag{2.12}$$

A more general expression of Δf, valid for small and large amplitudes, was derived using first-order perturbation theory in the Hamilton-Jacob approach [70]:

$$\begin{aligned}\Delta f &= -\frac{f_0^2}{kA}\int_0^{1/f_0} F(z + A[1 + cos(2\pi f_0 t)])cos(2\pi f_0 t)dt \\ &= -\frac{f_0}{\pi kA}\int_{-1}^{1} F(z + A[1 + u])\frac{u}{\sqrt{1-u^2}}\, du.\end{aligned} \tag{2.13}$$

This expression is a non trivial mathematical operation and an exact analytical inversion is not known. Different inversions procedures have been proposed by Gotsmann [78], Durig [50], Giessibl [73] and Sader and Jarvis [167]. The methods proposed by Giessibl and Sader and Jarvis are more robust against the presence of experimental noise. Giessibl's method needs powerful mathematics routines to invert a matrix of (n x n) elements, where n is the number of points of the Δf *vs.* z spectra. Sader and Jarvis' method can be easily implemented being the most commonly used method and the one used in this thesis. However, for a proper extraction of the tip-sample force the tip-sample distance range is needed to be extended to the free oscillation region, i.e. where the tip-sample force vanishes. Otherwise the whole force curve will be shifted to smaller absolute force values.

2.2.2.2 Tunneling Current for an Oscillating Tip

Due to the oscillation of the tip, the tunneling current is not constant and varies over one oscillation cycle. The bandwidth of the tunneling current is much smaller than the oscillation frequency and, therefore, the measured tunneling current is time-average over the entire range of oscillations. The time average tunneling current, $\langle I(z, A)\rangle$, can be expressed as [72]:

$$\langle I(z, A)\rangle = I_0 M_1^{1/2}(-4\kappa A)\exp(-2\kappa z), \tag{2.14}$$

where M_b^a is the Kummer function. When $\kappa A \gg 1$ the previous equation can be rewritten as:

$$\langle I(z, A)\rangle \approx \frac{I_0}{\sqrt{4\pi\kappa A}}\exp(-2\kappa z), \tag{2.15}$$

The absolute tunneling current can be extracted by applying the algorithm described by Sader and Sugimoto [168].

2.2.2.3 Combined STM/FM-AFM

Six parameters are needed to characterize an experiment with a combined STM/FM-AFM. Three are determined by the tip sensor and the other three can be freely adjust.

- **Spring constant, k:** for typical cantilevers this value can be found from its dimensions and density. For a length resonator (KolibriSensor) or qPlus sensors the spring constant can be calculated from the thermal noise [3]. In this thesis is used the spring constant value given from the commercial company (Specs, GmbH), that is 540 kN/m for the Kolibri sensor [206].

- **Resonant frequency, f_0:** is experimentally calculated by measuring the amplitude vs. frequency of the tip. The resonant frequency of the tip is the frequency value at which the response amplitude is a relative maximum (see blue plot in Figure 2.5). This value is calculated in each experiment and for the Kolibri sensor the resonant frequency is $\sim$ 1 MHz.

- **Quality factor, Q:** is defined as the ratio of the energy stored in the oscillating system and the energy dissipated per cycle:

$$Q = 2\pi \frac{E_{CL}}{\Delta E_{CL}}, \tag{2.16}$$

  where E_{CL} is the energy stored in the oscillating cycle and ΔE_{CL} the dissipated per cycle. For the Kolibri sensor the Q factor is $\sim$ 25000 in UHV.

- **Oscillation amplitude, A:** is a parameter set by hand while you are measuring. It is necessary to calibrate this value periodically following the procedure presented in Chapter 3.

- **Bias voltage between tip and sample V_{bias}:** when imaging in FM-AFM mode it is important to choose a bias voltage that compensates the electrostatic interaction of the tip-sample, so the contact potential different (CPD) of the tip-sample. It is also important to choose a small bias voltage to minimize the tunneling current when measuring the frequency shift to avoid the Phantom force effect [224, 225, 230].

- **Frequency shift of the cantilever, Δf or tunneling current, I:** they are the set point for the z-feedback. The frequency shift is selected when imaging in FM-AFM mode and tunneling current in STM mode.

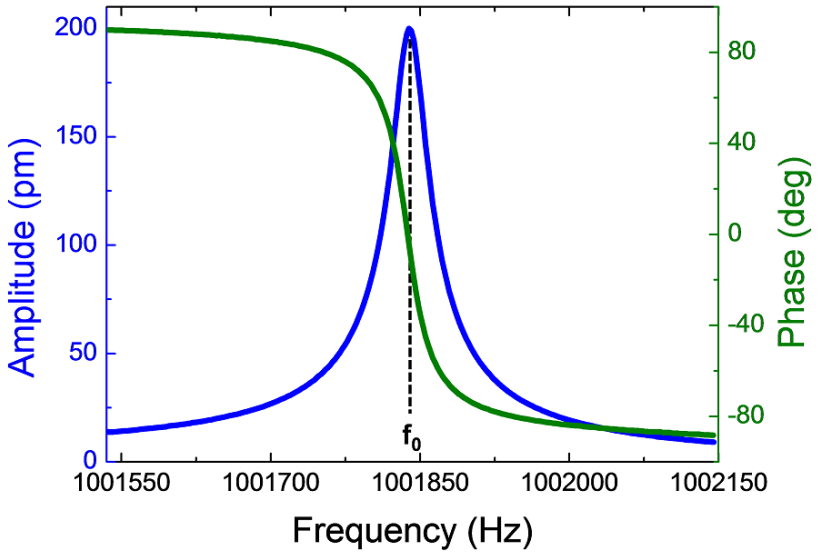

FIGURE 2.5: Amplitude and phase versus oscillation frequency when the tip is far away from the sample. The resonant frequency is calculated from this spectrum and corresponds to the frequency value at which the amplitude is maximum and the phase is 0°.

The spring constant, resonant frequency and quality factor are determined by the sensor used, and the oscillation amplitude and bias voltage are freely adjusted. Depending on the operation mode the tunneling current or frequency shift value is selected and used as the z-feedback signal.

The feedbacks in a combined STM and FM-AFM are represented in Figure 2.6. The STM feedback is represented in the left side (green box) and the FM-AFM in the right side. Three feedbacks are needed for FM-AFM: phase locked loop (PLL) (blue box), amplitude feedback (red box) and z-controller (blue box).

At each scanning point, (x, y), the oscillation amplitude (A_{osc}), frequency (f), phase and excitation are measured. In order to keep the force sensor oscillation always at resonance with constant amplitude, a phase locked loop (PLL) is used. In the PLL, the signal being proportional to the actual amplitude is phase shifted by $\pi/2$ to ensure resonance. The amplitude feedback circuit provides an enhancement factor needed to keep the amplitude constant called as excitation signal and carries information about dissipating energy. Both signals are amplified, and returned to the free prong, whereas Δf serves for distance control when working in AFM mode. The z-controller keeps Δf (AFM mode) or I (STM mode) constant.

By choosing the tunneling current or frequency shift as the z-feedback channel topographic images in STM and FM-AFM are respectively performed. It is also

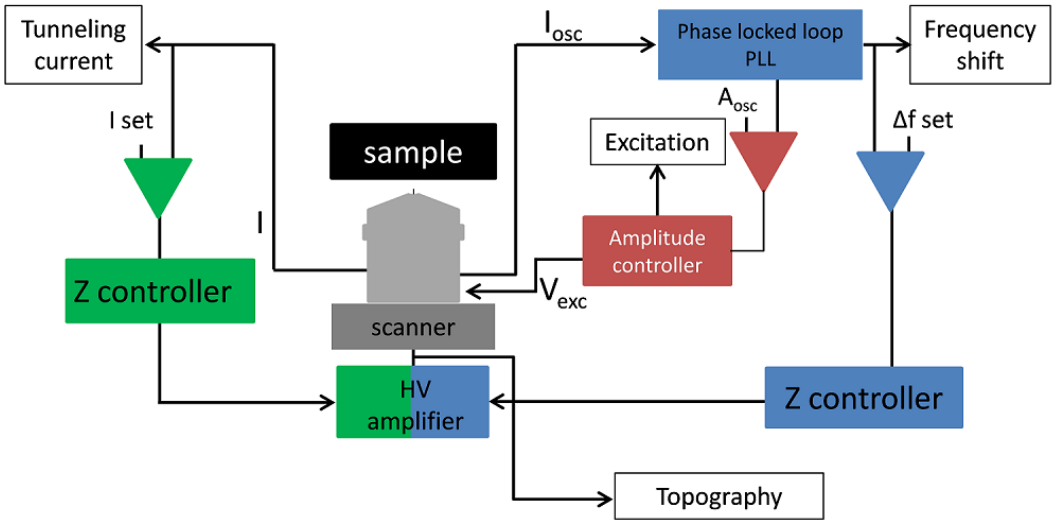

FIGURE 2.6: Schematic representation of a Kolibri sensor over a sample and the feedbacks circuits for a combined STM/FM-AFM. The STM feedback is represented in the left side (green box) and the FM-AFM in the right side. The four signal outputs are in white: topography, tunneling current, frequency shift and excitation.

possible to record images at constant hight, i.e. the z-feedback is switch off. Then, information about the tip-sample interaction can be extracted from the frequency shift channel while information about the density of states can be extracted from the tunneling current channel .

The stability of the z-feedback in FM-AFM mode is smaller than in STM due to the non monotonic relation of the force with the tip-sample distance. Force is attractive at larger distances and becomes repulsive at shorter tip-sample distances, which makes difficult to operate at stable z-feedback in FM-AFM.

2.2.3 Tip-Sample Forces

The force between the tip and the sample is composed of different contributions and can be classified by their range and strength. In vacuum, the long-range interactions (up to 100 nm) are composed by van der Waals, electrostatic and magnetic interactions and the short-range (fractions of nm) by chemical forces. In Figure 2.7(a) an schematic representation of the tip and sample as well as the forces that act between the tip and the sample are presented. In (b) the typical forces and their range are sketched. To get atomic resolution with AFM is necessary to measure only the forces which change at atomic level, therefore it is

desirable to minimize the long-range forces: van der Waals and electrostatic. It is only possible to distinguish between long- and short-range forces in dynamic AFM by proper choice of the oscillation amplitude of the cantilever. In the following, electrostatic, van der Waals and chemical forces are defined.

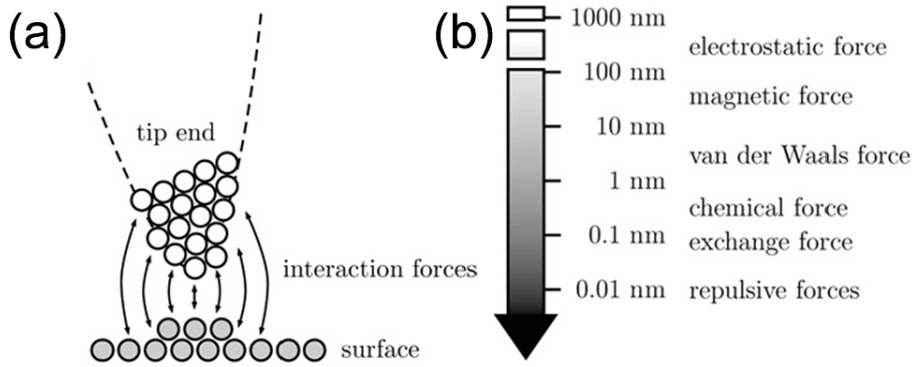

FIGURE 2.7: (a) Schematic representation of the tip and the sample and the interaction forces. (b) Representation of the forces that act at each z-scale.

Electrostatic Force

The electrostatic force is generated between a charged or conductive tip and sample that have a potential difference and follows the Coulomb law. Mathematically, the tip-sample geometry can be described as a plate capacitor with the capacitance $C = C(z)$, which depends on the tip-sample distance z, and on the tip structure [109]:

$$F_{elec}(z) = \frac{1}{2}\frac{\partial C}{\partial z}(V_{bias} - V_{CPD})^2, \tag{2.17}$$

where V_{bias} is the voltage applied to the sample and V_{CPD} is the contact potential difference between the sample and the tip. Considering the tip modeled by a sphere of radius R and for tip-sample distances smaller than the tip radius, the electrostatic force can be expressed as:

$$F_{elec}(z) = -\frac{\pi\epsilon_0 R}{z^2}(V_{bias} - V_{CPD})^2, \tag{2.18}$$

where ϵ_0 is the vacuum permittivity, V_{bias} is the voltage applied to the sample and V_{CPD} is the contact potential difference between the sample and the tip. Other expressions are found in the literature to account for more realistic tip

geometries [16]. However, this expression is illustrative to show two important issues: the electrostatic force has a parabolic dependence on bias voltage ($F_{elec} \propto V_{bias}^2$) and the electrostatic interaction can be minimized by choosing a $V_{bias} = V_{CPD}$.

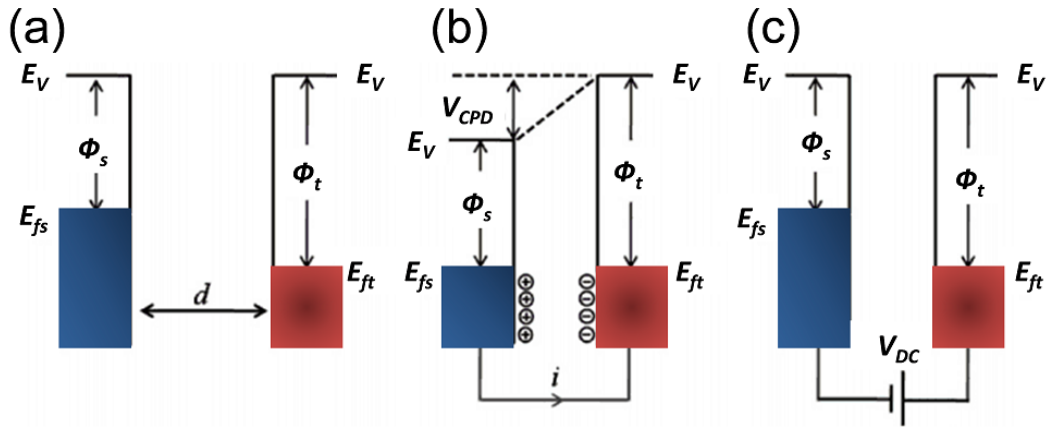

FIGURE 2.8: Origin of the CPD between two different materials (tip and sample) with work functions ϕ_t and ϕ_s and Fermi energies of E_{fs} and E_{ts}. (a) Tip and sample are separated a distance d and no electrical connected. (b) Establishment of an electrical connection causes a CPD and hence an electrical force F_{el}. (c) Compensation of the field by applying $V_{bias} = V_{CPD}$.

The contact potential difference is caused by a difference in the work function of the electrically connected tip and sample. In Figure 2.8(a) the CPD origin is illustrated using the example of two initially separated metallic materials with work functions ϕ_t and ϕ_s and Fermi energies E_{ft} and E_{fs} where the subindex t is refereed to tip and s to the sample. When an electrical connection is made, Figure 2.8(b), a flow of charge from the sample to the tip (because $E_{fs} > E_{ts}$) appears until both Fermi levels are aligned while the local vacuum level, E_v, is lowered by $eV_{CPD} = \phi_t - \phi_s = \Delta\phi$. Hence, an electric field builds up, which gives rise to a long range electrostatic force, similar to a charged capacitor. By applying an appropriate bias voltage $V_{bias} = V_{CPD}$ the electric field becomes compensated (Figure 2.8(c)). This is subject to a subfield of AFM, the called Kelvin probe force microscopy (KPFM), or local bias spectroscopy (Δf vs. V_{bias}) that will be presented in the last section of this chapter.

Van der Waals Force

Van der Waals forces (vdW) exist between atoms or molecules and have their origin in the fluctuation of the electric dipole moment of an atom induced by the

fluctuating moment of a second nearby atom. Van der Waals forces can be divided into three groups:

i Dipole-dipole force: molecules having permanent dipoles will interact by dipole-dipole interaction.

ii Dipole-induced dipole forces: the field of a permanent dipole induces a dipole in a non-polar atom or molecule.

iii Dispersion forces: due to charge fluctuations of the atoms there is an instantaneous displacement of the center of positive charge against the center of the negative charge. Thus at a certain moment a dipole exists and induces a dipole in another atom.

The van der Waals force between the tip and the sample is always attractive. Considering the tip modeled by a sphere of radius R and a flat surface, the vdW force is given by [111]:

$$F_{vdW}(z) = -\frac{A_H R}{6z^2}, \tag{2.19}$$

where A_H is the Hamaker constant (10^{-19} - 10^{-20}J) which depends on the type of material of the tip and sample and z is the tip-sample distance [85]. For a certain tip and sample material the van der Waals force only depends on the absolute tip-sample distance with a function determined by the geometric shape of the tip and is independent of the applied bias.

Chemical Force

Chemical force is the force that tightly binds two o more atoms to form a bond. For a covalent bond the range is about 0.1-0.2 nm with a bonding force of 3-9 nN [111]. Chemical forces are not easy to describe and the two empirical models more commonly used are the Morse and Lenard-Jones potentials. The Morse potential is induced by approximating the covalent bonding interaction and is described as:

$$V_{Morse} = -E_{bond}\,[2e^{-\kappa(z-\sigma)} - e^{-2\kappa(z-\sigma)}], \tag{2.20}$$

where E_{bond} is the bonding energy, σ is the equilibrium distance for this bond and κ is the decay length. The Lenard-Jones potential is derived from the approximation of two atoms interaction:

$$V_{LJ} = -E_{bond}\left(2\frac{\sigma^6}{z^6} - \frac{\sigma^{12}}{z^{12}}\right). \tag{2.21}$$

The z^6 is the attractive term and comes from the van de Waals interaction, z^{12} is the repulsive term and describes Pauli repulsion at short range due to the overlapping electron orbital.

2.2.4 Dissipation

The frequency shift of the tip is caused by conservative tip-sample forces. But non-conservative forces can also exist and produce an hysteresis in the force versus distance curve. The dissipation signal in FM-AFM is the extra amount of energy that the tip sensor requires to keep the oscillation amplitude constant and at resonance under the presence of non-conservative forces. The excitation signal is regulated by the amplitude controller. The extra excitation can be related with energy dissipated from the tip sensor within an oscillation cycle [36].

The non-conservative tip-sample energy per cycle can be expressed as:

$$\Delta E_{ts} = \oint F_{ts}(z + z')dz'. \tag{2.22}$$

When the tip is far from the sample, the damping of the tip sensor is due to internal dissipation and the energy loss per oscillation cycle, ΔE_{CL}, is:

$$\Delta E_{CL} = 2\pi\frac{E}{Q}, \tag{2.23}$$

where E is the energy of a tip sensor, E=$kA^2/2$, and Q is the quality factor. For a Kolibri sensor, the spring constant is $\sim$ 540 kN/m, the normal amplitude is 200 pm and the normal Q is $\sim$ 25000, then the energy loss per cycle (Equation 2.23) is $\sim$ 2 eV. When the tip sensor oscillates without external forces, the amplitude drive signal, A_{drive}, is related with the internal dissipation of the free oscillator:

$$|A_{drive}| = |A|\frac{\Delta E_{CL}}{2\pi E} = \frac{|A|}{Q}. \tag{2.24}$$

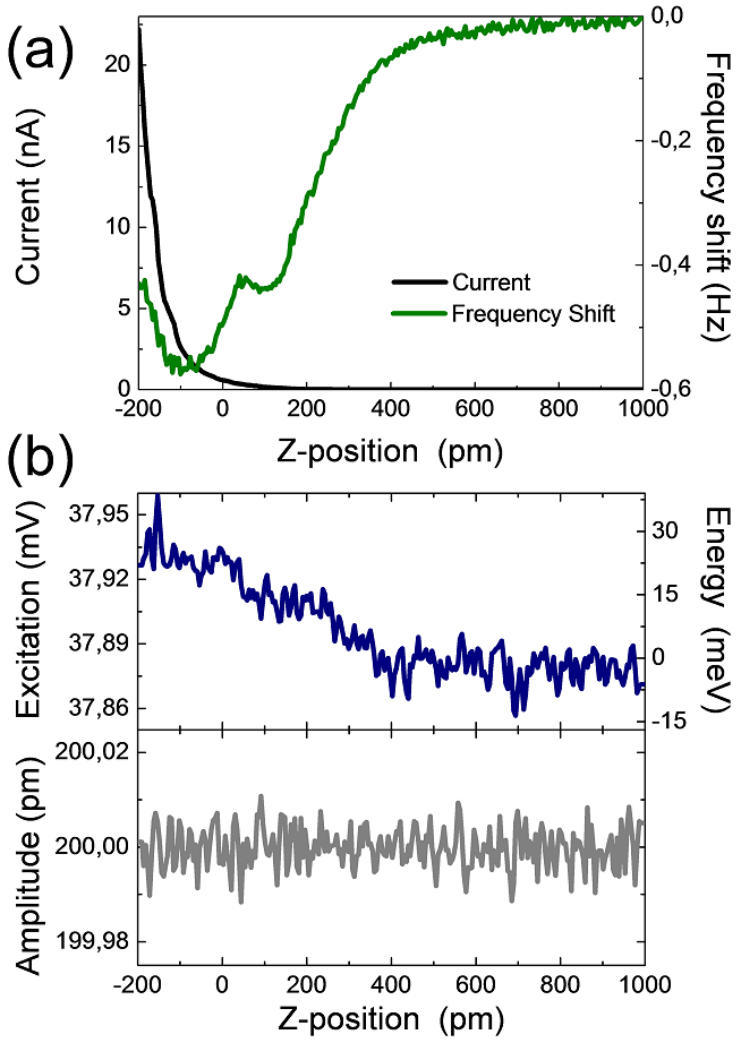

FIGURE 2.9: Example of z-spectroscopy performed over clean Au(111). (a) Tunneling current and frequency shift versus z, (b) amplitude and excitation versus z. (c) Calculated dissipative energy from (b) using Equation 2.26. Parameters: A = 200 pm, Q = 21779, k = 540 kN/m, the z=0 pm correspond to the setpoint position.

At short tip-sample distances, besides the internal dissipation (ΔE_{CL}), the dissipation for non-conservative forces tip-sample (ΔE_{ts}) has to be taken into account. The driving signal, $|A_{drive}|$, is increased by the amplitude controller to $|A'_{drive}|$:

$$|A'_{drive}| = |A|\frac{\Delta E_{CL} + \Delta E_{ts}}{2\pi E} = |A|\left(\frac{1}{Q} + \frac{\Delta E_{ts}}{2\pi E}\right). \tag{2.25}$$

The dissipation energy can be then calculated through [72]:

$$\Delta E_{ts} = 2\pi E \left(\frac{|A'_{drive}|}{|A|} - \frac{1}{Q} \right). \tag{2.26}$$

The SPM electronics measures the amplitude drive, that in this thesis is called excitation when is represented in spectroscopies. An example of z-spectroscopy is presented in Figure 2.9 where the tunneling current, frequency shift, amplitude and excitation are shown in (a) and (b). The frequency shift starts to change (at $\sim$ 300 pm) before the onset of the tunneling current and at this point the excitation changes evidencing energy dissipation. This is indicative of a tip ended with a non-conductive material. Although this is uncommon in the experiments presented in this thesis, it makes here a good example. From this value, and using the Equation 2.26, the energy dissipation per cycle was calculated and is presented in the right axis of Figure 2.9(b).

Since in this thesis there are no quantifications of dissipation energy the excitation will be presented as in the left axis of Figure 2.9(b). Some reviews are found in the literature where the origin and interpretation of the dissipation are discussed: [1, 49, 95, 119, 160, 208].

2.2.5 Spectroscopies

In this thesis, principally two spectroscopies have been used: distance and bias-spectroscopy. In a z-spectroscopy all STM and AFM channels are recorded while the tip-sample distance is swiped, while in bias-spectroscopy all STM and AFM channels are recorded while the bias voltage is swiped. The recorded channels in both spectroscopies are: tunneling current, frequency shift, amplitude and excitation. In all the spectroscopies, the tip is first stopped at a certain lateral position (x, y) and subsequently, the z-feedback is switched off for recording the spectra, while the amplitude feedback and PLL remains active. Before acquiring the spectroscopic data, the z-drift was measured and corrected if needed.

Frequency Shift versus Distance

Force spectroscopy is a technique to measure the local force acting between the tip and the sample and can be performed locally. Long range frequency shift versus z curves are needed to use the algorithm proposed by Sader and Jarvis to convert

frequency shift into force [167] as mentioned before. In Figure 2.10 an example of $\Delta f(z)$ curve and its inversion into $F(z)$ is given.

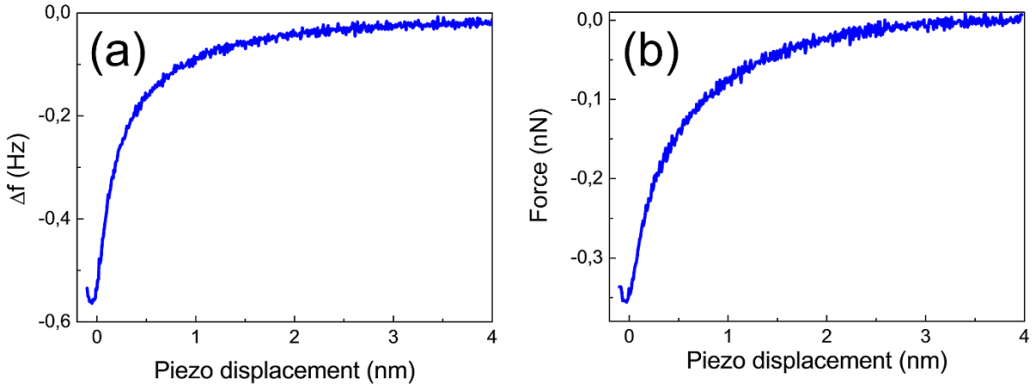

FIGURE 2.10: (a) Example of frequency shift versus z over Cu(111). The z = 0 pm correspond to the setpoint position. The z-feedback was switched off and the tip was retracted 4 nm before to start the z-spectroscopy. Parameters: Bias = +1.2 V and A=200 pm. (b) Inversion of (a) with the Sader and Jarvis method [167]. Parameters: f_0= 1001838.9 Hz and k = 540 kN/m.

The measured frequency shift and therefore the force, includes the interactions from electrostatic, van der Waals and chemical forces. The separation of these forces is not straightforward. The electrostatic contribution can be nullified by choosing the correct bias voltage ($V_{bias} = V_{CPD}$). Guggisberg et al. reported the separation of the van der Waals forces by fitting the data from distances from 1 to 6 nm and after subtracting it from the force curve. The remaining part is then related with the short-range chemical force [80]. However, to fit the van der Waals contribution a tip-sample model has to be considered. For this reason, a good fitting may not be possible for complex tip geometries. Another possibility for heterogeneous surfaces is to assume that the long-range force region includes a distance from the free-oscillation regime (no tip-sample interaction) to the position at which the total force curve for the different surface regions starts deviating from a common behavior. The long-range force is site-independent and can be eliminated by taking the difference of force-distance curves extracted at a few judiciously chosen surface sites [100, 129].

Tunneling Current versus Distance

Tunneling current versus tip-sample distance spectroscopies, $I(z)$, can be used to locally probe the decay length of the tunneling current trough the relation:

$$I = I_0 \exp\left(-2\kappa z\right), \tag{2.27}$$

where I_0 is the tunneling current at the point of contact. A simple approximation is that there is a square potential barrier between the tip and the sample surface with apparent height ϕ_{app}, and that only electrons from the Fermi level participate in the tunneling current, in this case:

$$\kappa = \frac{\sqrt{2\,m\,\phi_{app}}}{\hbar}, \tag{2.28}$$

with $\phi_{app} = \bar{\phi} - e\mathrm{V}_{bias}/2$, e being the elementary charge, m being the electron mass and $\hbar$ being the reduced Planck's constant. The apparent height depends on the tip and sample averaged work function, $\bar{\phi} = (\phi_{tip} + \phi_{sample})/2$, as well as on the applied bias voltage, V_{bias}.

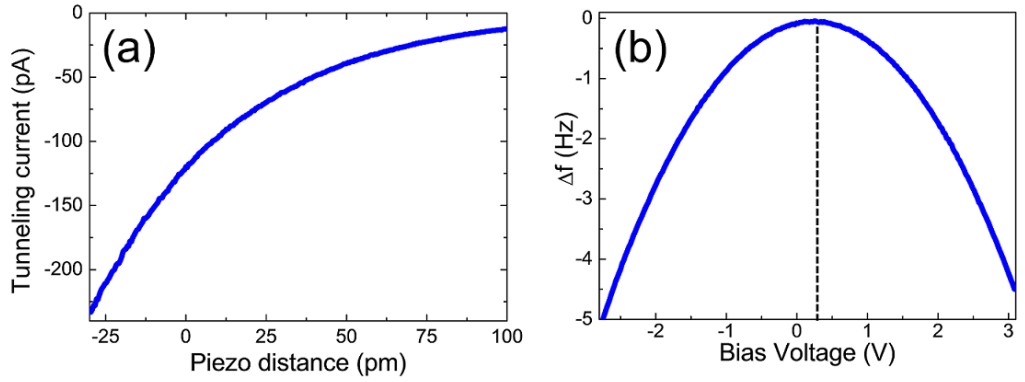

FIGURE 2.11: (a) Example of tunneling current versus z over Cu(111). The z = 0 pm correspond to the setpoint position. The z-feedback was switched off and the tip was retracted 100 pm before to start the z-spectroscopy. The kappa value, calculated from Equation 2.27 is 1.1Å^{-1}. Parameters: Bias = -1.3V and A=200 pm. (b) Example of frequency shift versus bias voltage over Cu(111). The tip was retracted 300 pm from the setpoint position before to start the spectroscopy. For this tip apex the CPD value, calculated from Equation 2.31, is +235 mV. Parameters: A=200 pm.

However, the conversion of the decay length into barrier height presented in Equation 2.28 is not straightforward and requires some caution. Equation 2.28 is valid for one-dimensional square barriers. If the tip and sample do not have equal work functions the barrier deviates from the square geometry. Previous equations have the assumption that only electrons from the Fermi level participate in the tunneling process. This is valid for small bias voltage, $\sim$ 10 mV, that is not the

common situation in this thesis. At higher bias voltage, states far from the Fermi level contribute to the overall current. Another important point is to perform the spectra with a stable tip-sample junction without tip-sample deformations. This is a critical issue discussed in this thesis.

Frequency Shift versus Bias Voltage

The contact potential difference can be measured from the dependence of the electrostatic force with the applied bias. From Equations 2.12 and 2.17 the expression for the $\Delta f(V_{bias})$ can be rewritten as:

$$\Delta f = -\frac{f_0}{4k}\frac{\partial^2 C(z)}{\partial z^2}\,(V_{bias} - V_{CPD})^2. \tag{2.29}$$

The dependence of the capacitance with the distance, $C(z)$, depends on the geometry. For example, if the tip-sample is modeled by an ideal plate capacitor of capacitance $C(z) = \varepsilon A/z$, where A is the surface area of the capacitor plate, Equation 2.29 is:

$$\Delta f = -\frac{f_0}{2k}\frac{\varepsilon_0 A}{z^3}\,(V_{bias} - V_{CPD})^2. \tag{2.30}$$

A general equation of the $\Delta f(V_{bias})$ and the one that will be used in this thesis is:

$$\Delta f = a - b\,(V_{bias} - V_{CPD})^2. \tag{2.31}$$

The contact potential difference value depends on the work function of the tip and sample and is defined as:

$$V_{CPD} = \frac{\phi_{tip} - \phi_{sample}}{-e}. \tag{2.32}$$

For quantitative analysis an adequate calibration is necessary (see for example [74]). For instance, if the CPD values are measured over surface areas A and B with the very same tip apex and the work function of one of the two areas are known, the other can be calculated:

$$\Delta\phi = \phi_B - \phi_A = e\ (V_{CPD}(B) - V_{CPD}(A)). \tag{2.33}$$

The CPD is based on the capacitive force between two macroscopic parallel metallic electrodes, which, do not have lateral electrostatic force distributions at the atomic-scale. In atomically resolved CPD measurements, CPD is defined as LCPD (local contact potential difference), which depends on the electrostatic interaction on the atomic scale (short-range electrostatic forces). The LCPD is based on the concept of a local work function, which illustrates the short-ranged (along the direction normal to surface) atomic scale variation of work function on metal surfaces which can arise, for instance, from local surface dipoles, inhomogeneous charge (re-) distributions, polarization effects and chemical interactions [22, 25, 215] and its origin was controversially discussed [74]. Additionally, variations of the LCPD with the tip-sample distance have been reported [10, 13, 177, 235].

Chapter 3

Experimental Setup

The following chapter is dedicated to experimental issues. The ultra-high vacuum system used during this thesis will be described. It is a commercial system that has been installed at the beginning of this thesis and therefore, the first months were devoted to the establishment of experimental and measuring protocols and the optimization of the preparation of tip and sample conditions. Additionally, many improvements and replacements have been performed in the course of this thesis producing a delay of the experimental results.

3.1 Description of the UHV System

The UHV system employed for the experimental part of this thesis consists in three connected chambers: scanning probe microscope (SPM) chamber, preparation chamber and load-lock as is depicted in Figure 3.1. Two plate valves are installed between each chamber. The SPM and the preparation chamber are normally connected and the load-lock is isolated from the rest. The pumps needed to obtain and maintain a base pressure of 3 x 10^{-11} mbar are:

- Two turbo pumps: one connected to the load-lock and the other to the preparation chamber.
- Ionic pump with a titanium sublimation pump: connected to the SPM chamber.

- Two rotatory pumps: connected to the turbo pumps to provide the initial pressure needed for the turbo pumps.

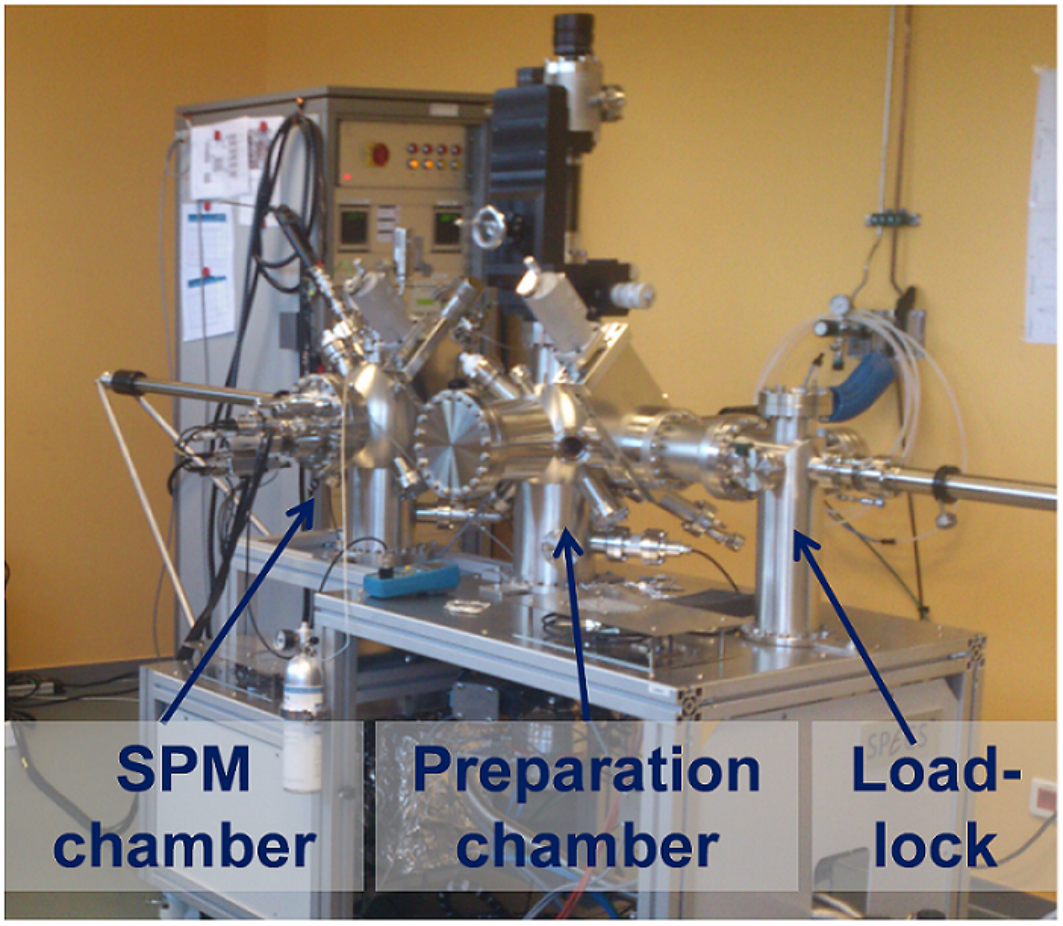

FIGURE 3.1: Picture of the UHV system employed in this thesis. The three chamber are labeled.

To measure the pressure, three controllers are installed, one per chamber. In the following, the components of each one will be presented.

Scanning Probe Microscope Chamber

This is the chamber where the scanning probe microscope is installed (Figure 3.2(a)). It is a variable temperature SPM Aarhus 150 with a Kolibri sensor (Specs, GmbH). There are two ion guns to perform argon sputtering of the tip and the sample and a parking stage with capacity for five samples with a sample heater.

Preparation Chamber

The preparation chamber is situated between the SPM chamber and the load lock. A picture is shown in Figure 3.2(b). In this chamber we mounted two organic molecular beam evaporators and a residual gas analyzer which detects masses up to 100 u. One of the organic evaporators has four independent cells and the other has two. Additionally, another sample heater is installed in the sample manipulator that enables the simultaneous heating of the substrates while molecules are evaporating.

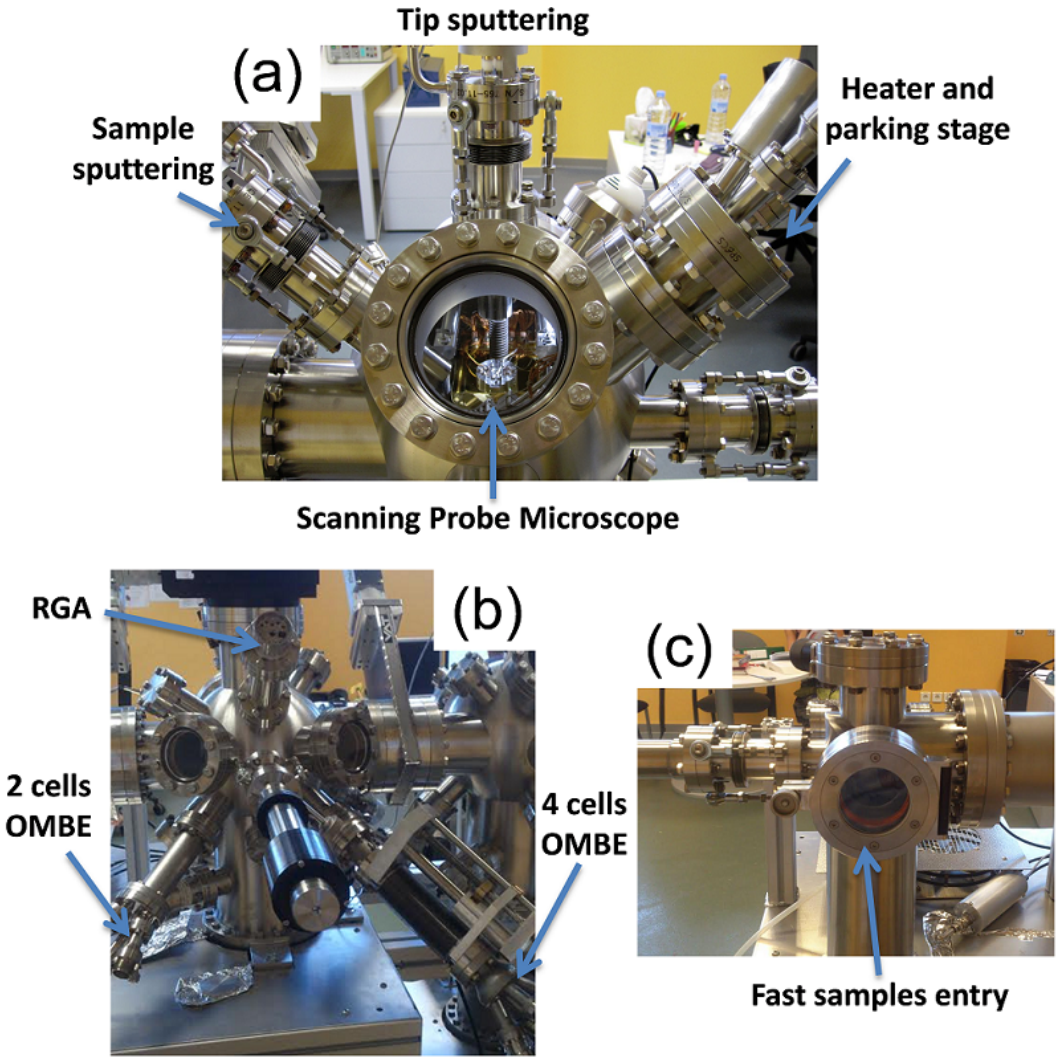

FIGURE 3.2: Pictures of the three chambers: (a) the scanning probe microscope (SPM), (b) the preparation and (c) the load-lock. The principal components are indicated.

Load-Lock

The load-lock is normally not connected to the rest of the chamber because the fast entrance does not allow to get a better pressure than 10^{-8} mbar and the valve

plate that separates the load-lock and the preparation chamber is always closed. It is used to transfer samples into and outside the UHV system without the needed to open the chamber and its pumping system works separately with a rotatory and turbo pumps. A picture is shown in Figure 3.2(c).

3.2 The STM/FM-AFM Setup

As already mentioned, the microscope is an Aarhus 150 variable temperature controlled by a Nanonis SPM control system.

Tip Sensors

Soft silicon cantilevers with spring constants on the order of 30 N/m and resonant frequencies on the order of 160 kHz are used in dynamic AFM. However, small oscillation amplitudes are needed to probe short-range force components and cantilevers require high oscillation amplitudes for stable operation. The used of piezoelectric quartz sensors allows to operate at small amplitudes overcoming this problem. Two fundamentally different types of quartz sensors are used in UHV: qPlus and Kolibri sensor.

In this thesis, commercial Kolibri sensors (Specs GmbH) have been used, except in Chapter 6 where the experimental part was performed in the group of Prof. F.J. Giessibl with a qPlus sensor [71]. The qPlus consists on one prong rigidly attached to a solid substrate while the second oscillating prong with metallic tip acts as a probe. This sensor has a stiffness of $\sim$ 1800 N/m and a resonant frequency of $\sim$ 25 kHz.

The Kolibri sensor is a piezoelectric quartz length-extension resonator (LER) [206] and a schematic representation is shown in Figure 3.3(a). The oscillation of the quartz rod is excited by applying a sinusoidal voltage U_{exc} to one of its sidewall electrodes. The electric field across the rod causes an extension or contraction of the quartz rod across its width due to the piezoelectric effect resulting in a sinusoidal length oscillation. Surface charges induced by the piezoelectric effect are read out as the current I_{osc} at the opposite sidewall electrode and converted by an ex situ I-V converter into a voltage which is used for the oscillation feedback. The U_{exc} is the electrical excitation and the I_{osc} is the electrical readout.

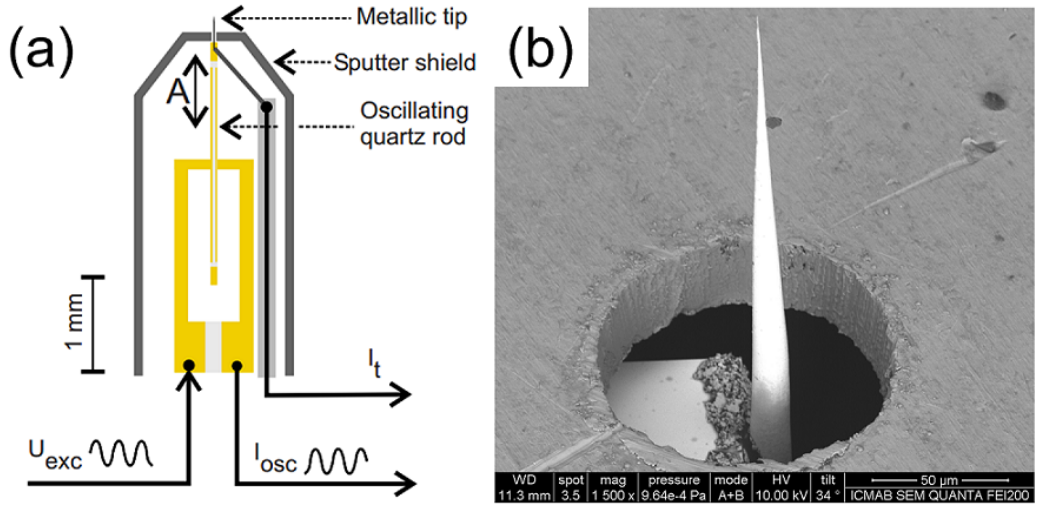

FIGURE 3.3: (a) Schematic representation of a KolibriSensor extracted from [206]. (b) Scanning electron microscope (SEM) image of Kolibri's tip.

A tiny chemically etched tungsten tip (about 400 μm in length and a width of 30 μm) is attached to one end of the quartz rod. A scanning electron microscope (SEM) image of the tip is represented in Figure 3.3(b). The tip is contacted separately by a conductive fiber, enabling independent readout of the tunneling current I_t from the oscillation current I_{osc} (see Figure 3.3(a)). The stiffness is even higher for the qPlus sensor, 540 kN/m, and the resonant frequency on the order of 1 MHz. The whole sensor is encapsulated in a metal housing shield (sputter shield). It protects the quartz sensor, enabling repeated in situ sputtering of the tip. Unfortunately, the design does not allow to in-situ tip-exchange and every time that a Kolibri sensor has to be replaced the SPM chamber has to be opened.

Tip Sputtering

The metal housing of the Kolibri protects the quartz sensor and allows in situ tip sputtering. However, sputtering into an SPM is delicate since sputtering ions could hit the piezos of the SPM scanner or the approaching motor. Those ions could electrically charge up the piezos, destroy the piezoelectric material or produce a cross between insulating pieces by deposition of metal atoms. To avoid these problems a special plate (tip sputtering plate) has to be located in the sample stage of the microscope as can be observed in Figure 3.4. The sputtering plate has a central hole and is adjustable. Every time that the Kolibri sensor is exchanged, the tip sputtering plate has to be readjusted to ensure that the hole is located exactly in the center of the Kolibri sensor.

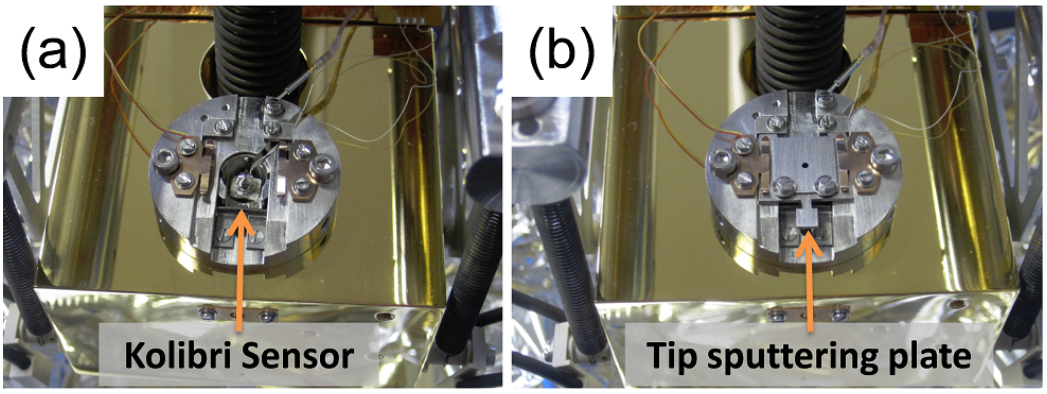

FIGURE 3.4: Picture of the SPM after a Kolibri sensor replacement. The tip sputtering plate has to be readjusted. In picture (a) there is only the Kolibri sensor and in (b) the tip sputtering plate has been inserted in the sample stage.

Once that the sputtering plate is in the sample stage, the tip has to be approached as much as possible using the STM feedback. When the tip is located in the hole, the sensor's housing will cause the tunneling contact. At this point, tunneling current has to be detected but a change in the oscillation frequency must not be observed. When it occurs, we can be sure that the tip is pointing through the hole in the sputter plate and the tip sputtering can be initiated. The resonant frequency is measured before and after the tip sputtering and due to the (very small) decrease of tip mass the resonant frequency (f_0) is slightly smaller before the sputtering. In Table 3.1 are summarized the typical parameters of a tip sputtering.

Time	Energy (keV)	Tip current (μA)	Δf_0 (Hz)
5 min	1.5-2.0	$\sim$ 1	$\sim$ 5-10

TABLE 3.1: Parameters of a normal tip sputtering.

Amplitude Calibration

The oscillation amplitude is periodically calibrated, necessarily after a tip replacement and recommended after a tip sputtering. For this procedure a clean metallic surface and a stable tip are necessary. The tip is placed above the sample surface with the STM feedback on. If the sensor is being oscillated, the time averaged tunneling current is measured due to the limited bandwidth of the STM preamplifier. In a first approximation, it can be assumed that the averaged measured tunneling current per oscillation cycle corresponds to a weighted tunneling current measured for a static tip at a certain tip-sample distance. Due to the exponential

dependence of the tunneling current with the distance, the major fraction of the registered averaged tunneling is dominated by the lower point of the oscillation. If the change in the oscillation amplitude is not too large, an amplitude change practically corresponds to a change in the absolute position of the lower point of the tip and thus the tip-sample distance is compensated by the z-feedback. A reduction in the oscillation amplitude results in a larger effective tip-sample distance and then the tip approaches towards the sample by the amount the amplitude has been reduced. On the other hand, an increase of the oscillation amplitude results in a smaller tip-sample distance, increased tunneling current, and thus the tip retracts. An example of amplitude sweep with the STM feedback on is presented in Figure 3.5. In this example, the slope is 1.035 which is the factor of deviation of the actual amplitude calibration.

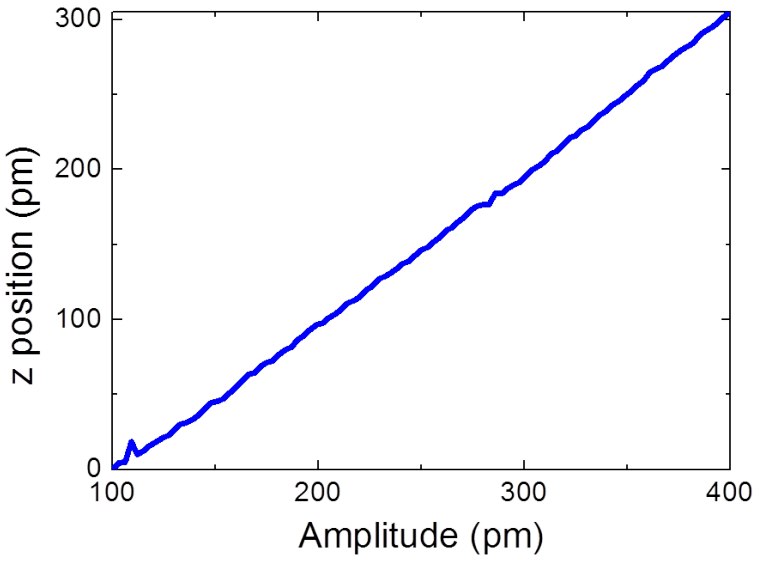

FIGURE 3.5: Example of oscillation amplitude versus piezo z-position for the amplitude calibration. The tip is placed over a point of the surface with the STM feedback on (I=120 pA and Bias=1.00 V) and the amplitude is swiped from 100 to 400 pm.

3.3 Preparation of Clean Substrates

The substrates used in this thesis are Cu(111), Au(111) and Si(111). Au(111) and Cu(111) monocrystals were purchased from MaTeck. Atomically clean surfaces were prepared by several cycles of sputtering and annealing in the SPM chamber.

A picture of both crystals, mounted in their sample holder, are presented in Figures 3.6(a) and (b). Sputtering was performed under a pressure of 10^{-5} mbar of Ar^+ ion gas with a beam energy of 600 eV. Annealing was made at 240°C and 300°C for Cu(111) and Au(111), respectively. In Table 3.2 are summarized the sputtering and annealing parameters for preparing atomically clean surfaces.

	Sputtering				Annealing	
	Time (min)	Energy (keV)	Emission (mA)	Current (μA)	Time (min)	T (°C)
Cu(111)	10-15	0.6-0.8	10	~ 10	20	240
Au(111)	10-15	0.6-0.8	10	~ 10	20	300

TABLE 3.2: Summary of the sputtering and annealing parameters for preparing atomically clean surfaces.

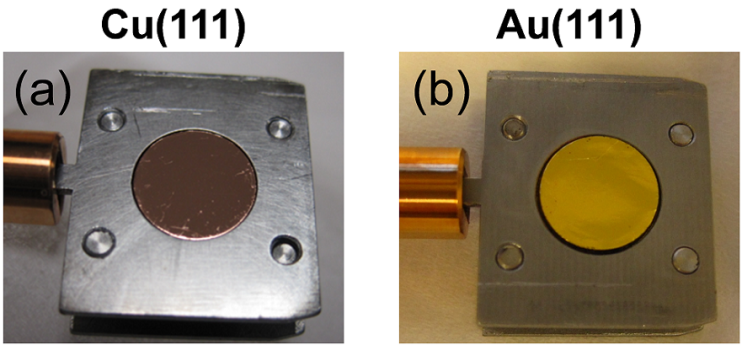

FIGURE 3.6: (a)-(b) Pictures of the Cu(111) and Au(111) monocrystal mounted in the sample holders.

Pieces of p-type Si(111) wafer were previously cleaned with acetone and ethanol, then loaded into the UHV chamber and degassed during few hours. To obtain the 7×7 reconstruction, the silicon was flashed several times to a maximum temperature of 1200°C during 20 s followed by a fast quenching at 900°C during 30 s and then a slow cooling down to room temperature.

3.4 Molecular Deposition of Organic Layers

Organic molecular beam epitaxy (OMBE) is a well-established technique to grow organic thin films under very clean and controlled conditions, like UHV. The molecular beam is generated by sublimation in a Knudsen cell, which consists on a crucible, a heating filament, a temperature sensor and a temperature shielding.

The molecules in solid state are put into the crucible and heated until sublimation. The small opening of the crucible points toward the center of the chamber and generates a rather focused molecular beam. The molecular beam can be blocked with a shutter. All molecules used in this thesis have a strong aromatic character. The structure and properties of each one are presented, together with the results, in the corresponding chapter.

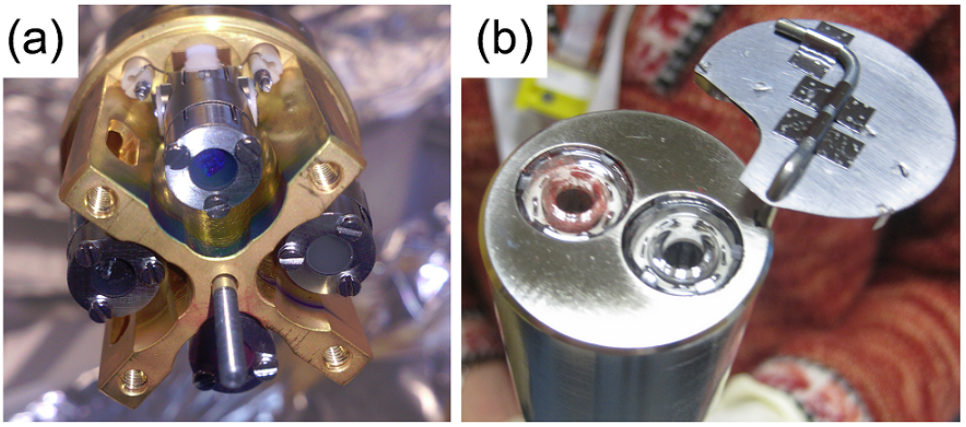

FIGURE 3.7: Pictures of the two molecular evaporator that are installed in the preparation chamber. In (a) is imaged the evaporator with four crucibles (Dodecon, GmbH) and in (b) the evaporator with two crucibles (Dr. Eberl MBE-Komponenten, GmbH).

In the UHV system two molecular evaporators are installed in the preparation chamber. A picture of each one are presented in Figure 3.7. The evaporator shown in (a) has four crucibles with four different molecules. In (b) is shown the other molecular evaporator with two crucibles. In Table 6.1 are summarized the temperatures and the corresponding deposition rates that have been calibrated in this thesis.

Molecule	Temperature (°C)	Deposition rate (ML/min)
DIP	225	0.05
F_{16}CuPc	315	0.05
ClAlPc	345	0.10
PTCDA	unknown	0.20

TABLE 3.3: Summary of the molecules that have been used in this thesis, the temperatures used and the corresponding deposition rate.

Chapter 4

Oxidation of Cu(111) by Air Enriched Argon Bombardment

4.1 Introduction

The electrical, mechanical, thermal and chemical properties of many technological devices are often intimately dependent on the structure, composition and morphology of internal metal/oxide interfaces. With the aim of creating well defined stoichiometric metal/oxide interfaces, we have investigated and presented in this chapter diverse two dimensional cooper oxides obtained by air-enriched argon sputtering plus annealing, an efficient and scalable methodology. As an added value to their particular functionalities, in general, air-induced surface structures are considered as passivating layers presenting robust mechanical and electronic properties. With the purpose of accounting for in-situ references, laterally heterogeneous surfaces consisting of one layer thick copper oxide regions coexisting with bare Cu metal have been investigated here. The local nanostructure of these surfaces have been measured at room temperature by means of STM and FM-AFM under ultra-high vacuum (UHV) conditions.

In addition to some already described cooper oxide structures of varying stoichiometry, a novel open honeycomb (OHC) structure with a large unit cell (~ 1.3 nm) is reported. We propose a model in which this low density oxide is made out of Cu_3O and is suggested to develop to denser phases by oxygen incorporation leading to different electronic attributes. Besides properties emerging from the

particular oxide nature, the OHC nanostructure itself can be viewed as a two dimensional framework with well-defined pore size. This high quality open network can provide precise and confined localization of guest functional nano-objects to be used as a multifunctional nanostructured system. Compared to other bottom-up approaches as supramolecular self-assembling in which two dimensional open networks are made out molecules, our ability to generate patterned surfaces without the need of additional organic building blocks presents unquestionable advantages for device integration.

4.2 Description of the Cu_2O

Oxides of copper predominantly exist in two forms: Cu_2O cuprous oxide and CuO cupric oxide. Both are intrinsic p-type semiconductors which can be synthesized from the oxidation of Cu metal at low processing costs. Copper (I) oxide, or cuprous oxide (Cu_2O), is one of the principal oxides of copper and is found in nature as cuprite. It is a red color crystal used as a pigment. Depending on their final electrical characteristics, copper oxide ultrathin films have been suggested to be candidates for uses as low resistance electrodes, catalysts, sensing materials and semiconductor materials for solar cell transformation [79, 142, 153, 171, 187, 188]. Cu_2O has been shown to be an effective photocatalyst for water splitting to H_2 and O_2 under visible light [88]. And due to its suitable band gap, it can be considered as candidate material for photovoltaic and photo-electrochemical device applications [173]. But it has been argued that device efficiencies are limited in part because there is no method for fabricating a reproducible, stoichiometric interface between the copper oxide and other heterojunction partners [227].

In bulk, Cu_2O is found in a cubic structure with a lattice constant of $\sim$ 4.3 Å. Figure 4.1(a) is the side view of 12 atomic layers of the bulk Cu_2O crystal with the (111) orientation. The copper atoms (gray) are arranged in a face centered cubic (fcc) sublattice and oxygen atoms (black) in a body-centered cubic (bcc) sublattice. In such a way, in the (111) direction, the structure can be viewed as a stack of trilayers, each consisting of planes of alternated composition, i.e., Cu-O-Cu. The corresponding top view of the surface is depicted in Figure 4.1(b), where the atoms at the first trilayer appear darker than those deeper below. The in-plane lattice parameters of the $Cu_2O(111)$ plane are a = b = 6.14 Å, and the rhomboid unit cell contains 4 copper atoms (1 Cu_{cus} and 3 Cu_{csa}) and two oxygen atoms (O_{cus} and

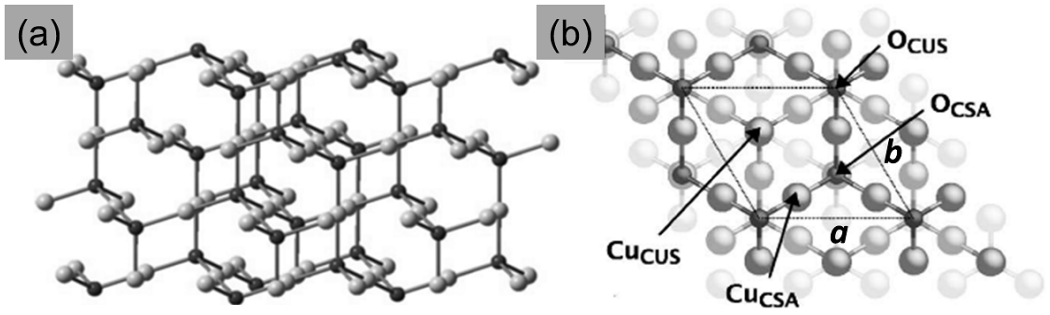

FIGURE 4.1: (a) Bulk structure of the copper oxide, Cu_2O and (b) the corresponding (111) surface. Oxygen atoms (black) and copper atoms (grey). The 2D (1x1) surface unit cell, indicated in (b), parameters are a = b = 0.614 nm. Figure adapted from [179] and [182].

.

O_{csa}), with "cus" and "csa" indicating coordinatively unsaturated and saturated atoms, respectively, which are vertically displaced within the corresponding plane of the trilayer. The surface can be viewed as well as a corrugated hexagonal lattice with both types of O at the vertex, Cu_{csa} atoms at the middle edges and one Cu_{cus} at the center. The distance between hexagon centers coinciding with the unit cell parameter (6.14 Å) and the distance between Cu_{csa} is half of this value (∼3 Å).

Oxidation of Cu(111)

The relevance of understanding the oxidation mechanisms on copper surfaces has motivated for years numerous investigations using single crystals under controlled conditions. The existing studies of Cu(111) oxidation indicate that the reactivity of this surface to oxygen is much lower than that of the (110) and (100) surfaces [6]. It is generally agreed that oxygen molecules dissociate at the Cu(111) surface at room temperature leading to a disordered surface layer [47, 83, 84, 137, 138, 147, 183, 205]. Though complex structures have been observed at elevated temperature or higher pressures, which eventually lead to more or less stoichiometric Cu_2O films, a certainly complicated scenario exists at the initial stages of oxygen incorporation [17, 57, 113, 115, 131, 137, 172, 210]. The reason why this copper oxide is formed instead others seems to have it basis on the fact that the nearest-neighbor (NN) and next nearest-neighbor (NNN) distances Cu-Cu in the Cu(111) surface are $a_{Cu(111)} = 2.56$ Å and $a_{Cu(111)}\sqrt{3} = 4.43$ Å. Though these value are considerably smaller/larger (by 15 % and 47 %, respectively) than the ∼ 3 Å Cu-Cu distance in $Cu_2O(111)$, commensurate strained/compressed lattices

of an oxide overlayer on Cu(111) are likely to exist. Thus, for instance we note that four times the NNN distance of Cu(111) coincides with three times the lattice parameter of $Cu_2O(111)$ (i.e. $4a_{Cu(111)}\sqrt{3})/3 = 6$ Å), or seven times the NN distance of the Cu substrate (7 x 2.56 Å = 17.92 Å) is close to three times the oxide lattice parameter (3 x 5.95 Å = 17.85 Å). These coincidences will be the reason also for the appearance of site coincidence lattices and Moiré patterns, some of which have been observed and will be described in this thesis.

Different methods have been employed for the oxidation of Cu(111), being the exposure of the clean surface to O_2 pressure in UHV plus annealing the most common one to obtain monolayer oxides [43, 47, 113, 114, 132, 137, 147, 183, 226]. However, small differences in pressure and temperature give to the presence of diverse surface structures. Interestingly, most of these structures were also achieved by using reactive air injection or even by reduction of the oxide monolayer [157, 231]. This observations indicating, on the one hand, the relative stability of the observed phases independently of the preparation methodology and, on the other hand, opening the possibility of creating "new" oxide layers with a different stoichiometry by introducing the use of new methodologies.

Among others parameters, as oxygen pressure, exposure time, substrate temperature, etc. it is likely that preparation parameters modifying the energetics of the oxidation process may lead to new metastable oxide structures. With the aim of pursuing this objective, in this thesis a different approach has been used to obtain partial coverages of Cu_2O on the Cu(111) instead of complete oxidized surfaces. The strategy consists in exposing the clean Cu(111) surface to an air-enriched Ar^+ sputtering followed by in-situ annealing at 240°C somehow similar to the pulse injection of air method [157]. The final laterally heterogeneous surfaces, formed by oxides patches and clean copper regions, result ideal systems for a good structural characterization provided the Cu(111) is used as in-situ reference.

4.3 Experimental Details

The STM and FM-AFM experimental results presented in this chapter have been performed in the STM/FM-AFM in an UHV system (Specs, GmbH). X-ray photoelectron spectroscopy (XPS) data were obtained in collaboration with Dr. Guillaume Sauthier in a XPS-UPS (Specs, GmbH) devoted system in the *Institut*

Català de Nanociència i Nanotecnologia and also equipped with a low energy electron diffractometer (LEED).

The Cu(111) single crystal (Matek GmbH, Germany) was prepared by repeated cycles of Ar^+ sputtering (1.2 keV) plus annealing at 240°C during 25-30 min. To obtain a semilayer of Cu_2O on Cu(111), an air-enriched Ar^+ sputtering plus annealing at the same temperature was performed. The pressure in the UHV chamber during oxide preparation was in the 10^{-5} mbar range and ion gun ionize the introduced mixture of air and Ar. Cleanness and order of the Cu(111) surface was checked by STM, LEED and XPS.

4.4 Structural Study of the Cu_2O/Cu(111) Surface

4.4.1 The Cu(111) Surface

Cleanness and order of the Cu(111) surface was checked by STM and LEED (Figures 4.2(a)-(c)). The high resolution images, as the one presented in Figure 4.2(b), were used to in-situ calibrate the in-plane distances ($a_{Cu(111)} = 2.56$ Å) and the step height ($d_{Cu(111)} = 2.1$ Å) in large scan areas, as the one shown in Figure 4.2(a), were employed for the vertical calibration of the piezo scanner. The LEED pattern, presented in Figure 4.2(c), confirmed a well-ordered and clean surface at larger scales and was used to have the external reference for crystal azimuth orientation. To check that no oxygen or carbon traces remained on the surface after the cleaning process, the Cu(111) was checked by XPS. The survey spectra and the O1s and C1s spectral regions are shown in Figures 4.2(d)-(e) where no important traces of oxygen and carbon are observed as expected for a clean surface.

4.4.2 Oxidation of Cu(111)

The surface composition of the as-prepared surface was ex-situ checked by XPS. The XPS spectra (survey, Cu2p, O1s, N1s and C1s) taken on the Cu(111) crystal after air-enriched Ar^+ bombardment plus 240°C annealing are presented in Figures 4.3(a)-(e). To minimize ambiance contamination the sample was transferred

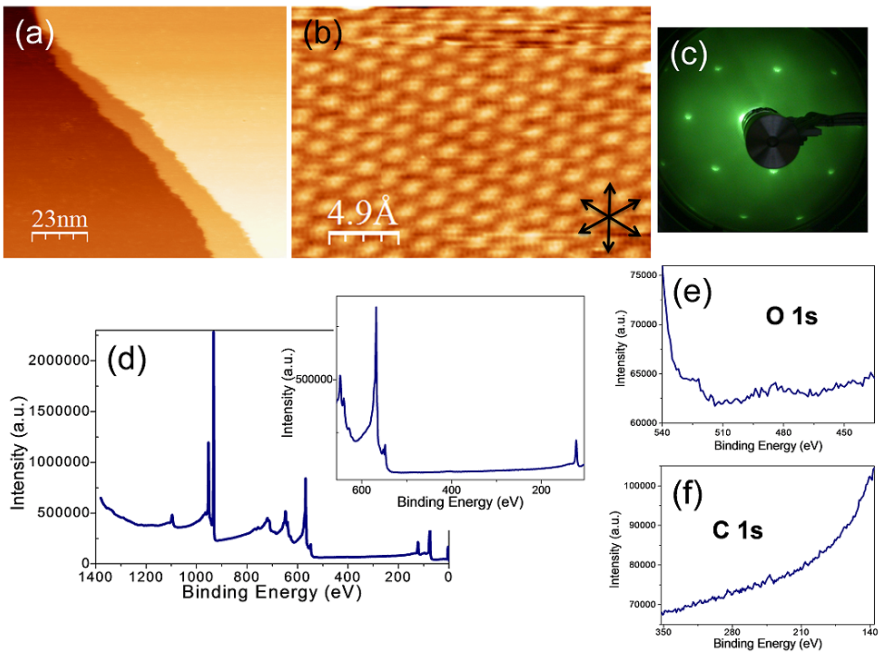

FIGURE 4.2: Clean Cu(111) surface. Large (a) and small (b) topographic STM images. The black arrows in (b) indicate the three equivalent ⟨110⟩ directions of the Cu(111). (c) LEED pattern of the clean Cu(111). (d)-(f) XPS spectra taken on the clean Cu(111): (d) survey spectra and a zoom in the inset, (e) O1s and (f) C1s spectra. Parameters STM images: (a) I = 375 pA, Bias = -1.40 V, A = 200 pm and (b) I = 240 pA, Bias = -0.30 V, A = 200 pm.

.

through air as fast as possible at clean conditions. However, though the presence of all expected constituents were seen, no clear identification of the O (Figure 4.3(c)) and N (Figure 4.3(d)) components attributable to the overlayers observed in these samples (copper oxide and copper nitride) can be made.

As it will be shown along this chapter, up to six different oxidic phases are seen to coexist on the same sample surface. Thus, depending on the local oxygen content or stoichiometry, we observe the oxygen adsorbed (OA) on bare copper, the four structures described so far in the literature (that we will term as short order honeycomb, SOHC, large order honeycomb, HC, O-deficient, OD, and "44") but also we have been able to obtain a largely open honeycomb (OHC) lattice with a lower oxygen content than the previous ones. This structure, which can be viewed as a 2D framework, is reported here for the first time. Thanks to the coexistence of some of the different phases and based on the accepted models, which provide the corresponding stoichiometry, the new OHC phase will be described. Using the construction of metastable phases from Cu_xO units employed in the existing theoretical calculations, a structural model including the expected oxygen content

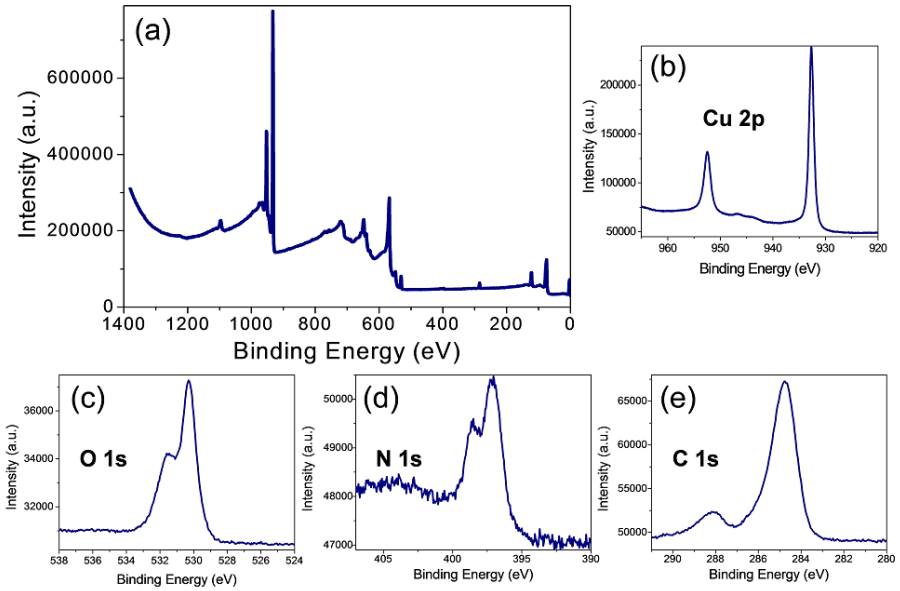

FIGURE 4.3: Top: XPS spectra taken on the Cu(111) after air-free Ar^+ bombardment plus 240°C. (a) Survey spectra, (b) O1s and (c) C1s spectra. Bottom: XPS spectra taken on the Cu(111) crystal after air-enriched Ar^+ bombardment plus 240°C. This sample was prepare ex-situ and transferred through air into the XPS chamber. (d) Survey spectra, (e) Cu2p, (f) O1s, (g) N1s and (h) C1s spectra. Due to possible air contaminations a quantitative analysis can not be performed.

.

will be proposed for this new phase.

Oxygen Adsorption on Cu(111)

The adsorption of oxygen atoms on the Cu(111) has been observed both, after exposure to O_2 at RT [226] and in the last stages of Cu_2O(111) reduction by CO [231] . Appearing either as isolated oxygen atoms or small oxygen clusters on the Cu(111) terraces, they are seen as depressions surrounded by concentric rings in high resolution constant current STM images but as dark or bright spots, depending on tip conditions, for large scale images (Figure 4.4(a)). These rings correspond to oscillations (standing waves) in the electronic density of states of the cooper surface due to the oxygen adsorption (Friedel's oscillations) [158, 226]. The adsorption site of the O atoms was determined to be threefold hollow [226] from atomically resolved STM images as the two consecutive STM images shown in Figures 4.4(b)-(c). As seen in these images, these oxygen features can be moved induced by the sweep action of the tip during STM, indicating a weakly interaction with the unreconstructed substrate. In Figures 4.4(d) and (e) a topographic STM

image of adsorbed oxygens and its line profile are presented. The diameter is ∼ 1.2 nm and the depth is ∼ 18 pm. These values are smaller than the reported by Wiame et al. but are expected to be dependent on the bias and tip conditions [226].

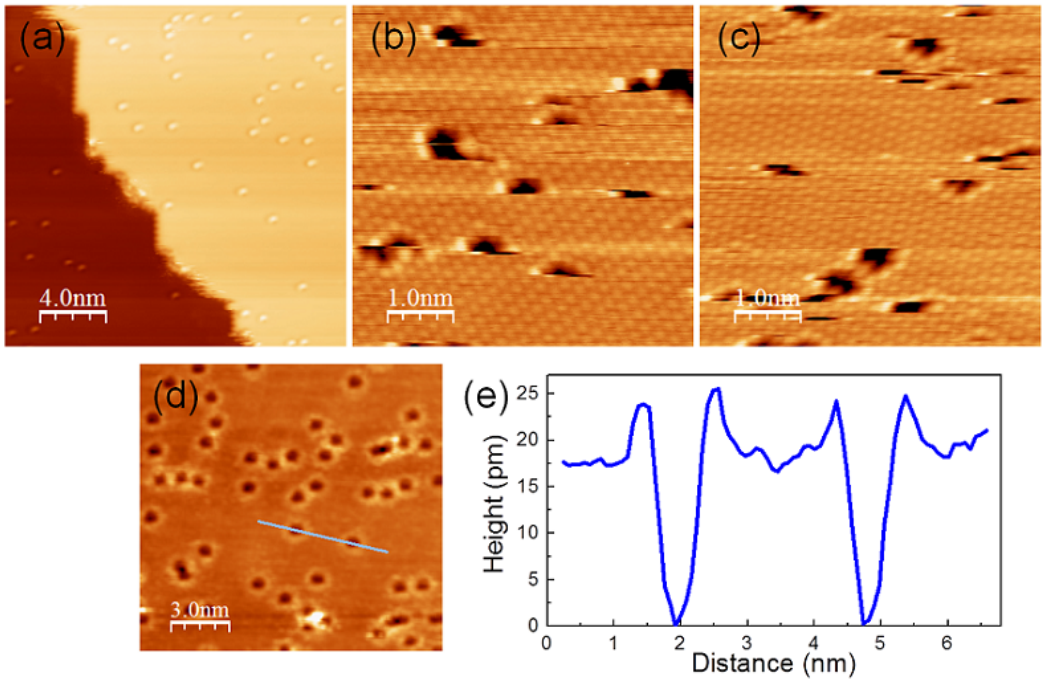

FIGURE 4.4: Topographic STM images of O adatoms in the unreconstructed Cu(111) terraces. (b) and (c) are consecutive scan images of the same area, the scan direction is (b) down and (c) up. (d) STM image and (e) the line profile indicated in (d). Oxygen atoms are imaged as holes of ∼ 15-20 pm in depth and a diameter of ∼ 1 nm. Parameters: (a) I = 240 pA, Bias = -0.30 V, A = 200 pm (b)-(c) I = 240 pA, Bias = -0.30 V, A = 200 pm (d) I = 240 pA, Bias = -0.30 V, A = 200 pm.

.

It can be concluded that the atomic oxygen adsorbs but do not react at the copper terraces, in fact, from the large scale image (Figure 4.4(a)) it is clearly seen that oxygen adsorbs on them but do not importantly attach to the step edges, which otherwise seem to exhibit a different reactivity depending on their orientation. Thus, for instance the frizzy appearance of some steps is a clear indication of the metal atoms diffusion along oxygen free step edges [67, 68] whereas the double height seen at other steps points to the beginning of oxidation. As it will be shown in this thesis, as oxidation proceeds, the copper regions exhibiting these adsorbed oxygen atoms coexist with regions of where partial oxidation takes place.

4.4.3 Copper Oxides: Nucleation, Structural and Stoichiometric Defects and Structural Phases

In the oxidation reaction of copper by oxygen have been suggested that the oxygen chemisorbed on threefold hollow sites, partially penetrates into the surface layer, causing an increase in the Cu-Cu distance which becomes more similar to the Cu-Cu of the $Cu_2O(111)$-like layer on Cu(111) [183]. In practice, the nucleation and growth at room temperature (RT) of an oxide layer on this surface proceeds by formation of patches in the STM images either as fringes at the step edges or as bright or dark areas at defects existing in the copper terraces [137, 226]. The propagation of the newly created steps would imply ejection and diffusion of Cu atoms, which aggregate with the impinging oxygen to form additional oxide islands. In fact, unless defects, e.g. vacancy islands, exist on the terraces, oxidation only takes place at the step edges. Similar results are seen in Figure 4.5(a), which shows that a semi-layer of copper oxide grows on the Cu(111) after Ar^+/air sputtering and annealing. Initially defect-free copper terraces are covered by the above described oxygen adsorbed species (OA) and partial oxidation of the surface takes place at the steps. The level of the oxide region is apparently lower (by about 1 Å) than that of the Cu(111) (Figure 4.5(b)) and some local order in the form of a nearly hexagonal lattice with parameter of $\sim$ 5-7 Å is found to exist (Figure 4.5(c)), in good agreement with the oxygen sublattice parameter of the $Cu_2O(111)$.

Figure 4.5(d) shows another example of a typical topographic STM image of the surface obtained with this method and (e) the simultaneously measured frequency shift. The final surface consists of atomically flat terraces of alternating Cu and Cu_2O composition. This later is attributed to an oxide grown on top of the lower copper terrace due to the reaction of oxygen atoms with the copper atoms at the step edges of the upper terraces [137, 157]. The schematics of the proposed growth mechanism at expenses of the original Cu(111) terraces is shown in Figure 4.5(g).

As it can be observed in Figures 4.5(e) and (f), the frequency shift remains close to zero over the copper terrace, while over the copper oxide reaches $\sim$ -200 mHz, i.e. the tip-sample interaction is larger and attractive over copper oxide. We note that interpretation of these data is, however, not obvious since the tip-sample distance is changed when scanning over the surface to keep constant the tunneling current by the STM feedback. Current Imaging Tunneling Spectroscopy (CITS)

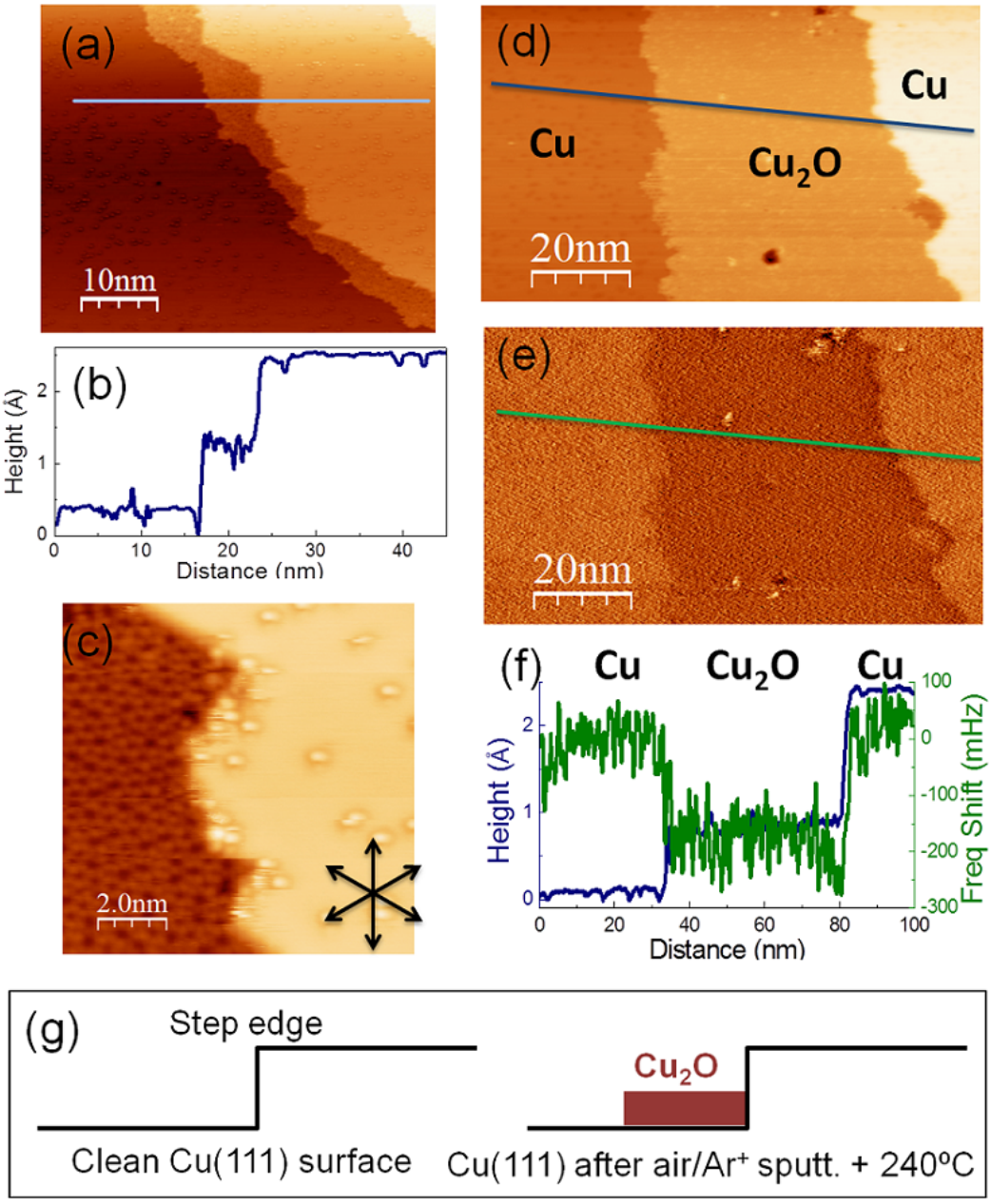

FIGURE 4.5: : (a) Topographic STM image of the initial stages of the formation of a Cu_2O layer at the step edges of the Cu(111) terraces, (b) the corresponding profile and (c) a magnified scan at the step between Cu_2O and Cu terraces. (d) Topographic STM image of a partial Cu_2O layer on Cu(111), (e) the simultaneously frequency shift channel and (f) profiles topographic (blue) and frequency shift (green). The Cu(111) step height is 2.1 Åand the Cu (lower terrace)-Cu_2O is 0.7 Å. (g) Schematics of the oxidation process at the step edges of the initial surface. Parameters: (a) I = 154 pA, Bias = -1.50 V, A = 200 pm (c) I = 265 pA, Bias = -0.44 V, A = 200 pm (d)-(e) I = 195 pA, Bias = -1.45 V, A = 200 pm.

.

recorded at fix tip-sample distance in similar partially oxidized Cu(111) surfaces indicated the existence of a $\sim$ 1.5 eV gap on the O-modified region in contrast with the density of states measured on the unmodified Cu(111) regions [226]. In principle, all copper oxides are semiconducting and the existence of a given gap is also likely to exist in our case. As a consequence, the STM tip-sample distance is smaller over the Cu_2O surface, i.e. the tip has to get closer to measure the same tunneling current that over the metallic terrace. On the one hand, this tip-sample distance reduction would be reflected as an increase in tip-sample interaction and, though the difference in frequency shift measured between regions (green line in Figure 4.5(f)) can provide some hints about the interactions over each material, its magnitude cannot be completely attributed to it. On the other hand, as already commented for Figure 4.5(b), the line profile across the step (Figure 4.5(f)) gives a step height of $\sim$ 0.9 Å between the copper lower terrace and the Cu_2O region, a value much smaller than the monoatomic step in Cu(111). This different step height is not due to a true different inter-plane distance because, it is known that for heterogeneous samples, presenting different local density of states (LDOS) quantitative topographic STM measurements can give erroneous height values. Moreover, the apparent height of the copper oxide layer will depend on the tunneling parameters due to the energy dependence of the LDOS.

To illustrate the different copper oxide step height when measuring in STM or FM-AFM feedback mode, in Figure 4.6 are presented two topographic images in both z-feedback modes. Figures 4.6(a)-(b) are the topographic STM image and the line profile. Figures 4.6(c)-(d) are the topographic FM-AFM image and the line profile. The lines profile across the step give a step height of $\sim$ 0.9 Å between the copper lower terrace and the Cu_2O region when measuring in STM mode and of $\sim$ 1.7 Å when measuring in FM-AFM.

Oxygen modified regions showing the nearly hexagonal lattice, which we will call for simplicity short order honeycomb (SOHC) from now on, were extensively observed (Figure 4.7). A mean distance of $\sim$ 6 Å obtained from the fast Fourier transformed (FFT) images as that shown in Figure 4.7(b), indicates that this structure is nearly Cu_2O, though the actual stoichiometry cannot be determined at this stage.

The relatively poorly ordered layer presented in Figure 4.5(c) and Figure 4.7 is expected to be the consequence of an initial process of heterogeneous nucleation starting at different locations and was already reported for RT oxidation [226]. In

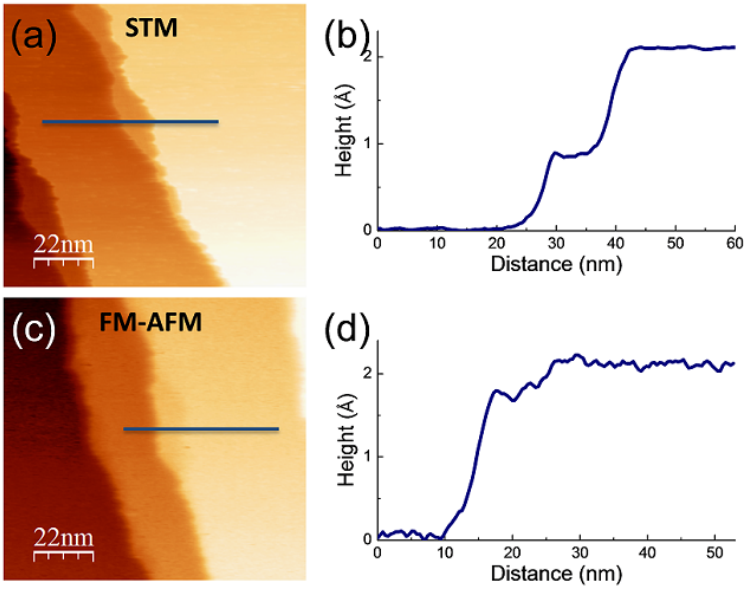

FIGURE 4.6: (a) Topographic STM image and (b) the line profile across the step. (c) Consecutive topographic FM-AFM image of the very same area and (d) is the line profile across the step. Parameters: (a) I = 420 pA, Bias = +1.08 V, A = 200 pm and (c) Δf = -1.00 Hz, Bias = +0.08 V, A = 200 pm.

.

this sense, more ordered structures are expected to appear the higher the annealing temperature. Thus, for instance, Matsumoto et. al reported that after few minutes of O_2 exposure at 173°C a well-defined LEED pattern was observed, indicating order over hundreds of angstroms [137]. Although, their STM images only very locally showed some atomic arrays. The pseudo-hexagonal short order phase reached much larger lateral size domains if formed by annealing to intermediate (250°C) [232] or higher (423°C) [137] temperatures and also obtained during the formation of the copper oxide surface via pulse injection of air onto Cu(111) [157], an approach similar to the employed in the present thesis. Very interestingly, it was also observed during the reduction of well-ordered "44"surface oxide (an structure described later on) by CO [231, 232] pointing to the SOHC configuration as an intermediate phase in both, oxidation and reduction processes. This oxide layer is not saturated in oxygen because the presence of vacancies and missing O-Cu-O chains within the oxide film and at the step edges.

Close inspection of the image in Figure 4.7(c) shows that the local order of this SOHC consists of intermixed pentagons and heptagons (5-7 defects) within an hexagonal lattice. This defective layer has been proposed to be analogous to the Stone-Wales (S-W) defects observed in graphene [89, 140] or carbon nanotubes [190] and predicted for other sp2 bonded materials but not of obvious

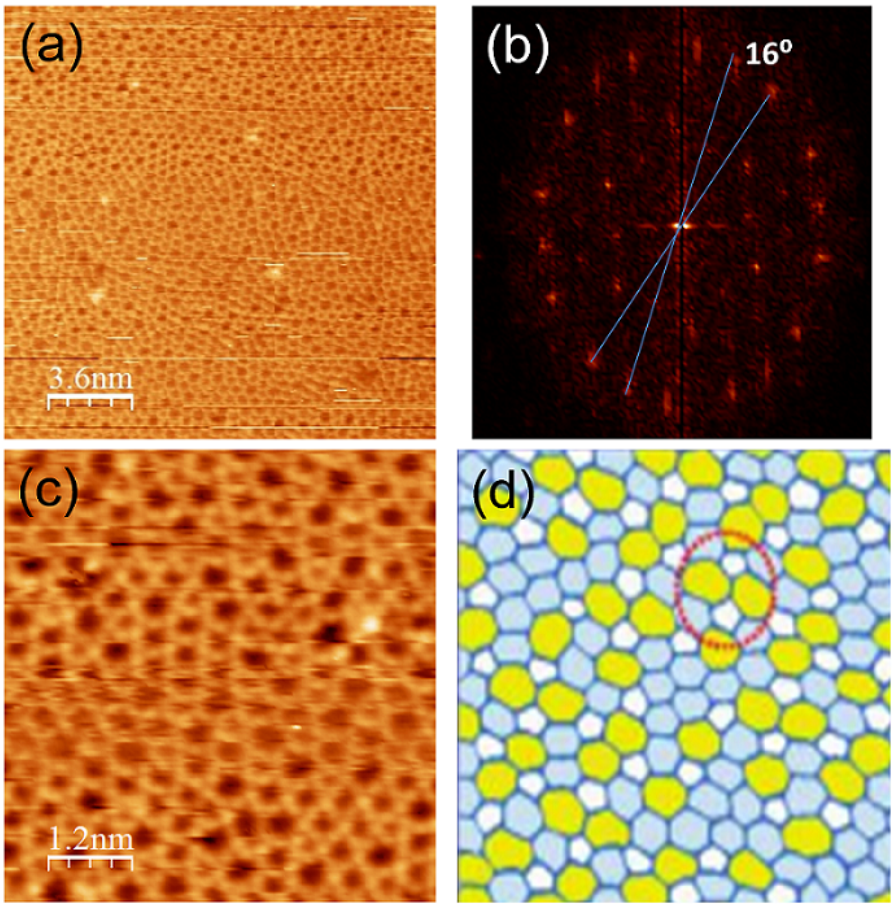

FIGURE 4.7: (a) Topographic STM image of an area of copper oxide in the short order honeycomb (SOHC) and (b) Fourier Transform of the image (a) and (c) a zoom of image (a). (d) Schematic representation of the short order honeycomb (SOHC) structure, ball model adapted from [232]. Parameters: (a) I = 194 pA, Bias = -0.47 V, A = 200 pm.

.

formation in non-sp2 materials, where the bonds between atoms have a strong ionic character as it is the case of copper oxide. Though at first glance, there is not clear ascription of the observed features to atomic structural details, as it can be seen in the high resolution STM image of Figure 4.8, each pentagon, hexagon or heptagon consists of a ball-like feature at each vertex. In Figures 4.8(b)-(c) reported STM simulations for the ordered HC and the defective structure are shown [232]. The great similarity between our experimental data and the calculations of the partial density, permits us interpreting the experimental data as coincident with the reported model, in which only the Cu atoms are seen. It has been stated [232] that when this structure covers the whole surface, it evolves to a long-range-ordered oxide which transforms in a hexagonal lattice corresponding to the $Cu_2O(111)$-like layer. The observation of the hexagonal or honeycomb (HC)

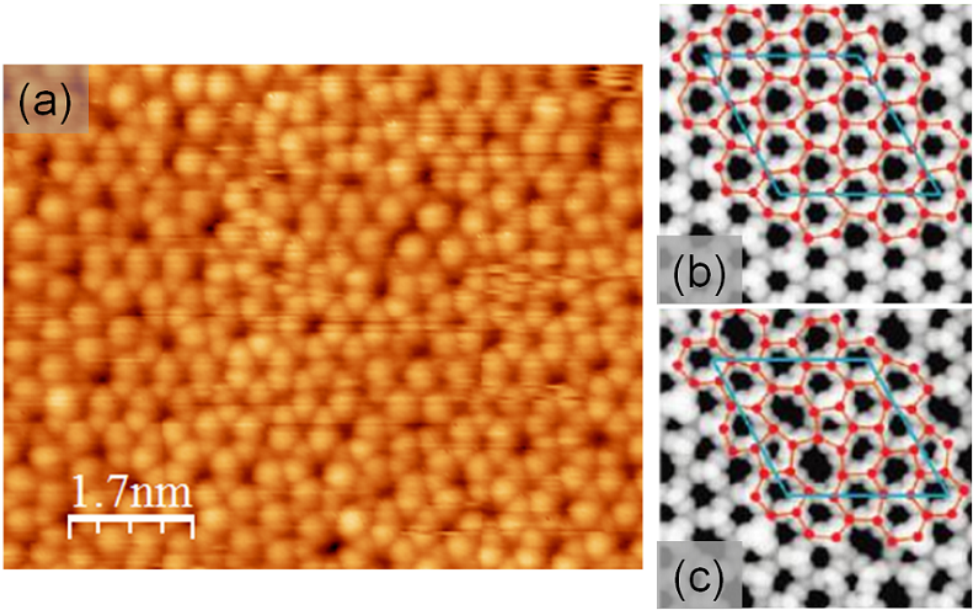

FIGURE 4.8: (a) High resolution topographic STM image of the copper oxide layer. (b) and (c) are STM simulated images using the p4vasp package of the ordered hexagonal Cu_2O surface layer (b) and S-W defective Cu_2O layer (c), they have been adapted from [232]. Parameters: (a) I = 80 pA, Bias = -0.53 V, A = 200 pm.

.

phase being the evidence of such transformation.

At this moment, it is worth remarking that in the present work, conversely to other works following the formation of different oxides as a function of oxygen content, all oxide structures presented are observed instead to coexist on determined locations of the same sample and, importantly, also coexist with vast regions of uncovered Cu(111) (see Appendix). Thus, only small regions of the HC have been found. This is the case of the area marked in Figure 4.9(a) and shown magnified in (b). The line profile taken at the indicated segment reveals the expected periodicity of $\sim$ 6 Å. Detailed observation of the large scale image shows, however, that the HC layer extends over the whole lower terrace but covered in part with some bright dots in the STM images. Moreover, the previously described OA (oxygen adsorbed) is seen at the upper Cu terrace. Figures 4.9(c)-(d) displays the model structure of the $Cu_2O(111)$-like layer on Cu(111) based on a perfect agreement between lattice parameters of the experimentally observed structure (6.10 Å x 5.95 Å) and $Cu_2O(111)$ plane (a = b = 6.14 Å). It has the same honeycomb structure that the (1x1)- $Cu_2O(111)$ surface (truncated bulk) but with the coordinately under-saturated Cu atoms (Cu_{cus} in Figure 4.1) at the center of the hexagons removed, leaving exposed the O adatoms of the $Cu_2O(111)$-like (which can be also viewed

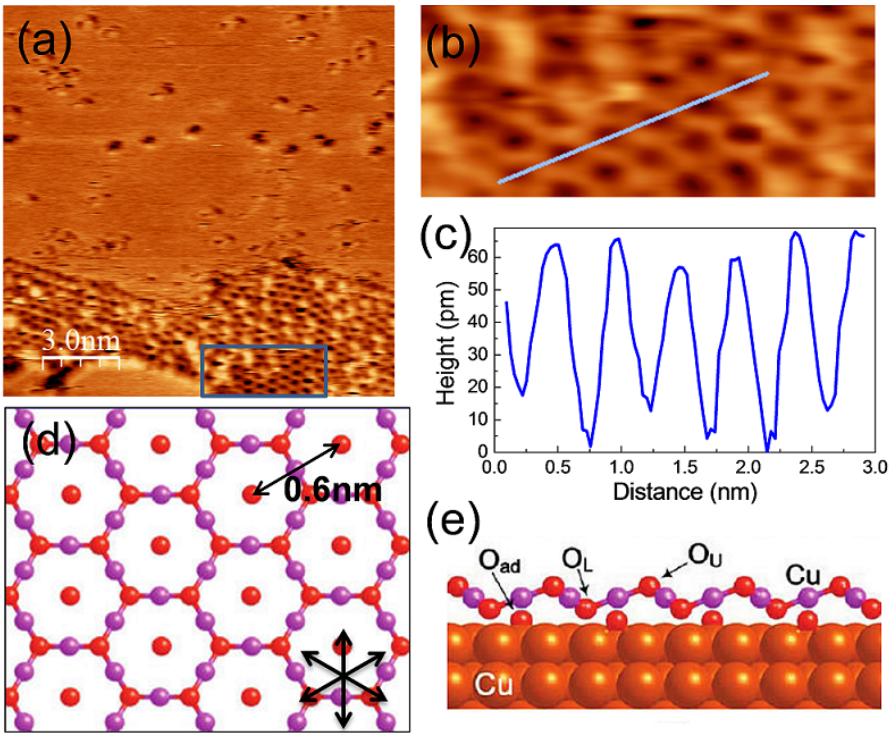

FIGURE 4.9: (a) Topographic FM-AFM image of a region in which OD and OH phases coexist at the upper and lower terraces. (b) Magnified region marked in (a) and (c) the corresponding line profile. Schematic representation of the top (d) and side view (e) of the $Cu_2O(111)$-like layer (Cu in purple and O in red, i.e. with two Cu atoms per O atom) over the Cu(111) structure (large orange balls) extracted from [231]. Black arrows indicate the three equivalent $\langle 110 \rangle$ directions. There are three types of adsorption sites (fcc, hcp and atop) for chemisorbed oxygen atoms (O_{ad}). The different oxygen atoms within the hexagonal net can be lattice (O_L) or upper (O_U). The bright dots seen in (a) are described in the text (Figure 4.10). Parameters: (a) Δf = -1.20 Hz, Bias = -0.22 V, A = 200 pm.

.

as the first oxygen layer of the second trilayer of the bulk $Cu_2O(111)$ depicted in Figure 4.1). There are three types of adsorption sites (fcc, hcp and atop) for the chemisorbed oxygen atoms (O_{ad}) and two types, lattice (O_L) or upper (O_U) in the hexagonal net, forming therefore two inequivalent triangular sublattices, as can be observed in Figures 4.9(d)-(e). In other words, the structure consists of a trilayer lateral repeated unit with each copper layer packed in between two layers of oxygen atoms. Note that, conversely to the bulk terminated surface in which the unit cell contains two Cu atoms per O atom, the oxide overlayer model in Figure 4.9 contains equal number of Cu and O atoms per unit cell.

The reason for the appearance of the mentioned bright dots has been interpreted as a deficit of oxygen content before completion of the HC. The lack of oxygen leads

to a defective structure seen as a higher intensity on the center of the hexagon. As in the case of the SOHC, this defective oxide has been observed either during oxidation or reduction [232] and can be understood by the removal of the chemisorbed oxygen atoms (O_{ad}) creating oxygen vacancies (O_v) at the center of the hexagonal mesh of the $Cu_2O(111)$-like layer. The existence of O_v leads a larger concentration of electron density around the Cu atoms (yellow rim in the model of Figure 4.10(a)) which are seen as bright dots in the topographic STM images (Figures 4.10(b) and (c)) for common tip resolution [231]. At the surroundings of the vacancies, small areas of the well-ordered honeycomb (HC) lattice can be very clearly seen in the current image of Figure 4.10(d). Interestingly, the observation of the bright dots is, in fact, a consequence of insufficient imaging resolution. A neat verification of this fact, and therefore of the proposed model, is illustrated in Figure 4.10(e), where we show that for better resolution STM, the whole structure can be seen as a honeycomb lattice with hexagons exhibiting larger or lower brightness depending on the oxygen absence (O_v) or presence (O_{ad}) [231]. Unfortunately, the desired resolution depends not only on tunneling parameters but also on tip conditions and, therefore, it is relatively fortuitous.

The brighter hexagons in the high resolution image of Figure 4.10(e) correspond to the Cu positions closer to the vacancy, i.e. to the bright dots observed in the rest of the images in Figure 4.10. This structure, termed as O-deficient (OD) can be considered as an intermediate phase and can be seen as more or less ordered at the large scale depending on the total oxygen content. Well-defined hexagonal arrays of bright dots have been reported [231]. As oxygen atoms are further incorporated to the lattice during oxidation (or vacancies propagate across the surface during reduction), the overgrowing layer becomes strained and, eventually, new ordered structures are formed.

In 1991, Jensen et al. published STM experiments reporting the first existence of two ordered structures induced by oxygen on Cu(111), with unit cells as large as 29 and 44 times the Cu(111) surface unit cell [113]. These superstructures, denoted as "29" and "44", respectively, are considered as coincidence lattices between the 1x1 surface lattice and a hexagonal substructure associated to the (111) plane of Cu_2O. The lower temperature "29" (obtained at 450°C) could be converted to the "44" by further annealing (at 500°C) [226]. Although they are considered analogous to crystallographic planes of $Cu_2O(111)$, which has the structure consisting of equilateral hexagons (Figure 4.1(b)), in fact they both arise from the growth of a

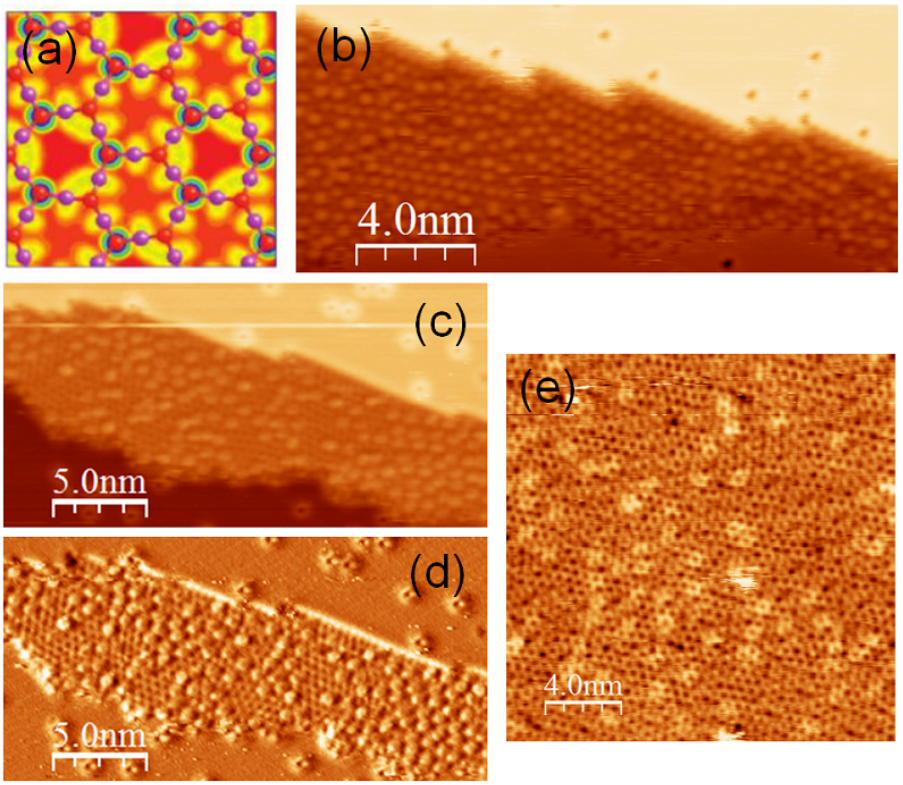

FIGURE 4.10: (a) Model of the O-deficient (OD) structure obtained from ELF calculations with and without O_{ad}, indicating a larger electronic density around the Cu atoms close to those locations where oxygen is removed extracted from [231]. (b)-(c) Topographic STM images of the observed OD phase, (d) is the simultaneous current image from (c). Because the relative resolution of the STM, the bright hexagons of the model are not resolved and bright dots are observed instead in the images in (b) and (c) but regions of the HC are clearly seen in the current image (d). (e) Topographic STM image obtained at higher resolution, where all hexagons are seen, with more or less bright depending on the oxygen absence (O_v) or presence (O_{ad}). Parameters: (b) I = 175 pA, Bias = +1.66 V, A = 200 pm (c)-(d) I = 120 pA, Bias = +1.51 V, A = 200 pm and (e) I = 195 pA, Bias = -1.46 V, A = 200 pm.

.

distorted hexagonal arrays of O atoms arranged in parallel lines in the first layer on the Cu(111). Because the different lattice parameters, the oxide $Cu_2O(111)$ plane must be deformed and adjusted to make it commensurate with the Cu(111) substrate leading to the superlattices. These two structures are identified in Wood's notation as ($\sqrt{13}$R46.1° x 7R21.8°, "29") and ($\sqrt{77}$R5.8° x $\sqrt{21}$R-10.9°, "44") and have quite similar lattice neighbor distances (5.6 Å x 6 Å and 6.1 Å x 5.9 Å, respectively) making them, in practice, hardly distinguishable. Moreover, their appearance strongly depends on the applied bias voltage for tunneling [157] and, most probably due to the solid reaction at their origin, these patterns contain a large amount of defects, both structural and stoichiometric, adding uncertainty at

their correct identification.

Figure 4.11 shows, for opposite bias polarities, the complex structure obtained by air/Ar^+ plus annealing process employed in this work. These topographic STM images perfectly coincide with those commonly observed [56, 137] and interpreted as consisting of a strained buckled hexagonal Cu-O layer containing additional O atoms forming the ($\sqrt{77}$R5.8° x $\sqrt{21}$R-10.9°). The unite cell vectors of the oblique superstructure are $\sim$ 2.2 nm and $\sim$ 1.18 nm (i.e. $\sqrt{77}$ x $a_{Cu(111)}$ and $\sqrt{21}$ x $a_{Cu(111)}$, respectively).

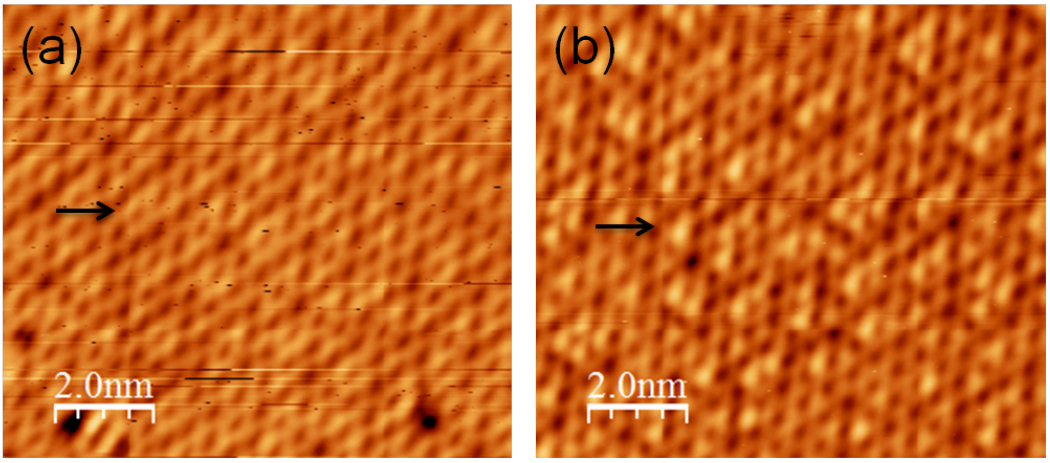

FIGURE 4.11: Consecutive topographic STM images at the very same area of the ($\sqrt{77}$R5.8° x $\sqrt{21}$R-10.9°, "44") obtained in air/Ar^+ plus 250°C on the Cu(111). The images were obtained with opposite bias polarity: (a) -1.40 V (filled states are imaged) and (b) +1.40 V (empty states are imaged). Black arrows in the images signal equivalent locations. Parameters: I = 88 pA, A = 200 pm.

.

As commented above, copper oxide STM images have been found to be strongly bias dependent. The reason is that the electronic states in a metal oxide are generally more localized than in a metallic surface and result in distinct maxima in the LDOS. This bias dependence is illustrated in Figures 4.11(a) and (b) showing two topographic STM images of the very same area of the "44" structure obtained at opposite bias voltage polarity ($\pm$ 1.4 V). The relatively homogeneous rhomboidal pattern of empty rings seen at the positive bias becomes a more marked pattern in which the better drawn hexagonal lattice contains some bright spots at some ring as indicated by arrows in the images. Similarly to the OD described above, these bright dots may be due to alteration in the DOS if the O_{ad} is missing. Interestingly, the structure in Figure 4.11(b) has a triangular appearance, reminding the non-equivalent halves (one Cu centered, the other O centered) of the bulk

$Cu_2O(111)$ unit cell described in Figure 4.1. On the other hand, during scanning the STM tip might undergo changes which importantly influence the visualized structure.

Figure 4.12 shows STM topographic images of the same "44" oxide structure at different tip and tunneling conditions. An impressive variation on the superlattice appearance is observed. In Figure 4.12(a) it is seen as the hexagonal array result of a high resolution imaging (similar to that of Figure 4.8) with faint triangular groups of brighter/darker hexagons. Instead of hexagons, bright features are seen in Figure 4.12(b) shows the oddest structure seen so far. Those presented in Figures 4.12(c) and (d) have been the most frequently observed during the present work and were found to transform the one into the other during scanning as illustrated in the bottom Figure 4.12. Starting with tip conditions in which the image shows an hexagonal array of well-defined and round dots separated by ~ 6 Å presenting different brightness (Figure 4.12(d)) in which few much brighter features (white in the image) are seen, which probably correspond to an adsorbed specie. As it is clearly seen in Figure 4.12(e), at a given moment during downwards scanning, the tip conditions change (arrow color change from blue to black). The new tip conditions remain during the subsequent upwards scan, Figure 4.12(f). In spite of these encountered changes, the types of images shown in Figure 4.12 were also observed for large scanned areas (see Appendix) indicating relatively stable tips or tip conditions in all cases. The reason of the bright/dark patches can be of different origin. On the one hand, as commented above, the lack of local stoichiometry (O_v) gives to a non-uniform LDOS and, on the other hand, as it will be described in the following overlayer misfits can be at their basis. Note that the nearly triangular shape and opposite orientation of the bright/dark groups reminds the existence of stacking faults during semiconductors epitaxial growth.

In addition to the bias and tip conditions dependence in STM and the easy occurrence of both, topological and stoichiometric defects, copper oxides imaging is quite troublesome because the large misfit between the oxide layer and the substrate leads, in practice, to similar but not identical surface structures and, commonly, site coincident lattice (SCL) or Moiré-like patterns can be observed. In these patterns, equivalent atoms of the overlayer adopt different sites on top of the substrate, therefore, exhibiting both a different local height reflected in true topographic differences and a different LDOS, that is reflected in a bias dependence. One of the proposed models to interpret such superstructures observed for the "44"

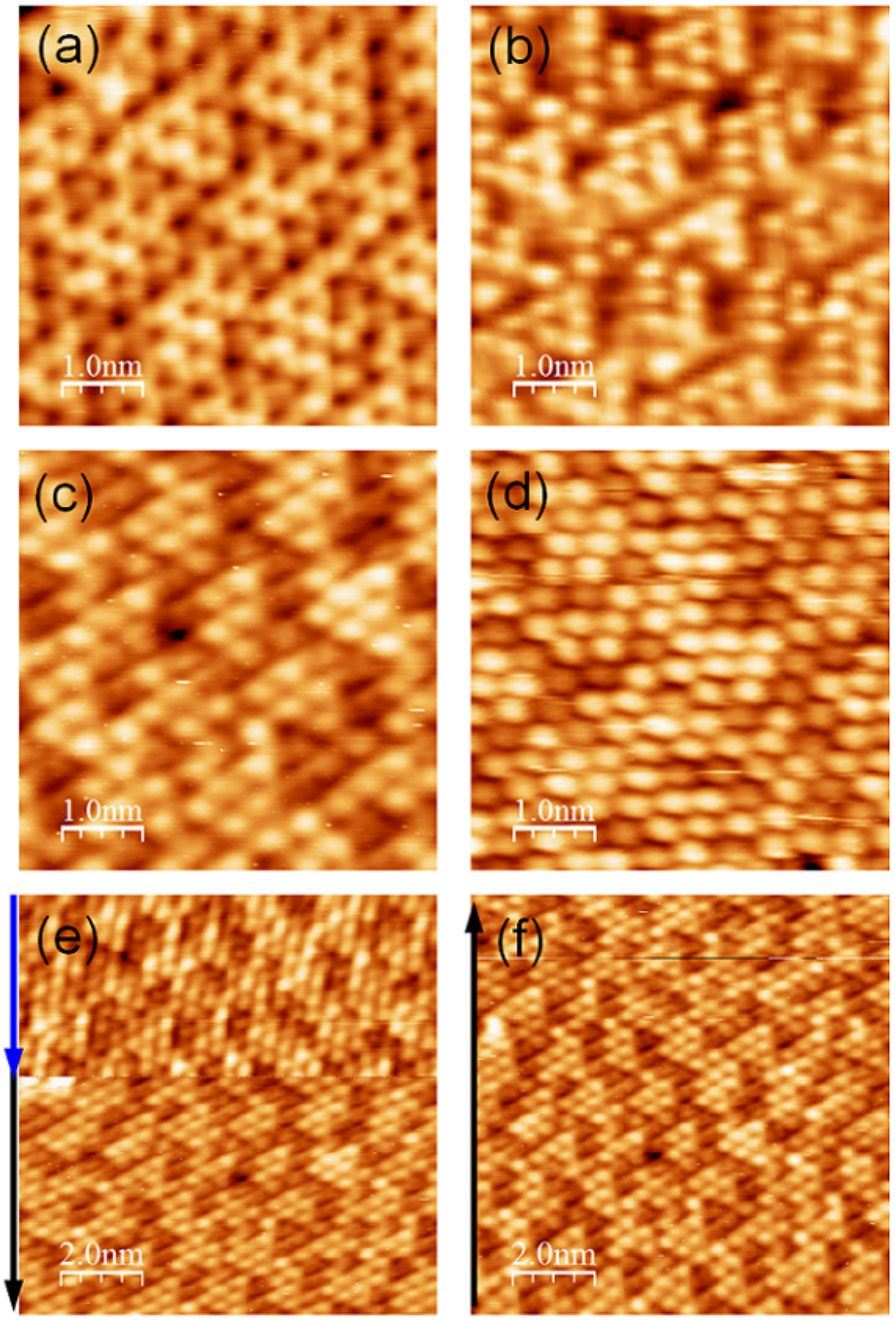

FIGURE 4.12: Topographic STM images of the non-stoichiometric "44" structure obtained at different tip conditions. (e)-(f) Consecutive STM images of the same area where a tip change occurred. The arrows indicate the fast scan direction. The arrow color change in (e) signals the point where resolution changes due to tip modification during scanning. Parameters: (a) I = 100 pA, Bias = +0.97 V, A = 200 pm (b) I = 126 pA, Bias = +1.20 V, A = 200 pm (c) I = 338 pA, Bias = -1.20 V, A = 200 pm (d) I = 180 pA, Bias = +0.97 V, A = 200 pm (e)-(f) I = 340 pA, Bias = 1.17 V, A = 200 pm.

.

is presented in Figure 4.13(a) as a superlattice with a coincidence boundary at the $Cu_2O(111)/Cu(111)$ interface [157]. The oxide layer (Cu_2O units represented by green dots) is strained to adopt the large misfit with the substrate. As three times of the overgrowth periodicity (3 x 5.95 Å = 17.85 Å) nearly equals seven times the NN distance of the Cu substrate (7 x 2.56 Å = 17.92 Å), the SCL described by the large oblique unit cell (dashed orange line in the Figure 4.13(a)) is 9 times the oblique Cu_2O unit cell (small rhomboid) and can be identified in Wood's notation by a $(7\sqrt{3}$ x $7\sqrt{3})$R30° or c(7 x $7\sqrt{3}$) superstructure of the Cu(111) (rectangular unit cell).

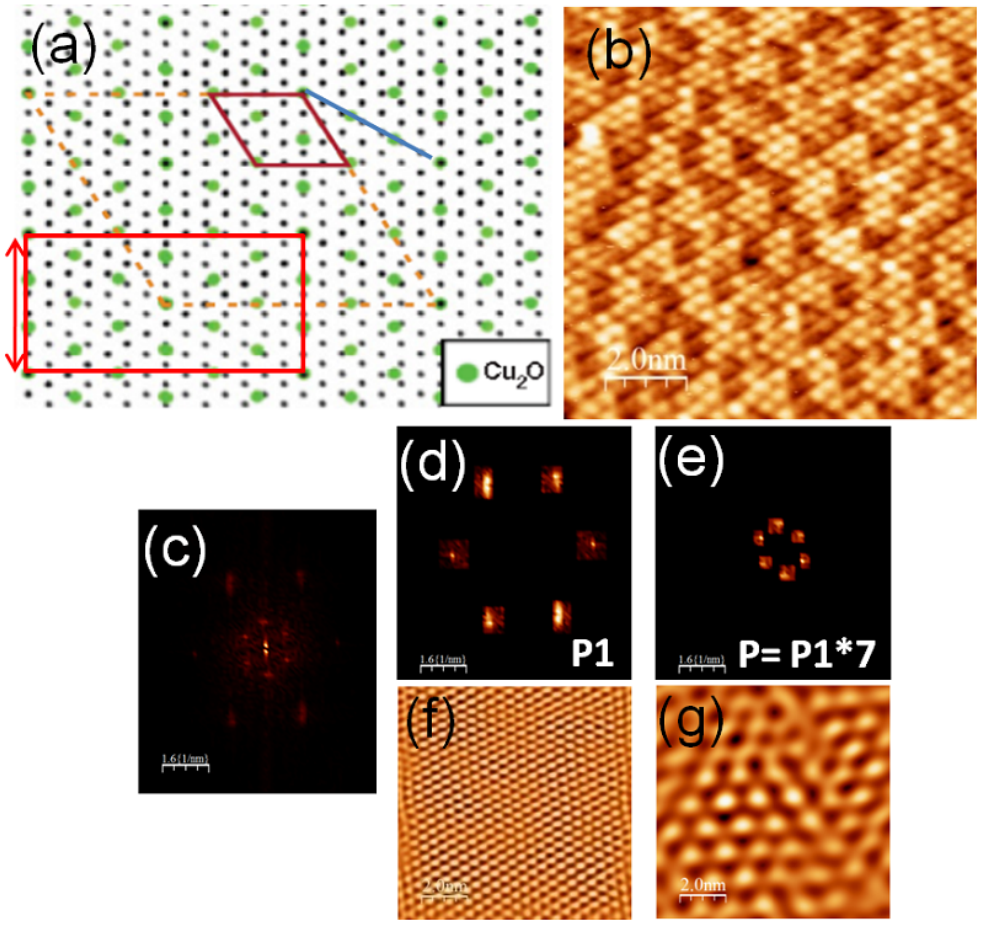

FIGURE 4.13: (a) Model for a coincident site lattice (CSL) of the $Cu_2O(111)$-"44" structure on Cu(111) extracted from [157]. The green dots are Cu_2O units and the different depicted unit cells are described in the text. (b) Topographic STM image of the "44" structure and (c) is its FFT where two concentric hexagonal lattices can be observed. (d) and (e) are the separated hexagonal lattices of (c) and (f) and (g) are the generated STM image (inverse of the FFT). Parameters: (b) I = 340 pA, Bias = 1.17 V, A = 200 pm.

.

As it is known from other systems depending on the relative orientation between

overlayer and substrate many different patterns may exist for the same overlayer structure (e.g., archetypical graphene Moiré patterns on (111) oriented metals). In the particular case of the copper oxide defective overlayers, the situation becomes even more complex. However, to illustrate the case with an example, an STM image presenting hexagonal packing with bright/dark groups (Figure 4.13(b)) is analyzed here. As it can be observed in the fast Fourier Transform (FFT) image (Figure 4.13(c)), two concentric hexagonal lattices can be distinguished, the outermost pattern (P) having a 7 times larger periodicity than the inner pattern (P1). The separated respective FFTs and the inverse FFTs (IFFTs) are also shown (Figures 4.13(d)-(g)). The hexagonal lattice in Figure 4.13(f) corresponds to the characteristic ~ 6 Å distance of the Cu_2O, while the large lattice is the result of the particular superstructure of this example.

Though the preparation parameters are crucial for obtaining good quality oxide layers, different procedures may give differences and, at first sight, the experimental data reported so far seem to present a certain scatter. This fact is actually due to the complexity of the system and all investigations support that the compact structure obtained at higher temperature ("44") is certainly the most stable one. In fact, most observed structures can be explained as different stages of the formation (or reduction) of this compact oxide layer. Starting from oxygen adsorption and after the first stages of oxide nucleation, oxidation proceeds passing from disordered and non-stoichiometric phases, until eventually evolving to a ordered $Cu_2O(111)$-like lattice, the "29" or "44" depending, as commented above, on the temperature used. The reversed path induced by reduction of the "44" leads, in addition, to oxygen deficient phases [231].

4.4.4 Theoretical models of oxide precursors configurations

From all the descriptions made in the previous sections, and in spite of the apparent controversy between preparation methods and complex structures observed, it is important to remark that the simplest model grouping together consists on a hexagonal array of Cu and O atoms with periodicity of 6 Å similar to $Cu_2O(111)$. Then, depending on differences in local stoichiometry or defects, diverse short range or largely ordered oxide layers can be found. Theoretical approaches based on density-functional theory (DFT) calculations reported the relative stability of

different surface oxides of the oxygen-Cu(111) system. To replicate the experimental observations, a (4 x 4) supercell was considered as starting point to model various possible configurations by varying the O content (Figure 4.14). Though being metastable, all of them resemble both geometrically and electronically to the bulk oxide phase, which makes them to be considered as possible precursors of the bulk material [180, 181]. It is interesting to note that the lattice parameters of these (4 x 4) structures are $\mathbf{a} = \mathbf{b} = 4$ x 2.56 Å = 10.24 Å but reduce to half of this value, i.e. $\mathbf{a} = \mathbf{b} = 2$ x 2.56 Å = 5.12 Å, for full oxygen content (Figure 4.14(h)). Therefore, though the overall configuration is very similar, the (4 x 4) periodicity is slightly smaller than the $\mathbf{a} = \mathbf{b} = 6$ Å of the "44" structure (Figure 4.1(a)). Moreover, the theoretical case implies all O_{ad} at identical adsorption sites instead of the three sites (fcc, hcp and atop) of the experimentally found.

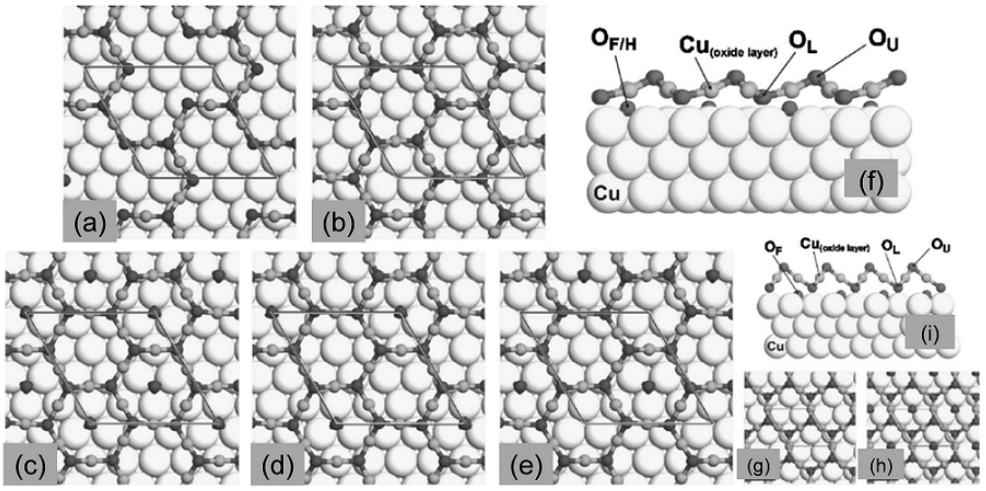

FIGURE 4.14: Theoretical models of the precursor oxide surfaces. Optimized p4- and p2-configuration oxidic structures. (a) p4-OCu_3, (b) p4, (c) p4+O_{FH}, (d) p4+O_F, (e) p4+OH, and (f) the side view of the p4-configuration structures. (g) and (h) are the unstable p2 and p2+O_F structures. The side view of the p2-configuration is shown in (i). The surface unit cell is indicated by the solid lines. The unreconstructed Cu layer is shown as large white circles, with the oxide layer Cu atoms in small light gray circles. Oxygen atoms are denoted by small dark gray circles. Figure extracted from [180].

.

Despite the simplicity of the theoretical structures versus the complexity and multi-colored experimental framework, these models offer valuable insight to understand the existing as well as the new oxide layer configurations. On the one hand, the lateral O-Cu-O lateral unit of the trilayer, which is also characteristic of bulk Cu_2O, can be laterally adapted (strained or compressed) to the substrate so the adsorption sites may be varied. On the other hand, if the oxide layer starts

nucleating at many different surface locations or nucleation sites (for instance due to energetic impinging oxygen, defective copper surfaces, reduced atom diffusion...), large order may be importantly inhibited. All these precursors (from Figures 4.14(a) to (h)) can be viewed as consisting of ordered arrays of connected Cu_3O units with increasing content of O_{ad} (O_F in the theoretical models). This fact is product of the high stability of these units that we will use in the following for the construction of our proposed model to understand the formation of a non-reported oxide phase that has been observed in the present investigation.

4.4.5 Oxide Nanowires and the Open Honeycomb Structure

In addition to the experimental structures described in precedent sections, two other oxidic phases have been obtained after the preparation protocol employed. The first one is shown in Figure 4.15(a) and appears as a prolongation of the "44" phase in the form of elongated chains formed by well-defined rounded units separated ~ 6 Å. These oxide nanowires can be more than 10 units long and they appear either in parallel but separated rows, meeting at coincident points in which the chains share one unit and form 120°, or visualized as end-free chains. While the first configurations keep stable during STM imaging, the free-end chains have the frizzy appearance typical of movable entities. This observation provides the clue for understanding the formation of the open honeycomb (OHC) structure seen in Figure 4.15(b) (where a small chain is also visible) and which is described in the following.

According to the S-W or 5-7 model, in which pentagons and heptagons are embedded in the hexagonal lattice, some hexagons are depicted on top of the OD in Figure 4.15(b). The lattice rotation implied by the creation of the 5-7 defects is reflected in the relative orientation of some of the hexagons (labeled A and B in Figure 4.15(b)). The small circles correspond to the Cu (black) and O (red) atoms forming the honeycomb structure of the $Cu_2O(111)$-like layer. In the A hexagons the O atoms are omitted for simplicity as well as central O atoms are omitted in all cases. The open overlayer shown in the lower part of Figure 4.15(b) cannot be related to reported configurations of different stoichiometric oxide layers. Appearing always in coexistence with other more compact structures (see Appendix) at the external region of the oxygen modified regions, as far as we know, this open

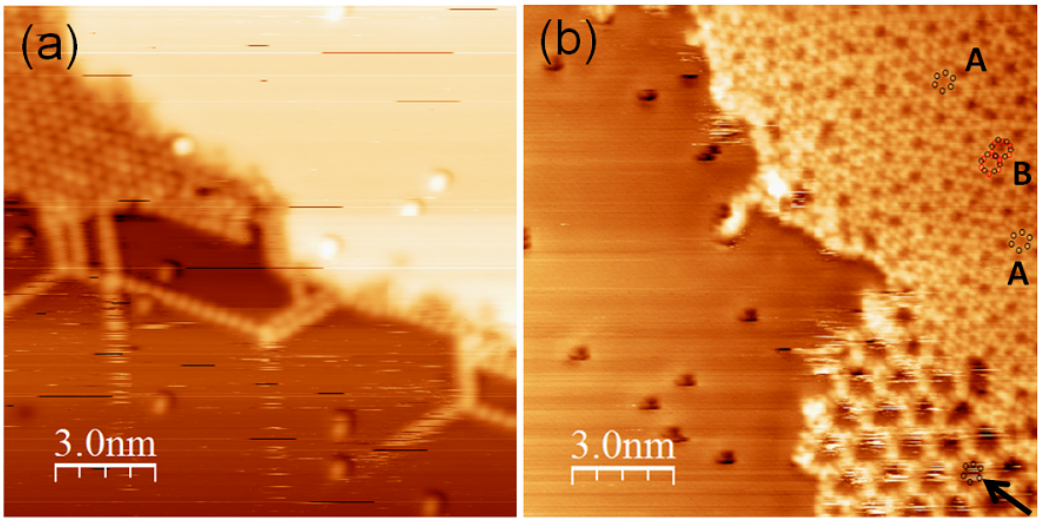

FIGURE 4.15: (a) Oxide nanowires emerging at the borders of the "44" structure. The angle between chains meeting and comparting one unit is 120°. Note the frizzy appearance of the non-bonded chains. (b) OHC structure seen at the border of OD regions (b). A and B in (b) denote hexagons differently orientated due to 5-7 defects formation and the black arrow at the right bottom signals the relative size of the configurations. The separation between units forming the chains and between the small bright spots in the OHC is $\sim$ 6 Å, coinciding of the oxide periodicity. Parameters: (a) I = 200 pA, Bias = -0.87 V, A = 200 pm (b) I = 62 pA, Bias = +0.50 V, A = 200 pm.

.

honeycomb (OHC) lattice is reported here for the first time. As it can be seen by the ball model hexagon depicted on top of it (black arrow in Figure 4.15(b)), this OHC structure is much larger than the OD network. Using the bare Cu(111) terraces as reference, we can establish that this OHC has a periodicity of $\sim$ 13 Å and is rotated 30° respect to the Cu(111) substrate. Consequently, it can be denoted in the Wood's notation as $(3\sqrt{3}$ x $3\sqrt{3})$R30° has an unit cell parameter of 13.3 Å. The lattice orientation is corroborated in Figure 4.16, where the OHC coexist with a well-ordered hexagonal phase (HC). As expected, the FFTs shown in of the indicated areas, OHC and HC, are rotated by 30°.

Based on the experimental observations, in particular making compatible the coexisting configurations to discard tip conditions dependence, this model is derived from the theoretical metastable phases described above. As commented these phases are considered as precursors of the $Cu_2O(111)$-like layer and consisting of Cu_3O units. Each Cu_3O unit is depicted in the model of Figure 4.17(a) as yellow (O) and red (Cu) circles on top of the Cu(111) substrate. The model perfectly mimics the nearly defect-free OHC oxide layer shown in the STM image of Figure 4.17(b). The plausibility of the model as corresponding to a precursor phase

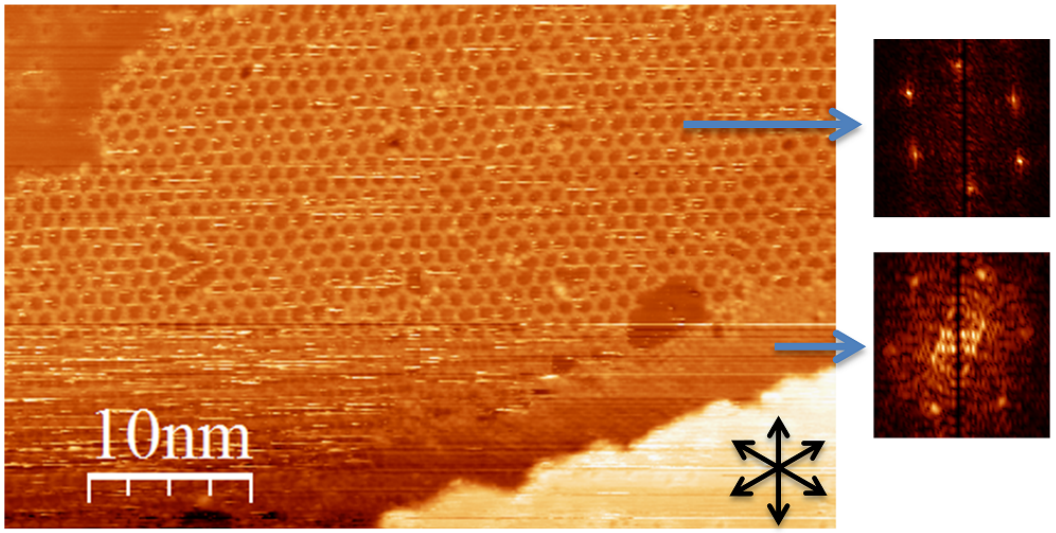

FIGURE 4.16: Topographic STM image of an area where the open honeycomb Cu_2O structure grows at the end of the Cu_2O terrace, to point out that the open honeycomb is 30° rotated the FFT of both areas appear in the inset. Black arrows indicate the three equivalent ⟨110⟩ copper directions. Parameters: I = 110 pA, Bias = -1.56 V, A = 200 pm.

.

with low O content is supported by the additional Cu (gray) and O (orange) placed inside one hexagon of Figure 4.17(a). Note that these added atoms do not appear in the defect- free experimental OHC.

A series of topological defects identified as irregular hexagons and individual, aligned or clustered missing Cu_3O units can be seen in Figure 4.16 and in the magnified image of Figure 4.17(d). All of them can be explained in terms of the proposed model as depicted in Figure 4.17(c). These defects correspond to missing or displaced Cu_3O units. The later depicted as green circles in the model and signaled by black arrows in model (Figure 4.17(c)) and experiment (Figure 4.17(d)), where a filled hexagon can be compared with that of Figure 4.17(a) (orange and brown circles).

Blue lines in the bottom panels are used to guide the eye along the missing rows of Cu_3O units, which are otherwise well resolved in the central part of the STM image as bright individual dots. Note that only at defects these units are individually seen in these images. It is worth emphasizing the fact that this structural model permits explaining its observation as one of the very first oxidic phases existing at the copper oxide formation. On the one hand, the preparation method used here is able to stabilize such low O content configuration, note the complete similarity between

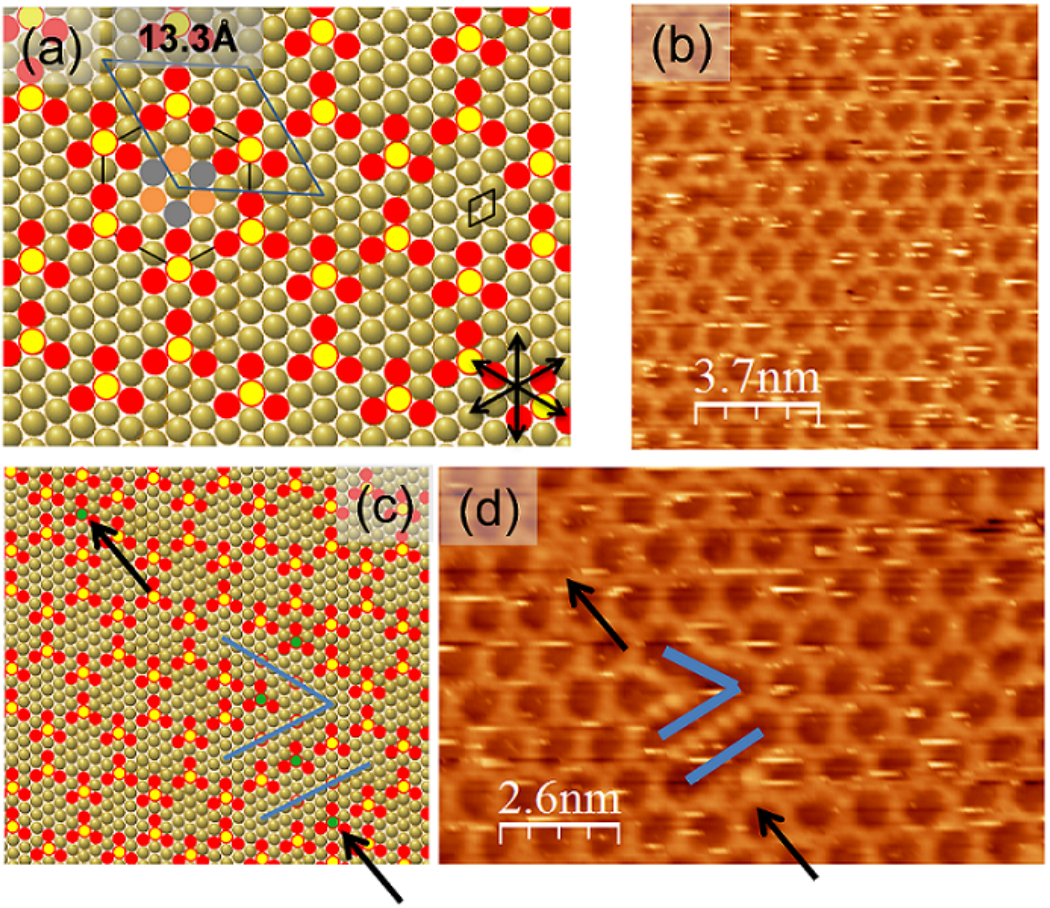

FIGURE 4.17: (a) Schematic representation of the model proposed for the OHC structure. Oxygen and copper atoms forming Cu_3O units are represented by yellow and red circles, respectively, on top of the Cu(111) topmost surface (golden). The unit cells of the OHC and substrate are depicted. (b) Topographic STM image of an OHC region. (c) Model of some of the topological defects (see text) observed in (d). The size of the Cu atoms of the Cu_3O units have been reduced here for clarity. (d) Magnified area of the STM image in Figure 4.16(a). Parameters: I = 110 pA, Bias = -1.56 V, A = 200 pm.

.

the chains (linear defects) formed within the lattice with the chains (nanowires) described in Figure 4.15.

Once established the structural model for this new structure, the already mentioned dependence on measuring tip and bias conditions is illustrated in Figure 4.18. Due to difficulties during STM measurements due to the high mobility of the units (probably induced by the sweep action of the tip), blurred images were often obtained for these small scans.

In order to clarify this point, we present a combined experiment in which topographic STM (constant current) and constant height measurements from the very

same area are presented. Figures 4.18(a)-(b) are the topographic STM image and the simultaneously frequency shift image and Figures 4.18(e)-(f) are the tunneling current and frequency shift acquired at constant height measurements. Both experiments are schematically presented in Figures 4.18(d) and (h). Interestingly, the center of the OHC in the topographic STM (Figure 4.18(a)) is at the same surface level than the copper terrace and the measured frequency shift is also the same (Figure 4.18(b)). As expected for a semiconducting layer, less current is detected on the OHC lattice than in the Cu(111) surface during the constant height measurements (Figure 4.18(e)). Because the height is kept constant, the tip-sample distance is smaller over the copper oxide because copper oxide is topographically higher than the copper terrace. As it can be seen in the g current image (Figure 4.18(e)) the same tunneling current is measured inside the porous of the OHC than in the external copper terrace. As a whole these experiments suggest that, in the perfect OHC, the center of the lattice exhibits the copper substrate.

4.4.6 Copper nitride

It has been reported that nitrogen gets hardly chemisorbed on copper surfaces unless the process is activated by ion implantation or atomic beam sources [53, 174]. Therefore, taking into account the Ar^+/air sputtering and annealing procedure used in this thesis, one may expect forming copper nitride at a given extent. However, despite the large content of nitrogen in air (air is a mixture of gases, 78 % nitrogen and 21 % oxygen with traces of water vapor, carbon dioxide, argon, and various other components) only a small percentage of a nitride phase (Figure 4.19) has been observed in a small percentage of the samples studied in this thesis.

The observed structure has been always found to coexist in the same surface regions with the higher O content copper oxide phase, namely the “44”, described in this chapter. Thus, in Figure 4.19(a), the CuN layer and the rounded features typical of OA are observed, while in Figure 4.19(c) the CuN layer appears coexisting with the “44” copper oxide structure (right region in the images) and a copper terrace (left in the image) where some OA are also seen. The simultaneously acquired frequency shift is shown in Figure 4.19(d). Not obvious conclusions can be extracted from the later channel because the different and unknown electronic characteristics of each material. However, a lower measured current in the CuN

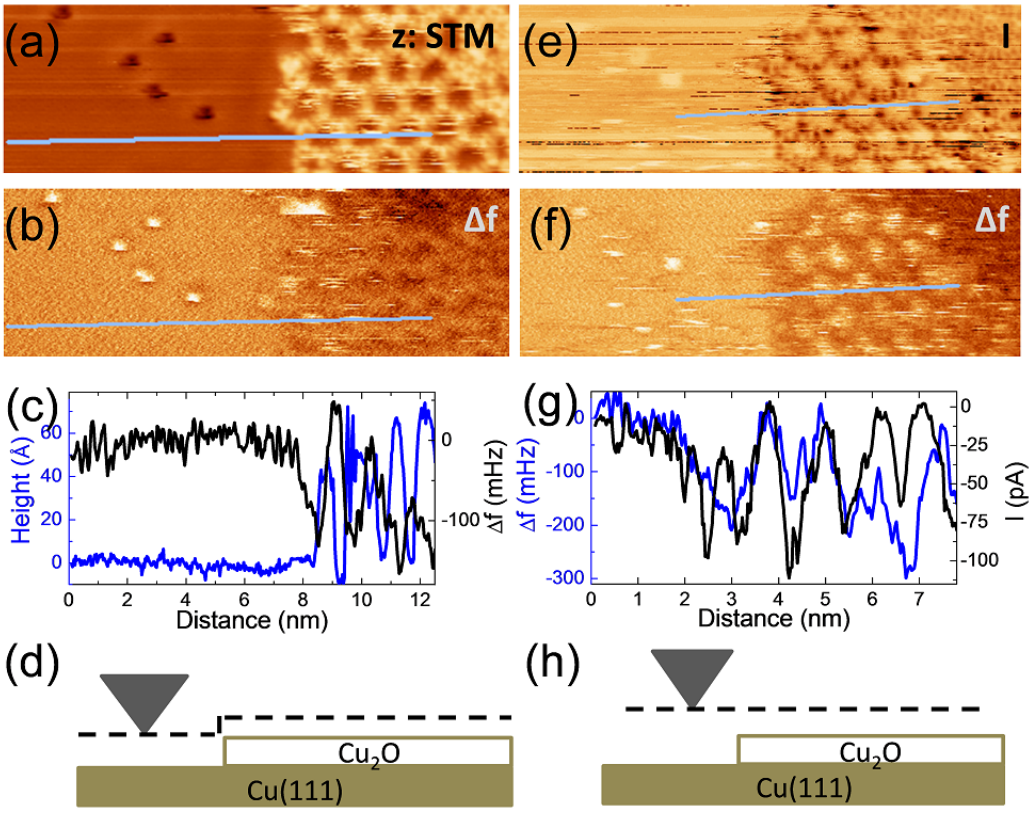

FIGURE 4.18: (a) STM topographic image of the OHC coexisting with bare Cu(111) and few OA features and (b) simultaneously measured frequency shift channel. (e) Constant height current image and (f) its simultaneously measured frequency shift channel of the very same area. The corresponding line profiles are depicted in (c) and (g). (d) and (h) Schematic representation of the tip-sample distances at STM (a)-(b) and constant height (e)-(f) imaging mode. Parameters: (a) I = 94 pA, Bias = -0.90 V, A = 200 pm (b) I = 200 pA, Bias = -0.76 V, A = 200 pm (c)-(d) I = 62 pA, Bias = +0.49 V, A = 200 pm and (f)-(g) Bias = +0.90 V, A = 200 pm.

.

than in the "44" and much lower than in copper indicates the semiconducting character of the nitride layer.

The structure is seen in the STM images as rather regular wavy bands (clearly seen in the frequency shift image of Figure 4.19(e)) running in a direction slightly deviated from the ⟨110⟩ of the Cu(111) substrate (represented by a red arrow). The angle between the mean orientation of the edge of the CuN layer (represented by the red black) and the ⟨110⟩ substrate is $\theta \approx 15°$. This copper nitride structure corresponds to the reported stripped CuN on Cu(111), also considered as a pseudo (001) reconstruction of this surface and consisting of elongated domains formed by stripes with their axis varying up to 10° from the close packed directions of the substrate [8, 46, 76, 174]. Figure 4.19(b) is an STM image from Driver and

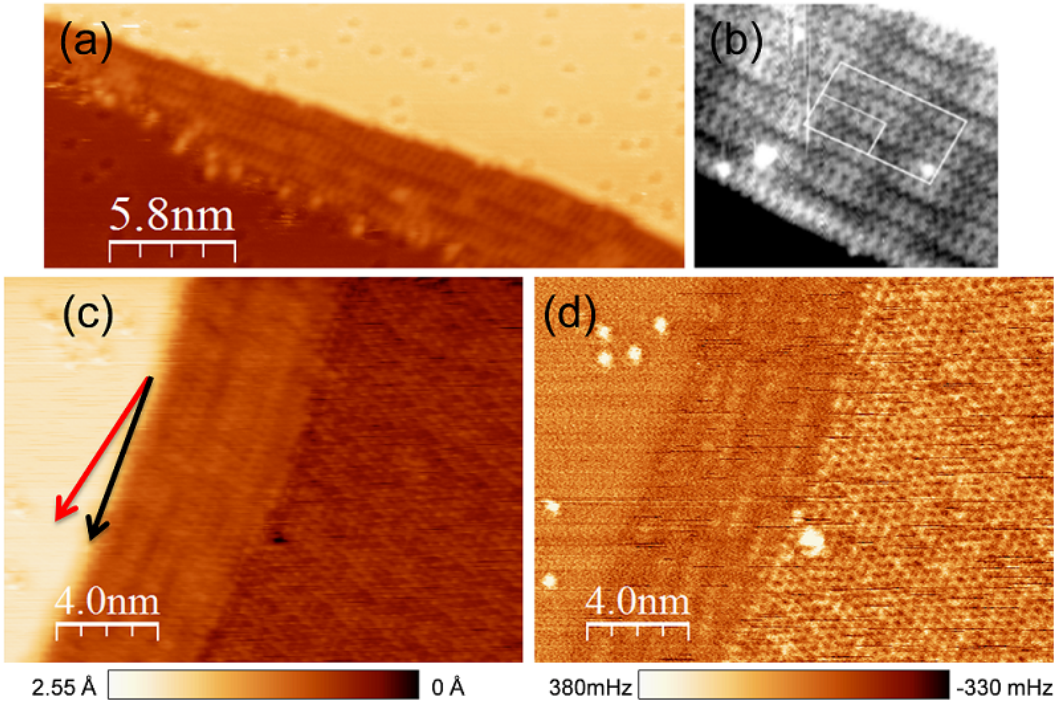

FIGURE 4.19: (a) Topographic STM image of the CuN structure observed at the edge of a Cu(111) step. Note the OA features on the upper Cu terrace. (b) STM image from [46]. (c) Topographic STM image and (d) simultaneously acquired frequency shift of a different region of the surface in which the CuN layer appears coexisting with the "44" copper oxide structure (right in the image) and the copper terrace (left in the image). The angle between the edge of the CuN layer (black arrow) and the ⟨110⟩ direction of the Cu(111) substrate (red arrow) is 15°. Parameters: (a) I = 126 pA, Bias = +1.20 V, A = 200 pm and (c)-(d) I = 200 pA, Bias = -0.8 V, A = 200 pm.

.

Woodruff [46] who obtained the N adsorbed phase on Cu(111) by operating an ion gun with nitrogen gas leading to ion nitrogen bombardment (500 eV) followed by annealing at 300°C. The structure was defined as a rectangular (25 x $7\sqrt{3}$) with characteristic dimensions of 66 Å x 30 Å [98].

The observed vertical rumpling is due to different relative height of the diverse atoms in the CuN overlayer because their different local registry with respect to the Cu(111) substrate and is characteristic of site coincident lattices (SCL) or incommensurate overlayers, similar to the described Moiré-like patterns observed for the copper oxide case. As it can be also seen in the images, the step edges of the nitride layer appear distorted. This observation has been interpreted as a distortion in the angle (θ) between the stripped pattern and the ⟨110⟩ of the Cu(111) substrate and the nearest Cu atom array at the CuN lattice [8]. For

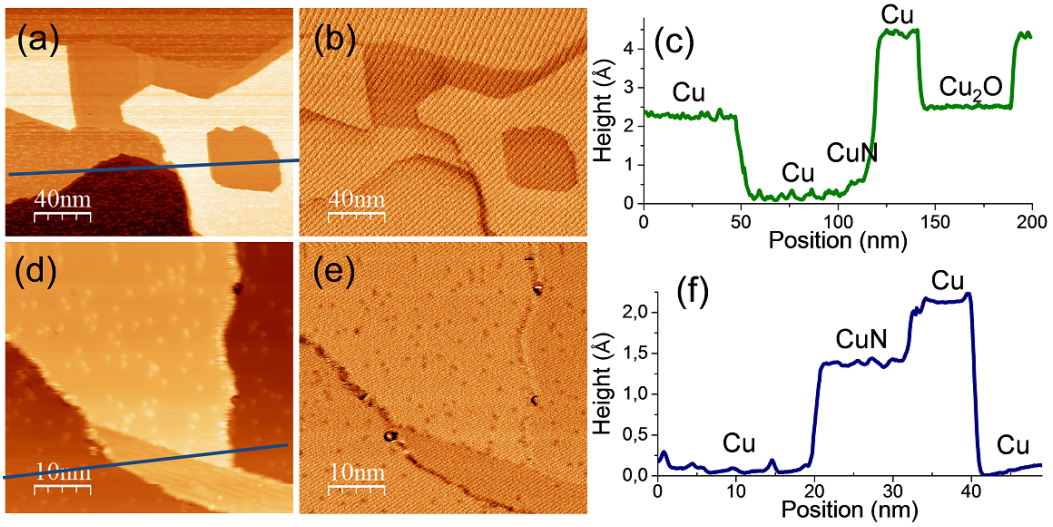

FIGURE 4.20: Topographic STM images of two different surface areas showing the CuN phase coexisting with: copper terraces and the "44" oxide layer (a) and copper terraces with OA features (e). The simultaneously acquired current (b and f) and frequency shift (e and g) channels are also shown. The topographic lines marked by segments in (a) and (e) are presented in (d) and (h), respectively.

.

$\theta \leq 15°$ the distorted striped patter may appear. This is indeed the case in the images presented in Figure 4.19.

Two different surface areas showing the CuN phase are shown in Figure 4.20. The different types of surface regions are indicated in the topographic images (Figures 4.20(a) and (e)). As it can be seen the nitride layer appears to coexist either with the "44" regions Figure 4.20(a) and copper terraces in which OA features can be seen. Not important intensity contrast is observed at this large scale, the topographic details are highlighted in the current image (Figures 4.20(b) and (f)). The different composition of the different regions is neatly seen in the frequency shift images (Figures 4.20(c) and (g)). The simultaneously acquired current and frequency shift images are also shown. From the topographic profiles (Figures 4.20(d) and (h)) taken along the different composition areas, Cu_2O regions appear as grown either at the step edges or developed at large vacancy islands on the Cu terraces (see height analysis in Figure 4.5). The differences in apparent height indicate that the CuN layer lies $\sim$ 0.8 Å than the upper Cu terrace and $\sim$1.2 Å higher than the lower one and, curiously, also is seen as a fine stripe embedded between the copper oxide layer in Figure 4.20(a).

4.5 Conclusions

By employing a particular preparation method consisting in air enriched Ar+ bombardment of the clean Cu(111) followed by annealing to 240°C, six different oxidic phases are observed to partially cover the sample surface and commonly coexist on the same sample surface. Depending on the local oxygen content or stoichiometry, these structures are: the typical individual or clustered oxygen atoms adsorbed (OA) on the otherwise bare copper terraces, the four 2D structures already reported and described in the literature (termed in this thesis as short order honeycomb, SOHC, large order honeycomb, HC, O-deficient, OD, and the complex "44") and a new open honeycomb (OHC) lattice with a lower oxygen content than the previous ones as well as linear atomic-like chains.

The 2D framework formed by the new OHC structure has been modeled as consisting of Cu_3O units arranged in an hexagonal lattice of dimensions 13.3 Å which is labelled as $(3\sqrt{3}$ x $3\sqrt{3})$R30° in the Wood's notation. The proposed model is in agreement with the construction of metastable phases made out of Cu_xO units employed in the existing theoretical calculations and is consistent with the expected stoichiometry of the observed structure always appearing at the external edges of other phases with higher O content. Of similar composition are suggested to be the linear chains also formed at the low coordination borders of the other overlayers. The isolated Cu_3O units forming both the OHC and the chains can be displaced without disruption by the scanning tip. This observation confirms they are very stable clusters and supports models in which all oxide layers may be constructed as different arrays of these units depending on the relative O/Cu stoichiometric ratio.

Because the air fraction in the ionized gas used for modifying the Cu(111) surface, a particular copper nitride (already reported in the literature) has been found to be formed along the different oxides.

In addition to the complex scenario derived from the variety of copper oxide and nitride overlayers found, the STM imaging results in added difficulty because of diverse factors: structural and stoichiometric defects and bias dependence of nearly all the structures due to a localized density of states but, unfortunately also to not controlled changes in tip conditions. The importance of the latter being such that, for instance, missing O atoms in the HC phase leading to the OD configuration can

be viewed either as bright dots centered in some of the hexagons or as hexagons of different brightness.

The surface structures and superlattices reported here can be seen as 2D frameworks with well-defined pore sizes (from angstroms to nanometers). In particular the high quality of the most open network can provide precise and confined localization of guest functional nano-objects (molecules, nanoparticles...) to become a multifunctional nanostructured system. Compared to other bottom-up approaches as supramolecular self-assembling in which two dimensional open networks are made out molecules, the ability of fabricating patterned surfaces by a scalable method and without the need of additional organic building blocks presents unquestionable advantages for device integration in diverse fields of application.

4.6 Appendix

Coexistence of the observed structures: adsorbed oxygen, copper oxides and copper nitride

As it has been repeatedly commented in this chapter, all observed structures coexist on one or other regions after air/Ar^+ plus 240°C annealing the Cu(111). To further illustrate this interesting result for partial coverages, different STM images are presented in this appendix. Provided all the structures have been already reported throughout the chapter, here they will be labeled using the terms employed in this thesis without any detailed description for which the reader may look at the corresponding sections.

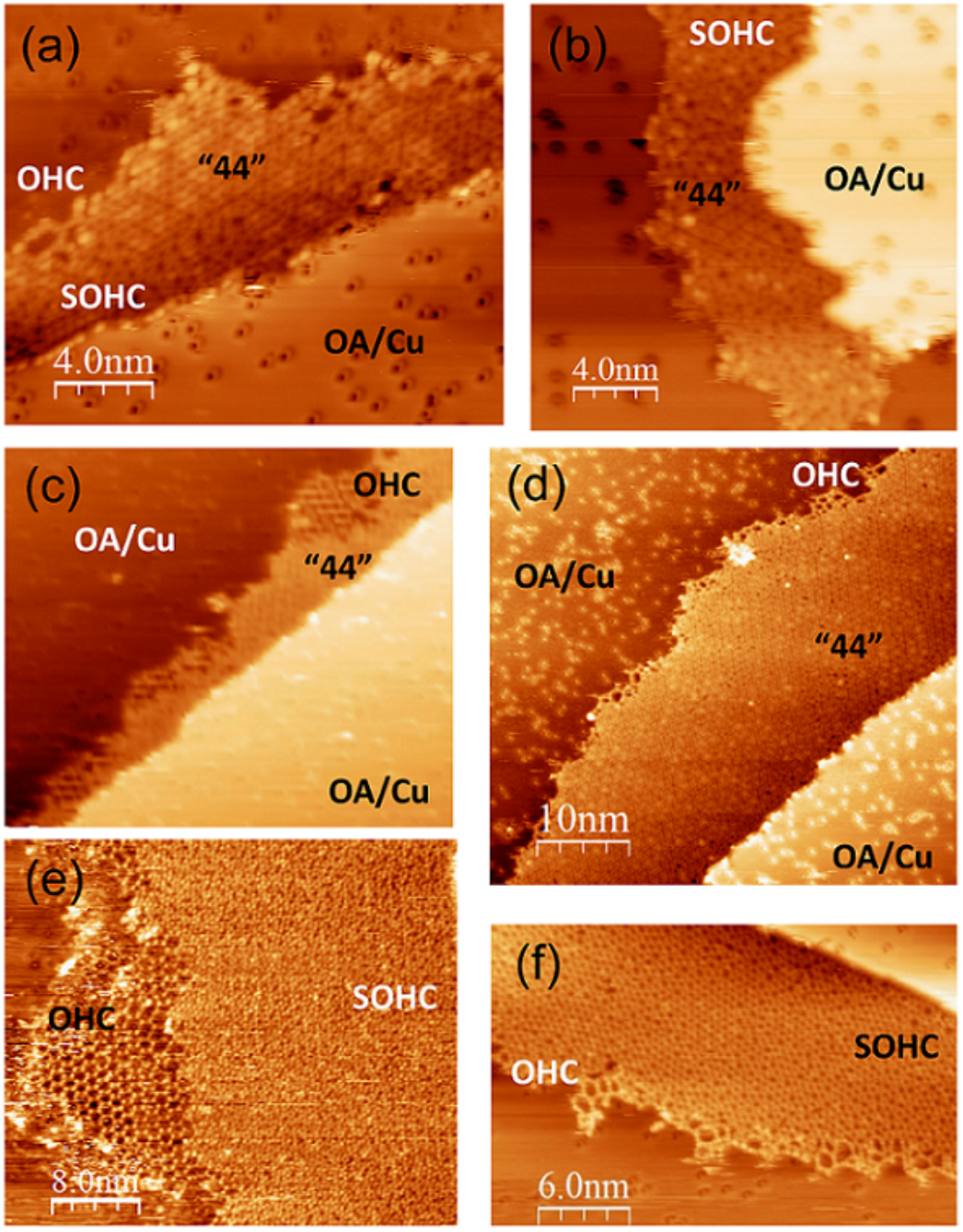

FIGURE 4.21: Coexistence of different O content structures: OA on the Cu(111) terraces, OHC, SOHC and "44". Some Cu_3O units forming chain-like structures at the outermost edges of the oxide overlayers can be also seen. In (a) the OA phase on the unreconstructred Cu(111) terraces coexist with the "44" structure and a small SOHC region at the left step edge where the bright dots associated to O_{va} and the formation of the OD phase can be also seen. Note the clear rim in the OA covering the upper and lower Cu terraces. Parameters: (a) I = 195 pA, Bias = -1.64 V, A = 200 pm, (b) I = 190 pA, Bias = -0.89 V, A = 200 pm, (c) I = 117 pA, Bias = -1.40 V, A = 200 pm, (d) I = 62 pA, Bias = -1.40 V, A = 200 pm, (e) I = 94 pA, Bias = -0.90 V, (f) I = 100 pA, Bias = -0.75 V.

.

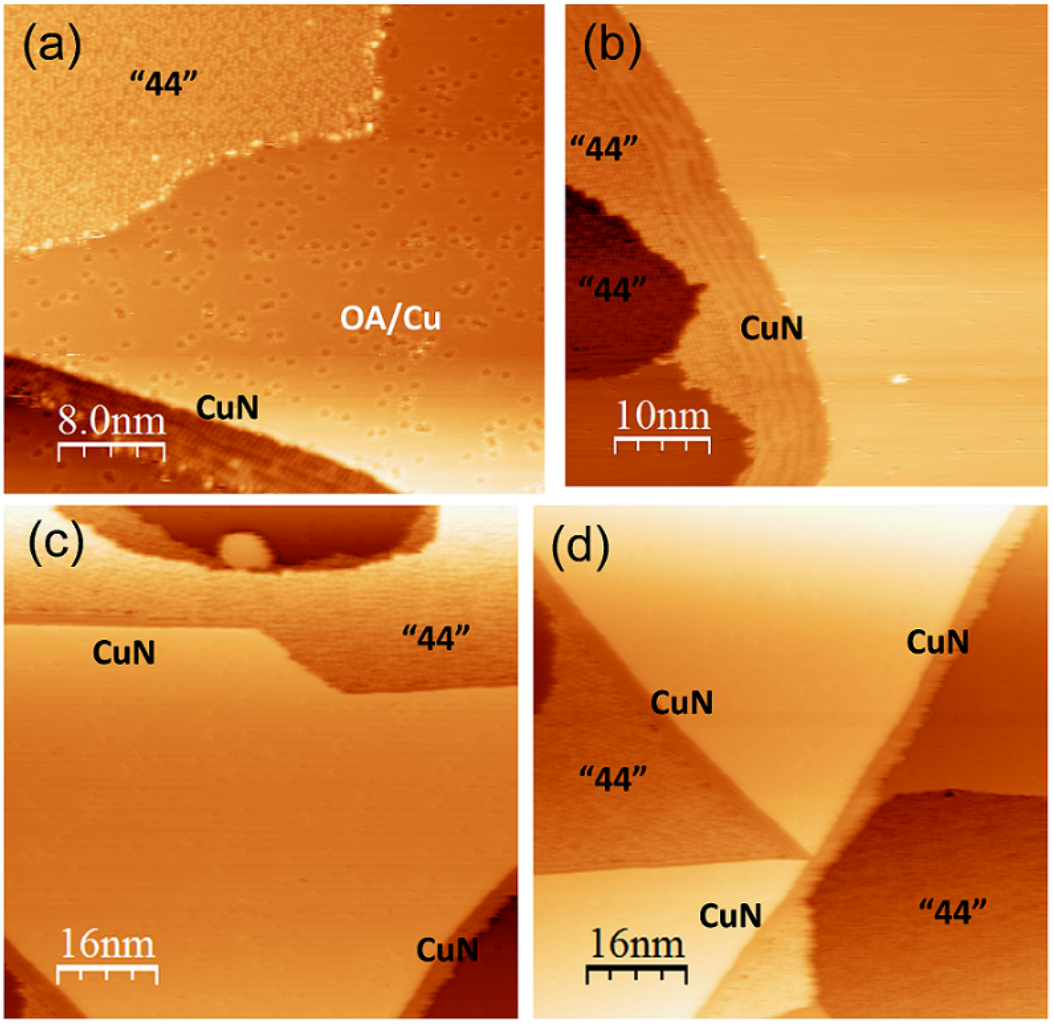

FIGURE 4.22: Coexistence of the CuN layer with the "44" copper oxide, and Cu terraces presenting the rounded depressions typical from oxygen adsorption (OA). Parameters: (a) I = 126 pA, Bias = +1.20 V, A = 200 pm, (b) I = 223 pA, Bias = +0.95 V, A = 200 pm, (c) I = 180 pA, Bias = +0.97 V, A = 200 pm, (d) I = 180 pA, Bias = +0.97 V, A = 200 pm.

.

Chapter 5

Spectroscopic Characterization of Copper Oxide

5.1 Introduction

The structural study of the different structures of a submonolayer of copper oxide growth on Cu(111) has been presented in Chapter 4. Further insights into the different mechanical and electronic properties of copper and the submonolayer of copper oxide can be obtained from contact potential difference and distance-spectroscopies. The electronic properties are intimately related to the structural properties of the interfaces. The study presented in this chapter is focused on the "44" structure introduced in the previous chapter and is here generically named as copper oxide. The lateral heterogeneity of the surface constitutes an ideal scenario where both surfaces, Cu and Cu_2O, can be tested with the same tip apex and exactly conditions, which allows to disregard tip changes that are very common when operating at room temperature due to tip-sample instabilities.

Over Cu_2O regions an unexpected $I(z)$ behavior is observed preventing even relative quantification of the local work function. Two models are proposed to explain it: a resistance added in series to the tunneling junction resistance and a tip-sample deformation. Finally, a mechanical tip instability observed over both surface regions when performing $I(z)$ are presented and analyzed. All these results point out the importance of the tip-sample junction stability and its influence on the determination of the electronic properties.

Before the results, a very brief introduction to previous studies of the work function of oxygen adsorbed on Cu(111) and bulk copper oxide are presented. The experimental results are organized as follow, first the contact potential difference measurement are presented continuing with distance spectroscopy (tunneling current and force versus tip-sample distance).

5.2 Previous Work Function Studies

There are conflicting reports in the literature as to whether oxygen exposure increases or decreases the work function of the Cu(111) surface. Delchar has previously studied the interaction of molecular oxygen on several planes of copper using macroscopic contact potential measurements and found that exposure to oxygen, without a post annealing process, results in a work function increases of 0.125 eV [43]. Spitzer and Luth, however, reported no change in work function with room temperature exposure to oxygen by ultraviolet photoemission (UPS) [183]. More recently, Takeuchi and coworkers investigated the work function as a function of oxygen exposure, stipulating that initial exposure that occurs near the step edges is correlated with an increase of the work function, and at a coverage near the full monolayer, the work function decreases [199].

Density functional theory (DFT) calculations of the work function of stoichiometric Cu_2O surface gives a value of 4.58 eV while a non-stoichiometric oxygen rich surface give a value of 5.36 eV [178]. Comparing these values with the Cu(111) work function (4.60 eV) an increases of only 0.02 eV is expected for the stoichiometric surface while an increase of 0.76 eV is expected for the oxygen rich copper oxide surface. These values point out the huge dependence of the surface stoichiometry on the work function value. Then, a small or zero work function difference is expected to be measured between both surface regions, copper and copper oxide. Due to the high variety of structures reported in the last chapter, that can be related with different stoichiometric copper oxides structures, a variety of work function is also expected.

5.3 Experimental Details

Experiments were performed at room temperature in a commercial STM/FM-AFM in an ultra-high-vacuum chamber with base pressure 1 x 10^{-10} mbar. For the image processing the freeware WSxM program has been used [101].

The sample was prepared as explained in Chapter 4. The Cu(111) single crystal (Matek GmbH) was prepared by repeated cycles of Ar^+ sputtering (1.2 keV, 10 mA) plus annealing at 240°C. To obtain a submonolayer of Cu_2O on the Cu(111) surface, an air-enriched Ar^+ sputtering plus annealing at the same temperature was performed.

Long and short z-range distance spectroscopies are presented in this chapter. Forward and backward of the tunneling current, frequency shift, excitation and amplitude have been recorded in each spectroscopy. Both ranges spectra were performed with the same setting time (200 μs), integration time (20 ms) and number of points (256 points). An oscillation amplitude of 200 pm was used. The z-drift was measured and corrected before acquiring the spectroscopic data. The amplitude was calibrated on a metallic surface, Cu(111), employing the amplitude vs. z piezo position method explained in Chapter 3.

5.4 Contact Potential Difference Measurements

Contact potential measurements have been performed on both areas, Cu(111) and Cu_2O, in order to determine the work function difference. Several sets of measurements have been recorded and the maximum CPD difference observed between both surfaces is that shown in Figure 5.1, where the obtained CPD value over Cu(111) (blue plot) is 131 mV and over Cu_2O (green plot) is 278 mV. The work function difference, $\Delta\phi$, can be calculated as explained in Chapter 2:

$$\Delta\phi = \phi_{Cu_2O} - \phi_{Cu(111)} = e\{V_{CPD}(Cu_2O) - V_{CPD}(Cu(111))\}, \qquad (5.1)$$

giving a work function difference of ∼+150 meV.

Other data sets, which are not presented here, show a smaller or even no variation of the work function between the two surface regions in agreement with DFT

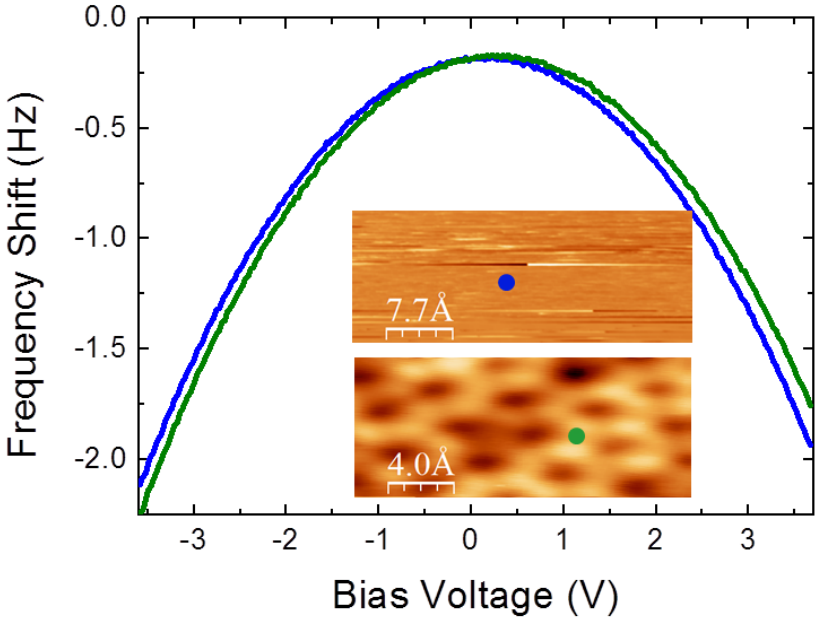

FIGURE 5.1: Example of frequency shift versus bias voltage performed over copper (blue plot) and over copper oxide (green plot). The obtained CPD values are 131 mV for Cu(111) and 278 mV for Cu_2O. The STM images where the spectroscopies were performed are located as an inset. The tip was retracted 800 pm from the setpoint position. STM image parameters: I = 100 pA, Bias = +1.20 V, A = 200 pm.

calculations for Cu_2O surface [178]. Since there is a great variety of copper oxide structures on Cu(111), the non-reproducible CPD values are expected due to different stoichiometric structures. Unfortunately, it was not possible to correlate the different data set values with the different copper oxide structures. The information that can be extracted from this data is that the work function difference between both surface regions, if it exists, is small.

5.5 Tunneling Current and Force Characterization

As explained in Chapter 2, the effective barrier height can be calculated from the z-dependence of the tunneling current. Thus, a priori, $I(z)$ spectroscopy allows us to quantify differences in the work function between Cu(111) and the Cu_2O layer. This is the motivation of the study presented here. The decay constant of the tunneling current, kappa, can be measured through the exponential dependence of the tunneling current with the distance (see e.g. [27]):

$$I = I_0 \exp\left(-2\kappa z\right), \tag{5.2}$$

where I_0 is the tunneling current at the point of contact, κ is the decay constant of the tunneling current and z is the tip-sample distance. The exponential dependence can be derived from the elementary one-dimensional model of electron tunneling through a square barrier with an apparent height ϕ_{app}, which depends on the tip and sample averaged work function, $\bar{\phi} = (\phi_{tip} + \phi_{sample})/2$, and the applied bias voltage, V_{bias}. Within this one-dimensional square-barrier model, the decay constant is:

$$\kappa = \frac{\sqrt{2\,m\,\phi_{app}}}{\hbar}, \tag{5.3}$$

with $\phi_{app} = \bar{\phi} - e\mathrm{V}_{bias}/2$, e being the elementary charge, m being the electron mass and $\hbar$ being the reduced Planck's constant.

Scanning tunneling microscopy can locally probe the tunneling current as a function of the tip-sample distance, having in principle access to the local work function of the surface under investigation. However, as it will be explained in this chapter, the analysis and interpretation of the $I(z)$ spectroscopy data is not straightforward and requires some caution.

For a better control and understanding of the measurements, it is important to have access to the tip–sample interaction. In this respect, the measuring of the distance dependence of the frequency shift and the dissipation bring the possibility of learning about tip-sample interaction. At far tip-sample distance, the interaction is attractive due to long-range van der Waals and electrostatic forces and depends on the macroscopic tip and bias voltage, whereas, at short distances, the chemical force between the atoms at the tip and the surface comes into play and the interaction becomes repulsive. Energy dissipation can arise from the establishment and/or breaking of chemical bonding or from hysteric motion of atoms. Thus, frequency shift and dissipation provide valuable information of the mechanical stability of the tip and the physical and chemical interactions acting during the acquisition of the $I(z)$ as will be seen in the following.

Long $\Delta f(z)$ spectra can be converted to $F(z)$ using the formalism of Sader and Jarvis [167] as explained in Chapter 2. Differences in the chemical interaction

are expected due to the different nature of both materials. Three data sets of spectroscopies, with three different tips, over both surface regions were collected and they will be called as A, B and C. Unfortunately, it was not possible to perform both, long and short range $I(z)$ curves, in all the experimental data sets without a change of the tip.

As explained in the last chapter, unreactive oxygen is adsorbed on the copper surface. Such features are generally imaged by STM as holes although in some cases they appear as bright protrusions [226, 231]. This is one of the key problems in scanning force microscopy, that the atomistic structure as well as the chemical composition of the tip can change in an uncontrolled way. Although without atomistic calculations, the atomic structure of the tip apex cannot be identified, the aspect of the adsorbed oxygen on the surface serve as a method to differentiate changes in the tip apex.

Figure 5.2 displays examples of typical long-range spectroscopy curves obtained over copper and copper oxide region with tip A. Tunneling current, force and excitation versus piezo distance on both surfaces are presented. The z-feedback was opened and the tip was retracted 4 nm from the setpoint position (z = 0 nm), the tip was then driven towards and backward the sample while all the mentioned channels were recorded and plotted versus the piezo displacement (z position). Over both surface regions, the total force (blue plot) increases in negative values (attractive force) when the tip is approaching the sample. Over copper regions, Figure 5.2(a), the tip has not reached the maximum attractive force where the attractive regime changes to repulsive regime. Over the copper oxide layer, Figure 5.2(b), the maximum attractive force point is reached with a maximum value of -0.35 nN and after this point the interaction force becomes more repulsive. The simultaneously acquired tunneling current (green curves) is averaged during the oscillation due to the limited bandwidth of the amplifier. However the range of tunneling regime was not enough for a reliable calculation of the tunneling decay constant. For this purpose, short-distance spectroscopy curves were performed. The excitation signal (gray plots), which is related to the dissipated energy, is plotted in the bottom panels. Note that in both cases the dissipation signal remains constant except of a slight increase of the excitation at closer distances.

In the inset of both graphs, Figure 5.2(a) and (b), the STM image where both spectroscopies were collected are shown. The oxygen adsorbed on Cu(111) is

imaged as holes and the copper oxide area corresponds to the non-stoichiometric "44" structure presented in Chapter 4.

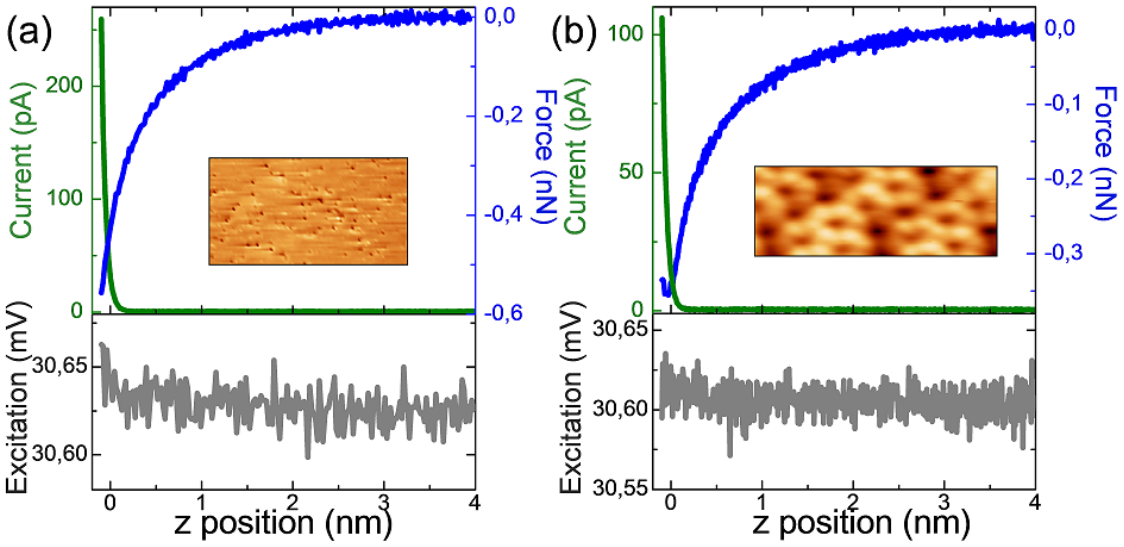

FIGURE 5.2: Tunneling current (green plot), force (blue plot) and excitation (gray plot) vs. piezo distance of long z-spectroscopy curves performed over copper (a) and copper oxide (b) with tip A. The STM images where the spectra were collected are located in the inset. The tip was retracted 4 nm from the setpoint position (z = 0nm). Parameters: (a) Bias = +1.17 V, A = 200 pm. STM image: I = 148 pA, Bias = +1.17 V, A = 200 pm, 33 nm x 18 nm. (b) Bias = +1.30 V, A = 200 pm. STM image: I = 137 pA, Bias = +1.30 V, A = 200 pm, 2.8 nm x 1 nm.

A set of short-distance curves were successively performed on surface regions of copper and copper oxide with tip B. Here is not possible to convert frequency shift into force because the Sader and Jarvis algorithm requires that the frequency shift is measured at the far distance regime where no interaction exist ($\Delta f = 0$ Hz) [167]. Representative examples are given in Figures 5.3 and 5.4 acquired on copper and copper oxide regions, respectively. Figure 5.3 plots the logarithm of the tunneling current (blue plot), the frequency shift (green plot) and the excitation (gray plot) versus piezo displacement. The linear dependence of the $ln(I)$ vs. piezo distance is clearly observed from which a decay constant of 1.11 $\pm$ 0.01 Å^{-1} is obtained, providing a tip-sample work function of ϕ_{app} = 4.70 $\pm$ 0.08 eV. This value is in agreement with previously reported values of Cu(111) [141]. The negative value of the frequency shift indicates that the average tip-sample interaction (averaged during the oscillation cycle) is attractive, getting larger for closer distances. The excitation signal does not show apparent signature of dissipative processes. The inset of Figure 5.3 shows an STM image of a copper area where an oxygen atom is adsorbed, obtained with tip B. Tip apex changes really affect the appearance of

these oxygen atoms and have been used here as a reference to detect tip changes before and after performing the spectroscopic measurements.

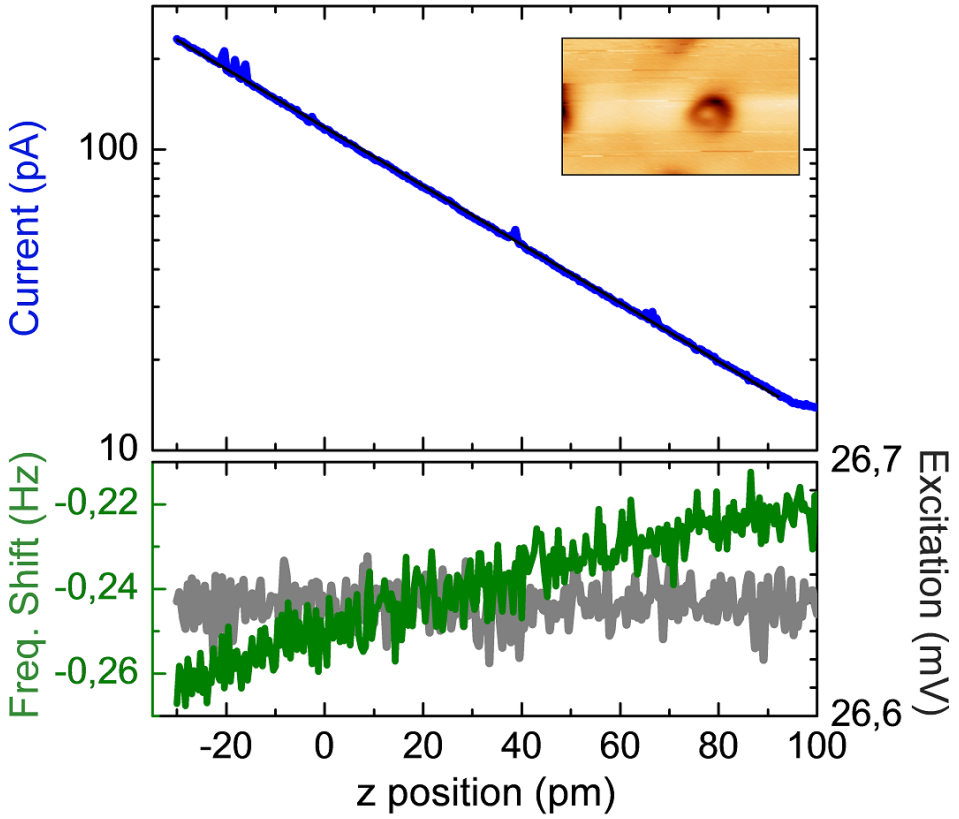

FIGURE 5.3: Top: Tunneling current (blue plot), in logarithmic scale, versus piezo displacement performed over Cu(111) with tip B and the STM image where the spectroscopy was performed in the inset. The semi logarithmic plot of the tunneling current present a linear dependence upon the piezo displacement as expected. Bottom: Simultaneously frequency shift (green plot) and excitation (gray plot). The frequency shift shows a higher tip-sample attraction when tip is approaching while no change in the excitation is observed. The z = 0 pm is the setpoint position. Parameters: Bias = -1.25 V, A = 200 pm. STM image: I = 119 pA, Bias = -1.25 V, A = 200 pm, 5 nm x 3 nm.

Figure 5.4 shows the logarithm of the tunneling current (blue plot), frequency shift (green plot) and excitation (gray plot) versus piezo displacement over Cu_2O acquired with tip B. At difference of the measurements performed on copper, Figure 5.3, the distance-dependence of the tunneling current deviates from the exponential behavior. Consequently, the logarithm plot of the tunneling current vs. z piezo displacement is no longer linear. Two linear regimes can be distinguished, which result in a decay length of $\kappa = 1.37 \pm 0.02 Å^{-1}$ (farther distance) and $\kappa = 0.98 \pm 0.02 Å^{-1}$ (closer distance). The related values of the effective

barrier height, calculated through Equation 6.2, are $\sim$ 7.2 and $\sim$ 3.7 eV, respectively. The frequency shift shows an increase of the tip-sample attraction when the tip is approached to the surface as observed over the Cu (Figure 5.3) but here a higher variation is observed. During the whole range of z-displacement the excitation remains constant without evidences of dissipative processes. No hysteresis is observed since all the recorded channels show similar behavior in forward and backward directions (only forward is presented here). Since not an unique effective barrier height value can be determined for the whole z-range a correct determination of the work function cannot be obtained.

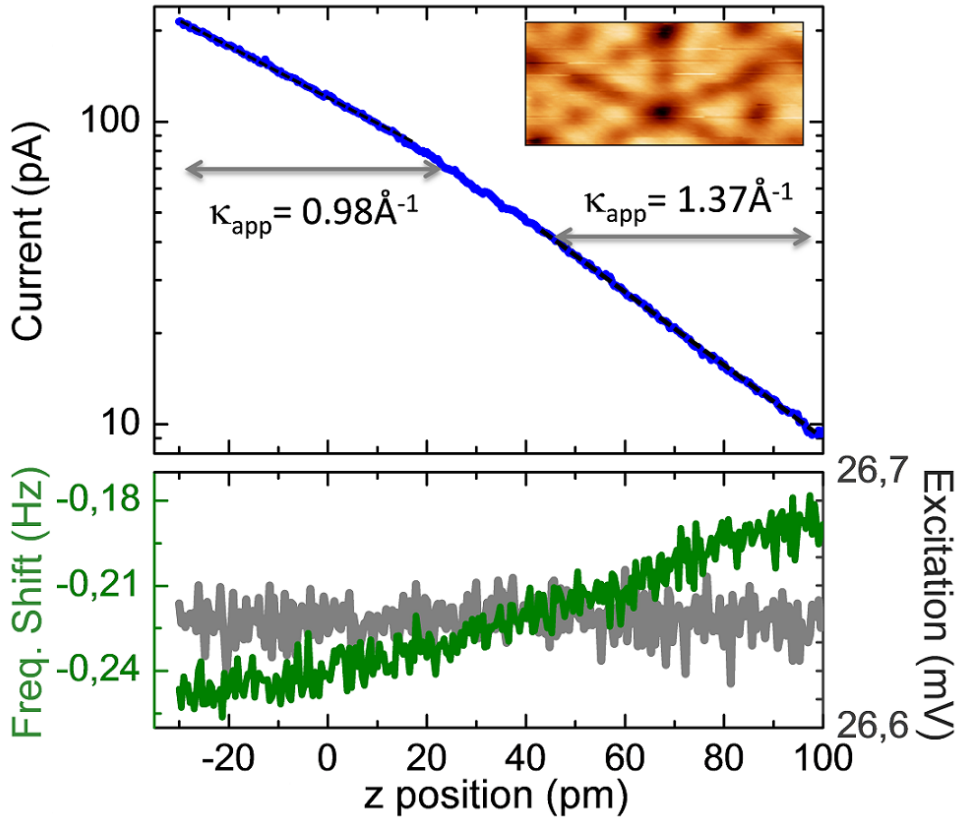

FIGURE 5.4: Top: Tunneling current (blue plot), in logarithmic scale, versus piezo displacement performed over Cu_2O with tip B and the STM image where the spectroscopy was performed in the inset. The tunneling current in logarithmic scale does not present a linear dependence upon the piezo displacement and two linear regimes can be distinguished. Bottom: Simultaneously frequency shift (green plot) and excitation (gray plot). The z = 0 pm is the setpoint position. Parameters: Bias = -0.89 V, A = 200 pm. STM image: I = 119 pA, Bias = -0.89 V, A = 200 pm, 2.7 nm x 1.2 nm.

Some effects have been reported in the literature to explain a non-exponential behavior of the tunneling current with the tip-sample distance, as tip induced band bending [59, 144], tip-sample deformations and collapse of the tunneling

barrier [112, 202, 240]. Previous STM studies of thin insulating layers have used $I(z)$ spectroscopy to measure the relative work functions over the bare copper and the insulating layers. Olsson and coworkers investigated NaCl islands on Cu(311), reporting that an exponential curve was a good fit to all the data [154]. Ruggiero and coworkers investigated CuN islands on Cu(100), and also reported that an exponential curve was a good fit for their $I(z)$ spectra [166]. The change of the decay constant as a function of distance is therefore unlikely to be caused by tip induced band bending within the insulating layer (in our case, in the copper oxide layer).

Another effect is the collapse of the tunneling barrier occurring at very short tip-surface distances due to the modification of the sample and tip wave functions [112, 202, 240]. This is experimentally manifested as a strong reduction of the apparent tunneling barrier when achieving high tunneling conductance values (close to atomic contact value of $G_0=2e^2/h=(12906\ \Omega)^{-1}$). In this regime, also known as "contact regime", the square-barrier model of the tunneling process is not longer valid. The maximum conductance in Figure 5.3 ($G_{max} = I_{max}/V_{bias}$) is of $\sim 3{\cdot}10^{-6}$ G_0, which is far away from the point contact value. In the presented experiments, the collapse of the tunneling barrier can be discarded due to the small conductance and since over all the z-range, the frequency shift stayed in the attractive regime, showing a monotonous and continuous decrease, and the dissipation remained constant. The behavior of the frequency shift and the excitation is indicative that the spectroscopy is performed in a distance range where no formation of chemical bond between the tip and the sample occurred.

Two other models will be discussed in detail in the following in order to explain the anomalous tunneling current-distance dependence observed over copper oxide. First, a resistance in series model and second a tip-sample distance deformation.

5.5.1 Resistance in Series Model

When a tunneling current is established at the junction between a metallic tip and a sample with limited conductivity, a voltage drop occurs through sample resistance which in turn lowers the electrostatic attraction, resulting in an apparently repulsive force. This effect was called "phantom force" and was first experimentally measured in Si(111) by FM-AFM/STM [225, 230]. The effect was also showed to alter the expected parabolic response of the frequency shift vs. bias voltage, when

tunneling current occurred [224]. To understand the experimental $I(z)$ behavior observed over the Cu_2O layer, a model is considered in which a sample resistance (R_s) is added in series to the metal-vacuum-metal tunneling junction resistance (R_j), as is schematically represented in Figure 5.5(a), to examine the effect on the tunneling current.

The total resistance can be expressed as the sum in series of a sample resistance (R_s) and the resistance of the tunneling junction (R_j):

$$R_{tot} = R_J + R_S = C\ exp(2\kappa z) + R_s \tag{5.4}$$

where C is independent of z but depends on the point contact resistance, $R_0 = 1/G_0 = 12.9\ k\Omega$, the real tip-sample distance offset, z_0, the decay constant, κ, and the oscillation amplitude, A. The dependence of C with the decay constant and the amplitude is due to the consideration of an oscillating tip. Applying the approximation of small amplitudes, $\kappa A \gg 1$, the tunneling current of an oscillating tip can be expressed as $\langle I(z,A)\rangle \approx I(z)/\sqrt{4\pi\kappa A}$. The tunneling current can be then expressed as:

$$I = \frac{V_{Bias}}{R_{tot}} = \frac{V_{Bias}}{C\ exp(2\kappa z) + R_s}. \tag{5.5}$$

The sample resistance is constant over all the z-range but the junction resistance is not. At long tip-surface distances, when the $R_j \gg R_s$, the tunneling current is dominated by the tunneling junction. However the effect of R_s starts to be significant at close tip-surface distances, i.e when R_j is reduced. As the tip is moved towards the sample, the tunneling current increases but also the voltage drop. The increase in the voltage drop produces a decrease of the effective voltage between the tip and the sample resulting in a lower growth of the tunneling current. Figure 5.5(b) shows two $I(z)$ spectra, one without voltage drop effect (black plot), i.e. $R_s = 0\ \Omega$, and another with a $R_s = 100\ M\Omega$ (green plot). When a voltage drop occurs, the tunneling current does not depend exponentially with the tip-sample distance. The difference between the tunneling currents for $R_s = 0\ \Omega$ and $R_s = 100\ M\Omega$ increases for larger tunneling currents.

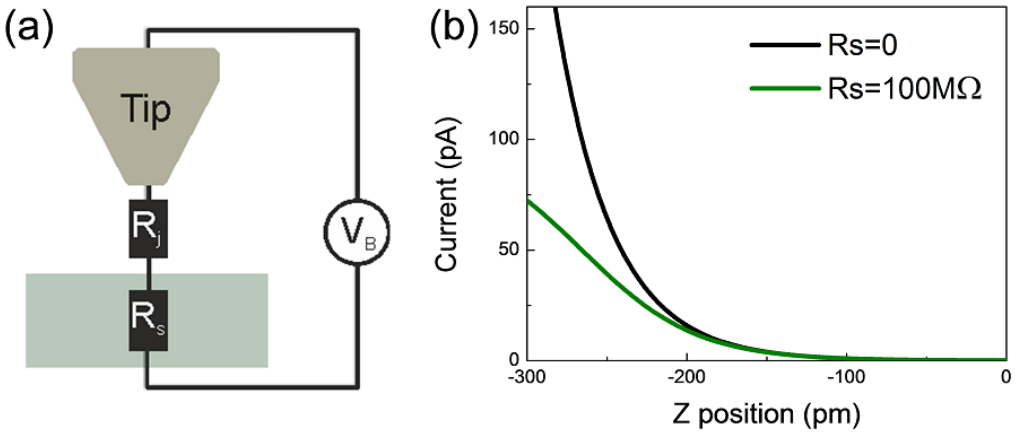

FIGURE 5.5: (a) Schematic representation of the STM tip, junction and sample and the two resistances in series R_j and R_s. (b) Simulated tunneling current vs. tip sample distance for $R_s = 0$ (blue line) and $R_s = 100$ MΩ (green line) Parameters: $\kappa = 1.40$ Å^{-1} and $I_0 = 1/12600$ A.

Copper oxide is a semiconductor but here only a monolayer of this material is grown over a metal. The final material cannot be considered as a bulk semiconductor and the sample resistance is assumed to be in the copper oxide monolayer as can be observed in the representation of Figure 5.6(a). In Figures 5.6(b) and (c), $I(z)$ collected over copper and copper oxide regions with tip B are presented. These spectra belong to the same data set that those presented in Figures 5.3 and 5.4. As described before, the spectrum over the bare copper surface fits very well with an exponential function, i.e., $R_s = 0$ Ω and $\kappa_{Cu} \sim 1.13$ Å^{-1} (black line in Figure 5.6(b)), but the single exponential model fails for the case of the copper oxide, as can be seen by the gray dotted line in Figure 5.6(c). This spectrum is instead well fitted with $R_s = 1.4 \pm 0.1$ GΩ and a decay constant $\kappa_{Cu_2O} \sim 1.23$ Å^{-1} (black line in Figure 5.6(c)), with a related work function of 5.76 eV. This value is in between the values, previously calculated, for the farthest and nearest z-range shown in Figure 5.4. The work function difference between copper and copper oxide can be then determined as 0.9 eV higher over copper oxide what agrees very well with the theoretical value for the oxygen rich Cu_2O surface [178].

As for a physical interpretation, a charge carrier transport taking place through the oxide plane may be at the origin of R_s. The obtained value of R_s would then be related to the resistance of one layer thick of Cu_2O, a value that is experimentally unattainable. However, a rough estimation of the specific copper oxide resistance, ρ_{Cu_2O}, can be done by considering a sample resistance of 1.4 GΩ and an oxide

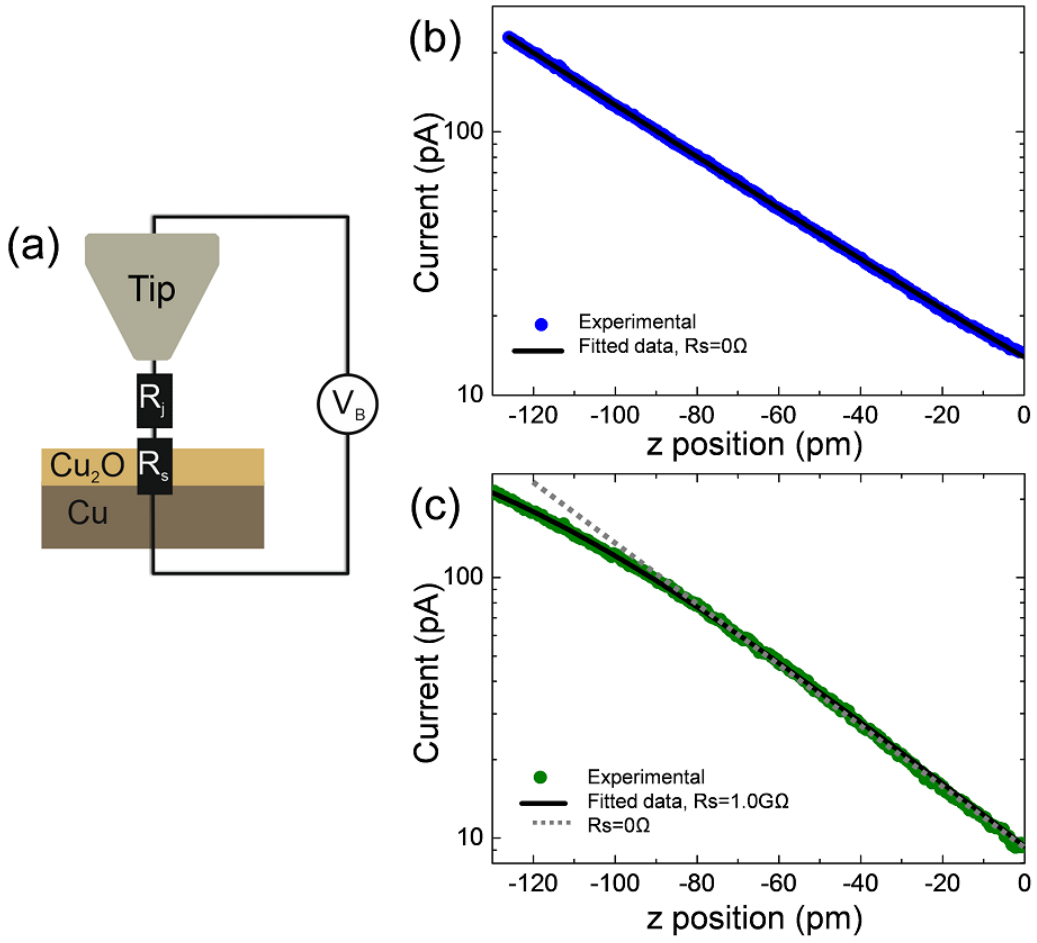

FIGURE 5.6: (a) Scheme of the proposed model with a resistance in series with the tunneling junction. (b) and (c) are the semilogarithmic plots of the tunneling current vs. z curve for Cu and Cu_2O, respectively, collected with tip B. In both panels the best fits appear as black lines. For comparison, in (c) the fit for $R_s = 0\ \Omega$ is also included (gray line). Parameters: (b) Bias = -1.25 V, A = 200 pm (c) Bias = -0.89 V, A = 200 pm.

thickness of $\sim$ 2 Å. The tunneling current is injected in a very small area and assuming that this area has a radius of a copper atom (r = 1.28 Å), the relation between the sample and the specific resistances can be expressed as:

$$R_s = \frac{\rho_{Cu_2O}\ l}{s} = \frac{\rho_{Cu_2O}\ l}{2\pi r^2}, \tag{5.6}$$

where r is the radius and l is the thickness. The deduced specific resistance for the copper oxide single layer is $\sim$ 70 Ω cm. This value is dramatically lower than the values reported for thicker Cu_2O films (between 10^4 - 10^6 Ω cm) [175] but

comparable to the lowest resistance reported for stoichiometric Cu_2O bulk. Divergences however, might also arise from specific electronic properties of the copper oxide/copper interface at atomic level [38]. The conductivity of an extremely thin (one atom thick) oxide will in addition depend on the local valence state of copper [178, 233]. The existence of R_s, that is caused from electron transport through the oxide interface before tunneling to the metal, has the implicit assumption that the interface has surface states near the Fermi Level [178]. The value of the series resistance R_s is then expected to be influenced by the local density of states, and therefore by the bias voltage used.

Although the proposed model has been reported and confirmed to play a role in both FM-AFM and KPFM spectroscopy, here it is used for the first time to demonstrate the important implications of $I(z)$ behavior on metal/semiconductor interfaces. This simple model was used to fit the other data sets (tip A and C) but the model fails and no good fittings were obtained. In the following, an alternative explanation is provided.

5.5.2 Tip-Sample Deformation

In normal STM operating conditions, the tip sample junction experiences a chemical interaction in the order of few nN but due to the small contact area this small force can yield a large strain that can produce deformation in the last nearest junction atoms. In this subsection, the behavior of the $I(z)$ experimentally observed for the two tips, so called B and C, will be analyzed on the basis of mechanical deformation of the junction.

Figure 5.7(a) shows a schematic representation of the tip apex and the sample in the ideal case of a rigid tip and surface (z) and with a mechanical deformation of the tip and the surface (ζ). In this representation, the deformation has a positive value, i.e. the repulsion between the tip and the sample produces enlarged separation between the last atoms, increasing the tip-sample distance in $z + \zeta$. In such case, because the change in the true gap width is smaller than the displacement of the piezo (z position), the tunneling current increases less than expected. The reverse argument can be applied when the deformation occurs under the regime of attractive interaction between the atoms at the tip and the sample, that is, a larger tunneling current occurs than expected because of the tunneling gap shortening. The deformation can occur at the tip apex or/and at the surface, being the total

deformation the sum of the relaxation on both. Experimental observations of such relaxations have been reported in STM on metal surfaces [21, 27, 35, 99, 152, 202], graphene on Ir(111) [5], the second layer of tin phthalocyanine molecules (SnPc) on Ag(111) [29, 90] and on C_{60} on Cu(111) [91].

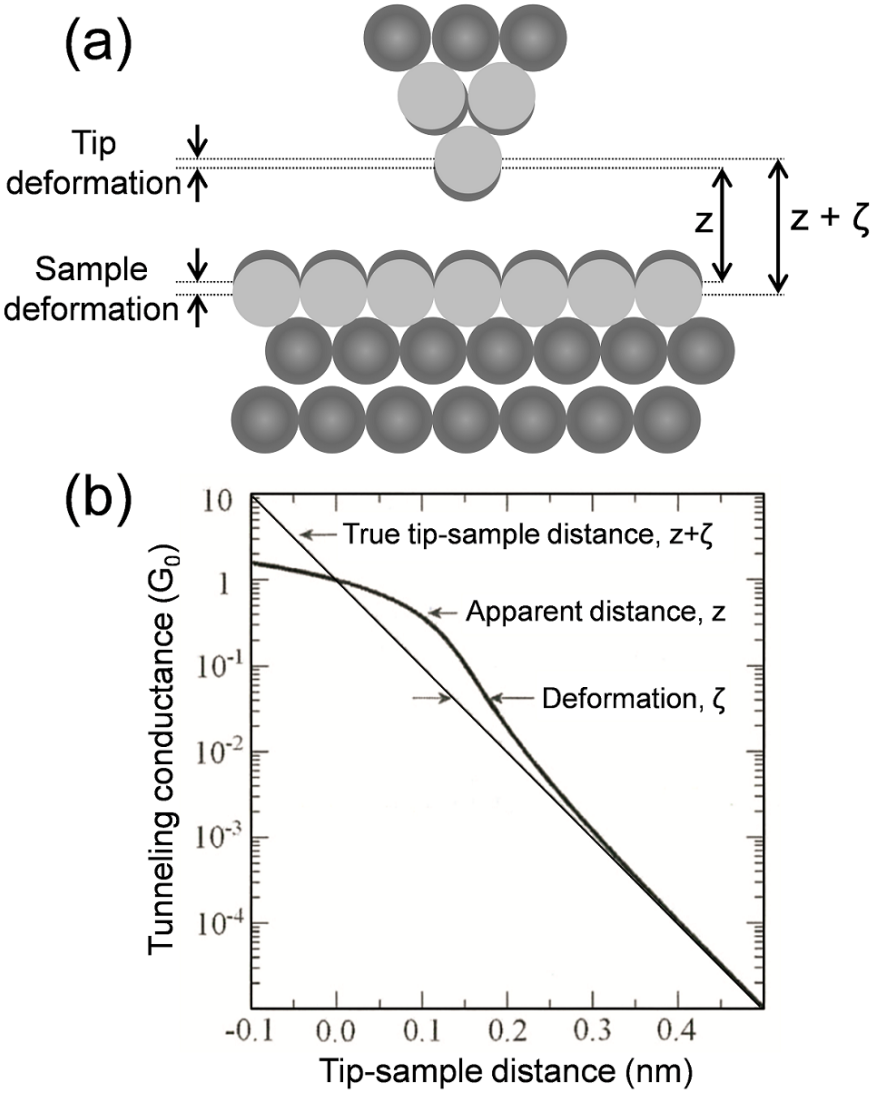

FIGURE 5.7: (a) Schematic representation of the tip and the sample with and without deformation. A positive deformation is represented; what means that the real tip-sample distance is larger than the measured by the piezo. (b) Effect of the relaxations on the apparent conductance (in G_0 units) versus tip-sample distance. The conductance has an exponential dependence with the true tip-sample distance. Parameters used: κ=1.1Å^{-1}, maximum relaxation = 60 pm. Figure extracted from [27].

Such relaxation effects can be estimated from the deviation of the tunneling current respect to the linear regime of the logarithmic plot of the tunneling current vs.

the z piezo displacement, as illustrated in Figure 5.7(b). The response of the deformation under the attractive and repulsive force regimes has been observed on a metallic surface, in agreement with experimental and numerical observations [134].

In Figure 5.8 the linear behavior, expected for hard tip and surface junction, has been plotted with a green dotted line together with the experimental data obtained with tip B (continuous blue line). The deformation (ζ), gray lines, has been calculated as the difference between the z-piezo for the measured tunneling current and the corresponding z-position for the same tunneling current in the ideal case of no deformation. It has been calculated for the approach (forward) and the retraction (backward) of the tip to the surface. As observed, the deformation is positive overall the z-range, implying that the atoms from tip and surface are feeling a repulsive interaction that tend to increase their separation. The maximum value of the measured deformation is 11 pm. The simultaneous frequency shift vs. piezo displacement was already plotted in Figure 5.4 showing an attractive average tip-sample interaction during whole z-range. This is not contradictory, as frequency shift is caused by the summed of all the forces, attractive and repulsive, it is possible to have net negative frequency shift and still be in the repulsive force short-range regime.

The experimental data set obtained over copper oxide with tip C was not correctly fitted with the resistance in series model (fit not shown here) and is now evaluated with the tip-sample deformation assumption. In Figure 5.9(a), the logarithm of the forward and backward tunneling current and the ideal tunneling current vs. z piezo are presented. The deformation vs. z piezo was calculated for the forward (gray plot) and backward (dark gray plot). The inset shows the STM image of the copper oxide terrace where the spectrum was performed. With this tip, adsorbed oxygen atoms on copper appear as protrusions and not as holes as obtained with tip B, see for example inset in Figure 5.3. Here the deformation is negative in the forward curve, in the range of -100 pm to -150 pm, and becomes positive for a further approach of the tip to the surface. This behavior can be explained as an attractive tip-sample interaction when the separation is large (electrostatic and van der Waals attractive interaction) and a repulsive attraction at close distances (chemical interaction). The maximum deformation value is 60 pm. This value is approximately six times bigger than the value obtained in the previous data set (tip B) indicating important structural differences between both tips.

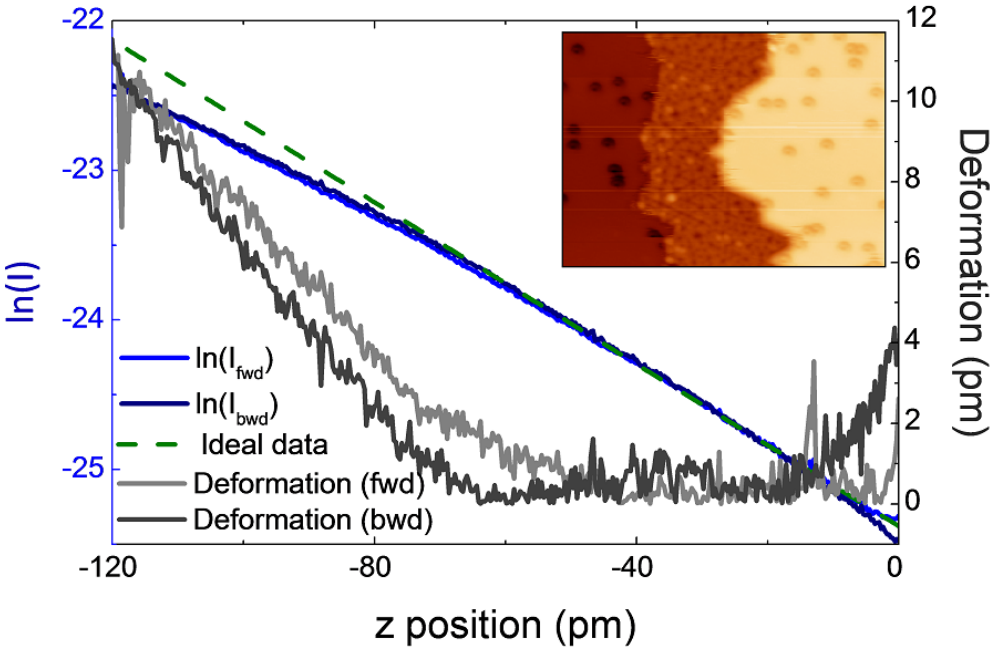

FIGURE 5.8: Logarithmic plot of the forward (light blue plot) and backward (blue plot) tunneling current vs. piezo displacement over copper oxide obtained with tip B. The tunneling current was fitted in the range where no deviation from its exponential behavior was yet observed, from 0 pm to 100 pm, and it was extrapolated over all the z-range (green plot). This is assumed to be the ideal tunneling current vs. piezo displacement when no deformation exists. The calculated deformation was plotted for the forward (light gray plot) and backward (dark gray plot) tip-displacement. The inset is the STM image where spectroscopy was performed (20 nm x 14.5 nm, I = 120 pA, Bias = -0.89 V, A = 200 pm).

As mentioned before, it is not possible to convert frequency shift, from short z-range spectroscopy, into forces. To get information about the force range that corresponds to the deformation regime, a long z-range spectrum is presented in Figure 5.9(b), where force (blue plot) and conductance (gray plot) are plotted. The corresponding conductance of the short-range $I(z)$ presented in (a) is overlaid (green plot). Since the real tip-sample distance is unknown and both spectra (short and long-range) were collected from different setpoint positions, the z position of the short-range was freely adjusted to make overlap both spectra. Note that the conductance, and not the tunneling current, is plotted here because the two spectra were collected at different bias voltage, the short-range at -0.44 V and the long-range at -0.05 V. The z-range of the tip-sample deformation corresponds to a force range of -2 to -3 nN. The interaction force measured with tip C is considerably higher that the obtained for tip A (see Figure 5.2(b)) indicating a

larger long-range component for the tip C probably due to a larger macroscopic tip radius.

From the maximum chemical force of a covalent bond, ∼3 nN, and the maximum deformation measured in this study, ∼60 pm, the stiffness of the tunneling junction, k_j can be estimated through the Hooke's law:

$$k_j = \frac{F}{\zeta}. \tag{5.7}$$

A k_j of ∼ 50 N/m is obtained. The stiffness of the tunneling junction is related to the stiffness of the tip, k_t, and that of the sample, k_s, as:

$$\frac{1}{k_j} = \frac{1}{k_t} + \frac{1}{k_s}. \tag{5.8}$$

Assuming a pyramidal tungsten tip with a k_t of 157 N/m [27], a surface stiffness of 73 N/m is obtained from the last equation. This value is plausible since is in the same range than the obtained for other systems. To give some examples, for the close-packed copper surface a surface stiffness of 104 N/m is given [27] and for a C_{60} molecule a surface stiffness of 112-129 N/m [91].

Since the deviation from the exponential dependence is here interpreted as a tip-sample deformation, the correct decay constant for the copper oxide is assumed to be that obtained when the deformation is zero. For tip B, the measured decay length is 1.37 ± 0.02 $Å^{-1}$ over copper oxide and 1.105 ± 0.007 $Å^{-1}$ over Cu(111). The calculated apparent work functions are 7.1 eV and 4.6 eV, respectively. For tip C the measured decay constant is 1.4 ± 0.1 $Å^{-1}$ over copper oxide and 1.09 ± 0.02 $Å^{-1}$ over Cu(111). The calculated apparent work functions are 7.5 eV and 4.5 eV, respectively. The work function difference between both surface regions are much higher than the obtained with the resistance is series model.

Additionally, it can be observed a hysteresis in the tip-sample deformation of Figures 5.8 and 5.9, with a maximum value of ∼ 5 pm. This hysteresis can be related with a non-conservative process as a plastic deformation. The fraction of energy that is dissipated can be estimated from:

$$E = \frac{1}{2} k_j \Delta\zeta^2, \tag{5.9}$$

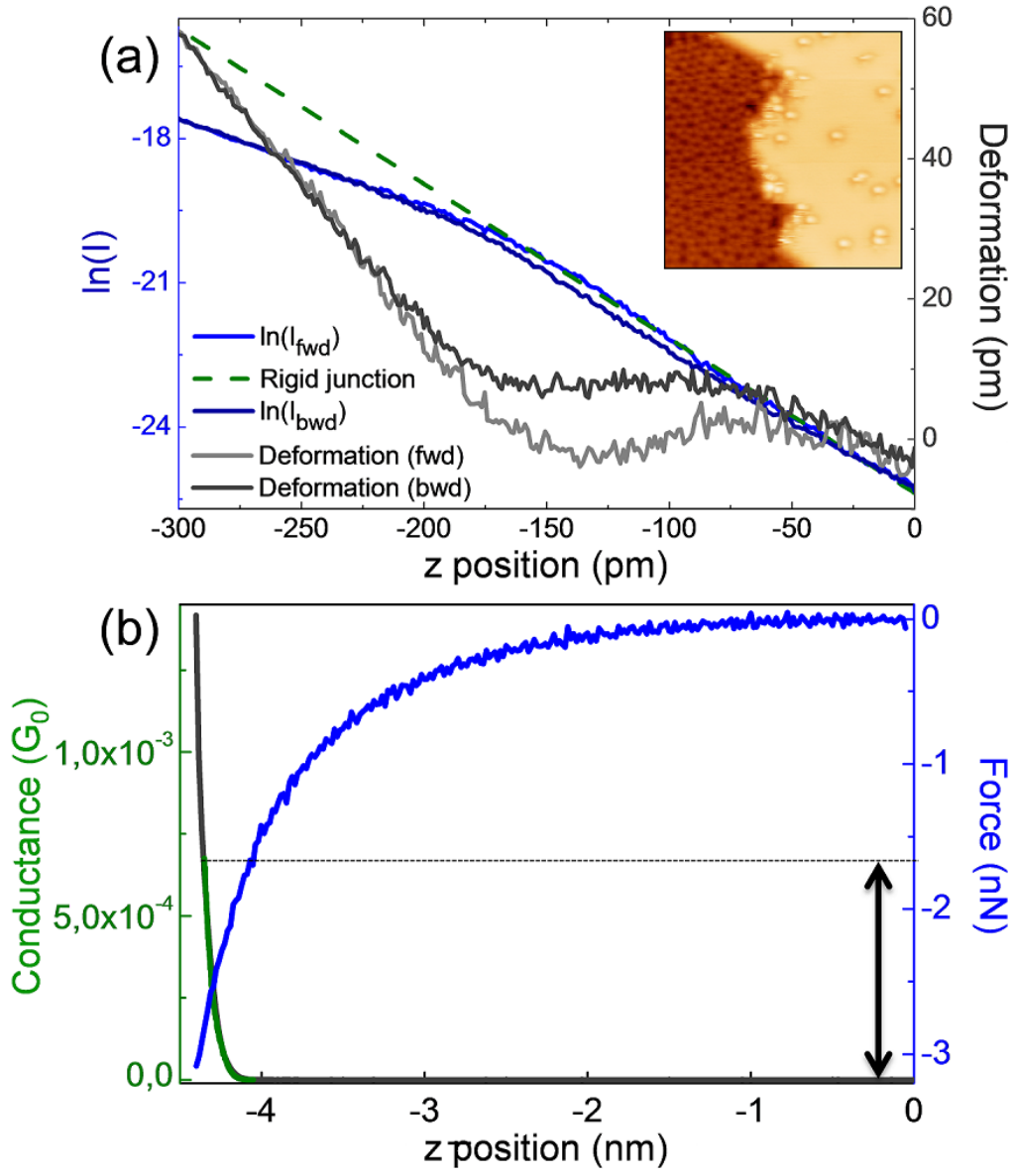

FIGURE 5.9: (a) Logarithm of the forward (light blue plot) and backward (blue plot) tunneling current vs. piezo displacement over copper oxide obtained with tip C. The tunneling current was fitted in the range where no deviation from its exponential behavior was yet observed, from 0 pm to 100 pm, and it was extrapolated over all the z-range (green plot). The deformation was calculated as explained in the text and plotted for the forward (light gray plot) and backward (dark gray plot) tip-displacement. In the inset is an STM image that shows the area where the spectroscopy was performed over the copper oxide. Parameters: Bias = -0.44 V, A = 200 pm. STM image: I = 265 pA, Bias = -0.44 V, A = 200 pm, 10 nm x 10 nm. (b) Conductance (dark gray plot) and force (blue plot) vs. piezo displacement over copper oxide collected with the same terminated tip. The conductance of the shorter spectroscopy (green plot) shown in (a) is overlaid in (b) and the corresponding force range is marked. Parameters: Bias = -0.05 V, A = 200 pm.

where k_j is 50 N/m and $\Delta\zeta$ is 5 pm, giving an energy value of 4 meV. This value is too small to be detected in the excitation signal (see gray plot in Figure 5.4). The dissipated energy per oscillation cycle is calculated as $\Delta E_{CL} = 2\ \pi E/Q$, where E is the energy of the sensor (E=$kA^2/2$) and Q is the quality factor. For a Kolibri sensor, the spring constant is $\sim$ 540 kN/m, the typical amplitude is 200 pm and the quality factor is $\sim$ 25000, then the energy loss per cycle is $\sim$ 2 eV. An extra dissipative mechanism of 4 meV is only around the 0.02 % of the dissipation of the tip and is not detectable.

It cannot be concluded whether the relaxation occurs, in the sample and/or the tip. The deformation observed here is not necessarily due to vertical compressions of the atom layers, it can be caused by lateral deformation as have been pointed out by Hapala et al. [87]. The effect of tip-sample deformations has been also observed in force-distance spectroscopy [63, 118, 189]. Additionally, these relaxations have been demonstrated to play a major role in the STM imaging corrugation since the relaxations are not the same when the tip is positioned in top or hollow positions [21, 27, 99].

5.5.3 Discussion

Two models have been presented in an attempt to understand the anomalous deviation from the exponential dependence of tunneling current versus z performed over copper oxide. The first one is a simple resistance in series model where a sample resistance, R_s, is added to the tunneling junction resistance, R_j. This model is able to explain the non-exponential dependence of the tunneling current upon distance, getting a plausible kappa value. However, this model cannot describe all the spectra collected over copper oxide indicating that could fail for more complicated tips. This is a very simple and attractive model in the sense that relates the observed behavior with an electric property of the interface that is not otherwise accessible. A systematic study as a function of the bias could help to probe its general validity.

The second model relates the deviation from the exponential dependence of the tunneling current with the distance to a deformation of the tip-sample distance. It is generally applicable and it has recently been discussed in the literature [5, 29, 91, 189]. It would explain the variability between experiments due to variation in the tip shape and structure. It is plausible that it gains importance at room

temperature compared to low temperature studies. This model assumes that the kappa obtained for larger tip-sample distances is without deformation and then the kappa from this range is the correct one.

The deformation of hard surfaces has been described as a compression at long tip-sample distances and an elongation at short distances (see Figure 5.7(b)). It is not possible to discard that in the onset of the tunneling current, that is where we have assumed no deformation, a deformation exists due to attractive forces. This deformation would explain the high kappa value obtained for long tip-sample distances.

For both models, the work function difference between copper and copper oxide surface regions is much higher than the measured by contact potential difference. However, differences in the measured work function by $I(z)$ and $\Delta f(V_{Bias})$ have been previously reported (see supplementary materials of [144]). More systematic studies are needed to elucidate the influence of the tip structure, termination, size, etc. We emphasize the importance of measuring interaction and tunneling current simultaneously to understand the mechanical atomic-scale properties of the junction.

5.6 Atomic "Flip-Flop" in Tunneling Current Spectroscopies

Interestingly, some reversible jumps in the tunneling current in $I(z)$ spectra were observed in both, copper and copper oxide, surface areas. At some z-point the tunneling current underwent a jump to higher values and after some picometers the jump was reversed. It means that before and after the jump, the tip-sample distance is smaller or that a sudden change of the conductance happened, for instance, by the adsorption of a different atomic species at the tip. It was observed only with tip B and over both surfaces a jump was recorded in the 33% of the total number of spectra. It always occurred in the backward and after the setpoint position (in the z range -100 pm to 0 pm) and in one spectrum it happened twice.

An example of this jump in both surface areas will be presented in the following. In Figure 5.10 a jump was recorded in a $I(z)$ spectra over copper surface. The tunneling current (blue plot), frequency shift (green plot) and excitation (gray

plot) are presented in Figure 5.10(a). The jump occurred in the backward and it was reversed approximately 25 pm after. The tunneling current before and after the jump is exactly the same as the forward, pointing out the reversibility of the process. The decay constant during the jump is the same, indicating that an important change in the tip ended material and crystallographic orientation do not occur. Therefore, the jump is interpreted here as a change in the tip-sample distance as explained in the last section. The variation in the tip-sample distance, Δz, is represented in Figure 5.10(b). Note that Δz is the sum of the z-piezo and the deviation. No deformation is observed over all the z-range and the tunneling current jump corresponds to a jump in the tip-sample distance of 24 pm. The same Δz was obtained for the 6 spectra where a jump was recorded. In the simultaneous frequency shift and excitation channels is not possible to observe an evident variation when the jump occurs.

In Figure 5.11 an example of this jump over copper oxide is presented. The tunneling current (blue plot), frequency shift (green plot) and excitation (gray plot) are presented in Figure 5.11(a) and the calculated tip-sample deformation in Figure 5.11(b). The deformation over this surface is a combination of the tip-sample deformation that starts at $\sim$-80 pm and two reversible jumps in the backward. The jumps over copper oxide also correspond to a jump in the tip-sample distance of 24 pm. The same value is obtained in the five analyzed jumps (the jumps occurred in four $I(z)$ spectra but in the one presented here it happened twice). The jumps presented here occurred in the z region with 0 deformation, but it is also observed in the z region with tip-sample deformation. Contrary to the observed over copper, here it is possible to observe a jump also in the simultaneous frequency shift. A possible explanation is that the frequency shift dependence with the distance is higher over copper oxide than over copper.

Since over both surfaces the jump corresponds to the same Δz and only occurred with tip B it can be related with an atomic instability occurred in the tip apex. A jump in the tip apex between top and hollow position is one of the possibilities to explain an enlargement of 24 pm of the tip apex. Attractive tip-sample forces have to be responsible of this tip instability.

It is interesting to remark that over copper oxide two types of tip-sample distance deformation occur. The reported in the last section produces an increase of the tip-sample distance and is then related to repulsive forces and the jumps that produce a reduction of the tip-sample distance and are then related to attractive forces.

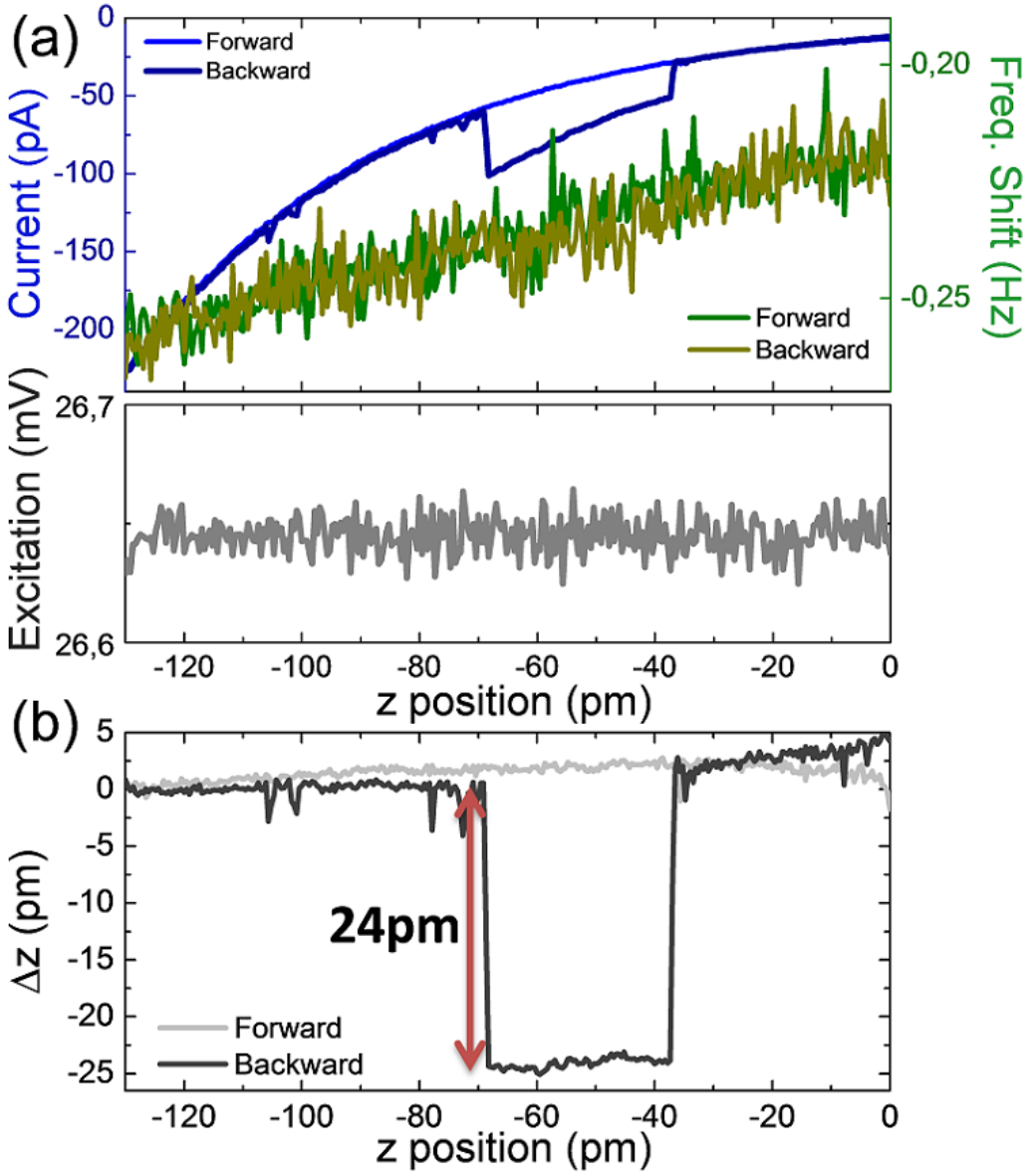

FIGURE 5.10: Short z-range spectra collected over Cu(111) with tip B. (a) Tunneling current, frequency shift and excitation vs. piezo displacement and (b) deformation vs. piezo displacement calculated from the tunneling current. The tip was retracted 100 pm from the setpoint position and driven toward and backward the sample 130 pm, (setpoint position is z = -100 pm). Parameters: Bias = -1.30V, A = 200 pm.

Both deformations occur at a net negative frequency shift (attractive forces) and reflect the averaging tip-sample forces due to the oscillation of the tip. Then, even when the frequency shift is negative important repulsive forces can play a significant role in the tip-sample junction.

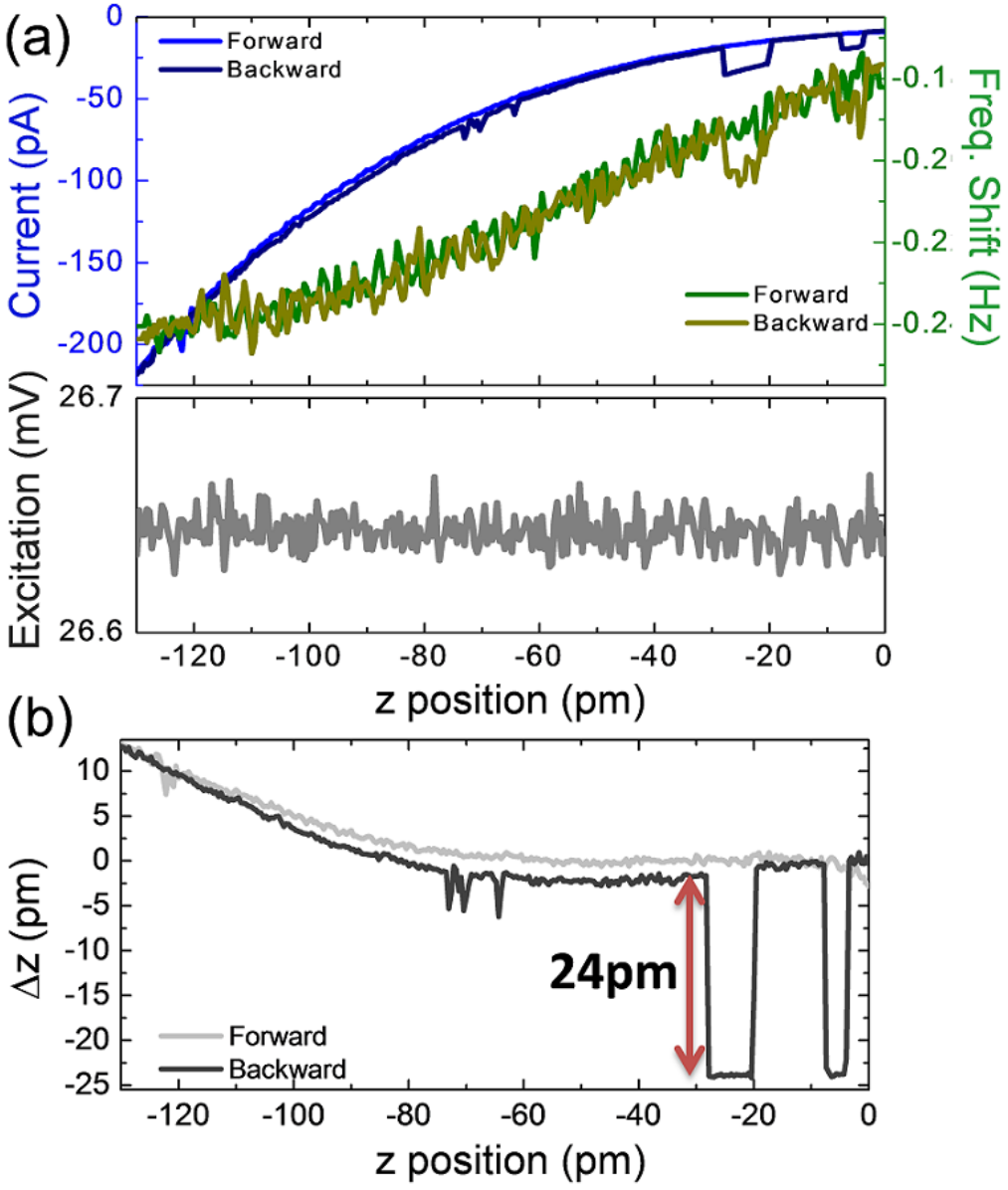

FIGURE 5.11: Short z-range spectra collected over Cu_2O with tip B. (a) Tunneling current, frequency shift and excitation vs. piezo displacement and (b) deformation vs. piezo displacement calculated from the tunneling current. The tip was retracted 100 pm from the setpoint position and driven toward and backward the sample 130 pm, (setpoint position is z = -100 pm). Parameters: Bias = -0.89 V, A = 200 pm.

It is not expected that a bond breaking process is involved in the observed "flip-flop". An atom is not transferred to or from the surface, only a change in its

position is expected. The dissipation channel in both spectra, Figures 5.10(a) and 5.11(a), is flat in all the z-range even when the jump occurs. For a maximum chemical force of $\sim$ 3 nN and a stiffness of the tunneling junction (k_j) of 50 N/m, the dissipated energy in a bond breaking can be calculated as $\Delta E = F^2_{max}/2k_j$ $\sim$ 60 meV. As mentioned before, the intrinsic energy loss of the oscillating tip is $\sim$ 2 eV and an extra energy dissipation of 60 meV (3%) could be observed but it is not, what agrees with the prediction of no bond breaking.

Non reversible jumps in the tunneling current have been previously observed on molecules/metal systems when $I(z)$ were performed [90]. The reported jump corresponded to a tip sample distance of 1.4 Å and was related with a molecule that slips laterally to another adsorption position. In the study presented here, the observed jumps are reversible and reproducible over both surface regions suggesting the existence of two stable geometric tip states. These two configurations differ in its z direction in 24 pm and the transition between them is an abrupt jump. Here, we have interpreted the change in the tunneling current as a change in the tip-sample distance. However, other processes cannot be excluded as, for example, an increase in the tip area involved in the tunneling process.

5.7 Conclusions

A partial monolayer of copper oxide growth on the Cu(111) surface has been studied by contact potential measurements and z-spectroscopies. Since both surface regions, copper and copper oxide, coexist in the same area both areas have been tested with the same tip apex allowing to disregard tip changes.

Contact potential measurements show a work function maximum difference of $\sim$ +150 meV over copper oxide in respect of copper. Another sets of measurements do not show a difference between both areas.

Distance spectroscopies have been performed over both surface regions with different tips, called as A, B and C. An anomalous non exponential behavior of the tunneling current upon the distance was observed when $I(z)$ was performed over copper oxide. To explain this behavior two models have been suggested: a resistance in series model and a tip-sample deformation. In the resistance in series model, a sample resistance is added to the tunneling junction and the tunneling current versus distance spectra were correctly fitted for one of the three tested

tips. A sample resistance of $\sim$ 1.4 GΩ was extracted when measuring over copper oxide regions and a reasonable kappa value was obtained. In the tip-sample deformation model a positive deviation from the z-piezo distance was calculated, i.e. the tip-sample distance is higher than the z-position. This deformation is expected to be caused by repulsive forces and a maximum deformation of 60 pm was calculated. Both models are able to explain the non-exponential behavior of the tunneling current with the tip-sample distance.

Additionally, a tip-sample instability has been observed on the set recorded with tip B. The instability corresponded to an abrupt, reversible and reproducible tip-sample change of 24 pm and was observed over both surface regions. The jump is attributed to the presence of two stable tips that differs in a z-distance of 24 pm. The instability has been interpreted here as a change in the tip-sample distance. However, other processes cannot be excluded as an increase in the tip area involved in the tunneling process.

Chapter 6

Study of PTCDA on Si(111)-7x7 and AgSi(111) Surfaces

6.1 Introduction

The interaction between molecules and inorganic surfaces plays an important role in the final electronic and structural properties of the interface. In this chapter, the study of the adsorption of perylene-3,4,9,10-tetracarboxylic anhydride (PTCDA) is presented on two different surfaces with different molecule-substrate interaction. PTCDA is one of the most studied π-conjugated organic molecules and it has become a model system for various benchmark studies [116, 124, 130]. This molecule shows interesting optical and electronic properties which are strongly related to the degree of crystalline ordering of the film. For these reasons, the understanding of PTCDA systems at atomic level is an important issue for the future development of organic semiconductor devices.

The first surface of study is the Si(111)–7×7 surface, a representative case where PTCDA molecules highly interact with the substrate and the adsorption of single molecules can be found at room temperature. The second surface is the Ag/Si(111)-$\sqrt{3} \times \sqrt{3}$ that enables the ordering of the molecules in molecular layers due to the weaker molecule-substrate interaction. The influence of the surface on the structural and electronic properties of the PTCDA has been studied by STM, FM-AFM and kappa imaging in UHV conditions. Kappa (or decay constant) imaging is a dynamic method that enables the local measurement of the

effective tunneling barrier and can be achieved to complement the information obtained from STM and FM-AFM. First the molecule and the substrates will be introduced. A description of the technical part of the acquisitions of kappa measurement are given before presenting the results of the two systems of study, PTCDA on Si(111)–7×7 and PTCDA on Ag/Si(111)-$\sqrt{3} \times \sqrt{3}$ surface.

6.2 The PTCDA Molecule

General Properties of PTCDA

Perylene-3,4,9,10-tetracarboxylic dianhydride ($C_{24}O_6H_8$) is a π-conjugated organic molecule, called PTCDA, which has been extensively studied on metallic surfaces [116, 124, 130]. This molecule consists of a perylene core (five carbon rings) with two anhydride groups (O=C-O-C=O) at either end as shown in Figure 6.1. The sp^2 hybridization of the carbon atoms results in π-conjugate and delocalized orbitals which expand mainly over the perylene core of the molecule. Anhydride groups have oxygen atoms in two local environments (carboxylic and anhydride) and give rise to a quadrupole moment with the positive partial charge localized around the aromatic core and the negative partial charge localized around the anhydride groups. This electrostatic moment has a strong influence on the formation of PTCDA films and crystals.

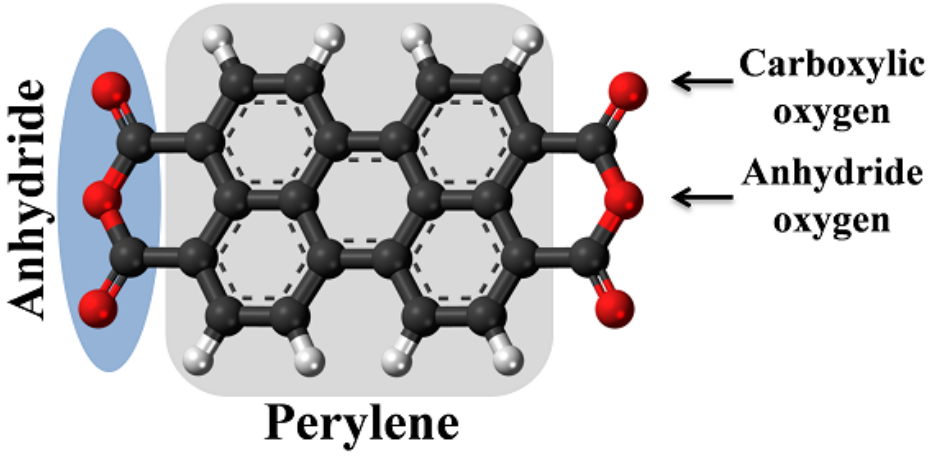

FIGURE 6.1: Schematic drawing of the PTCDA molecule where the central perylene core and the anhydride end group are indicated as well as the two environments of the oxygen atoms. Atoms in black are carbon, in white hydrogen and in red oxygen. The molecular size is 14.2 Å× 9.2 Å.

This molecule has three C_2 symmetry axis which can transform the molecule into itself upon rotation of 180°, three planes with reflection symmetry $\sigma(xy), \sigma(xz), \sigma(yz)$ and an inversion (I) center. As a result, the symmetry of all molecular orbitals can be described by the D_{2h} point group.

O. Paz and J. M. Soler calculated the electronic structure of a free standing PTCDA molecule using the SIESTA method in the local density approximation (LDA) [145]. Figure 6.2 shows the energy level diagram of the PTCDA molecular orbitals relative to the Fermi level. The molecular orbitals are labeled according to their symmetry. It can be observed that the highest occupied molecular orbital (HOMO) is well separated from the lowest unoccupied molecular orbital (LUMO). The obtained gap represented by the HOMO-LUMO energy difference is of about 1.5 eV. This value is smaller than the experimentally reported but is well known that DFT underestimates the gap. The calculated electronic structure of the free PTCDA molecule will be used as a reference in the results presented in this chapter, since a direct comparison of the original molecular orbitals to those resolved in STM images will help in the understanding of the adsorption process and the interaction strength at different molecule-substrate interfaces. The degree of molecule-substrate interaction at different interfaces can be inferred from the modification of the spatial distribution of the molecular orbitals and their relative energy positions.

Crystalline Structure of Bulk PTCDA

In bulk, PTCDA molecules are found in a monoclinic lattice structure in the $P2_{1/c}$ space group with two molecules per unit cell. Two polymorphic phases, α and β, of very similar lattice constants but with different inclination of the stacking axis were observed by x-ray diffraction [62]. The molecular layers are approximately parallel to the (102) planes. Within the layers the molecules are arranged in a herringbone like structure of coplanar molecules with a rectangular unit cell. The parameters of the two-dimensional unit cell of the herringbone for the α phase and the β phase [62, 143] are presented in Table 6.1.

PTCDA on Surfaces

As a very general rule, molecules which form layered van der Waals bonded crystals in their bulk states allow quasi-epitaxy on inorganic substrates [62]. Ordered

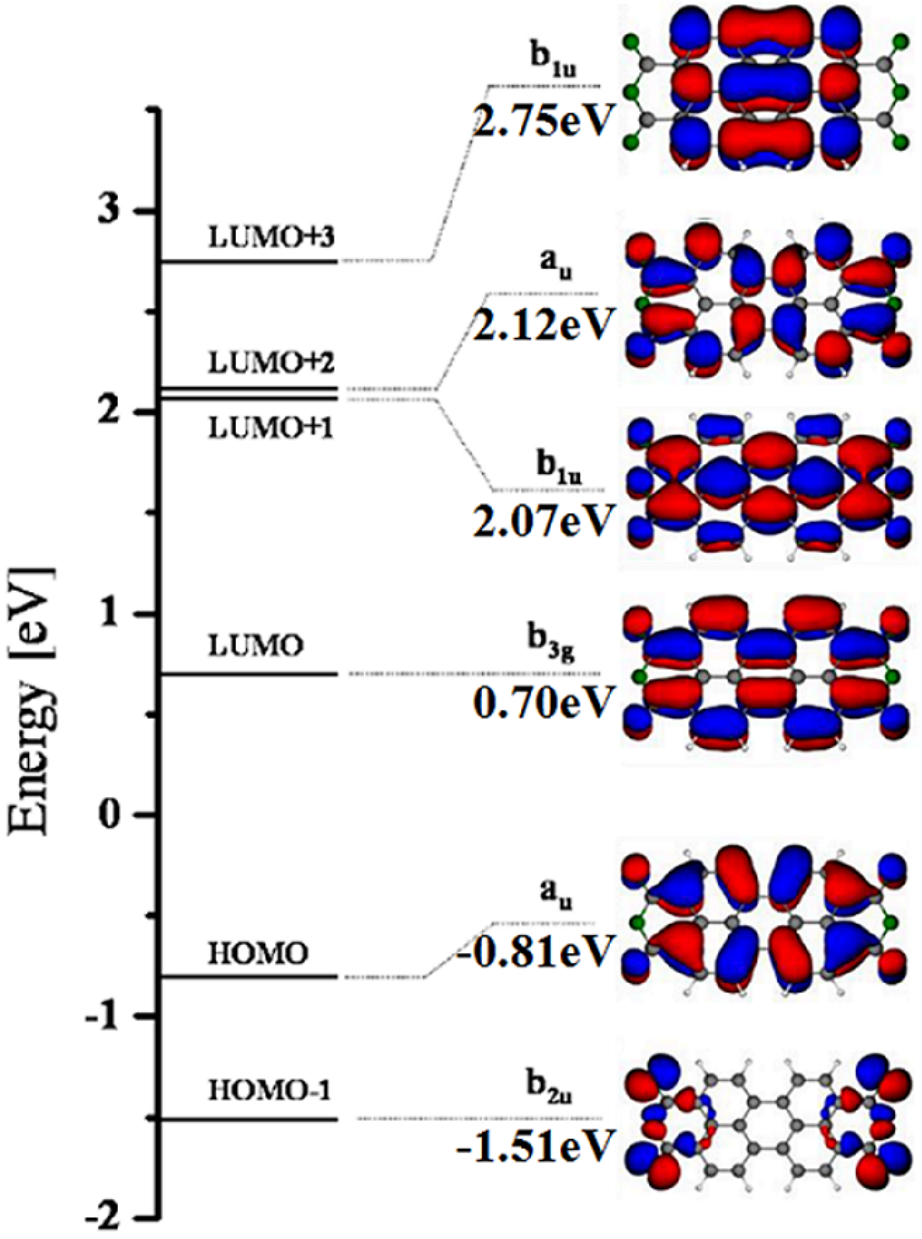

FIGURE 6.2: Energy level diagram of PTCDA molecular orbitals with respect to the Fermi level calculated for the free standing PTCDA molecule using DFT-LDA. The molecular orbitals are labeled according to their symmetry operation corresponding to the D_{2h} point group. The molecular orbitals are represented slightly rolled, relative to their longitudinal axis for a better visualization of the sign of the molecular orbital wave function, represented by red/blue colors. Figure adapted from [145].

monolayers of PTCDA are formed on surfaces where the local interaction with the substrate is not very strong allowing sufficient lateral mobility of the molecules as to adopt a long-range periodic arrangement. Systems where the molecule-substrate interaction is weak, like Au(100) [135] and HOPG [102], give quasi-epitaxial growth

	a (Å)	**b** (Å)
α-PTCDA	11.96	19.91
β-PTCDA	12.45	19.30

TABLE 6.1: Parameters of the two-dimensional unit cell of PTCDA (102)-plane for the bulk α and β polymorphic phases.

of flat lying molecules ordered in a structure similar to the (102)-planes of the bulk but lightly strained to match the structure of the surface. This is commonly referred as herringbone structure.

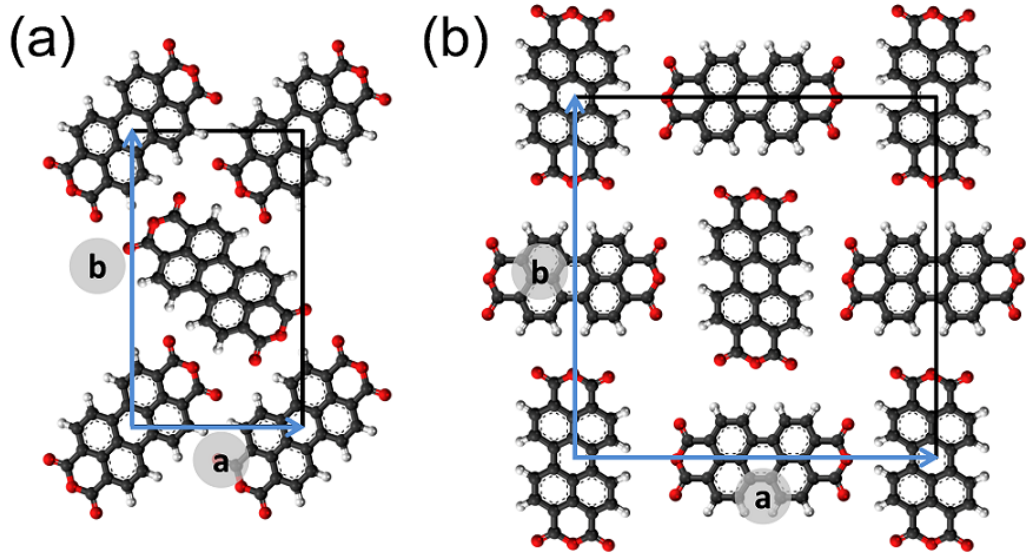

FIGURE 6.3: Schematic representation of the herringbone (a) and the square (b) phases of the PTCDA molecule. In both the unit cell vectors are indicated by blue arrows.

On surfaces with intermediate molecule-substrate interactions, such as Ag(111) [75], Ag(110) [75] and Au(111) [34, 135], PTCDA forms true epitaxial films with site recognition. In addition to the formation of the referred herringbone structure, a squared (or quasi-squared) structure has also been reported on Ag(110), Au(100) and AgSi(111). A schematic representation of both structures is shown in Figure 6.3. The unit cell of the herringbone phase contains two molecules and in the square phase there are four molecules per unit cell. In both phases, the long axis of adjacent molecules is rotated 90°. Both structures are stabilized due to hydrogen bonds and the orientation and molecule-molecule distance play an important role. An extensively studied system is the PTCDA on Ag(111) where molecules form a herringbone phase. The electronical properties of the PTCDA on Ag(111) and Ag/Si(111) are quite different. Scanning tunneling spectroscopy (STS) studies for

the PTCDA on Ag(111) show that the HOMO appears at -1.6 eV, while a peak at -0.3 eV derives from the former LUMO of the molecule [127, 162, 241]. For the PTCDA on Ag/Si(111) it was measured by photoemission spectroscopy that the HOMO is at +2.66 eV and HOMO-1 at +4.34 eV [82]. It means that the net charge transfer from the substrate to the molecules is quite different for the two situations.

Rohlfing et al. studied theoretically the PTCDA/Ag(111) system and calculated a series of STM images by the Tersoff-Hamann framework at different tunneling currents (different tip-sample distances) for s- and d-like tips [162]. These images are presented in Figure 6.4. At small distances, the maximum tunneling current comes from six lobes along the long axis of each molecule accompanied by four lobes near the hydrogen atoms. These features can be distinguished in the LUMO representation of the Figure 6.2. At larger distances the features along the central axis of the molecule die off rapidly, while the features near the hydrogen atoms merge into two elongated peanut-shaped lobes at each side of the molecule, which finally dominates the topography. The resolution of the LUMO, that is observable at short distances, is lost at larger tip-sample distances. The resolution of the STM image is also tip orbital dependent as can be observed if one compares the simulated images for an s- and d-like tips. The resolution, for the same distance, is better with a d-like tip.

6.3 Method for Kappa Imaging

Kappa data was obtained according to the method developed in the group of Prof. F. J. Giessibl and described in detail in the Master's Thesis of F. Huber (University of Regensburg, 2013) [107, 108]. In this section, the most important aspects of the methodology are summarized.

One signature of quantum tunneling through an insulating barrier is the exponential dependence of the current upon the insulator thickness [19, 61] and generally characterized by the decay constant, κ (see, e.g. [27]):

$$I = I_0 \exp\left(-2\kappa z\right), \tag{6.1}$$

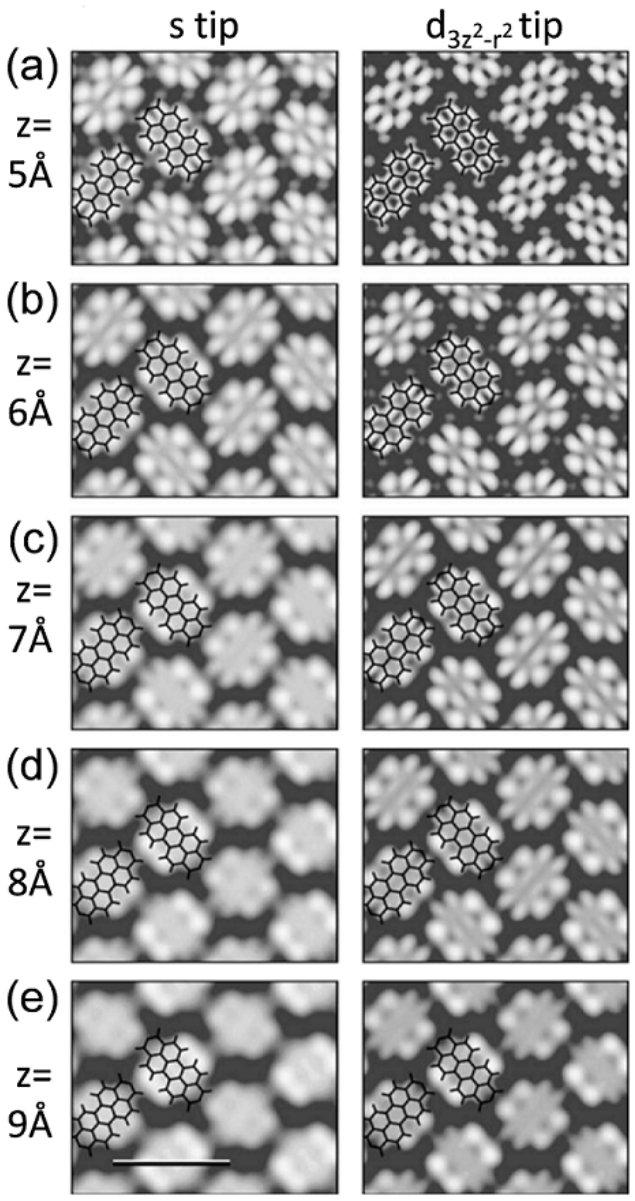

FIGURE 6.4: Calculated constant-current topographical image of a monolayer of PTCDA on the Ag(111) surface, using various tip orbitals and at various maximum tip heights ranging from 5 to 9 Å above the Ag atoms. The maximum tip height is defined as the distance between the center of the tip orbital and the nuclei of the Ag surface atoms, and refers to the maximum tip height achieved for a given current. The tunneling voltage has been set to -1 V in all images. Note that in the set up used in this chapter the bias is applied to the tip and then the bias polarity is opposite to the used in that study. Figure extracted from reference [162].

where I_0 is the tunneling current at the point of contact, defined at $z = 0\,\mathrm{m}$. The exponential dependence can be derived from a one-dimensional model of electron tunneling through a square barrier with an apparent height ϕ_{app}, which depends on the tip and sample averaged work function, $\bar{\phi} = (\phi_{tip} + \phi_{sample})/2$, as well as on the applied bias voltage, V_B. Within this one-dimensional square-barrier model, the decay constant is

$$\kappa = \frac{\sqrt{2\,m\,\phi_{app}}}{\hbar}, \tag{6.2}$$

with $\phi_{app} = \bar{\phi} - e\mathrm{V}_B/2$, e being the elementary charge, m being the electron mass and $\hbar$ being the reduced Planck's constant.

Scanning tunneling microscopy can locally probe the tunneling current as a function of the tip-sample distance, $I(z)$, having in principle access to the local work function of the surface under investigation, ϕ_{sample}. This spectroscopic method has been employed to map surfaces at low temperature and to study the effect of atomic and molecular adsorbates [44, 163], but it is time consuming and not easy to apply when working at room temperature due to tip changes.

Binnig et al. implemented the measurements of $I(z)$ in a dynamic mode by modulating the voltage applied to the z piezo at a frequency ($\sim kHz$) above the feedback response [18]. When the tip-sample distance oscillates vertically with a subnanometer amplitude (Δz), the tunneling current amplitude (ΔI) is measured using a lock-in amplifier. However, the extraction of the decay constant from $\sim \Delta I/\Delta z$ [30, 128, 201] neglects the fact that dI/dz is not constant over one oscillation cycle of the tip due to the exponential dependence of I with the distance. This method has been employed to obtain simultaneously topographic STM images and barrier height maps of atomic adsorbates [128, 136]. In 1988 Marchon et al. used this method to study the influence of chemisorbed sulfur atoms on Mo(001) surface at atmosphere pressure. A higher barrier height was measured over the sulfur atoms what agrees with the calculations [136]. In 1997 Kurokawa et al. used barrier height imaging to study the oxygen adsorbed on the Si(111)–7×7 reconstruction. A higher barrier height was measured over the reacted sites as predicted for a higher electrical dipole due to a charge transfer from the silicon to the oxygen atoms [128].

As previously suggested by Herz et al. [97], we have been combined a dynamic method to extract the decay constant of the tunneling current using the tip oscillation in FM-AFM and have, therefore, simultaneous information of the tip-sample forces.

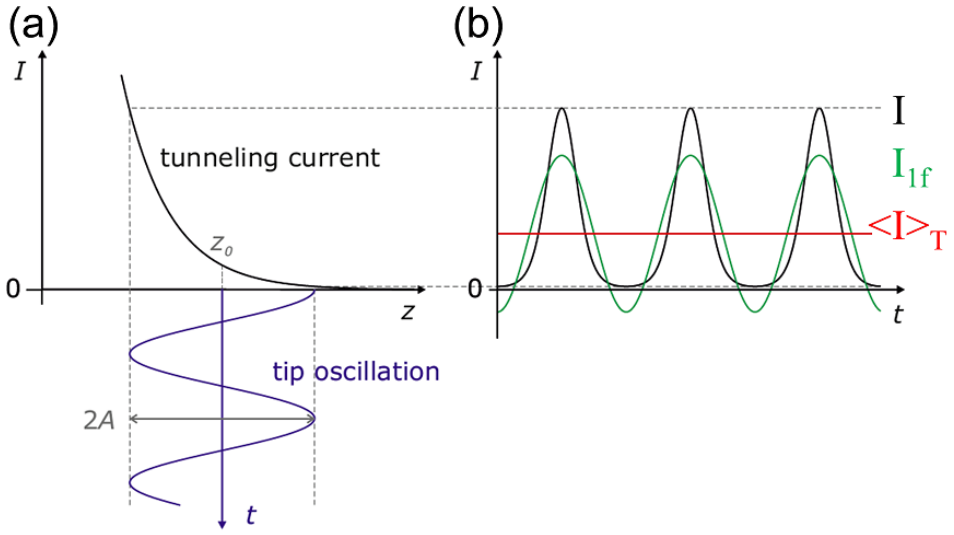

FIGURE 6.5: Simulated plots of the tunneling current of an oscillating tip with an amplitude A (a) vs. distance and (b) vs. time. The tip oscillates over the z_0 point. (b) The plots correspond to the tunneling current (black line), the Fourier series of I up to the zeroth (red line) and first order (green line). Figure extracted from [107].

During one oscillation cycle of the tip (in the harmonic oscillator approximation), the tip-surface distance (z) varies accordingly to $z = z_0 + A\cos(2\pi ft)$ and the tunneling current is therefore not constant but can be described by:

$$I = I_0 \exp[-2\kappa\,(z_0 + Acos(\omega t))], \tag{6.3}$$

where ω is the oscillation frequency of the tip, I_0 is the tunneling current at the point of contact and A is the amplitude. Expanding the Equation 6.3 with a Fourier series gives:

$$I = I_{DC} + \sum_{n=1}^{\infty}(I_{n\omega}cos(n\omega t)). \tag{6.4}$$

The first coefficient (I_{DC}) is time independent and gives the time-averaged tunneling current $\langle I\rangle_T$:

$$I_{DC} = \frac{1}{T}\int_0^T I_0 exp\left(-2\kappa z_0\right) exp\left(-2\kappa A cos(\omega t)\right) dt = I_0 \exp\left(-2\kappa z_0\right) \mathcal{I}_0\left(2\kappa A\right) = \langle I\rangle_T, \tag{6.5}$$

where $\mathcal{I}_n$ is the modified Bessel function of the first kind. Only the components of the Fourier series up to n=1 will be considered:

$$I_{1\omega} = -2I_0 \exp\left(-2\kappa z_0\right) \mathcal{I}_1\left(2\kappa A\right) = -2\frac{\langle I\rangle_T}{\mathcal{I}_0\left(2\kappa A\right)} \mathcal{I}_1\left(2\kappa A\right). \tag{6.6}$$

Then the tunneling current, Equation 6.4, can be rewritten as:

$$I = \langle I\rangle_T - 2\langle I\rangle_T \frac{\mathcal{I}_1\left(2\kappa A\right)}{\mathcal{I}_0\left(2\kappa A\right)} cos(\omega t). \tag{6.7}$$

In Figure 6.5 a simulated plot of the tunneling current versus distance (a) and time (b) are presented. The tip oscillates with an amplitude A over the z_0 point. The set point is the time-averaged tunneling current dotted in red in Figure 6.5(b).

A lock-in amplifier is used to record the first harmonic of the tunneling current at the oscillation frequency of the tip, in green in the Figure 6.5(b), while STM constant tunneling current feedback is on. The lock-in output signal, (V_{LI}), can be expressed as:

$$V_{LI} = 2Z_f\langle I\rangle \frac{\mathcal{I}_1\left(2\kappa A\right)}{\mathcal{I}_0\left(2\kappa A\right)}. \tag{6.8}$$

The STM preamplifier converts I to V therefore the transimpedance (Z_f) has to be taken into account, which is frequency dependent and acts as a low-pass filter. The second part of the Equation 6.7, multiplied by the transimpedance is what the lock-in measures. In order to determine the kappa value for each pixel, five inputs have to be considered: $\langle I\rangle_T, I_{1f}$, A, f and Z_f. Then, using a mathematical program the kappa map is obtained from the Equation 6.7.

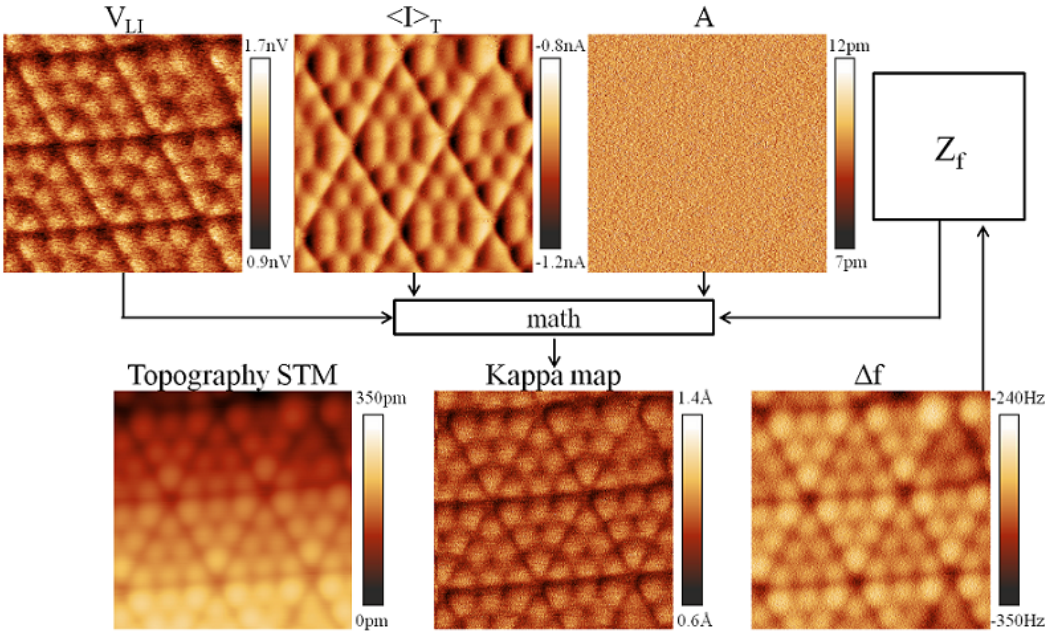

FIGURE 6.6: Schematic diagram with the channels needed to obtain the kappa map in dynamic STM/FM-AFM: lock-in output, tunneling current and amplitude. The transimpedance of the STM's preamplifier, Z_f, is frequency dependent and, therefore, the frequency shift channel is needed. Figure extracted from [107]. Parameters: I = 1.00 nA, Bias = +1.40 V and A = 10 pm.

In Figure 6.6 a schematic diagram with the channels needed to obtain the kappa map image of the Si(111)–7×7 surface in dynamic STM/FM-AFM is shown: lock-in output, tunneling current and amplitude. The transimpedance is calculated from the frequency shift channel.

As already demonstrated in the last chapter, the interpretation of kappa in terms of work function is often not straightforward. For this reason, kappa images will not be converted to work function maps. However, it will be shown that obtaining kappa at atomic and molecular scale is a powerful method to identify differences in the electronic coupling of molecules adsorbed on surfaces.

6.4 Experimental Details

The experimental results presented in this chapter have been performed during my stay in the University of Regensburg (Germany) in the group of Prof. Franz J. Giessibl. All measurements were performed with a custom-built combined AFM and STM equipped with a qPlus sensor [71] with a tungsten tip operating at room temperature in ultra-high vacuum. The sensor had a quality factor Q $\sim$ 3000 and

$f_0 \sim 26$ kHz. For the image processing the freeware WSxM program has been used [101].

Pieces of p-type Si(111) wafer were previously cleaned with acetone and ethanol, then loaded into the UHV chamber and degassed during few hours. To obtain the 7×7 reconstruction, the silicon was flashed several times to a maximum temperature of 1200°C during 20 s followed by a fast quenching at 900°C during 30 s and then a slow cooling down to room temperature. PTCDA molecules (Sigma-Aldrich) were sublimated from a home-built Knudsen cell and the rate of deposition was measured with a quartz crystal microbalance. To prepare the PTCDA/Si(111)-7×7 system, a small coverage of molecules (0.1 - 0.3 ML) was sublimated on a clean Si(111)-7×7 surface at room temperature in order to get the clean 7×7 surface decorated with some molecules.

For the preparation of the Ag/Si(111) structure, a monolayer of silver was evaporated from a home-built Knudsen cell onto a clean Si(111)-7×7 surface during 6 min with the sample held at 550°C, followed by 20 min of annealing at the same temperature. Once the sample was checked for cleanliness in the STM, about one monolayer of PTCDA was evaporated during 6-7 min. In both preparations the current used to sublimated PTCDA was the same and the pressure in the chamber remained under 3×10^{-10} mbar.

For the kappa measurements, an SR850 DSP lock-in amplifier (Stanford Research Systems) was connected to a home-built STM preamplifier. All the kappa maps presented in this chapter were acquired with a scan speed of 4 ms per pixel. This was to accommodate the relatively slow acquisition time of the lock-in amplifier. The amplitude was calibrated on a metallic surface before performing the kappa measurements employing the amplitude vs. z piezo position method as explained in detail in the Chapter 3.

6.5 Characterization of the Substrates

6.5.1 The Si(111)-7×7 Surface

Silicon is a semiconductor from the group IV of the periodic table with a diamond structure in bulk. When the (111) surface is formed, the atoms from the last layer

have a dangling bond and the most stable structure is the 7×7 reconstruction where the number of dangling bond is minimized. To obtain this reconstruction, silicon (111) surface has to be annealed in UHV at elevated temperature.

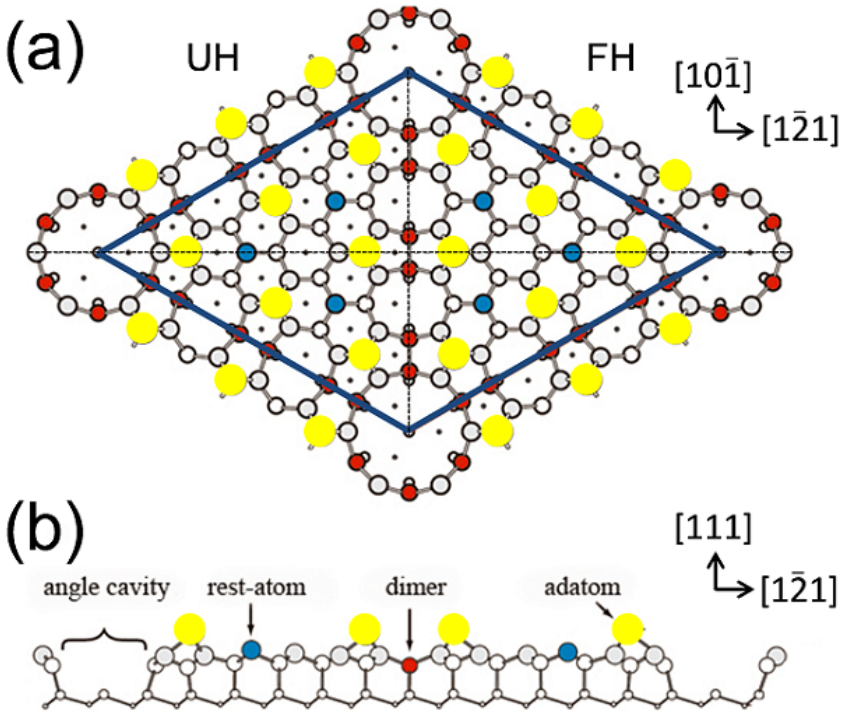

FIGURE 6.7: (a) Top and (b) side views of structural representation of the DAS (Dimer-Adatom-Stacking fault) model for Si(111)-7×7 surface adapted from [198]. Different silicon atoms are presented: yellow circles are adatoms, red circles are dimeritzate atoms and blue circles are the second layer of rest atoms. In blue is marked the 7×7 cell. Unfaulted half (UH) is marked in the left side and faulted half (FH) the right one.

The 7×7 reconstruction was discovered in 1959 by Schlier [169] but the geometric structure were still unknown. The first STM image of this reconstruction was obtained by Binnig [20] in 1983. It was a really important step in the history of surface science. Two years after Takayanagi proposed the dimer-adatom-stacking-fault (DAS) model to explain the geometric structure of the 7×7 reconstruction [198]. This model, shown in Figure 6.7, involves several types of atomic positions in the top four atomic layers. A rhombic unit cell with 7×7 (blue line) consists of an angle cavity and two triangular subcells separated by dimer chains (red atoms). Each subcell contains 6 adatoms (yellow atoms) which are the ones that appear in STM images. In the corners of the 7×7 unit cells, corner-hole, atoms from the top three layers are missing.

The unit cell contains twelve adatoms and six restatoms but the two half-cells are not equivalent. The unfaulted half (UH) has the first bilayer with same stacking sequence as ideal Si(111) and the other, the faulted half (FH) has the first bilayer rotated 180° respect the ideal Si(111). This structural difference is easiest to observe in the side view of the DAS model shown in Figure 6.7(b). There are 19 dangling bonds per unit cell: 12 located at the 12 adatoms, 6 at the 6 restatoms from the second layer and the last one on the corner hole atom in the fourth layer.

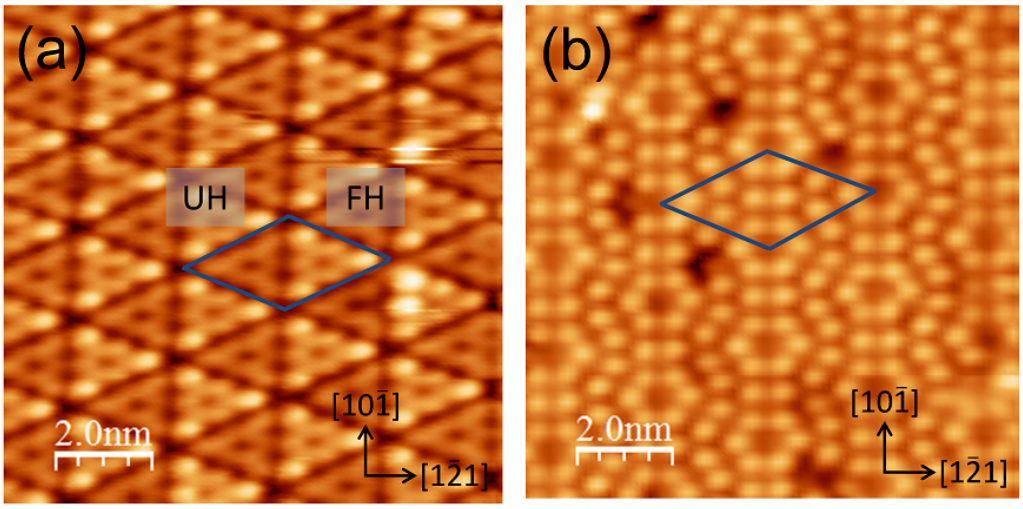

FIGURE 6.8: STM topographic images of the Si(111)-7×7 surface with the 7x7 unit cell marked in blue. (a) Imaging of filled electron states (I = 160 pA, Bias = 1.18 V, A = 60 pm) and (b) empty electron states (I = 100 pA, Bias = -1.00 V, A = 60 pm) are presented. In the filled states imaging, the faulted half (FH) appears in the right half brighter. The [10$\bar{1}$] and [1$\bar{2}$1] silicon directions are indicated.

In Figure 6.8 typical STM images of the filled and empty states, acquired in this thesis, are presented. In the filled states STM image, Figure 6.8(a), the observed protuberances correspond to the 12 dangling bonds from the 12 adatoms and the depressions from the vertexes of the unit cell correspond to the dangling bond of the corner hole. These dangling bonds do not appear with the same contrast and it is then possible to distinguish between the corner and center adatoms due to its different electronic properties. Depending on the bias voltage it is also possible to observe the dangling bonds from the restatoms. In the filled states image, the right triangular subcell appears brighter and corresponds to the faulted half (FH). The origin of this contrast is a mixture of electronic and topographic contributions [120, 156]. From the electronic part, a charge transfer from the unfaulted to the faulted half-cell occurs inducing a difference in the last atomic layer. In the empty states STM image, Figure 6.8(b), the observed protuberance

are also coming from the dangling bonds of the 12 adatoms and the depressions from the vertexes of the unit cell correspond to the dangling bond of corner hole. It is not possible to distinguish the faulted and unfaulted half at this bias polarity. The six adatoms appear as bright circles. Corner holes are surrounding by the six adatoms that appear with the same contrast.

6.5.2 The Ag/Si(111) Surface

When evaporating Ag on Si(111)-7×7, keeping silicon at 550°C, a surface reaction occurs. Dangling bonds from silicon are saturated with silver atoms and the resulting surface is AgSi(111). Depending on the annealing temperature and Ag coverage different phases can be observed: $\sqrt{3} \times \sqrt{3}$, 3×1 and 5×2. In the study presented here, the Ag/Si(111)$\sqrt{3} \times \sqrt{3}$ is grown and for simplicity from now on it will be called AgSi(111) or Ag/Si(111).

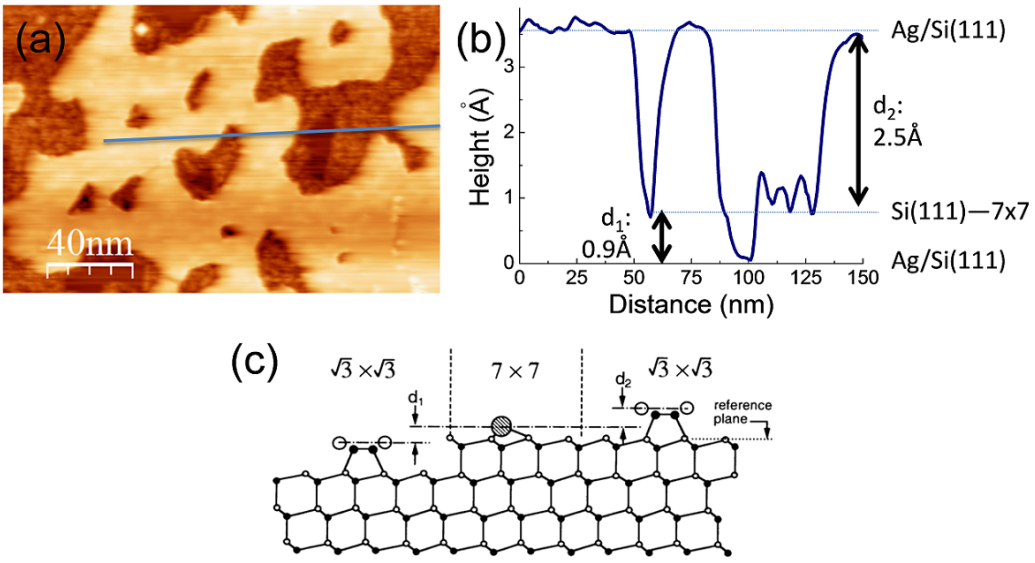

FIGURE 6.9: (a) Topographic STM image of a surface where both Ag/Si(111) and Si(111)—7×7 are observed. The Ag evaporation was smaller than the monolayer and there are clean silicon areas that appear rougher than the Ag/Si(111). (b) Line profile, market in (a) where d_1 appears with a height of 0.9 Å and d_2 with 2.5 Å. (c) Schematic view of the two types of boundaries between the 7×7 structure and the honeycomb-chain-trimer (HCT) model for the AgSi structure extracted from [213]. Parameters: (a) I = 140 pA, Bias = +0.38 V, A = 100 pm.

The large scale STM image in Figure 6.9(a) shows the topography obtained after the deposition of a submonolayer coverage of Ag on the clean Si(111)—7×7 surface. The AgSi(111) and the Si(111)—7×7 regions coexist in this image. The areas

with higher roughness correspond to the clean Si(111)-7×7 whereas flat areas correspond to the formation of the AgSi(111). In Figure 6.9(b) the line profile indicated in (a) is shown. In the literature, it was pointed out the influence of the bias in the step height boundaries [213]. In Figure 6.9 filled states are imaged and the measured step values are: 0.9 Å for d_1 and 2.4 Å for d_2. The sum of d_1 and d_2 is in agreement with the bilayer steps of the Si(111) (3.14 Å in height).

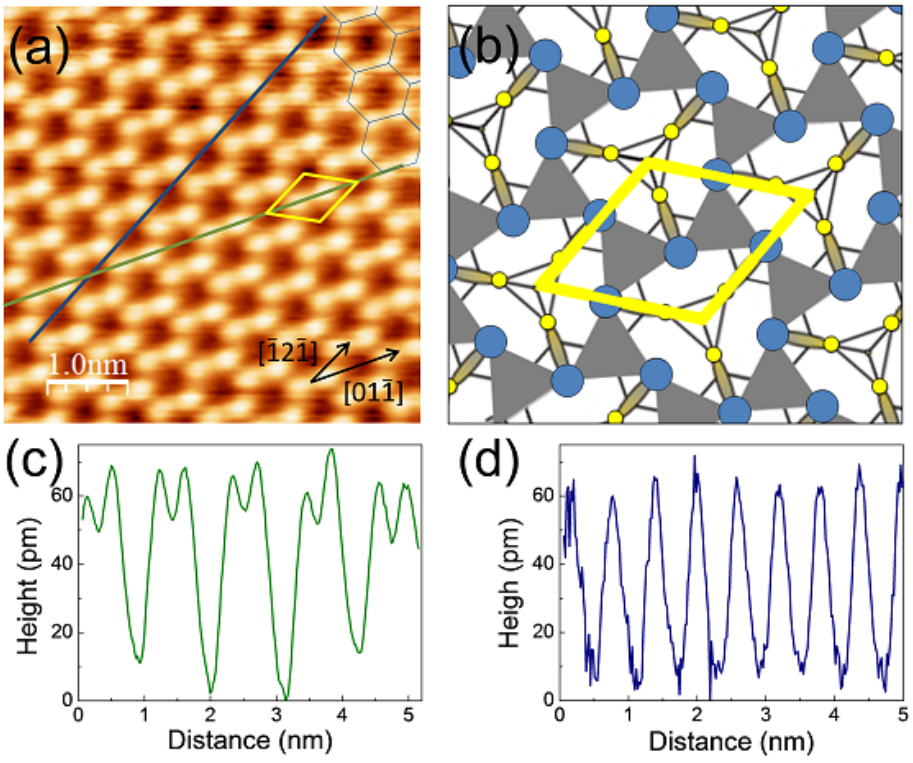

FIGURE 6.10: (a) Topographic STM image of Ag/Si(111) surface where the darker areas (minimum) are related with the Si trimers and the brighter (maximum) with the Ag trimers. (b) HCT structural model of Ag/Si(111) taken from ref [194]. Yellow and blue circles represent Si and Ag atoms respectively. In (c)-(d) the line profiles marked in (a) are presented. Parameters: (a) I = 680 pA, Bias = -1.30 V, A = 100 pm.

The most accepted model in the literature is the so-called honeycomb-chained-trimer (HCT) [45, 213, 214] for the structure imaged at room temperature. In this structure, Si atoms (yellow circles in Figure 6.10(b)) form covalently bound Si trimers. The Ag atoms form trimers (gray triangles in Figure 6.10(b)). This structure results in a chained honeycomb arrangement of Ag trimers. Low temperature STM studies (<66 K) [2] show inequivalent trimers configuration in the so-called inequivalent trimer chain (IET) due to a 6° rotation of the Ag-Si bonds. This

rotation can occur in two directions and at room temperature, due to thermal-averaging effects, the structure results in the HCT model.

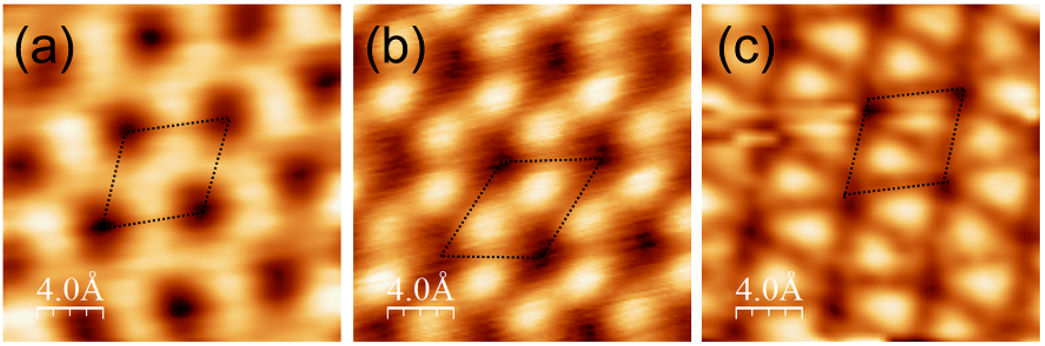

FIGURE 6.11: Topographic STM images of the Ag/Si(111) surface acquired at different tip-sample bias. Image (a) was acquired at positive bias (filled states are imaged) and (b) and (c) at negative bias (empty states are imaged). Parameters: (a) I = 325 pA, Bias = +1.30 V, A = 50 pm, (b) I = 680 pA, Bias = -1.30 V, A = 100 pm and (c) I = 325 pA, Bias = -0.13 V, A = 50 pm.

The density of occupied states (DOS) on the surface is not uniform and is concentrated on the Ag trimers, in contrast to a metal surface where the DOS is nearly homogeneous. In Figure 6.10(a) an example of STM image of the empty states of the Ag/Si(111) structure is shown and two lines profile along the $[10\bar{1}]$ (green line) and $[\bar{1}2\bar{1}]$ directions (blue line) in (c) and (d) respectively. In the STM images, the Si trimers appear as a minimum and trimers of Ag as a maximum. Figure 6.10(b) depicts a scheme of the reported HCT structure where yellow and blue circles represent Si and Ag atoms respectively and the Ag trimers are represented by gray triangles.

In Figure 6.11, three STM topographic images of the Ag/Si(111) surface at different tip-sample bias and distances are presented. This surface has a strong dependence on the bias voltage polarity. In Figure 6.11(a) the filled states are imaged and in Figures 6.11(b)-(c) the empty states. The unit cell is overlaid on the three STM images. As shown in Figure 6.10(b), the corners of the unit cell correspond to the Si trimers and in the three images presented here they appear as a minimum. In contrast, the observation of the Ag trimers changes in the STM images as a function of the bias: a continue hexagon around the Si trimers (Figure 6.11(a)), as bright circles associated to dimmers (Figure 6.11(b)) and with a triangular shape (Figure 6.11(c)). Filled state images show protrusions in the positions of Ag atoms in the honeycomb-chain-trimer (HCT) model. Empty state images show a characteristic honeycomb pattern with two maximum per unit cell [222].

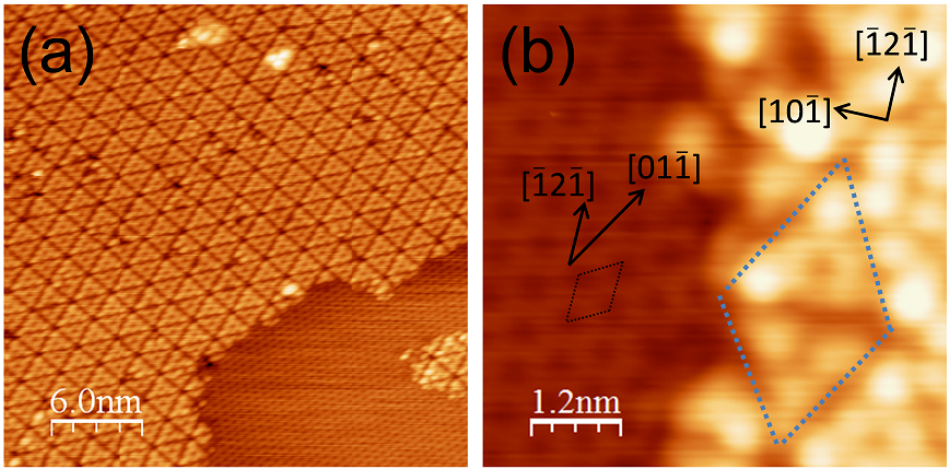

FIGURE 6.12: Topographic STM images of the Ag/Si(111) – Si(111)–7×7 step boundary. Both images were acquired with positive bias, filled electron states imaging. Parameters: (a) I = 75 pA, Bias = +1.50 V, A = 0 pm (non oscillating tip) and (b) I = 325 pA, Bias = +1.33 V, A = 50 pm.

Figure 6.12 shows two topographic STM images of different samples with sub-monolayer coverage of Ag on Si(111)–7×7 where the boundary of the Si(111)–7×7 and the AgSi(111) is observed. In Figure 6.12(b) the unit cell of both surfaces are marked and it is possible to observe that they are 30° rotated, i.e. the angle between [$\bar{1}2\bar{1}$] and [$01\bar{1}$] directions.

6.6 PTCDA on Si(111)–7×7 Surface

6.6.1 Structural Study

When PTCDA is evaporated at low coverage (0.1 - 0.3 ML) on a clean Si(111)–7×7 surface, molecules are randomly adsorbed and even broken [146] and STM images reveal a great variety of adsorbates with different shapes and sizes. Figure 6.13 shows topographic STM images of the Si(111)–7×7 surface after dosing a low coverage of PTCDA. The PTCDA adsorbates appear as bright protrusions on the surface and only those adsorbed on the corner hole exhibit defined structural features. The great quantity and variety of adsorbates suggests that some molecules are broken due to the high molecule-substrate interaction or that they do not lie flat. Molecules adsorbed on the corner hole are marked by a black circle in Figure 6.13. The study in this section will be focused on these molecules. For

higher molecule coverage, PTCDA does not self-assemble in ordered structures and the high tip interaction with the sample hinders stable imaging.

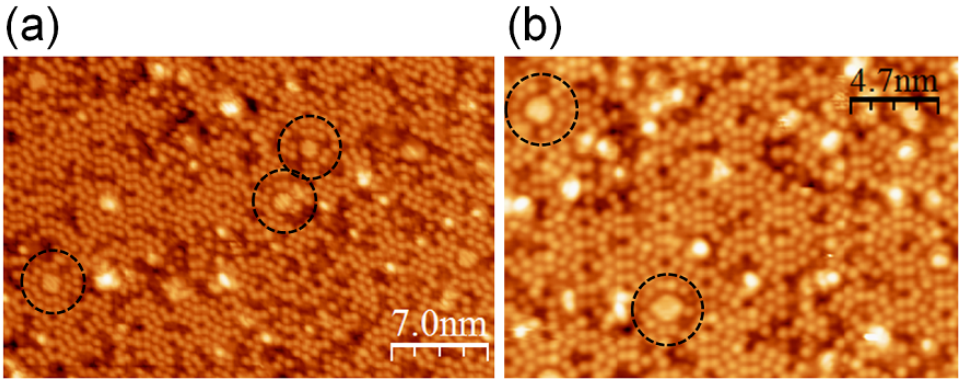

FIGURE 6.13: Topographic STM images of the Si(111)–7×7 surface after a low coverage evaporation of PTCDA molecules. Marked by circles are the PTCDA molecules adsorbed on the corner hole of the 7x7 structure. Parameters: (a) I = 250 pA, Bias = -1.00 V, A = 50 pm and (b) I = 220 pA, Bias = -1.50 V , A = 100 pm.

Figure 6.14(a) shows an STM image of a PTCDA molecule adsorbed on the corner hole of the Si(111)–7×7 measured at a negative bias voltage (empty states). In agreement with previous studies, the PTCDA molecule appears with five parallel lobes [146]. The spatial features of the empty states do not correlate with molecular orbital calculations for the LUMO of the free molecule (Figure 6.2). To explain similar observations, Nicoara et al. [146] proposed that upon chemisorption, the LUMO and the LUMO+1 orbitals drop in energy, resulting in the LUMO being completely filled and the LUMO+1 being partially filled. These results suggest an electronic interaction of PTCDA with the substrate causing charge transfer from the silicon to the molecule.

It was determined that the five stripes are perpendicular to the long axis of the molecule and in Figure 6.14(b) the profile length of approximately 1.3 nm is in agreement with the long axis of the molecule. The constant height over the molecule suggests that it lies flat on the corner hole of the 7×7 structure. Due to tip instabilities it was not possible to obtain images of opposite bias polarity where the FH and UH of the Si(111)–7×7 can be distinguished. According to Nicoara et al. the long axis of the molecule is aligned parallel to the dimer line which separates the UH and FH, i.e. the $[10\bar{1}]$ substrate direction (see Figure 6.7(a)), which have been used to assign the directions in Figure 6.14(a) [146]. It was also concluded that the charge transfer occurs principally from the silicon to the

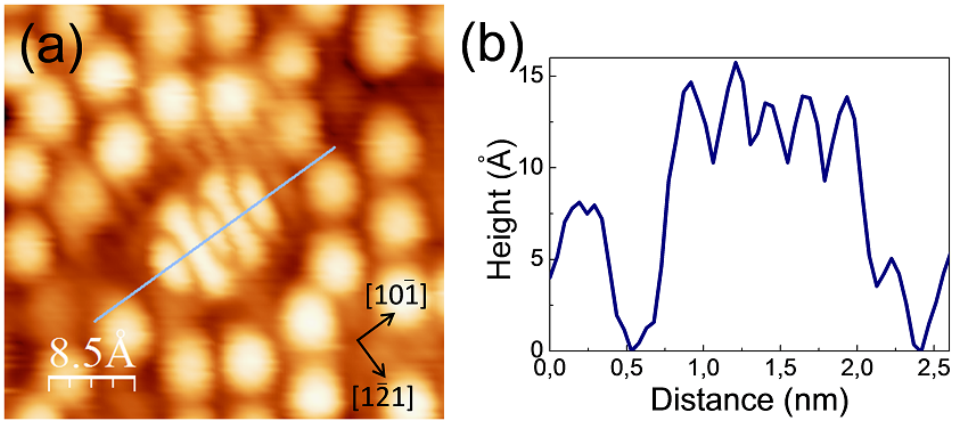

FIGURE 6.14: (a) Topographic STM image of a molecule of PTCDA adsorbed on the corner hole of the Si(111)–7×7 surface and (b) its line profile along the long axis of the molecule. Parameters: I = 200 pA, Bias = -1.40 V, A = 50 pm.

four carboxyl oxygens and DFT calculations agree with this prediction showing a variation of the C=O distances respect to the free molecule [146].

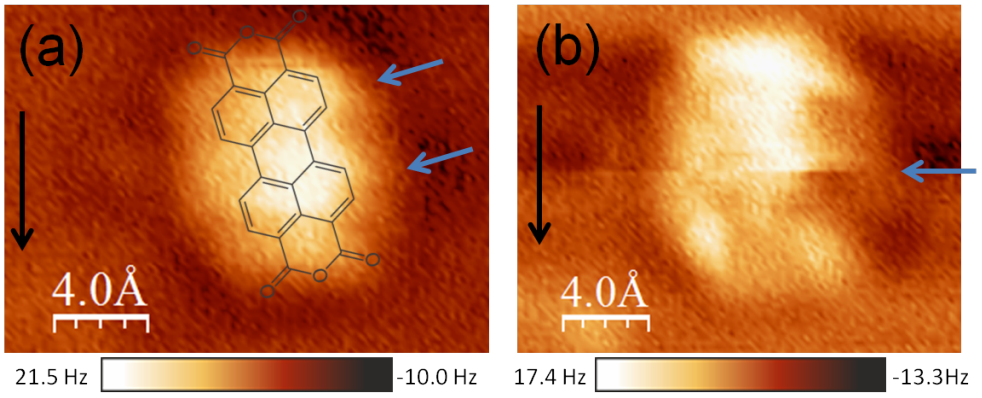

FIGURE 6.15: Consecutive FM-AFM images in constant height mode of a molecule of PTCDA adsorbed on the corner hole of the Si(111)–7×7 surface. Scan direction is marked by a black arrow. In (a) the PTCDA molecular structure is overlaid and the extremes of the perylene are marked with arrows. In (b) there is a tip changed in the line indicated with a arrow. Parameters: Bias = +0.20 V, A = 50 pm.

Two consecutive constant height FM-AFM images are presented in Figure 6.15 showing the frequency shift channel. A weak intermolecular contrast can be appreciated which is very different from the features previously observed by STM. In Figure 6.15(a) a PTCDA scheme is overlaid, showing that the perylene part of the molecule can be distinguished with slightly brighter contrast than the rest. Figure 6.15(b) is the consecutive scan image and a tip change occurred (marked with an arrow), in the first half of the image the contrast is similar to the observed in

Figure 6.15(a), but after the tip change the area where the two carboxylic oxygens are expected appears brighter.

6.6.2 Imaging the Decay Constant

The results of the decay constant (kappa) maps obtained for this system are now presented. Figure 6.16(a) shows an STM topographic image of a PTCDA molecule adsorbed on the corner hole of the Si(111)–7×7 and in (b), to help with the interpretation, a scheme of the PTCDA is overlaid and the six adatoms around the corner hole are marked. The four Si adatoms that participate in the bonding with the PTCDA molecule according to DFT calculations [146] are represented in gray whereas in yellow are the two that do not participate. The kappa map simultaneously calculated is shown in Figure 6.16(c). The simultaneous channels recorded in the STM/FM-AFM are also presented in Figure 6.16: (d) lock-in output, (e) tunneling current, (f) amplitude, (g) excitation, (h) frequency shift and (i) the cosine of the angle between the slope of the image and the z axis calculated from image (a). Note that no contrast is observed on the simultaneous dissipation channel shown in Figure 6.16(g), discarding dissipative forces between the tip and the sample. In Figure 6.16(c) can be observed that the mean value of kappa over the silicon is lower than over the molecule. This implies a higher effective tunneling barrier over the molecule that is in qualitative agreement with an interface dipole originated from electron charge transfer from the silicon to the molecule. However, the difference between the obtained kappa values is too high to assume that it is only due to charge transfer. The kappa average values for silicon and PTCDA are 1.2 Å^{-1} and 1.9 Å^{-1}, respectively.

A revision of the literature regarding the experimental calculation of kappa for the Si(111)–7×7 from the distance dependence of the tunneling current reveals a disparity of results. Herz et al. reported a dynamic kappa study of the Si(111)–7×7 surface [96] showing strong atomic contrast observed in the kappa map with a maximum value of 0.80 Å^{-1} (related work function of 2.9 eV) and an average over the surface of less than 0.77 Å^{-1}. This value is significantly smaller than the work function of the Si(111)–7×7. They suggested several mechanisms to explain the strong contrast over the surface and the low kappa values: geometry effects in the orbital model, displacement of tip-sample atoms at small tip-sample distance, formation of chemical bonds and/or changes in the barrier shape. Sugimoto et al.

reported a kappa value of 2.01 $Å^{-1}$ from $I(z)$ point spectroscopy performed above the corner adatom (related work function of 15.4 eV) without providing further discussion [191].

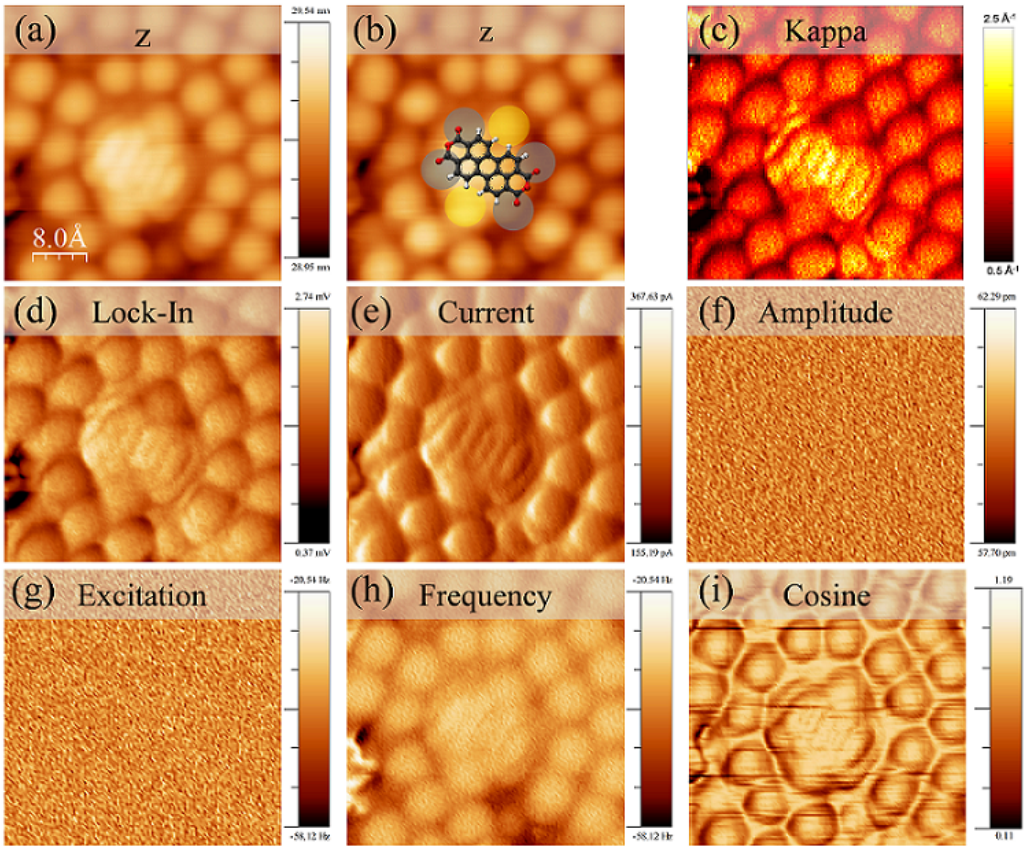

FIGURE 6.16: (a) Topographic STM image of a PTCDA at the corner hole of the Si(111)–7×7 and (b) the same image with the molecule scheme and the 6 adatoms of Si around it. We distinguish between the 4 adatoms that take part in the charge transfer (gray) and the 2 that do not (yellow). (c) Simultaneously kappa map obtained during imaging (a). Images (d)-(h) are the raw data channels that are measured at the same time: lock-in, tunneling current, amplitude, excitation and frequency shift. Image (i) is the cosine of the angle between the slope of the signal and the z axis calculated from image (a). Parameters: I = 250 pA, Bias = -1.50 V, A = 60 pm.

Both, physical effects (tip-sample relaxation) and electronics effects (wave function geometry) can influence the experimental determination of the decay constant. The topography can also influence the measure of kappa for surfaces with large topographic corrugation as in the case of the Si(111)–7×7 structure [77, 97, 159]. However this effect is expected to result in a reduction of the measured value since this effect is related with the cosine of the angle formed by the gradient vector of the surface at each point and the modulation direction (Figure 6.16(i)) [77]. For this reason, in Figure 6.16 it has been included the cosine of the angle between the slope

of the signal and the z axis calculated from the topographic image. A correlation between the kappa map and the cosine image is not observed and therefore a "cross-talk" with the topography is ruled out. The surface of Si(111)–7×7 has also been explored by Kelvin Probe Force Microscopy (KPFM) [117]. Induced polarization due to the tip-surface interatomic interaction producing herein a local redistribution of the charge density has been invoked as mechanism for the atomic contrast observed by KPFM and the drop of local contact potential difference (i.e apparent increase of the work function) at closer tip-surface distances.

The negative frequency shift and the absence of features in the dissipation channel during the measurements indicate, that on average, the tip is in the attractive regime of the interacting potential during the oscillation cycle. The strong attractive forces between the Si adatoms and the tip, causing a reduction of the distance between the atoms in the tip and the sample, and/or polarization effects are thus possible causes of the larger values measured for kappa. It is relied therefore in a quantitative comparison of values rather than in the absolute values of effective barrier height as well as in kappa.

Note in Figure 6.16(c) that the two adatoms around the corner hole (marked with yellow circles in Figure 6.16(b)) which are not involved in the bonding appear in the kappa map with the same contrast that the rest of the silicon atoms. The PTCDA molecule appears in kappa map as five stripes, Figure 6.16(c), as in the STM images but a difference is observed: the central stripe of the molecule appears with a higher kappa value while in the STM image the five stripes appear with approximately the same contrast (see also Figure 6.14). The increased value of the decay constant at the central lobe of the PTCDA implies a larger effective barrier height. Since the central stripe is above the corner hole, a possible interpretation could be that the higher distance between the surface and the molecule produces an effective larger dipole in the central stripe. This is still an open question which could be solved with the help of theoretical calculations.

6.7 PTCDA on Ag/Si(111) Surface

6.7.1 Structural Study

After the evaporation of Ag on the Si(111)–7×7 surface the dangling bonds are saturated and the PTCDA molecules are able to diffuse across the surface and to form ordered layers. On the Ag/Si(111) surface, PTCDA molecules lie flat and self-assemble forming a complete monolayer. Different phases have been reported before for this system: herringbone and square [81, 193]. In Figure 6.17(a) there is an example of large area topographic STM image after a low evaporation of PTCDA molecules ($\sim$ 0.2 ML) on a clean AgSi(111) surface. It is possible to observe two molecular islands (labeled as A and B) on the clean AgSi(111) surface. The contrast over the islands is homogeneous and it is attributed to a monolayer of molecules. From the line profile of Figure 6.17(b) the height of the PTCDA island is measured as $\sim$ 2.7 Å, that is in agreement with the typical height of π-conjugate molecules lying flat measured by STM [81]. The height of the AgSi(111) step is 3.3 Å, agreeing with the value obtained in Figure 6.9.

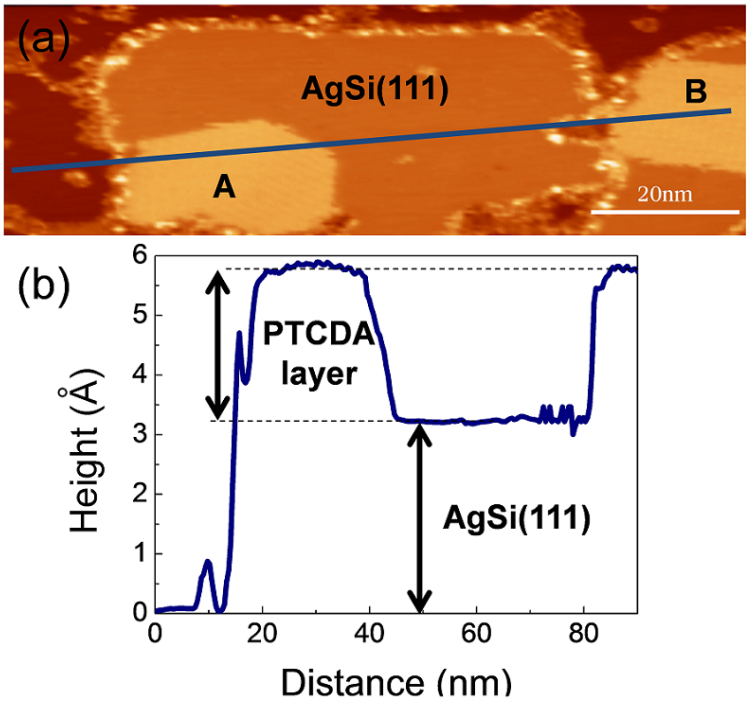

FIGURE 6.17: (a) Topographic STM image of two island of PTCDA on the AgSi(111) surface, labeled as A and B. (b) Step profile, marked in image (a), where height of a PTCDA layer is 2.7 Å and AgSi(111) layer 3.3 Å. Parameters: I = 160 pA, Bias = -1.50 V, A = 50 pm.

Square Phase

As previously mentioned, it is not common to observe a square phase over hexagonal substrates but it was previously observed also on other surfaces as Au(111) [135].

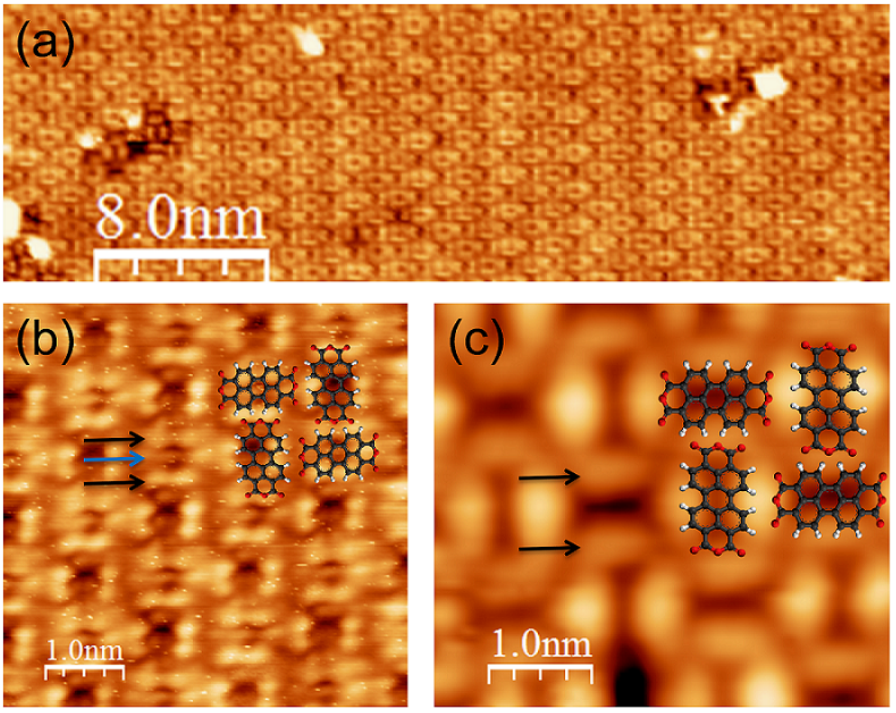

FIGURE 6.18: Topographic STM images of the square phase of PTCDA on Ag/Si(111). Images (a) and (b) correspond to the same area and were obtained consecutively. Parameters: (a) I = 130 pA, Bias = -2.00 V, A = 50 pm, (b) I = 130 pA, Bias = -2.00 V, A = 50 pm and (c) I = 152 pA, Bias = -1.15 V, A = 50 pm.

Figure 6.18 shows three examples of STM topographic images of PTCDA on AgSi(111) in a square arrangement observed at negative bias. Each PTCDA molecule is imaged as having two parallel lobes along the long axis of the molecule, in agreement with previous observations [192]. Figures 6.18(a) and (b) display consecutive images obtained with the same STM parameters. A tip change occurred between them and molecules are imaged quite differently. In both, two parallel lobes appear (black arrows in Figures 6.18(b) and (c)) but in (b) some contrast between these two lobes can be distinguished (blue arrow). The tip change increases the orbital resolution and the molecules appear in a peanut-like shape similar to the one shown in Figure 6.4(e). Differences between the STM appearance of the molecules in the two orientations of the unit cell are observed. In Figure 6.18(b) the molecules aligned along the vertical axis of the image appear as two parallel lobes with a central depression, but those aligned along the horizontal axis appear

with an extra central lobe. In Figure 6.18(c) the molecules in the two orientations appear as two parallel lobes but the contrast along the lobes over molecules aligned along the vertical axis of the image are not homogeneous. This inequivalent STM appearance has not been previously reported for the square phase.

The unit cell is measured to be squared with a lattice vector approximately as 4**a** (where **a** = 6.65 Å is the lattice constant of the AgSi(111)), that corresponds to 26 Å. Swarbrick et al. reported a unit cell of $2\sqrt{3}$ that corresponds to 23.1 Å. The relation with the substrate was not clear in one direction and two models were suggested [192]. On the other hand, Gustafsson et al. reported a unique commensurate unit cell with two molecules of 16.2 Å , and a recalculated unit cell with four molecules of 22.9 Å [81].

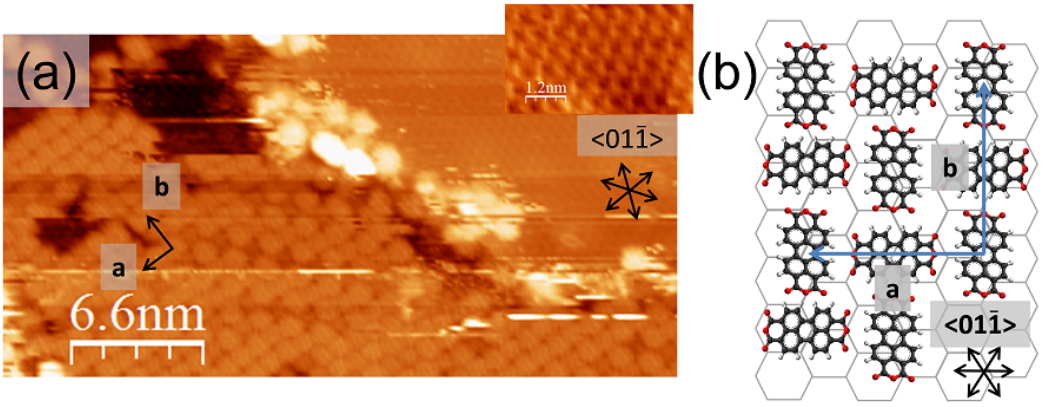

FIGURE 6.19: (a) Topographic STM image of a semilayer of PTCDA in the square phase on the AgSi(111) surface. Both, molecules and substrate, are resolved and the ⟨110⟩ directions of the AgSi(111) and the unit cell vectors of the square phase are indicated. (b) Schematic representation of the square PTCDA arrangement on the AgSi(111) surface. Parameters: (a) I = 250 pA, Bias = +1.50 V, A = 40 pm.

In order to determine the relation between the molecular square phase and the hexagonal substrate, an STM image where molecules and the AgSi(111) surface are resolved is presented in Figure 6.19. The AgSi(111) structure is observed on the upper right side of the image and the PTCDA square phase in the left side. The family of directions of the ⟨110⟩ is indicated over the substrate and the unit cell vectors over the PTCDA island, the vector denoted as **a** in Figure 6.19(a) is in the [01$\bar{1}$] direction and **b** in the [12$\bar{1}$] direction. A schematic representation of the molecules in a square phase on the AgSi(111) surface is shown in Figure 6.19(b). The alignment with the directions of the substrate is in agreement with previous studies [81, 192].

Herringbone Phase

The other principal phase on the AgSi(111) surface is the herringbone. This phase, that is the found in the (102) bulk plane, has been also observed on other surfaces as for example Ag(111) [75, 200], Au(111) [135], Au(100) [135], HOPG and epitaxial graphene [217]. The PTCDA/Ag(111) has been widely theoretical and experimentally studied as a prototype system.

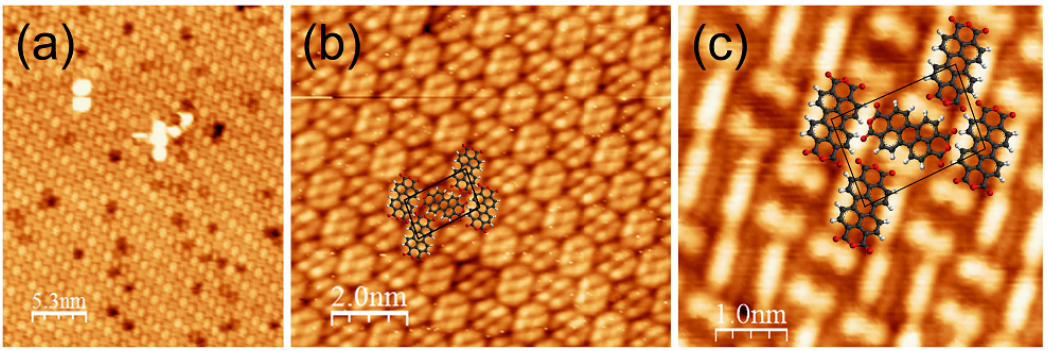

FIGURE 6.20: Topographic STM images of the herringbone phase of PTCDA on AgSi(111) with different imaging conditions. In (b) and (c) the unit cell is indicated, as well as the PTCDA structure. In (b) the STM image reveals six lobes, three at each side of the long axis of the molecule. In (c) each molecule is imaged as two parallel lobes along the long axis of the molecule. Parameters: (a) I = 170 pA, Bias = +1.50 V, A = 50 pm, (b) I = 250 pA, Bias = -1.00 V, A = 50 pm and (c) I = 250 pA, Bias = +1.50 V, A = 50 pm.

Figure 6.20 shows three topographic STM images of the PTCDA in the herringbone arrangement with different tips and STM conditions. Images from Figures 6.20(a) and (c) were acquired at a bias of +1.50 V (filled states) and (b) at -1.00 V (empty states) and the unit cell is marked in (b) and (c). In image (a) the molecules in the two orientations of the unit cell present different contrast, as well as molecule vacancies and defects, while in images (b) and (c) the contrast is approximately constant. In (c) the lobes shape differs between the two inequivalent PTCDA molecules. In the herringbone structure, the two molecules of the unit cell often appear with different apparent height providing the appearance of alternated bright and dark rows, for instance visible in the STM image of the Figure 6.20(a). Such contrast is not always observed, being very dependent on the tip conditions. The origin of the different contrast is not yet clear and it has been attributed to the differences in the hydrogen bonding between the two molecular orientations that exist when the angle between **a** and **b** is slightly distorted from 90°. Similar contrast variations have previously been reported for the herringbone phases of PTCDA on different substrates as on Ag(111) as mentioned

before [55, 127]. In some images, the difference between the two molecules is not appreciated by a different topographic contrast in STM but it is in the orbitals shape as has been observed in Figure 6.20(c). The LUMO was calculated as to have ten lobes and a central node along the PTCDA and the LUMO+1 as to have eight lobes and without a central node [236]. In both, the four lobes situated at the hydrogen were equal and only the lobes from the perylene were changed (see Figure 6.2). It is difficult to say how many lobes are imaged in Figure 6.20(b) but a central node is observed, being more similar to the LUMO state. In the STM image presented in Figure 6.20(c) the bias is the same as in (a) but the molecules look quite different with two lobes along the molecule and a central node similar to the one from Figure 6.4(e) and, therefore, probably due to a different tip termination.

Herringbone phase		**A** (nm)	**B** (nm)
On surfaces	In this study	1.3	2.3
	Swarbrick et. al	1.15	2.00
	Gustafsson et. al H-1	1.24	1.96
	Gustafsson et. al H-2	1.22	1.92
On bulk	α-phase	1.20	1.99
	β-phase	1.25	1.93

TABLE 6.2: Unit cell parameters of the herringbone phase of the PTCDA on AgSi(111) obtained in this study and reported by Swarbrick et. al [192] and Gustafsson et. al [81] and the two-dimensional unit cell of PTCDA (102)-plane for the bulk α and β polymorphic phases.

Previous STM studies by Swarbrick et al. reveal commensurate unit cell of $\sqrt{3}\mathbf{a} \times 3\mathbf{a}$ that corresponds to 1.15 nm $\times$ 2.00 nm [193]. Gustafsson et al. reveal that two herringbone phases exist, the H-1 with a unit cell size of 1.24 nm $\times$ 1.96 nm and the H-2 with a unit cell of 1.22 nm $\times$ 1.91 nm [81]. The H-1 phase is commensurate and the H-2 is not. The obtained parameters from the STM images presented in this chapter give a unit cell size of 1.3 nm $\times$ 2.3 nm. The closer relation between the unit cell and the parameter of the substrate is $2\mathbf{a} \times 2\sqrt{3}\mathbf{a}$. This relation does not agree with the previously reported. Table 6.2 summarizes the unit cell parameters of the herringbone phase on AgSi(111) and the bulk α and β polymorphs.

In order to determine the relation between the herringbone phase and the hexagonal substrate, an STM image where molecules and the AgSi(111) surface are resolved is presented in Figure 6.21. Previous studies do not completely agree

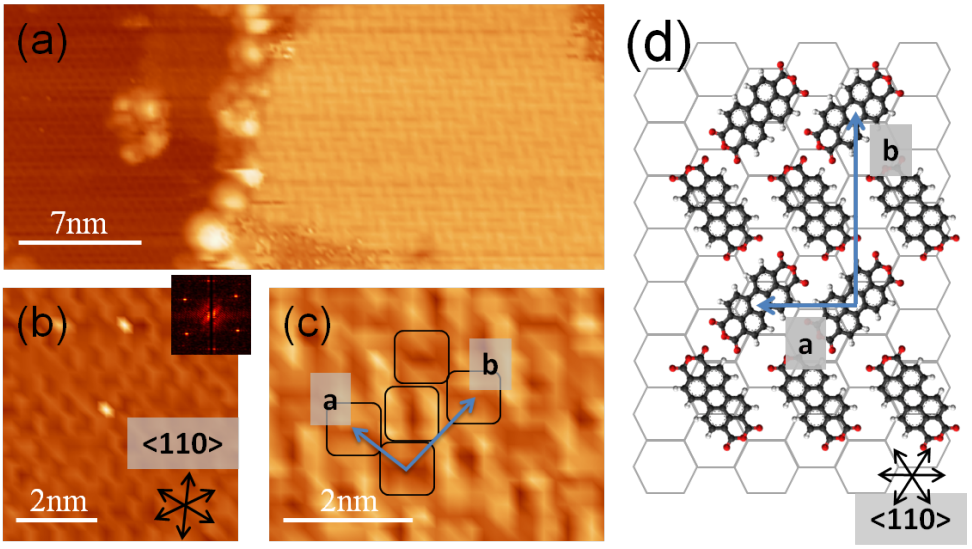

FIGURE 6.21: (a) Topographic STM image where an island of PTCDA in the herringbone phase and the substrate are imaged. (b) Zoom image of the AgSi(111) area with the FFT in the inset. (c) Zoom image of the PTCDA area of (a) with the unit cell vectors **a** and **b** marked.(d) Schematic representation of the PTCDA molecules in the herringbone phase on the AgSi(111) surface represented by a hexagonal network according to the HCT model. The family of directions of the ⟨110⟩ is marked in (b) and (d). Parameters: I = 170 pA, Bias = -1.40 V, A = 50 pm.

with this relation, Swarbrick et al. reported a herringbone phase with **a** aligned with the ⟨110⟩ and **b** with the ⟨121⟩ substrate directions. Gustafsson et al. reported two herringbone phases as mentioned before, both are slightly misaligned respect to the substrate directions but very close to agree with Swarbrick. In the topographic STM image presented in Figure 6.21(a), the substrate structure is resolved on the left side and the herringbone PTCDA phase in the right side of the image. Figures 6.21(b) and (c) are magnification of the AgSi(111) and the PTCDA island respectively. The high symmetry directions ⟨110⟩ of the substrate are indicated in Figure 6.21(b) (extracted from the STM image) and its FFT as an inset. The PTCDA unit cell is marked on Figure 6.21(c). From both images, it can be extracted that **a** of the unit cell is aligned with ⟨110⟩ and **b** with the ⟨121⟩. Because of thermal drift and creep there are some image distortions over both areas and cannot be said if the unit cell is completely aligned with the substrate directions or they are slightly misaligned. In Figure 6.21(d) a schematic representation of the AgSi(111) as a hexagonal network and the herringbone phase of the PTCDA are represented.

The two structures previously described, the square and the herringbone, can

coexist in the same area as can be observed in the topographic STM image from Figure 6.22 indicating that their stabilities are quite similar as suggested before [81, 192]. The directions of the unit cell of the square and the herringbone phases are indicated in Figure 6.22 and it can be observed that the **a** and **a'** unit cell vectors are oriented along the ⟨110⟩ and the **b** and **b'** along the ⟨121⟩ substrate directions.

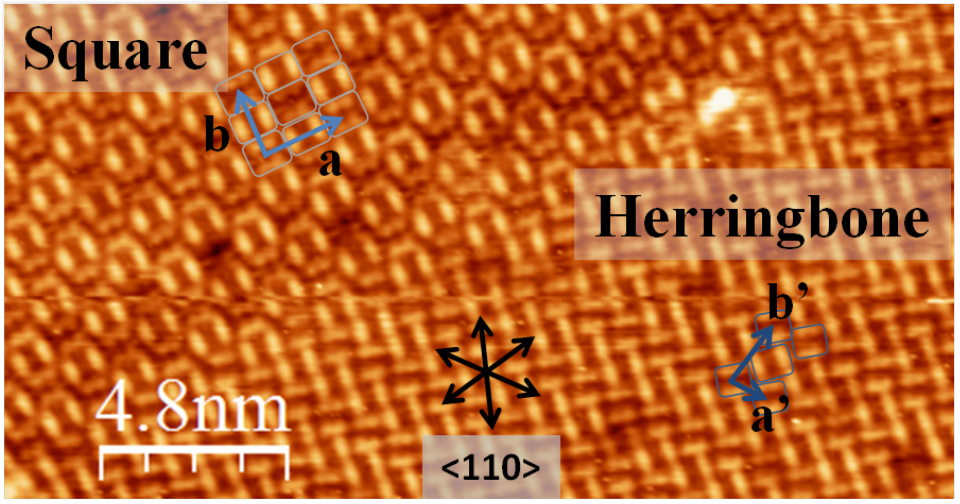

FIGURE 6.22: Topographic STM image of a monolayer of PTCDA on AgSi(111) where the herringbone and square phases coexist. The unit cell of both phases (**a** and **b** for the square phase and **a'** and **b'** for the herringbone), as well as the family of directions of the substrate ⟨110⟩ are marked. Parameters: I = 250 pA, Bias = -1.00 V, A = 50 pm.

FM-AFM images at constant height were performed to achieve intra and intermolecular resolution and are presented in Figures 6.23 and 6.24. This is, to our knowledge, the first high resolution AFM imaging at room temperature of this system (FM-AFM images with less resolution were published recently of the herringbone phase of the PTCDA on Ag(111) [130]). Two consecutive constant height images of the PTCDA herringbone phase were obtained and are presented in Figures 6.23(a) and (c) which are the simultaneously acquired frequency shift and tunneling current images. In Figures 6.23(a) and (c) some features between molecules are resolved at the position where the hydrogen bonds are expected to be as it has been previously reported for similar molecular structures [195, 223]. The frequency shift is positive (repulsive regime) over the molecules and negative (attractive regime) in between. Hapala et al. have recently suggested that is not possible to directly correlate the intramolecular contrast observed by STM and AFM with hydrogen bonds. They suggest a mechanical model that takes into account the geometric distortion of the tip apex due to interaction with the sample. Then, the intermolecular contrast does not necessary arise from an increase in

electron density but due to the sharp boundaries between basins of the repulsive short-range potential produced by surface atoms that are close to each other. The simultaneously acquired tunneling current image, Figure 6.23(b), shows ten bright lobes with a central node as expected for the LUMO [236]. A different shape between the two molecules of the unit cell is observed on the tunneling current channel, this will be discuss later and no correlation between the appearance of the frequency and the current is observed.

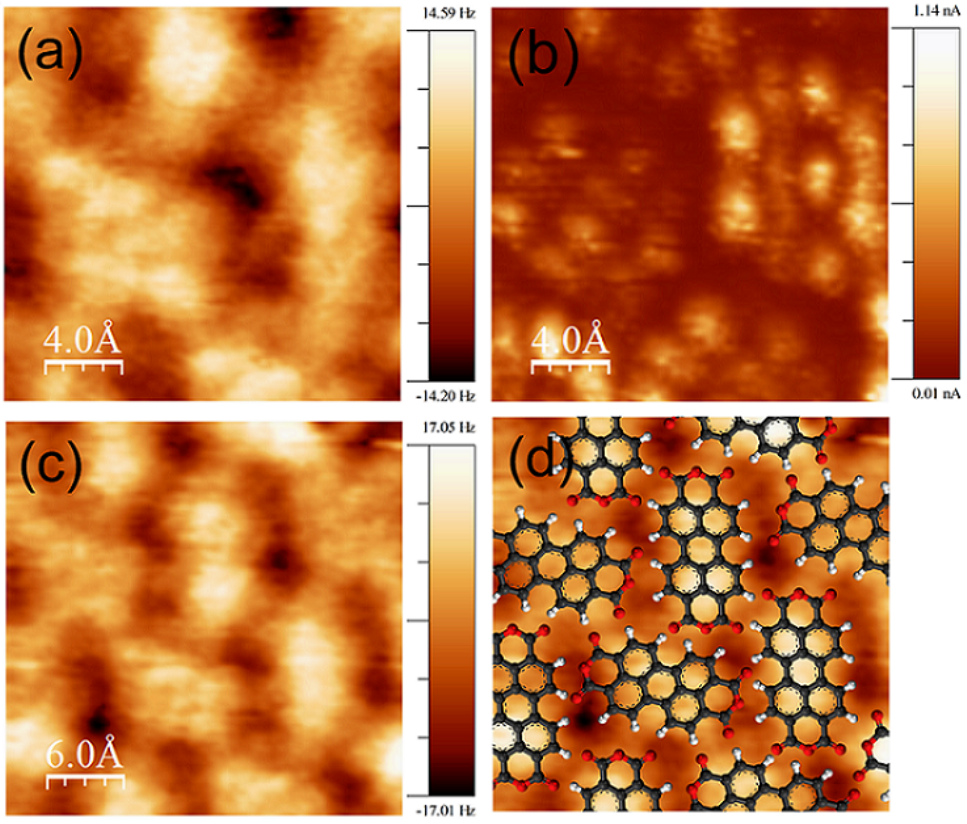

FIGURE 6.23: Images (a) and (c) are constant height FM-AFM of a herringbone phase of PTCDA on AgSi(111). Image (b) is the simultaneous tunneling current to image (a). Image (d) is the same than (c) with the structural PTCDA model added. Intra- and intermolecular contrast are observed in both FM-AFM images. Parameters: Bias = -0.13 V, A = 50 pm.

Higher intramolecular resolution was acquired by constant height FM-AFM and is shown in Figure 6.24 where the skeleton of the PTCDA molecules can be resolved. The frequency shift is positive over the molecules and negative over the intermolecular area as in Figures 6.23(a) and (c). It indicates a repulsive tip-sample interaction over the molecules and attractive over the intermolecular region. The simultaneously tunneling current image is not presented since no current were

recorded. The highest frequency shift contrast in Figure 6.24 respect to Figure 6.23 can be attributed with a different tip ended material that enhance the imaging resolution. According to Hapala et al. sharp resolved structural resolution, as the shown in Figure 6.24, is due to strong lateral relaxations of the probe particle attached to the metallic tip apex [87]. At close tip-sample distances these relaxations follow the potential energy basins produce by the Pauli repulsion. Therefore, the sharp features appear always coinciding with the borders of neighboring basins. In the FM-AFM images presented here, the frequency shift contrast over both molecules of the unit cell is similar, indicating that the two molecules are at approximately the same height. The non-equivalent orbital shape observed in the STM Figure 6.23(b) between the two molecules of the unit cell indicate an electronic difference.

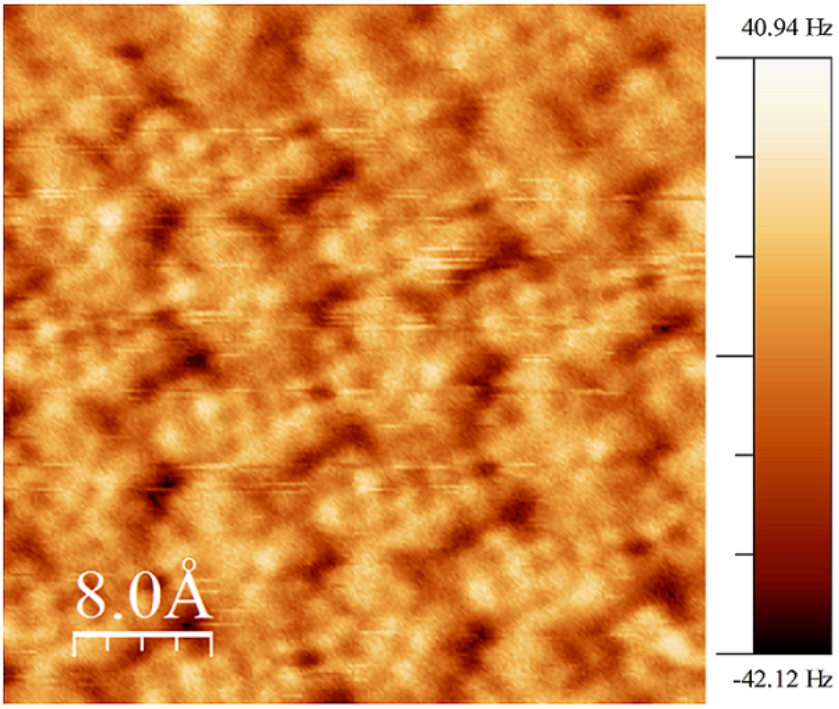

FIGURE 6.24: Constant height FM-AFM image of the herringbone phase of PTCDA on AgSi(111). The intramolecular structure is resolved and the perylene core structure can be distinguished. Parameters: A = 40 pm, Bias = 0.10 V and no current were observed.

6.7.2 Point Spectroscopy

In addition to imaging, the combination of FM-AFM and STM enables two different spectroscopic methods to investigate local changes in the local work function: (i) the decay constant obtained from the distance dependence of the tunneling

current (I vs. z) and (ii) the contact potential difference (CPD) measured from the frequency shift vs. bias voltage (Δf vs. Bias). As explained before, the decay constant measured from STM is directly related to the effective tunneling barrier whereas CPD corresponds to the bias voltage that minimizes the electrostatic force gradient between tip and substrate.

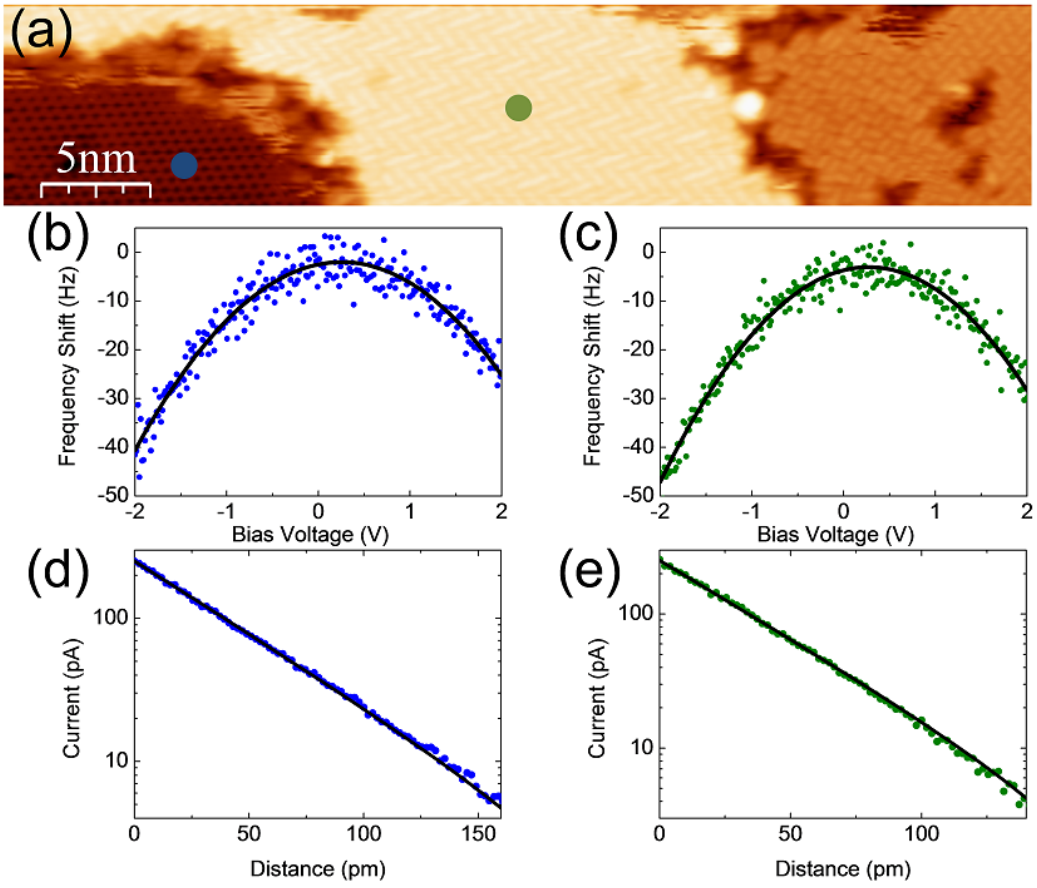

FIGURE 6.25: (a) Topographic STM image of an area where PTCDA and AgSi(111) are resolved. Frequency shift vs. bias voltage, (b) and (c), and current vs. distance, (d) and (e), were performed on the AgSi(111), (blue plot) and on the herringbone PTCDA island (green plot). To perform the Δf vs. z the tip was retracted 5 Å from the z_0. Parameters: I = 250 pA, Bias = -1.40 V, A = 40 pm.

Both types of spectroscopic methods have been employed here to characterize the difference of work function caused by the adsorption of PTCDA on AgSi(111). A submonolayer coverage of PTCDA was chosen for in-situ comparison between the two areas (covered and no covered) as shown in the topographic STM image of the Figure 6.25(a). The data were acquired at the marked points over a molecular island (green circle) and over bare AgSi(111) (blue circle). The measured dependence of the Δf vs. bias and the parabolic fit curves are shown in Figures 6.25(b)

and (c) for each region. The obtained CPD values are 250 ± 20 mV on the PTCDA island and 270 ± 20 mV on the AgSi(111) surface, giving a work function difference of only 20 meV. In contrast, the obtained kappa values are 1.167 ± 0.006 $Å^{-1}$ on the PTCDA island and 1.34 ± 0.01 $Å^{-1}$ for the AgSi(111). Expressed in terms of work function, according to Equation 6.2, the kappa values correspond to 5.19 eV for the PTCDA and 6.84 eV for the substrate, i.e. a work function difference of 1.65 eV.

The discrepancy between the values obtained from CPD and kappa is here attributed to an averaging in the CPD values between both regions due to the lower spatial resolution of the point Δf vs. Bias spectroscopy. Due to the long-range nature of the attractive electrostatic interaction between the tip and the sample, the lateral resolution is largely influenced by the size of the tip apex and the tip-surface distance. Since both regions are separated only by few tens of nanometers, the measured CPD most likely results from the electrostatic contribution of both, PTCDA and bare substrate. Enhanced lateral resolution can be achieved by reducing the tip-surface distance down to few angstroms at low temperature. However, this is hardly achievable at room temperature due to tip changes that result in unstable and irreproducible measurements. Thus, dynamic kappa imaging offers a more powerful tool to measure local changes with atomic resolution at room temperature than CPD measurements. The adsorption of atomic or molecular species on metal surfaces may induce significant changes in the work function, depending on the interaction between the adsorbate and the surface. A clear electronic interaction between the PTCDA molecules and the AgSi(111) surface was measured by high-resolution photoelectron spectroscopy (PES) and near edge x-ray absorption fine structure (NEXAFS) [82]. Two kinds of substrate-molecules interactions were measured, with the perylene core of the molecule and with the anhydride end groups. The interaction induces changes in the HOMO and LUMO levels as seen in the valence band and NEXAFS measurement. A shift in the core levels indicates charge transfer from the substrate to the perylene core of the molecule. A change to lowering binding energies of the anhydride end groups was measured, what also indicates charge transfer from the substrate to the end group, resulting in a more polarized molecule as well as an interface dipole. Both interactions produce a charge transfer in the same direction (from the surface to the molecule) but there are no experimental or theoretical values of the net charge transfer for this system that fills partially the LUMO of the molecule. The observed decrease of the potential barrier measured by $I(z)$ point spectroscopy on

the molecules does not agree with this scenario of an overall negatively charged molecule suggesting that more effects are playing an important role as pillow effect and/or charge reorganization.

In the PTCDA/Ag(111) system, a net charge transfer of 0.35 electrons per molecule was calculated by DFT [162]. When measuring the work function more effects have to be taken into account, apart from the net charge transfer the Pauli repulsion effect (also known as pillow effect) plays an important role. This effect is associated with the compression of the metal wave function tails at the molecule-metal interface due to the Pauli repulsion between electrons of the same spin. The measured work function is the result of a competition between the effect to have a surface dipole and the Pauli repulsion effect. The surface dipole due to the net charge transfer would increase the work function over the PTCDA molecules respect the substrate and the Pauli repulsion effect would decrease the work function over the molecules. Experimentally, two opposite values of the variation in the work function of the PTCDA and the Ag(111) measured by UPS have been published. Zou et al. reported an increase of 0.1 eV over the PTCDA molecules [241] and Duhm et al. a decrease of 0.1 eV over the PTCDA molecules [48]. In this case, a charge-back donation from the perylene to the Ag(111) was suggested in order to explain the experimental results.

Unfortunately, there are no results in the literature to establish any comparison of the work function of the PTCDA/AgSi(111) system. In the results presented here we have observed a decrease of the work function of 1.65 eV over the PTCDA molecules by $I(z)$ spectroscopy. The dynamic kappa measurements, presented in the next section, will allow to obtain intramolecular information of the charge distribution.

6.7.3 Imaging the Decay Constant

On Figure 6.26 a topographic STM image and its simultaneously obtained kappa map of the boundary between a PTCDA herringbone island and the AgSi(111) surface are shown and the unit cell of the herringbone phase is indicated as well as the directions of the substrate. A higher kappa value is observed over the AgSi(111) compared with the molecule island as measured by $I(z)$ point spectroscopy. The averaged kappa value obtained for the AgSi(111) is 1.69 $Å^{-1}$ and 1.49 $Å^{-1}$ over the PTCDA molecules. Note that whereas the decay constants obtained from

$I(z)$ correspond to values obtained in two points, these decay constant values are averaged.

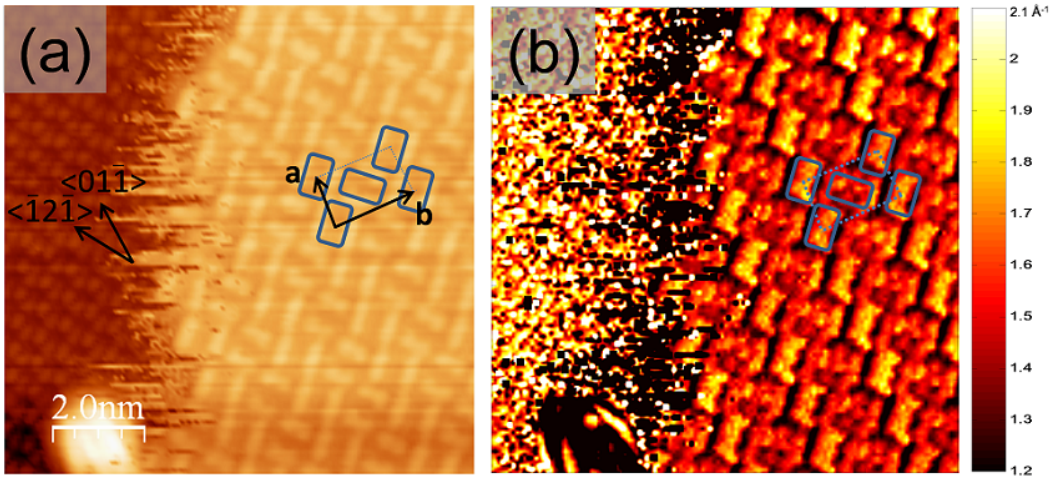

FIGURE 6.26: (a) Topographic STM image where the herringbone phase of PTCDA and the Ag/Si(111) are observed and (b) its simultaneously measured kappa map. Parameters: I = 200 pA, Bias = -1.30 V, A = 50 pm.

In the herringbone structure, the two molecules of the unit cell often appear with different apparent height that alternates from row to row, as mentioned before. Therefore, the investigation of this system by kappa imaging in FM-AFM/STM is of most interest to elucidate if the observed contrast by STM, that was attributed to an electronic effect in the last section, is manifested in the local decay constant. Figure 6.27(a) depicts an example of STM image where no contrast variations in the herringbone phase are observed in the topography and each PTCDA molecule appears with two parallel lobes as shown in Figure 6.20(c). The simultaneously obtained kappa map is shown in Figure 6.27(b) where differences in the kappa value between non-equivalent PTCDA molecules can be appreciated. No correlations between the contrast observed on the STM image and the kappa map are observed. The kappa average over the A molecules is 1.61 Å^{-1} and over B molecules is 1.54 Å^{-1}, this difference of 0.07 Å^{-1} can be related with a difference in work function of 0.8 eV (Equation 6.2). It shows that there is a local spatial variation of the effective tunneling barrier between non equivalent PTCDA molecules, which could be interpreted as caused by differences in the molecular charge transfer with the substrate and/or the differences in the hydrogen bonding between the molecules A and B.

Intramolecular resolution is visible in the kappa maps and can be attributed to a non-homogeneous charge distribution in the PTCDA molecule. Molecule A

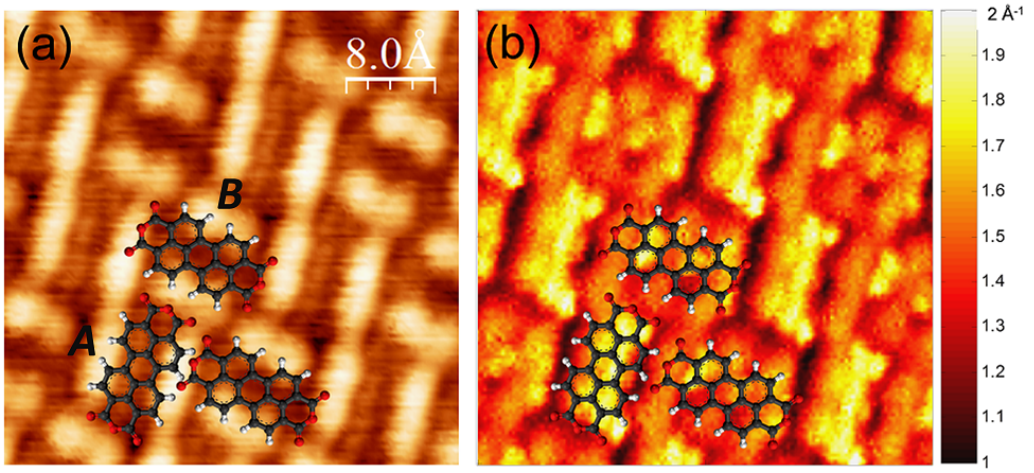

FIGURE 6.27: (a) Topographic STM image of a herringbone phase of the PTCDA on AgSi(111) and (b) its simultaneously acquired kappa map. In the topographic image, molecules appear in the peanut-like shape without appreciable contrast between the two molecules of the unit cell. In the kappa map the contrast is observable. PTCDA models are added in both images. Parameters: I = 200 pA, Bias = -1.20 V, A = 50 pm.

appears in kappa as a brighter lobe along the molecule that coincides with the node in the topographic STM image and some bright features appear in the areas where the anhydride part of the molecule is expected to be. Molecule B appears quite different in the kappa map, but again, the areas where the anhydride is expected to be the kappa value is higher. Other features are also observed.

6.8 Conclusions

The PTCDA molecule has been studied on two surfaces, Si(111)—7×7 and AgSi(111), by STM, FM-AFM and kappa imaging. In the PTCDA on Si(111)—7×7 system, the high molecule-substrate interaction does not allow molecules to diffuse and to form monolayers. STM images reveal a great variety of adsorbates with different shapes and sizes after a low PTCDA coverage and the study that has been presented here is focused on PTCDA molecule adsorbed on the corner hole of the 7×7 reconstruction where a charge transfer from the substrate to the molecule occurs. The STM contrast reveals five parallel stripes perpendicular to the long axis of the molecule and the FM-AFM images with intramolecular resolution are able to distinguish the perylene core. Kappa imaging reveals a higher kappa value over the molecule compared with the Si(111)—7×7, agreeing with an interface dipole originated from electron charge transfer from the silicon to the molecule. The

obtained difference is too high to be assigned only to the dipole formation due to the charge transfer and some effects are expected to occur as tip-sample deformation. The adatoms, around the corner hole, that do not participate in the charge transfer appear with the same kappa contrast that the rest of the Si(111)—7×7.

In the second system, PTCDA on AgSi(111), the molecule-substrate interaction is smaller and molecules diffuse and self-assemble in two phases: herringbone and square. On the herringbone phase, the two molecules of the unit cell are imaged with different apparent height by STM. The different apparent height can be due to a topographic and/or electronic effect. In FM-AFM images, both inter- and intramolecular contrast can be observed at room temperature and no contrast between the two molecules is observed by AFM. Then, a topographic difference is not expected to be the origin of the contrast. Kappa imaging shows a contrast between these two molecules, even when it is not observable in the simultaneously topographic image. A higher kappa value can be related to a larger dipole surface. Then a possible explanation is a different charge transfer between the substrate and the two molecules of the unit cell yielding a different surface dipole. Moreover, contrast within the molecules are observed in the kappa image that can be caused by a non homogeneous charge distribution.

Chapter 7

Study of the Monolayer of DIP on Cu(111)

7.1 Introduction

Diindenoperylene (DIP) is a perylene derivate organic semiconductor with promising properties for organic optoelectronic devices. It has been studied in thin films [31, 52, 92, 126, 212] and in monolayers on noble metal surfaces [39, 103, 155]. In contrast to the intensely studied perylene derivate PTCDA (Chapter 6) with two anhydride groups, the DIP-substrate interaction is not complicated by polar side groups and the influence of intermolecular interactions is expected to be smaller than for PTCDA.

In this chapter, first-principles calculations are combined with STM/FM-AFM measurements in UHV to analyze the adsorption of DIP molecules on the Cu(111) surface. A brief introduction to the DIP molecule, structure and properties as well as the state-of-the-art of studies of this molecule on different surfaces are given at the beginning. The influence of the substrate on the geometry of single adsorbed molecules, their diffusion barriers, as well as intermolecular interactions for molecular self-assembly and structure growth are studied. Long-range ordered arrangements of DIP molecules are found to be most favorable irrespective of the terrace width and short-range order structures are found to be less stable. In the experimental part, the initial growth is presented first followed by the monolayer of DIP molecules on the Cu(111) surface. Both long and short-range are observed

on copper terraces. The different phases observed by STM are presented together with a different tip-induced ordering effect that provide information about their relative stability. To complement the structural study, the work function difference that produces a monolayer of DIP molecules is determined by contact potential measurements (CPD) and compared with previously reported values achieved by photoemission techniques.

7.2 The DIP Molecule

General Properties of DIP

Diindenoperylene (DIP) is an organic semiconductor molecule with molecular formula $C_{32}H_{16}$ and molecular weight of 400.48 g/mol. The molecular structure is presented in Figure 7.1 where carbon atoms are represented in black and hydrogen atoms in white. It is an aromatic planar molecule with dimensions of ∼1.84 nm × 0.7 nm that exhibits a D_{2h} symmetry. As indicated in Figure 7.1, it consists of a perylene core with two indeno groups located to opposite sides. The sp^2 hybridization of the carbon atoms results in π-conjugated and delocalized orbitals that expand mainly over the perylene core of the molecule. Its ambipolar behavior [209], its high stability against oxidation at elevated temperatures, as well as its ability to form ordered films [40, 52] on different substrates make it a promising candidate for organic optoelectronic devices. This molecule has been studied over the last decade in thin films [31, 52, 92, 126, 212] and monolayers on noble metal surfaces [39, 103, 155].

In bulk, two phases are found depending on the temperature. Both the low temperature, α-phase, and the high temperature, β-phase, have a herringbone type structure. The α-phase is triclinic with a unit cell volume that is the double of the monoclinic β-phase. An enantiotropic polymorphic phase transformation has been reported at $\sim$ 400 K [94].

The DIP molecular structure is very similar to the PTCDA (3,4,9,10-perylene tetracarboxylic) molecule studied in Chapter 6. Both molecules are composed of a central perylene core but PTCDA is ended with polar groups (anhydride). For this reason the molecule-molecule interaction in DIP phases is expected to be smaller than in PTCDA and only driven by van der Waals interactions between DIP molecules.

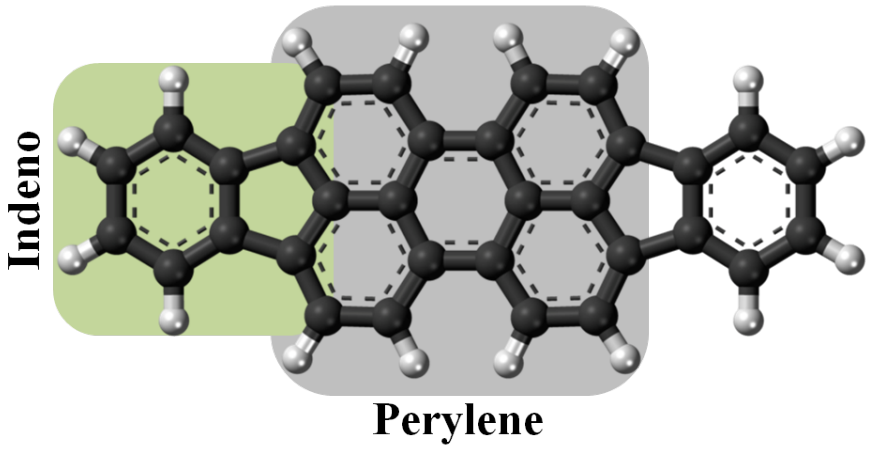

FIGURE 7.1: Schematic representation of the DIP molecular structure where carbon atoms are represented in black and hydrogen atoms in white. The perylene central core as well as the indeno end group are indicated.

The HOMO and LUMO of the DIP molecule have been calculated with the hybrid functional B3LYP in a triple basis set with polarization functions TZVP and are presented in Figure 7.2 [93]. The frontier orbitals are orbitals extending over the entire molecular area with the various lobes of the electronic wave functions typically delocalized over two neighboring carbon atoms. Both, HOMO and LUMO, present a central node along its long axis and are quite similar to the PTCDA ones. The obtained gap represented by the HOMO-LUMO energy difference is 1.47 eV [161].

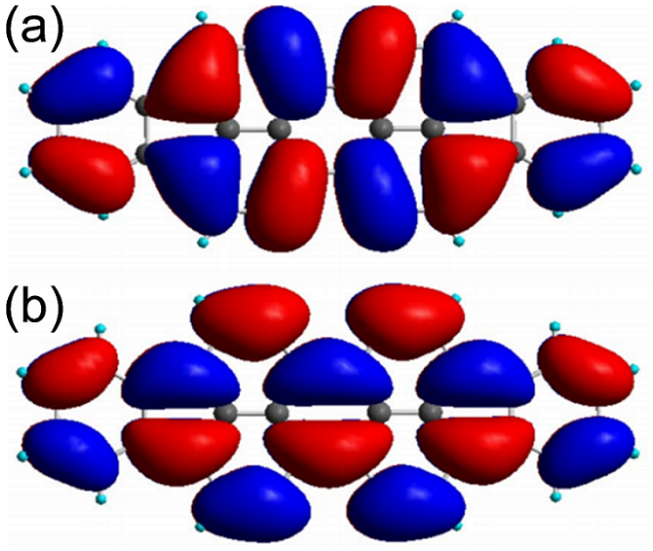

FIGURE 7.2: (a) HOMO and (b) LUMO of DIP calculated with B3LYP/TZVP. Figure adapted from [93].

The DIP Molecule on Surfaces

Depending on the molecule-substrate interaction diindenoperylene molecules stand upright, as on SiO_2 [52, 92, 237] and rubrene [126], or lie flat as happen on various metal surfaces as gold [12, 26, 32, 33, 39, 51, 155], silver [26, 103], and copper [26, 40, 42, 170, 238]. Bürker et al. have recently studied the adsorption of DIP on three different noble metal surfaces by measuring the molecule-substrate distance experimentally and by DFT calculation on Cu(111), Ag(111) and Au(111) [26]. The molecule-substrate distance on the Cu(111) was measured by normal-incidence X-ray standing wave (XSW), for coverages between 0.3 and 0.9 ML, obtaining a value of 2.51 ± 0.03 Å and calculated by DFT as 2.59 Å [26]. They have found that the vertical DIP position weakly depends on the surface coverage what they have also confirmed by DFT calculations [26]. The trend of the molecule-substrate interaction is Cu(111) > Ag(111) > Au(111), that is the same trend than the obtained for the PTCDA on the three same surfaces [48].

Different phases have been found depending on the surface orientation as observed on Au(100), Au(110) and Au(111) surfaces [32]. The molecular deposition rate has been also demonstrated to be an important factor, for example on the Ag(111) surface DIP molecules form a herringbone or brick-wall superstructure at $\sim$ 0.05 ML/min and $\sim$ 0.2 ML/min respectively [103].

On the DIP/Cu(111) system Oteyza et al. have reported by STM that the structure depends on the copper terrace size [40]. On wide terraces ($\geq$ 15 nm), molecules form a short-range (SR) ordering where molecules are oriented along three directions related by 60° rotations and thus clearly dictated by the hexagonal substrate symmetry. On narrow terraces ($<$ 15 nm), where the confinement enhance the step edge effect, long-range ordered phases (LR) are formed with an oblique unit cell ($\mathbf{a}$ = 0.87 ± 0.04 nm, $\mathbf{b}$ = 1.85 ± 0.07 nm and γ = 71 ± 1°).

7.3 Experimental Details

Experiments were performed at room temperature in a commercial STM/FM-AFM (Specs Gmbh) in an ultra-high-vacuum chamber and a base pressure of 1×10^{-10} mbar. For the image processing the freeware WSxM program has been used [101].

The Cu(111) single crystal (Matek GmbH, Germany) was prepared by repeated cycles of Ar^+ sputtering (0.6 keV, 10 mA) plus annealing at 240°C. After check the surface quality by STM, DIP molecules (Sigma Aldrich) were sublimated from a Knudsen cell at 225°C with a deposition rate of 0.05 ML/min. During deposition the substrate was kept at room temperature. The molecules were purified twice by gradient thermal annealing before introduced in the system and subsequently degassed in the UHV chamber.

7.4 Theoretical DIP Structures on Cu(111)

In this section, first principle calculations of a single molecule and a monolayer of DIP on the Cu(111) surface are presented. These calculations have been performed by Hazem Aldahhak, Dr. Eva Rauls and Prof. Wolf Gero Schmidt from the University of Paderborn (Germany) using the Vienna ab initio simulation package (VASP) implementation of DFT. More details about the methodology are given in Ref. [4].

Single Molecule Adsorption

The most stable adsorption geometry of a single DIP molecule on the Cu(111) surface was calculated by DFT and is presented in Figure 7.3. DIP molecules adsorb parallel to the surface, but not completely flat. When the center of the molecule is located over a hollow site, the long axis of the molecule is aligned parallel to one of the three equivalent ⟨112⟩ orientations of Cu(111) as can be observed in Figure 7.3(a). Defining the height of the molecule center as the average between d_1 and d_2 (see Figure 7.3(b)) the obtained value, 2.51 Å, fits perfectly well with the experimentally obtained by Bürker and co-workers [26]. Both sides of the molecule are lifted upwards by 0.42 Å (d_3) and 0.12 Å (d_4) resulting in a slightly concave and asymmetric adsorption as can be observed in the side view representation (Figure 7.3(b)). The adsorption energy of the structure presented in Figure 7.3 is -4.84 eV. This high value implies a strong molecule-substrate interaction. However, when the center of the molecule is located in a top position the long axis of the molecule is aligned parallel to one of the three equivalent ⟨110⟩ orientations of Cu(111). The adsorption energy is then -4.72 eV.

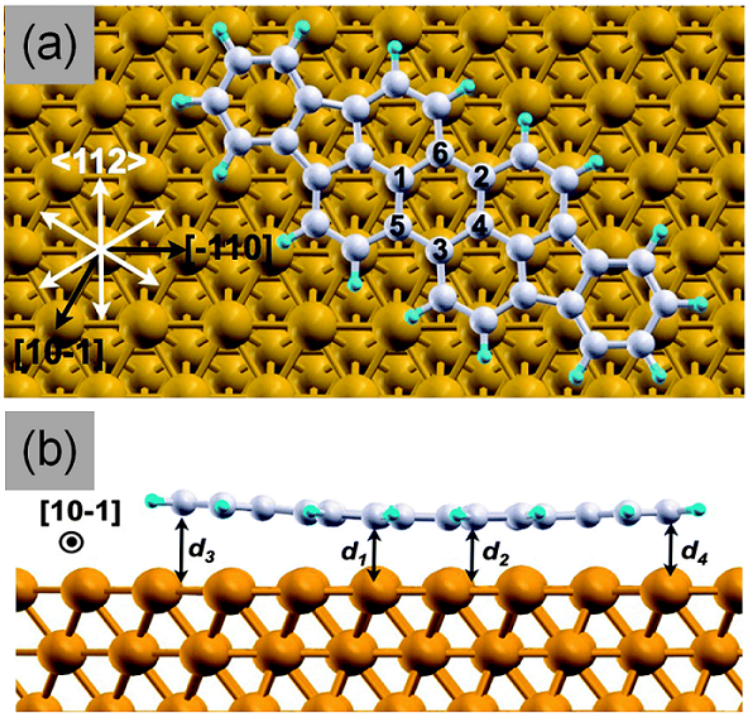

FIGURE 7.3: (a) Top and (b) side view of the most favored structure of single DIP molecules on Cu(111) calculated by DFT. In (b) are represented the vertical distances: $d_1 = 2.54$ Å, $d_2 = 2.48$ Å, $d_3 = 2.93$ Å and $d_4 = 2.63$ Å. Figure adapted from ref [4].

In order to evaluate the mobility of the DIP molecules on the Cu(111) surface the diffusion barrier was determined by calculating the potential energy surfaces. In spite of the strong molecule-surface interaction the calculated potential energy surfaces show a small corrugation of 0.35 eV, meaning that DIP molecules are quite mobile.

Molecular Monolayer

The influence of the intermolecular interactions has been evaluated by calculating the adsorption energies of DIP in different supramolecular arrangements. In most cases, molecule-molecule interactions increase the adsorption energy and, thus, stabilize the molecular aggregates. Structures which are closer to the experimentally observed [40] are obtained and the most stable are the two oblique cells represented in Figures 7.4(a) and (b), labeled A and B respectively. The parameters are $A_1 = B_1 = 8.77$ Å, $A_2 = B_2 = 16.82$ Å and $\beta = 97.77°$ (black arrows in Figures 7.4(a) and (b)) and the molecular density is 0.68 molecules/nm^2. The unit cell of both structures is indicated with white arrows in Figure 7.4(a)

and the parameters are **a** = 8.77 Å, **b** = 17.89 Å and $\theta = 69.69°$. The registry of each molecule is almost similar to that of the single molecule, while the long axis (LA) deviates by 10° from the $[1\bar{1}2]$ direction of the surface in order to avoid the repulsion between the hydrogen atoms of neighboring molecules. This causes adjacent molecules to have their centers shifted along the long axis with respect to each other. Phase A and phase B have the same unit cell dimensions, but differ with respect to the orientation of the molecules within it. The adsorption energies are -5.63 eV for phase A and -5.76 eV for phase B.

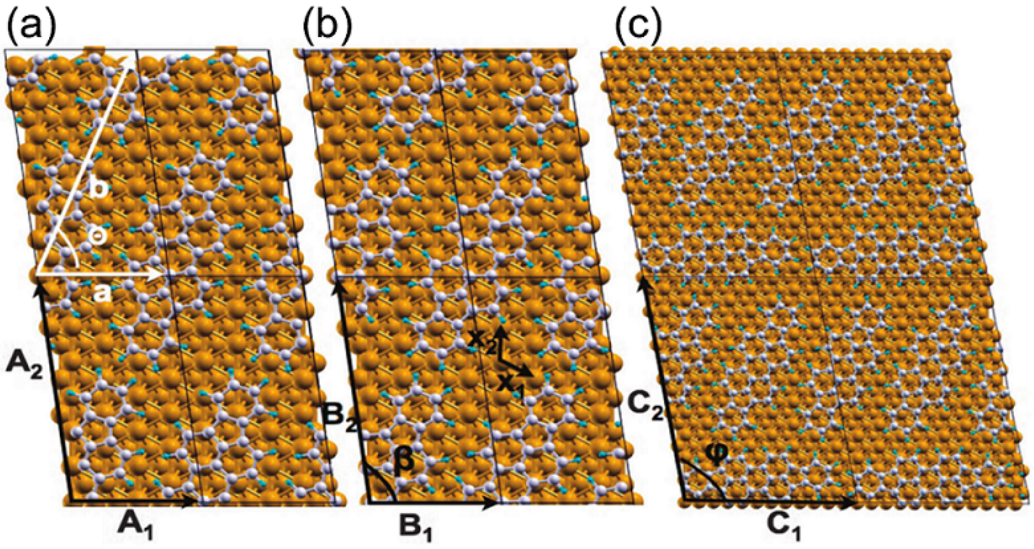

FIGURE 7.4: Representation of the two most stable oblique phases that have been found for the long-range order arrangement: (a) phase A and (b) phase B. The parameters are $A_1 = B_1 = 8.77$ Å, $A_2 = B_2 = 16.82$ Å and $\beta = 97.77°$. (c) Representation of the short-range order phase with a primitive unit cell parameters $C_1 = 17.61$ Å, $C_2 = 25.83$ Å, $\varphi = 99.96°$. Figure adapted from Ref. [4].

The molecule-molecule interactions gain importance in these structures while the molecule-surface interactions are reduced compared with the single molecule adsorption. The calculated values are presented in Table 7.1. When the influence of the intermolecular interactions are taken into account in the calculations and a monolayer is formed, the vertical molecule-surface distance is enlarged slightly to 2.90 Å where molecules lie flat in an almost planar geometry.

The short-range ordering reported experimentally [40] was also calculated in a model comprising three molecules per unit cell. Two of them are arranged side-by-side with their long axis parallel to each other while the third is rotated by 60° with respect to them. The individual molecules in the primitive unit cell have

almost the registries of the molecules in the long-range order, while their long axis are along two of the three equivalent ⟨112⟩ orientations of the surface as can be observed in Figure 7.4(c). The primitive unit cell is indicated in Figure 7.4(c) with the following parameters: C_1 = 17.61 Å, C_2 = 25.83 Åand φ = 99.96° and the molecular density is 0.66 molecules/nm^2, in agreement with the value reported by Oteyza et al. [40]. The short-range order is slightly less dense than the LR order. The adsorption energy per molecule in this structure is -5.47 eV and the adsorption energy per molecule, as well as the contributions of the molecule-surface and molecule-molecule for the three phases are presented in Table 7.1. The short-range phase is energetically slightly less stable than the two most stable long-range but due to the small adsorption difference both are expected to coexist in large terraces or at least long-range order islands should be formed experimentally in co-existence with the short-range orders. Note that, however, in previous STM observations of the DIP/Cu(111) system, as already mentioned, only short-range domains were observed on wide terraces [40].

TABLE 7.1: Adsorption energies per molecule for the two most stable LR phases (A and B) and the SR order and the contributions from the molecule-surface and molecule-molecule interactions.

	Phase A	Phase B	Short-range
E_{ads} (eV)	-5.63	-5.76	-5.47
Molecule-surface contribution (eV)	-4.47	-4.50	-4.48
Molecule-molecule contribution (eV)	-1.16	-1.26	-0.99

7.5 Experimental Study of DIP on Cu(111)

7.5.1 DIP Phases on Cu(111)

The early stage of DIP growth on Cu(111) reveals that molecules nucleate in the step edges as can be observed in the topographic STM image presented in Figure 7.5 where some molecules are highlighted with blue arrows. Each molecule shows an oval shape. DIP molecules nucleate flat along both step edges, with non-clear preferential orientation, while mobile molecules are adsorbed on the terraces.

After the evaporation of ∼ 1ML of DIP on the Cu(111) surface, molecules lie flat and self-assemble forming different phases as can be observed in the topographic STM images presented in Figure 7.6. Short- and long-range ordered domains

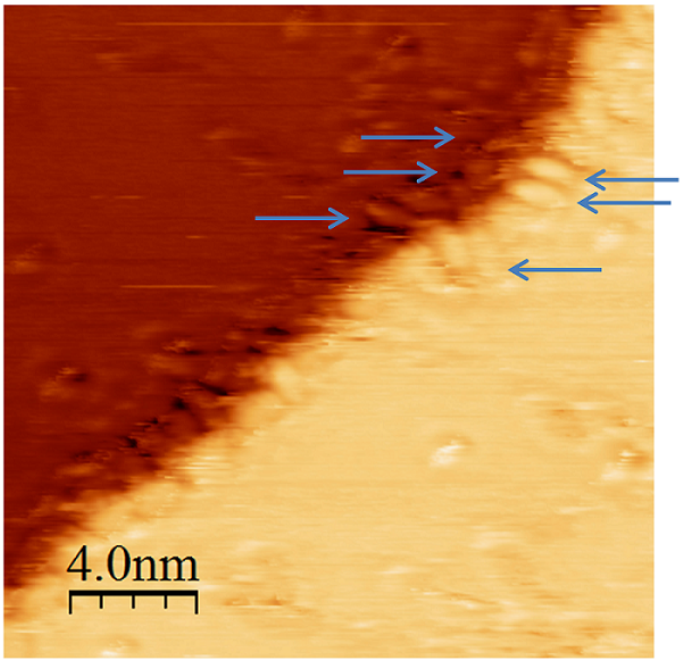

FIGURE 7.5: Topographic STM image of the early stage growth of DIP on Cu(111). Some molecules in the step edges are highlighted with blue arrows. Parameters: I = 75 pA, Bias = +0.660 V and A = 200 pm.

are found. In the large STM image presented in Figure 7.6(a) molecules are not resolved but it is possible to distinguish some areas with a homogeneous pattern that corresponds to long-range domains. In Figure 7.6(b) three long-range ordered domains, indicated with black boxes, are resolved. These areas are surrounded by short-range ordered domains exhibiting different packing. In the STM images presented in Figures 7.6(c)-(d) (smaller area), the coexistence of short- and long-range ordered domains on large terraces is again demonstrated and this time they coexist with a two-dimensional gas phase. In Figure 7.6(c) an oblique phase is observed at the bottom right side of the image and in Figure 7.6(d) a rectangular phase is observed at the top left side. The presence of areas of mobile molecules is indicative that the complete monolayer is not reached.

Both long-range structures, rectangular and oblique, are often found and always surrounded by short-range ordered domains. These observations disagree with previous STM studies where in large copper terraces only short-range domains were found [40] and agree with the DFT calculations previously introduced. The prepared Cu(111) surface used in this study presents large terraces ($\sim$ 100 nm). However, effects generated by the step edges in the growing of DIP structures have not been observed, i.e. ordered domains are observed in the step edges and far from them. Only an initial growth was observed to start preferentially at the

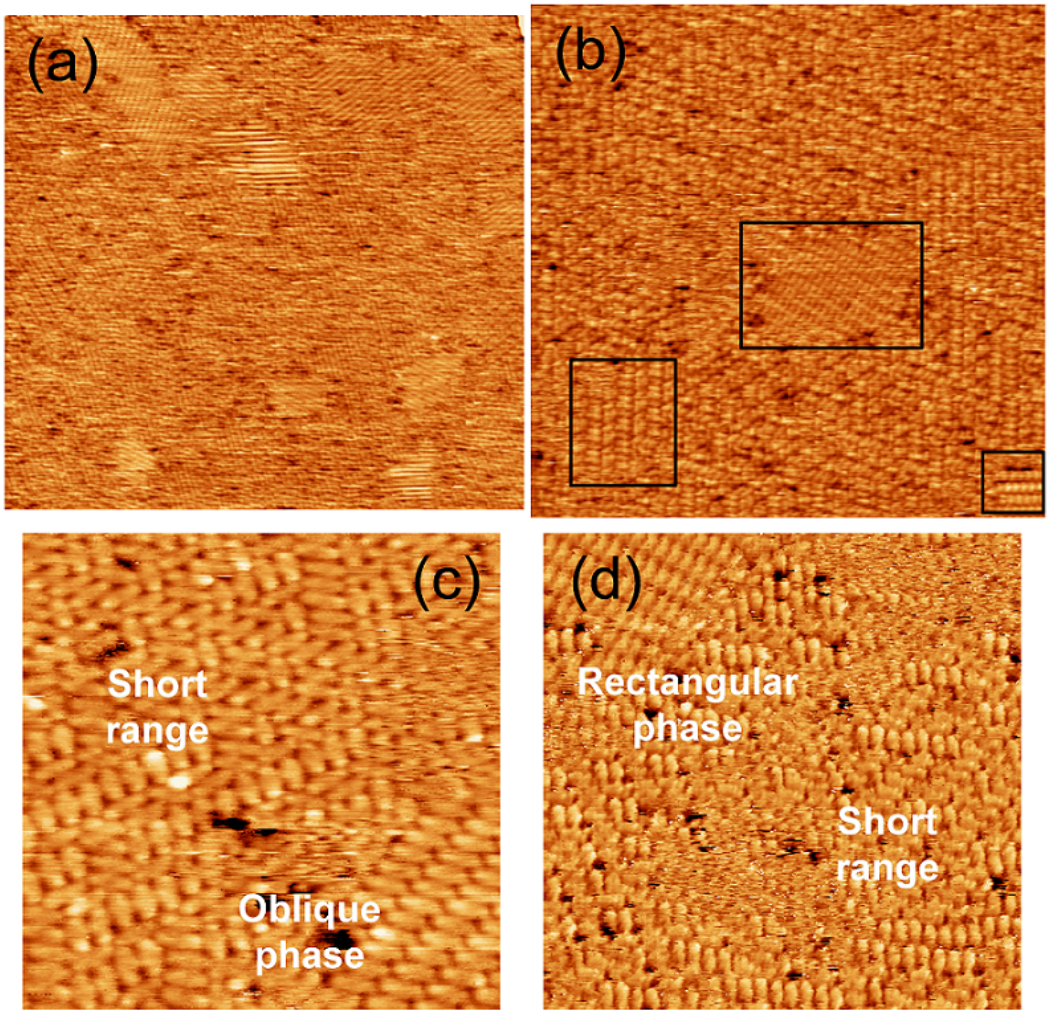

FIGURE 7.6: Topographic STM images of ∼ 1 ML of DIP on Cu(111). In (b) three long ordered domains are highlighted with black boxes. In (c) and (d) short-range, oblique and rectangular phases are indicated. Parameters: (a) 125 nm x 120 nm, I = 270 pA, Bias = +0.325 V, A = 200 pm, (b) 50 nm x 50 nm, I = 270 pA, Bias = +0.325 V, A = 200 pm, (c) 15 nm x 15 nm, I = 130 pA, Bias = -1.250 V, A = 200 pm and (d) 30 nm x 30 nm, I = 370 pA, Bias = -0.370 V, A = 200 pm.

step edges. In the following, the short-range, oblique and rectangular phases are described.

Short Ordered Domains

The short-range order structure is formed by molecules oriented along three directions related by 60° rotation as can be observed in Figure 7.7. In Figure 7.7(a) rows formed by the side-by-side stacking of adjacent co-directionally oriented molecules are observed along three directions and the three molecular packing directions are

indicated by black lines and labeled as **a**, **b** and **c**. In Figures 7.7(b) and (c) the simultaneously acquired frequency shift and excitation channels are presented. The interpretation of this data is not straightforward since the tip-sample distance is kept to constant tunneling current by the STM feedback. To help with the interpretation, over the three simultaneous images (topography, frequency shift and excitation) three long molecular axis and two DIP molecules are overlaid at the same position. The frequency shift image does not present a homogeneous contrast even in the marked rows where molecules are parallel adsorbed. The excitation image shows a more homogeneous contrast and the borders of each molecule appear slightly lighter meaning a higher excitation signal. This contrast is more clearly observed in the row labeled as **b** and this can be due to a tip asymmetry.

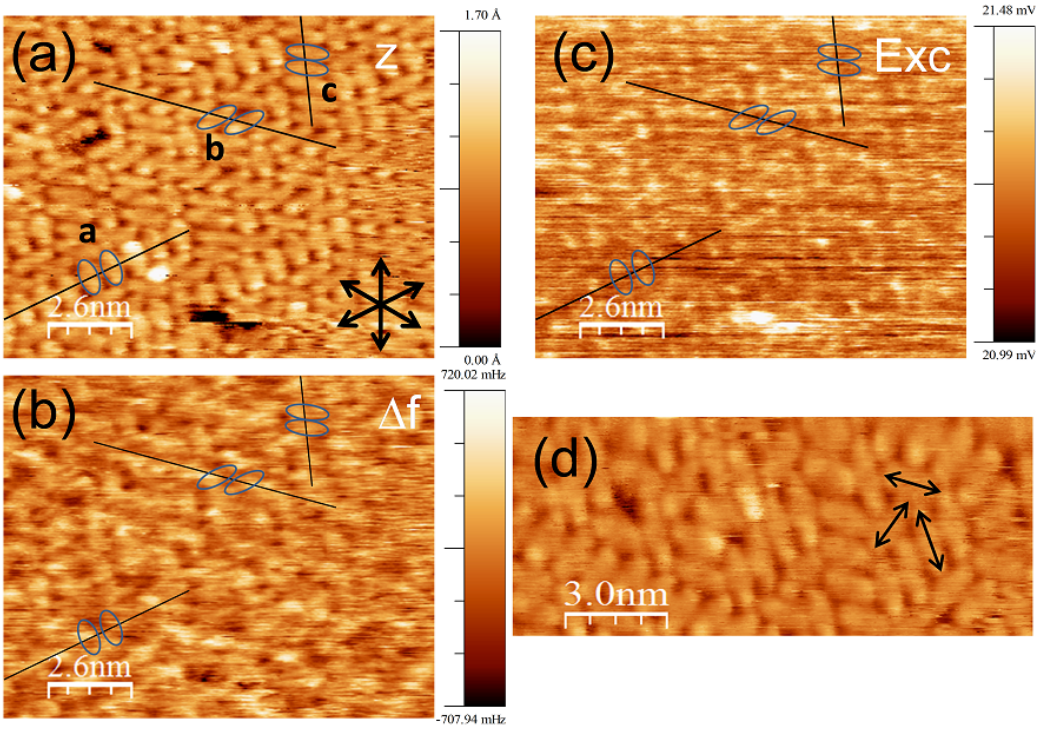

FIGURE 7.7: Topographic STM image of $\sim$ 1 ML of DIP on Cu(111) and the simultaneous (b) frequency shift and (c) excitation channels. In the three images, the three molecular packing directions are indicated by black lines (labeled as **a**, **b** and **c**) as well as two molecules per row by blue ovals. The $\langle 110 \rangle$ substrate directions are indicated in (a) by black arrows. (d) Topographic STM image where the long axis of three DIP molecules, which are 60° rotated, are indicated. Parameters: I = 130 pA, Bias = -1.250 V and A = 200 pm.

The molecular side-by-side distance of the rows labeled as **a** and **b** in Figure 7.7(a) is 9.02 $\pm$ 0.05 Å while in row **c** is 6.24 $\pm$ 0.08 Å. This difference can be attributed to a thermal drift effect. The DFT calculations presented in the last sections predicts a model of the SR with a unit cell C_1 and C_2 (see Figure 7.4(c)). The

side-by-side distance of the rows is calculated as 8.80 Å (C_1 / 2 molecules) and this value is in good agreement with the experimentally determined for rows **a** and **b**. In Figure 7.7(d) another STM image of the short-range phase is presented. The long axis of three molecules are indicated by black arrows and correspond to the ⟨112⟩ substrate direction in agreement with the DFT calculations presented in the last section.

Oblique Phase

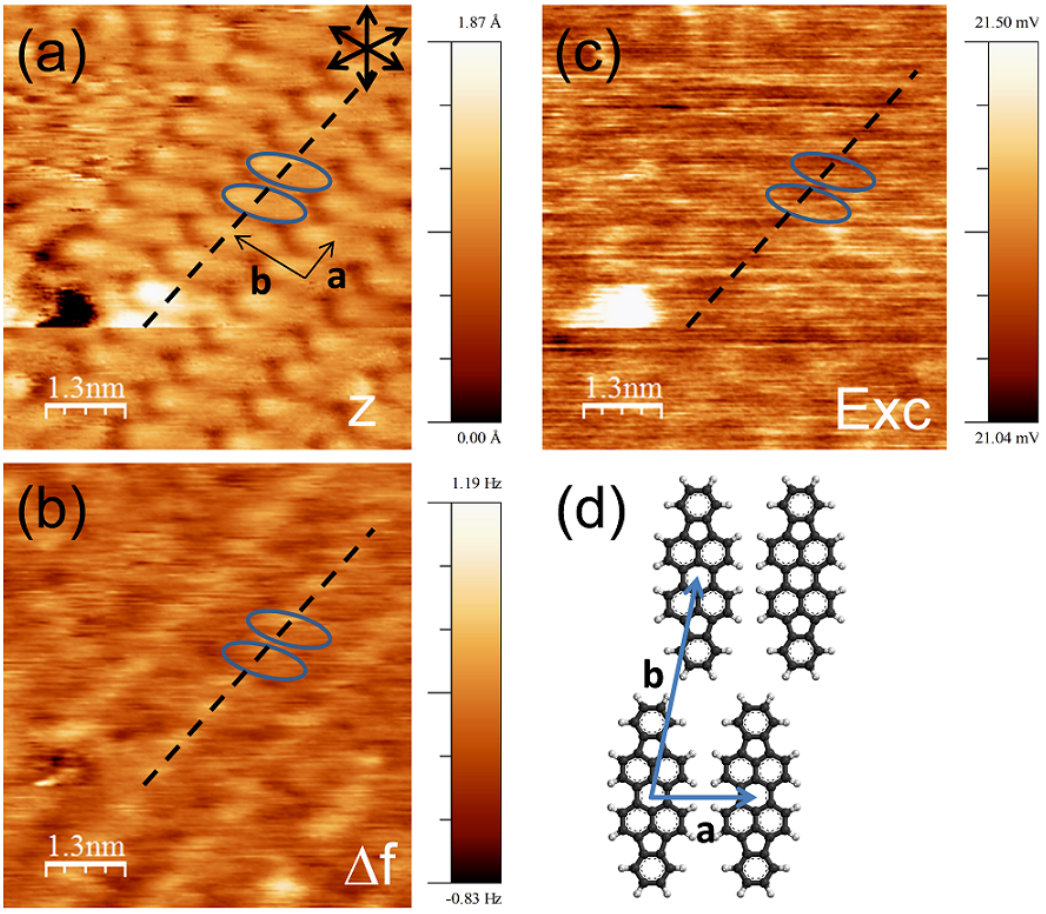

FIGURE 7.8: (a) Topographic STM image of the oblique phase, (b) the simultaneously frequency shift and (c) excitation channels. In the three images two molecules, schematically represented by blue ovals, are overlaid. The ⟨110⟩ substrate directions are indicated in (a) by black arrows. (d) Schematic representation of the oblique unit cell (**a** = 8.8 ± 0.4 Å, **b** = 17.5 ± 0.3 Å and $\beta \sim 80°$). **a** is oriented along the ⟨112⟩. Parameters: I = 130 pA, Bias = -1.250 V and A = 200 pm.

In Figures 7.8(a)-(c) a topographic STM image of the oblique phase and its simultaneous frequency shift and excitation images are presented. In Figure 7.8(a) the

unit cell, indicated by black arrows, is $\mathbf{a} = 8.8 \pm 0.4$ Å, $\mathbf{b} = 17.5 \pm 0.3$ Å and $\beta \sim 80°$ where $\mathbf{a}$ is oriented along the $\langle 112 \rangle$ as is schematically represented in Figure 7.8(d). These values are in good agreement, within a 10% of experimental error, with the reported by Oteyza et al. [40] and the obtained by DFT and presented in last section. The molecular density is 0.65 molecules/nm^2. The long axis of the DIP molecules has been predicted by DFT calculations to be 10° deviated from the $\langle 112 \rangle$, consistent with the observed in Figure 7.8(a). This phase has been observed with their molecular long axis oriented along the $\langle 110 \rangle$ and $\langle 112 \rangle$ as will be discuss in the next subsection.

The frequency shift image (Figure 7.8(b)) shows a more homogeneous contrast compared with Figure 7.7(b). A slightly more repulsive interaction, more positive frequency shift value, is observed over the center of the DIP molecules. The same contrast is observed for all the parallel molecules of one row creating a line as it is indicated by a black dash line. This contrast in the frequency shift image is not observed in the rows of the short order domains. As mentioned before the interpretation of the simultaneous channels when measuring in STM feedback mode is not straightforward and it is even more complicated when tip-ended materials and tunnel parameters (tunneling current and bias) are changed. Both images, Figure 7.7(a) and Figure 7.8(a), are zooms of the image presented in Figure 7.6(c). It means that the setpoint is the same and the tip-ended material can be assumed to be the same since a tip change was not detected. Then, the different contrast in the frequency shift image is not expected to be due to tip changes or tunnel conditions and could be attributed to a different molecular configuration. In the excitation image of the oblique phase, Figure 7.8(c), the edges of the DIP molecules appear with a slightly higher excitation, this contrast is similar than the observed in the short-range phase (Figure 7.7(c)).

In some high-resolution STM images, as the one shown in Figure 7.9, a non completely flat molecular adsorption is observed. This contrast is more clearly seen in the zoom image presented in Figure 7.9(b). In this image, a long-range ordered domain coexists with a 2D gas phase. The apparent height over the molecule is not constant, and one of the sides of the molecule, the marked with an arrow in Figure 7.9(b), appears higher. In Figures 7.9(c) and (d) the simultaneously frequency shift and excitation channels are presented and in the three images, topography, frequency shift and excitation channels, a schematic DIP molecule is overlaid. In the areas between DIP molecules and parallel to the molecular long

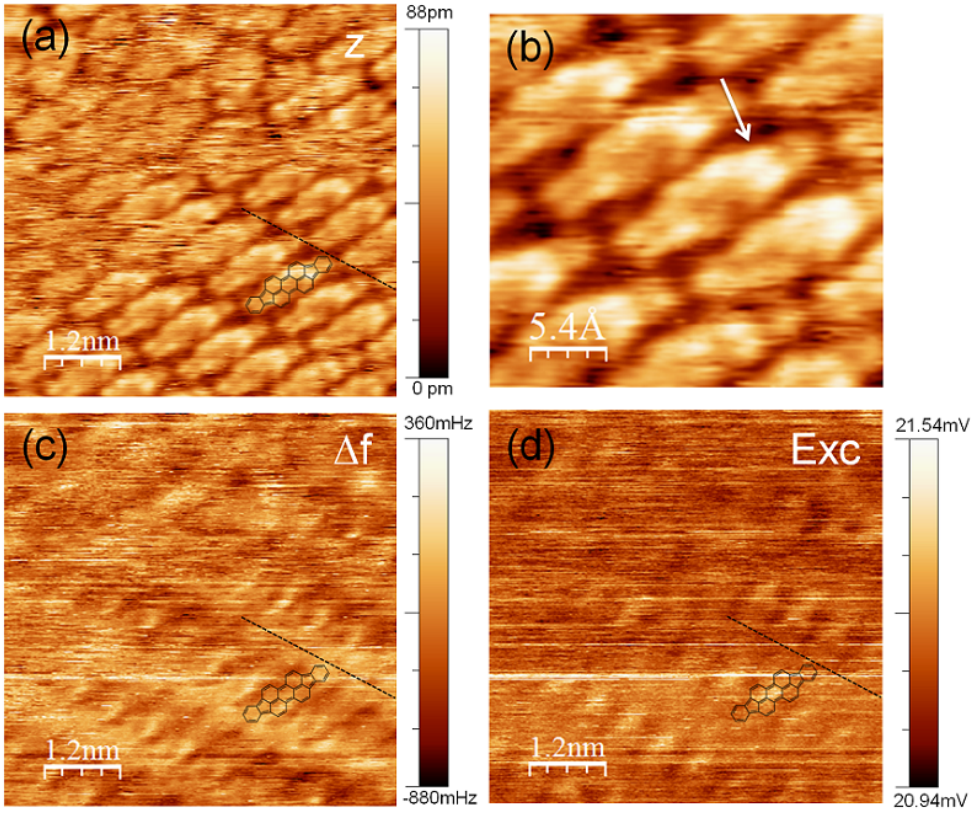

FIGURE 7.9: (a) Topographic STM image of the oblique phase and (b) is a zoom of the bottom right area. (c) and (d) are its simultaneously frequency and excitation channels. A DIP molecule is overlaid in the three images. Parameters: I = 465 pA, Bias = -1.430 V and A = 200 pm.

axis a more attractive force (more negative frequency shift) is recorded while over the molecules a more repulsive force is measured, particularly at the edges (indeno groups). The excitation image shows a higher value in the center of the molecule indicating a more non-conservative interaction. The molecular resolution obtained in this image indicates that the tip ended material is different regarding the last presented images (Figures 7.7 and 7.8) and this can be the reason for the different frequency shift and excitation differences.

Rectangular Phase

By last a rectangular phase will be introduced which has not been previously observed in the DIP/Cu(111) system. In Figure 7.10(a) an example of topographic STM image of this structure is presented, together with its simultaneously frequency shift (b) and excitation (c) images. The appearance of the molecules forming this structure is slightly different from the rest and molecules are imaged

with a more rectangular shape. The long axis of the molecules is oriented along the ⟨112⟩ substrate directions, differently than DIP in the oblique cell. The rectangular unit cell size is **a** = 10.0 ± 0.2 Å, **b** = 19.3 ± 0.6 Å and $\beta \sim 90°$), where **a** is oriented along the ⟨110⟩ substrate directions. A schematic representation is presented in Figure 7.10(d). The molecular density is 0.52 molecules/nm^2 that is less dense than the oblique phase.

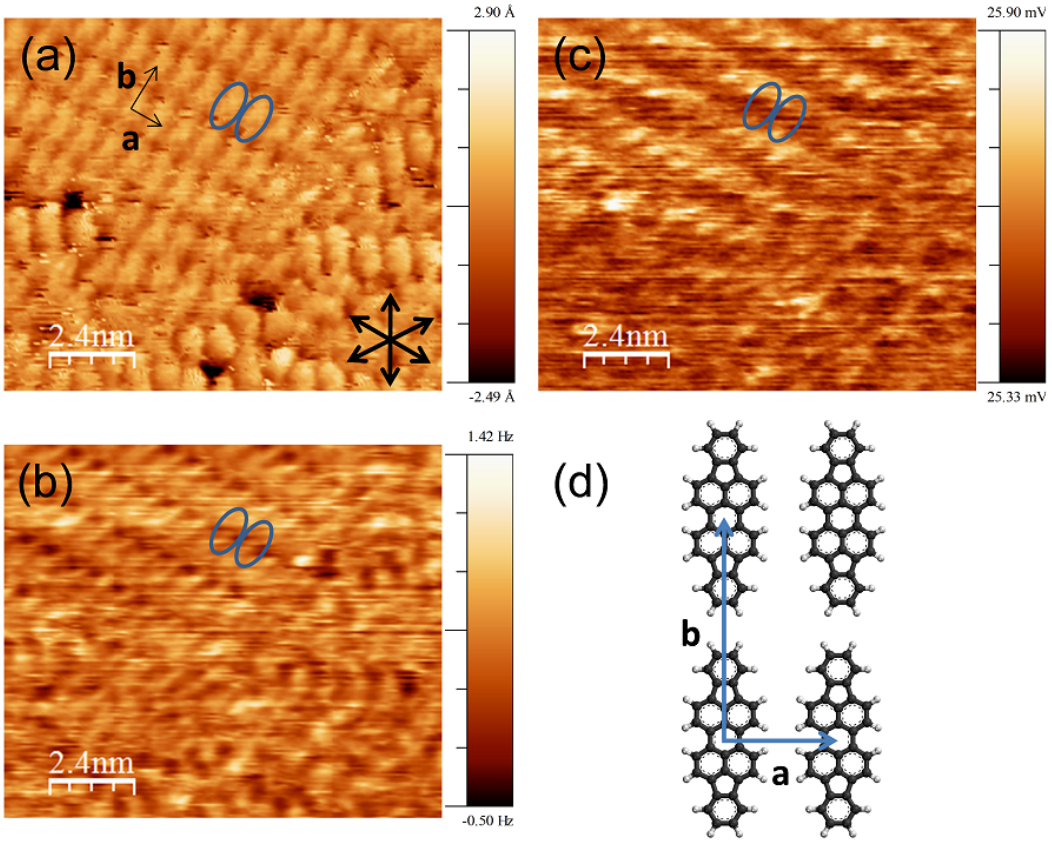

FIGURE 7.10: (a) Topographic STM image of the rectangular phase, (b) the simultaneously frequency shift and (c) excitation channels. In the three images two molecules, schematically represented by blue ovals, are overlaid. The ⟨110⟩ substrate directions are indicated in (a) by black arrows. (d) Schematic representation of the oblique unit cell (**a** = 10.0 ± 0.2 Å, **b** = 19.3 ± 0.6 Å and $\beta \sim 90°$). **a** is oriented along the ⟨110⟩ substrate direction. Parameters: I = 370 pA, Bias = -0.370 V, A = 200 pm.

The simultaneous frequency shift (Figure 7.10(b)) and excitation images (Figure 7.10(c)) are quite different from the previously presented. To help with the interpretation two molecules, represented by blue ovals, are overlaid on the three images. The apparent molecular orientation that can be extracted from the frequency shift and excitation images does not correspond with the observed in the topography. The frequency shift of the area that corresponds to a molecule is not uniform and present a central depression with a more negative frequency shift

value (more attractive interaction) and this central depression is also observed in the excitation image. A possible explanation for these complex images is that molecules are not adsorbed in a completely planar configuration.

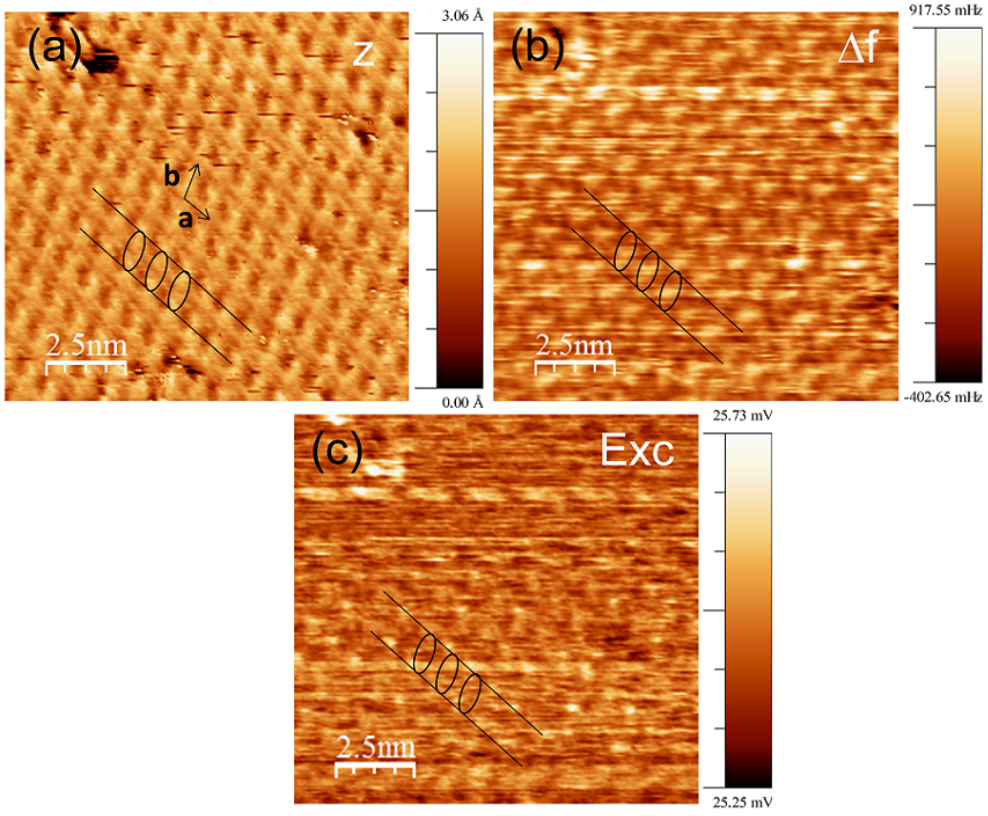

FIGURE 7.11: (a) Topographic STM image of the rectangular phase and the simultaneous (b) frequency shift and (c) excitation channels. The unit cell is overlaid in (a). Three DIP molecules and two lines are overlaid in the three images. Parameters: I = 365 pA, Bias = +0.330 V and A = 200 pm.

A last series of topographic STM, frequency shift and excitation of the rectangular phase are presented in Figure 7.11. The contrast observed in the frequency shift and excitation images of this phase was already mentioned in Figure 7.10 but here the appearance of the molecules is quite different from the one presented in Figure 7.10(a). The different appearance can be attributed to a different tip-ended material and/or geometry. While in Figure 7.10(a) each molecule appears with a rectangular shape, here (Figure 7.11(a)) each molecule is imaged with an oval shape. The most interesting fact is that the center of parallel molecules seems to be "connected" in the topographic image, while it is not observed on the others channels. The center of the molecule appears in frequency shift with a more positive value, i.e. a more repulsive interaction and in excitation with a higher value. It means that when the tip is positioned over the center of the

molecule and adjusts the tip-sample distance to keep constant tunneling current, the tip-sample interaction is more repulsive and dissipative than over the rest of the molecule. Between parallel molecules, the apparent height is approximately the same than over the center but the interaction is quite different. The frequency shift reveals now a more attractive force and the excitation channel a less dissipative interaction.

In this section we have presented several topographical STM images with a great variety of frequency shift and excitation contrast that depends on the molecular arrangement and tip. We have suggested that DIP molecules are arranged in different configurations however a more systematic study combined with theoretical calculations would be needed to elucidate its origin.

7.5.2 Stability of the Long-Range Ordered Phases

Once the three observed phases have been presented, the relative stability of two oblique domains is discussed in the following. In Figures 7.12(a)-(c) three consecutive STM images are presented. In Figure 7.12(a) two long-range domains, named as I- and II-type, are circled with continuous green line and with blue dotted line respectively. The I-type domain corresponds to the oblique phase, it is not located in the step edge and is surrounded by a region with short-range order and with mobile molecules. The DIP long axis is aligned along one of the $\langle 112 \rangle$ substrate directions. At the step edge of the lower terrace another oblique domain is visible, labeled as II-type, which is 30° rotated with respect to domain I and has therefore the long axis of DIP aligned along one of the $\langle 110 \rangle$ directions. The two domains observed in (a) are zoomed in (d) and (e) where the unit cells are marked. The DFT calculations of single DIP molecules, presented before, concluded that the most favorable orientation is along the $\langle 112 \rangle$ substrate directions. However, the different stability with molecules aligned along the $\langle 110 \rangle$ substrate directions is small.

Consecutive scanning in the same area shows tip-induced ordering with two main effects: (i) increased area of domain I and growth of other domains equally oriented at expenses of regions with mobile molecules, and (ii) reduction and disappearance of the domain II giving rise to SR order. Although for these growth conditions, ordered domains can be formed by DIP following the $\langle 110 \rangle$ directions (II-type)

what has been calculated by DFT as to be less stable, and from the presented results it is possible to conclude that such orientation is metastable.

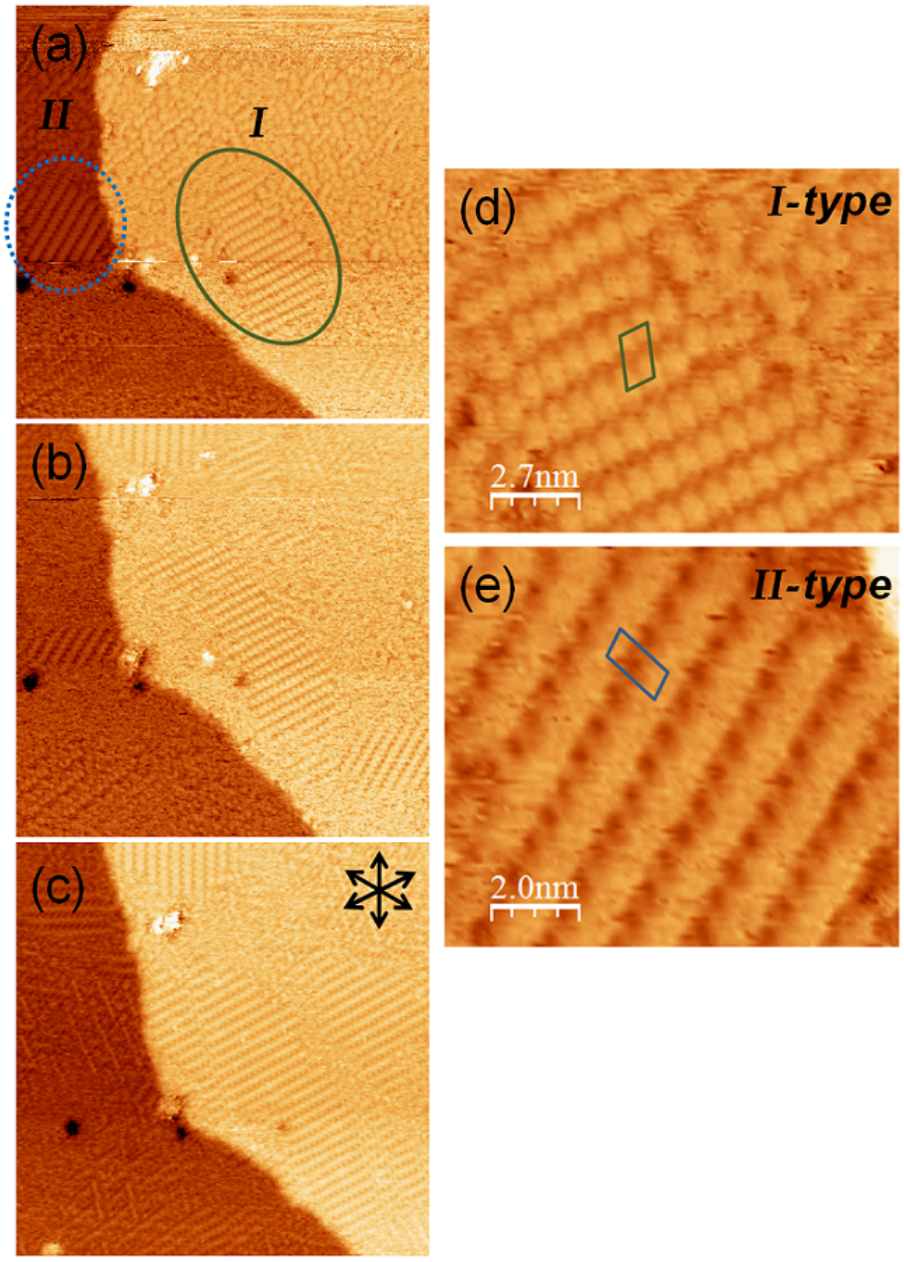

FIGURE 7.12: (a)-(c) Consecutive topographic STM images of the same area. The long range domains I and II are circled with a continuous green line and with dotted blue line respectively. Consecutive tip scanning causes an increase of long-range ordering of I-type domains (circled with a green continuous line) and the disappearance of II-type domains (circled with a dotted blue line). The ⟨110⟩ substrate directions are indicated in (c) by black arrows. (d) and (e) are a zoom of the I and II domains in (a). The unit cell is marked in both. Parameters: 50 nm × 50 nm, I = 90 pA, Bias = -0.450 V and A = 200 pm.

As mentioned before, Oteyza et al. have studied the DIP/Cu(111) system and observed only short-range ordered domains on large terraces (> 15 nm) [40]. In the

results presented here (large copper terraces) both short- and long-range ordered domains are observed. The different results between these two studies can be attributed to the different molecule evaporation conditions and due to a slightly smaller coverage in the present work. In the study presented here the evaporation rate is 0.05 ML/min while Oteyza et al. have used 0.10 ML/min [40]. Growth conditions have been previously demonstrated as to be a significant factor on the final DIP ordering in different systems [103]. Additionally, in the presented work the coverage is slightly smaller than the monolayer what is deduced by the existence of a two-dimensional gas phase of mobile molecules. This slightly smaller coverage yields to less compact and more mobile phases obtaining a greater variety of phases.

7.6 Electronic Study of DIP on Cu(111)

The molecule-molecule and molecule-substrate interactions not only determine the crystalline structure of organic layers, the electronic properties are also affected. When a monolayer of molecules are adsorbed on a metallic surface some interfacial effects, as for example "push back" effect and charge transfer, affect the final electronic properties. In the case of DIP molecules on Cu(111), a large interaction has been calculated by DFT where a large charge transfer (0.367 electrons/molecule) takes place from the molecule to the copper [42]. This charge transfer and the push back effect produce a surface dipole pointing towards the vacuum thus lowering the surface work function. The work function of a monolayer of DIP on Cu(111) has been measured experimentally (as the difference between the vacuum level and the Fermi level) by X-ray absorption spectroscopy, $\Delta\phi = \phi_{DIP} - \phi_{Cu(111)}$, of $\sim$ -1 eV [42]. This value is very similar to the obtained for other molecules with similar molecule-substrate interactions on Cu(111) such as benzene ($\Delta\phi$ = -1.05 eV) [228] or pentacene ($\Delta\phi$ = -0.90 eV) [125]. Contrary, in the PTCDA/Cu(111) system a smaller change was measured ($\Delta\phi$ = -0.15 eV) [48]. DIP and PTCDA have the same central group, perylene, but note that contrary to DIP, benzene or pentacene, PTCDA has two end polar groups that maximize the molecule-molecule interaction minimizing the molecule-substrate interaction.

Figure 7.13 shows a representative examples of contact potential difference (CPD) measurements performed on Cu(111), blue plot, and just after the evaporation of a monolayer of DIP molecules, green plot. Several CPD measurements were

performed on the clean copper and over the monolayer on various evaporations and the same CPD difference has been observed. In the example shown in Figure 7.13, the measured CPD value over Cu(111) is +266 ±1 mV and over DIP/Cu(111) -725 ±2 mV yielding a change in work function of -0.99 eV since:

$$\Delta\phi = e\Delta CPD \tag{7.1}$$

being e the elementary charge. This result is in complete agreement with previous experimental measurements by NEXAFS [42] and demonstrate the enormous utility of the technique employed here.

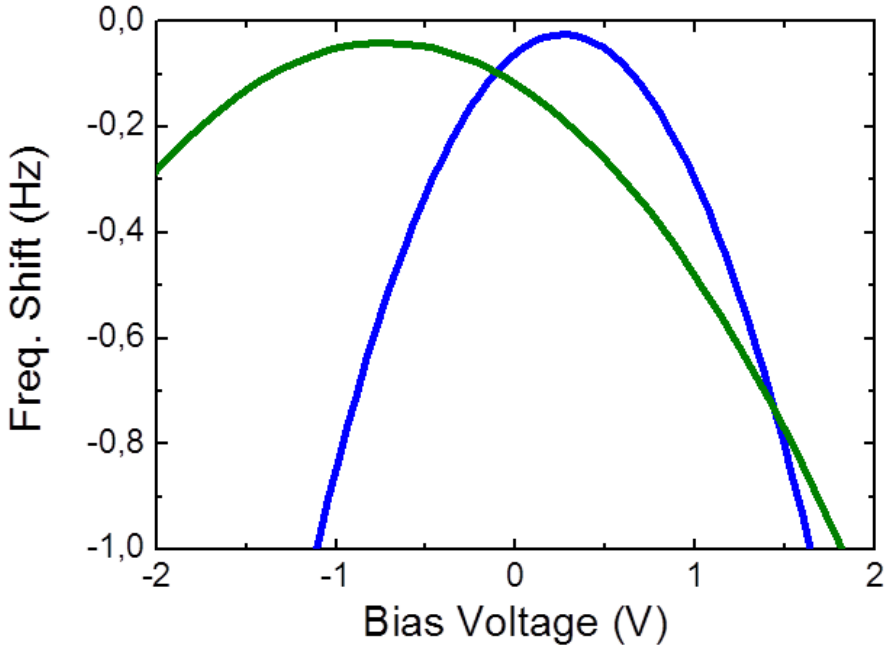

FIGURE 7.13: Frequency shift versus bias voltage collected over clean Cu(111) (blue plot), CPD = +266 ±1 mV, and over a monolayer of DIP on Cu(111) (green plot), CPD = -725 ±2 mV.

To detect tip changes between CPD measurements, is desirable to have the areas of study in the same sample allowing consecutive measurements. Unfortunately, it was not possible to get a semilayer of DIP molecules with areas of clean copper and areas with condensed molecular phases.

Note that the different parabola width of Figure 7.13(c) is due to different tip-sample distances. On the DIP monolayer to obtain stable spectra a higher tip-sample distance was needed. This could be a problem in non-homogeneous surfaces due to an average effect but it is not the case.

7.7 Conclusions

In this chapter the DIP/Cu(111) system has been studied by DFT calculations and experimentally using STM/FM-AFM in UHV conditions. DFT calculations of the adsorption of a single DIP molecule on the Cu(111) surface have revealed the most favorable configurations. When the center of the molecule is located over a hollow site of the surface, its long axis is aligned parallel to one of the $\langle 112 \rangle$ surface directions. In this configuration, the molecule is adsorbed parallel to the surface but not completely flat. The adsorption energy is -4.84 eV. When the center of the molecule is located in a top position, the most favorable configuration is with its long axis parallel to one of the $\langle 110 \rangle$ surfaces directions. The adsorption energy is -4.72 eV. The mobility of the DIP molecules has been evaluated by calculating the potential energy surfaces. Regardless of the strong molecule-surface interaction a small corrugation energy of 0.35 eV is obtained.

The molecular monolayer has also been studied by DFT. The two most favorable structures, and closer to previous STM observations, are two oblique phases with the same unit cell but different registry with the Cu(111) surface. In these phases, molecules have their long axes 10° deviated from the $\langle 112 \rangle$ substrate directions. The two oblique cells, labeled as phase A and B, have adsorption energies of -5.63 eV and -5.76 eV. A short-range structure has been also calculated. The long-axis are aligned along two of the three $\langle 112 \rangle$ surface directions. The adsorption energy per molecule is -5.47 eV. Based on these results, both phases (LR and SR) are expected to coexist.

Experimentally, the first stage of DIP growth on the Cu(111) surface, as well as the phases observed in a monolayer, have been studied by STM/FM-AFM. The first stage of growth has been determined as to start in the steps edges with non preferential orientation. When a ~ 1 ML of DIP is evaporated on Cu(111) different phases are formed. Both short- and long-range ordered domains, together with a mobile gas phase, have been observed. This is in agreement with the DFT calculations. Two long-range domains have been found: oblique and rectangular phases. The oblique cell fits well with the calculated values and the rectangular phase is a new one that has not been previously reported. Molecules of the SR have their long axis aligned along the three $\langle 112 \rangle$ surface directions and then are 60° rotated respect to each others. Molecules of the oblique phase also have their long axis along the $\langle 112 \rangle$ directions but the ones of the rectangular phase along

the ⟨110⟩ directions. A contrast in one of the extremes of the DIP molecules is observed in some topographic STM images of oblique domains. This contrast can be related with a non completely planar absorption of molecules on Cu(111) in agreement with DFT calculations.

The relative stability of two oblique phases, with molecules oriented along the ⟨110⟩ and ⟨112⟩, has been evaluated by the influence of continuous tip scanning. From these measurements it has been concluded that the ones with molecular long axis oriented along the ⟨110⟩ are metastable. Contrary, tip induces growth of the domains with its molecular long axis oriented along the ⟨112⟩ (oblique phase) as expenses of the others.

The measured work function difference between copper and a monolayer of DIP molecules has been measured by frequency shift vs. bias spectroscopy. The work function is lowered $\sim$ 1 eV when a monolayer of DIP is adsorbed on the Cu(111) surface, in excellent agreement with previous experimental measurements.

Chapter 8

Study of ClAlPc on Au(111)

8.1 Introduction

Phthalocyanines with permanent electrical dipole, perpendicular to their π-plane, are promising materials for organic devices with high stability in air [164, 196, 216]. These molecules can adopt two distinct electric dipole configurations, up and down, depending on whether their dipole moment is pointing to the substrate or vacuum, respectively. Unidirectional alignment of molecular dipoles can effectively modify the substrate work function and simulate the charge injection or collection at the molecule-electrode interface [204, 234].

An important issue in the energy level alignment of organic/metal interfaces is the influence of surface dipoles. Due to the complexity of organic/metal systems and the mixed origins of surface dipoles (charge transfer, electron rearrangement ...), the surface work function can be influenced in a non-trivial way by the orientation of the molecular electrical dipole. For these reasons, a molecular ordered layer with unidirectional dipoles is a good system in order to understand dipole surfaces effects. Another interesting question, rarely addressed, is how the molecular order and the work function evolves beyond the growth of the first monolayer.

In this chapter, the structural and electronic properties of a monolayer and a bilayer of chloroaluminum phthalocyanine (ClAlPc) on Au(111) are presented. The structure of the first and second layer has been determined by combined STM/FM-AFM in ultra high vacuum and at room temperature. The first layer is formed by unidirectional molecular dipole with molecules in the Cl-up configuration while

this effect is compensated over the second layer where molecules adopt the Cl-down configuration. The structural study is complemented with a study of the influence of the opposite orientation of dipoles in the first and second molecular layers on the work function measured by contact potential difference measurements (CPD).

8.2 Introductory Concepts to the Molecular System and Substrate

The ClAlPc Molecule

Chloroaluminum phthalocyanine (ClAlPc) is a non-planar molecule with molecular formula $ClAlC_{32}H_{16}N_8$ and molecular weight of 570.96 g/mol. A schematic representation is shown in Figure 8.1(a). In non-planar phthalocyanine molecules, the central group is outside the molecular plane and exhibits a permanent dipole moment perpendicular to the molecular π-plane. Other examples of non-planar phthalocyanines are chlorogallium phthalocyanine (ClGaPc) [66], vanadyl phthalocyanine (VOPc) [54, 64, 150], titanyl phthalocyanine (TiOPc) [196] and tin phthalocyanine (SnPc) [86, 184, 185, 220, 221]. ClAlPc has been used as donor material in organic solar cells in combination with C_{60} molecules [15].

After adsorption onto surfaces, non-planar phthalocyanines can adopt either up or down configurations with the Cl-atom, O-atom or Sn-atom pointing towards the vacuum or substrate which depends on the molecule-substrate interaction and coverage. As a consequence, these dipolar molecules can feature as the basic components in reversible molecular switches suggesting potential application in ultra-high-density data storage [105] and serve as the inserting layers to tune the energy level alignment in organic devices [64, 66, 104, 121]. The controllable construction of molecular dipole arrays would be of great interest for these fundamental applications.

The ClAlPc molecule, with a protruding Cl atom, exhibits a permanent electric dipole along the direction perpendicular to the molecular plane and the Al-Cl bond measures 2.167 Å. The reported dipole moment of the free molecule calculated from DFT varies between studies, Kera et al. reported a value of 1.87 D [122] while Fukagawa et al. reported a much higher value of 5.28 D [64]. Experimentally, the electric dipole per molecule of a monolayer of ClAlPc on HOPG was estimated

from the variation of work function with molecular coverage as 3.7 D [64]. Both configurations, Cl-up and Cl-down, are represented in Figure 8.1(b) together with the dipole orientation. In the Cl-up configuration a dipole pointing toward the substrate is induced.

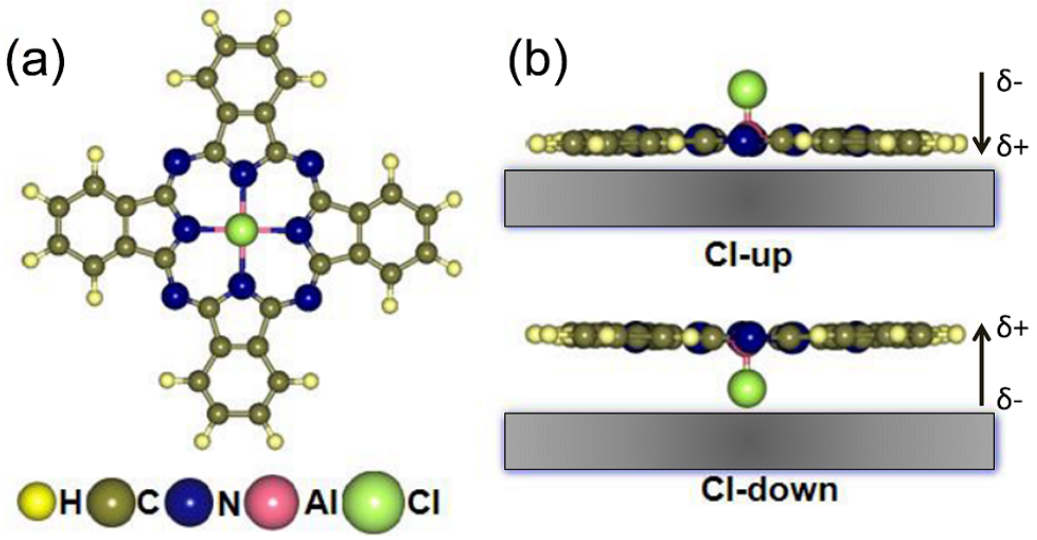

FIGURE 8.1: (a) Schematic representation (ball stick model) of the ClAlPc molecule (12.35 Å x 12.35 Å) and (b) side view of ClAlPc on the substrate with Cl-up and Cl-down configurations. Cl-up configuration represents the molecule oriented with Cl atom pointing towards vacuum what produce a dipole pointing toward the substrate.

Phthalocyanine molecules normally grow parallel to the surface when are evaporated on metal and semiconductor surfaces due to a large molecule-substrate interaction. The growth of ClAlPc has been studied by STM on HOPG [105, 106], Ag(111) [148], Au(111) [148, 149] and Au(111)/mica [148, 149]. The dipole orientation of ClAlPc is strongly substrate dependent. When a monolayer of ClAlPc molecules is evaporated on HOPG molecules self-assemble in a square phase with Cl-up configuration forming unidirectional molecular dipole array. The second layer of molecules adopts the Cl-down configuration. The interlayer dipole-dipole attraction and the π-π interaction facilitate the second layer of molecules to adopt the Cl-down configuration and, in order to maximize the attraction and the π-orbital overlap, the Cl-down adsorbed ClAlPc molecules prefer to reside at the hollow sites of the monolayer. The uniformed alignment of the molecular dipoles is favored to optimize the intermolecular C-H–N hydrogen bonds [218, 219].

On Au(111)/mica [148, 149] and Ag(111) [105, 148] both orientations, up and down, were found by LT-STM in the "as growth" first monolayer. Post-annealing

was found to lead to all the molecules in the Cl-up configuration. The ClAlPc/Au(111) system has been studied by UPS [104] and LT-STM (5K) [104, 149]. By LT-STM it was determined that ClAlPc molecules, evaporated with the substrate kept at room temperature, show a square phase where 60% of the molecules are in the Cl-up configuration and 40% in the Cl-down configuration. After annealing at 250°C during 6h all the molecules were found in the Cl-up configuration. The Cl-up configuration was attributed then as the thermodynamically more stable configuration [104].

The Au(111) Herringbone Reconstruction

Differing from other fcc(111) noble metal surfaces, the Au(111) is known for its herringbone reconstruction with a super cell of 22 x $\sqrt{3}$ [14, 229]. This reconstruction occurs spontaneously at room temperature and is due to the contraction of 4.4% with respect to the bulk in the close-packed [1$\bar{1}$0] direction. Along this direction, 23 surface atoms occupy 22 substrate positions resulting in the formation of alternating areas where surface atoms occupy fcc (face centered cubic) or hcp (hexagonal closed packed) sites on the underlying bulk lattice with a periodicity of 63 Å. These two areas are separated by disconmesuration lines (DL) along the next-nearest neighbors directions of the Au(111) that appears topographically higher in STM. The DL may form zigzag lines that are bended ± 120° at the borders between adjacent 22 x $\sqrt{3}$ areas and form the typical contrast in STM images. One of the disconmesuration lines is pinched at the elbow while the partner line is bulged at the adjacent elbow. In Figure 8.2 a schematically representation of the herringbone reconstruction is presented.

8.3 Experimental Details

Experiments were performed in an ultra-high vacuum chamber, base pressure 1 x 10^{-10} mbar, at room temperature. The Au(111) single crystal (Matek GmbH, Germany) was prepared by repeated cycles of Ar^+ sputtering (0.6 keV) plus annealing at 300°C. After checking the surface quality by STM, ClAlPc molecules (Sigma Aldrich) were sublimated from a Knudsen cell at 345°C with a deposition rate of 0.10 ML/min. During the deposition the substrate was kept at room temperature and after the molecular deposition a thermal annealing of 10 min

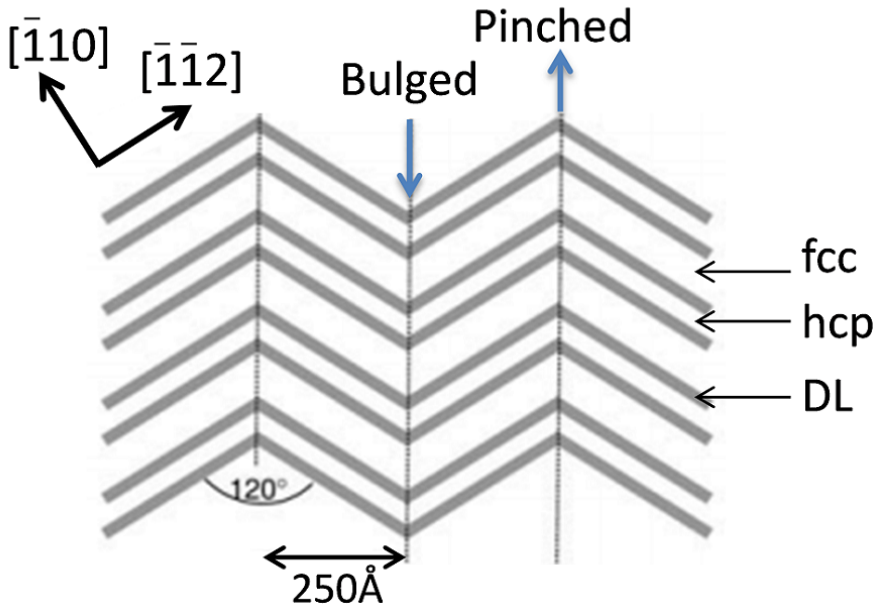

FIGURE 8.2: Schematically representation of the herringbone reconstruction.

at 100°C was performed. The molecules were purified twice by gradient thermal annealing before to be introduced in the system and subsequently degassed in the UHV chamber.

8.4 Results and Discussion

8.4.1 The Au(111) Surface

In the experiments presented in this chapter, the structure of the Au(111) surface was checked prior to molecular evaporation and the observation of the herringbone structure was one of the criteria for surface cleanness. An example of topographic STM image is given in Figure 8.3(a) where an area with a monatomic step and the characteristic herringbone pattern are imaged. The line profile, Figure 8.3(b), shows the characteristic height of the Au(111) step of $\sim$ 2.4 Å.

In Figure 8.3(c) two of the three possible 22 x $\sqrt{3}$ domains, that are 120° rotated, are observed. As can be seen, the width of fcc-like regions, energetically the most stable, is larger than that of the hcp-like due to the modulation in the surface stress [216]. In Figure 8.3(d) a high resolution FM-AFM image is presented where

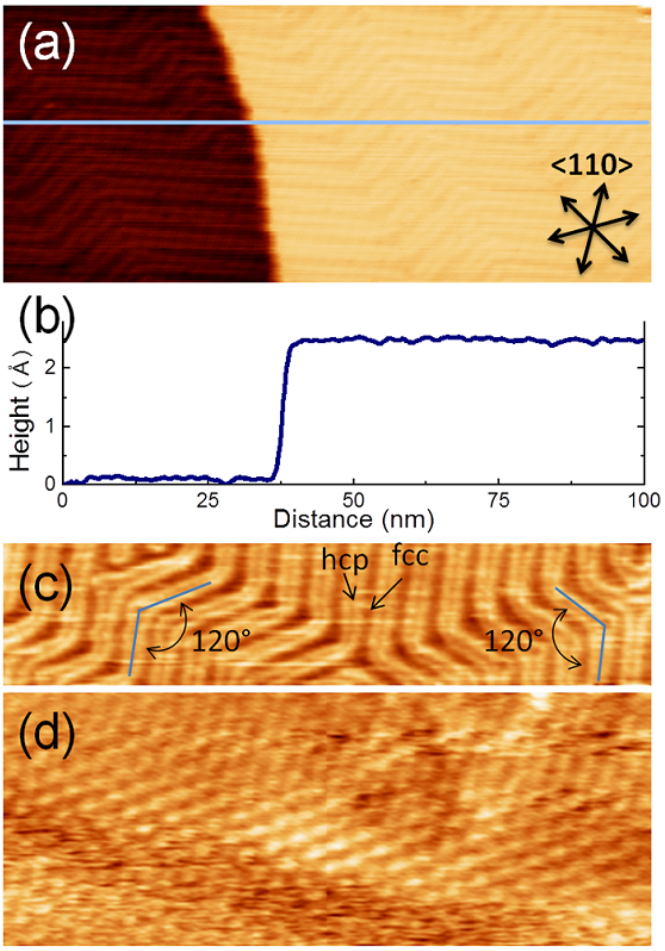

FIGURE 8.3: Au(111) herringbone reconstruction. (a) Topographic STM image of an area with a monatomic step and (b) the line profile indicated in (a). The step height is $\sim$ 2.4 Å. (c) Another topographic STM image where the fcc and hcp areas of the reconstruction are indicated. There are two domains of the herringbone (each domain is indicated) rotated 120°.(d) High resolution topographic FM-AFM where atoms are resolved. Parameters: (a) I = 240 pA, Bias = +1.30 V, A = 200 pm, (c) I = 320 pA, Bias = +1.20 V, A = 200 pm and (d) Δf = +1.94 Hz, Bias = +1.00 V, A = 140 pm, 6.0 nm x 2.4 nm.

gold atoms are resolved. The observed periodicity is used to calibrate the *xy* piezo directions (2.8 $\pm$ 0.2 Å).

8.4.2 Monolayer and Bilayer of ClAlPc/Au(111)

After the evaporation of $\sim$ 1 ML of ClAlPc onto the Au(111) (kept at room temperature) and followed by a soft annealing, molecules self-assemble in a square phase as can be observed in the STM images of Figure 8.4 where the herringbone

pattern of the Au(111) is still visible. The post annealing was found to be necessary to obtain an ordered monolayer and it was not possible to get structures at partial coverage. Other studies have already demonstrated that charge redistribution upon molecular adsorption on metallic substrates can indeed cause repulsion between molecules and influence the molecular ordering [184]. This behavior is not exclusive of molecules with permanent dipoles. The molecule-molecule interaction is usually attractive owing to van der Waals forces and causes the formation of 2D islands but with phthalocyanine repulsive intermolecular interactions have been reported [86, 184]. In some cases, permanent quadrupole or dipole moments enhance this attractive force as occurred with the PTCDA molecule [200]. in other cases as for the SnPc/Ag(111) system, a dominant substrate-mediated repulsive intermolecular interaction between the molecules, that exceeds van der Waals and other attractive forces. This repulsion produce that at low coverages and room temperature, a disordered overlayer is formed [184].

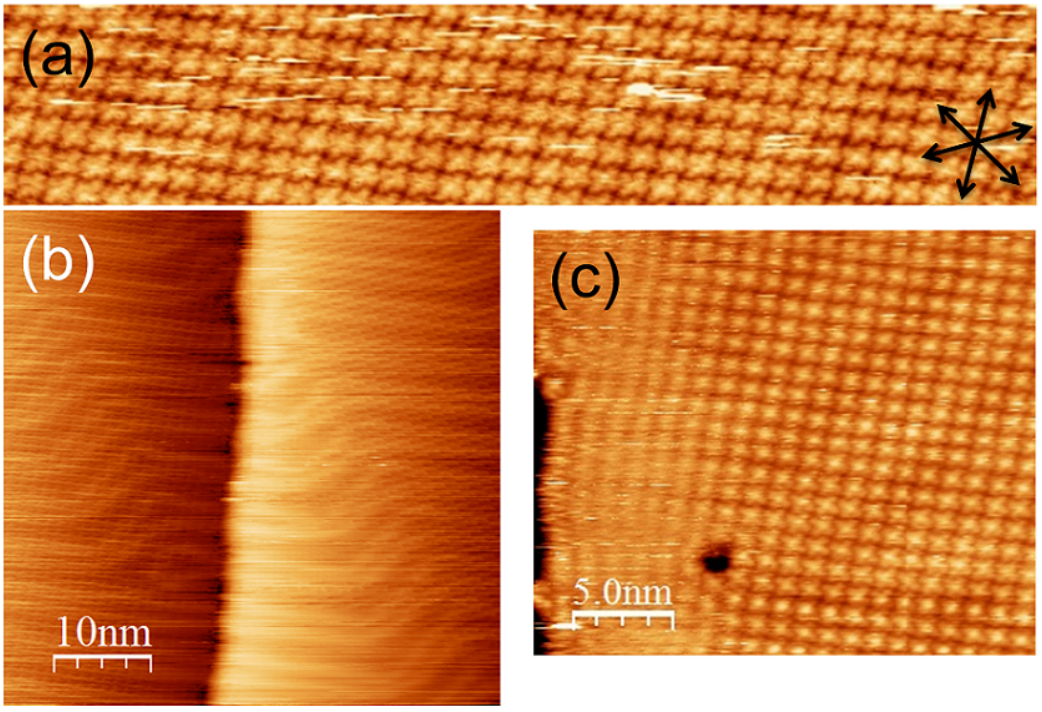

FIGURE 8.4: (a)-(c) Large STM images of a monolayer of ClAlPc on Au(111). In (a) the three ⟨110⟩ equivalent directions of the Au(111) are indicated. Parameters: (a) I = 60 pA, Bias = +1.12 V, A = 200 pm, 40 nm x 8 nm, (b) I = 130 pA, Bias = -1.04 V, A = 200 pm and (c) I =130 pA, Bias = +1.25 V, A = 200 pm.

In Figures 8.4(b) and (c) the coverage is slightly lower than the complete monolayer and the areas next to the step edge, both in the upper and lower terraces, present molecules with higher mobility. It indicates that the step edge does not

stabilize the molecule nucleation as occurred in other molecular/metal systems. Each molecule is imaged as a four-leaf feature and a homogeneous contrast along the monolayer is observed.

In the high resolution STM image presented in Figure 8.5(a) each molecule is imaged as a four-leaf feature with a central bright protrusion what has been interpreted in the literature as the molecule in the Cl-up configuration [105, 106, 151]. All the molecules show the same structural features and appear with the same contrast, which suggest an unidirectional alignment of the molecular dipoles. There is no presence of molecules in the first layer in the opposite configuration. The line profile, indicated in Figure 8.5(a) and presented in (b), shows a height of ~ 60 pm. In Figure 8.5(c) an area where a tip change occurred is presented. Before the tip change, molecules are imaged as in Figure 8.5(a) and after the tip change the bright central protrusion is not observed. This tip ended material does not seem to be the most stable since in the majority of the images molecules are imaged as in Figure 8.5(a).

As mentioned before, the Cl-up configuration has been reported as to be the thermodynamically more stable on Au(111) where the coupling of the molecular π-orbitals with the metal electronic states is maximized. This configuration has been reported as to be the one obtained after a long annealing (6h) at 250°C [104] but here, a complete unidirectional molecular dipole film is obtained after a short annealing of 10 min at 100°C.

The parameters of the unit cell of the square phase, indicated in Figure 8.5(a), are $\mathbf{a} = \mathbf{b} = 1.38 \pm 0.02$ nm where $\mathbf{a}$ is oriented along the $\langle 112 \rangle$ and $\mathbf{b}$ along the $\langle 110 \rangle$ gold directions. This unit cell size is slightly smaller than the one reported for the same system by Huang et al. of $\mathbf{a} = 1.63 \pm 0.03$ nm and $\mathbf{b} = 1.59 \pm 0.03$ nm [104] and more in agreement with the unit cell of the CuPc on Cu(111) ($\mathbf{a} = 1.42$ nm, $\mathbf{b} = 1.35$ nm) [41]. The molecules are slightly rotated from the $\mathbf{a}$ and $\mathbf{b}$ unit cell vectors, ~ 5 °, as can be observed in the schematic representation of the square phase in Figure 8.5(d).

When evaporating < 2 ML plus annealing at 100° a partial second layer of molecules grows as can be observed in Figure 8.6. Molecules of the monolayer are imaged as four lobes with a central bright protrusion, as the ones in Figure 8.5, while molecules of the second layer are imaged as four lobes with homogeneous central contrast. By comparison with the STM study of the ClAlPc/HOPG system it can

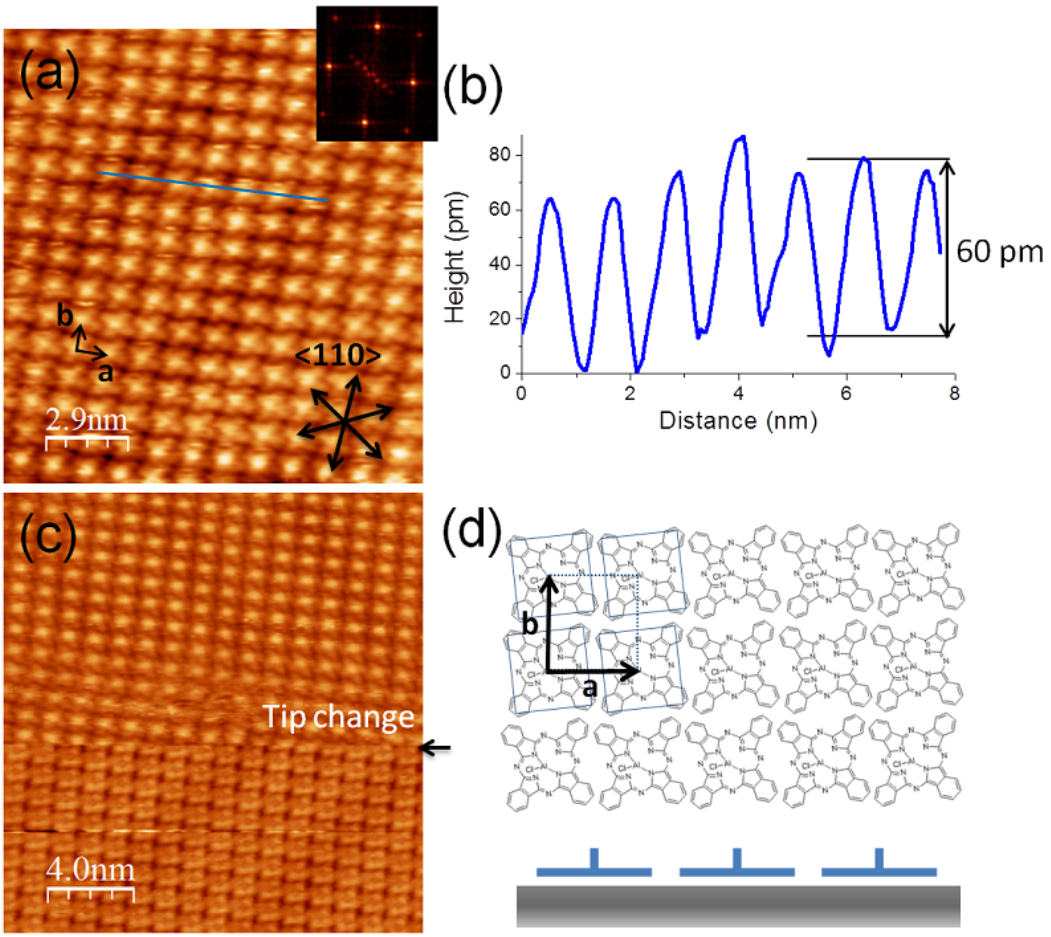

FIGURE 8.5: (a) Topographic STM image of a monolayer of ClAlPc on Au(111). The FFT of this area is in the inset and the lattice vectors, **a** and **b**, are indicated in the STM image as well as the three ⟨110⟩ equivalent directions of the Au(111) and (b) the line profile indicated in (a). In (c) is presented another topographic STM image of the monolayer but, in this case, a tip change occurred (indicated by a black arrow). (d) Front and side view representation of the ClAlPc in the square phase. In the side view is pointed out that molecules are in the Cl-up configuration. Parameters: (a) I = 130 pA, Bias = +1.25 V, A = 200 pm and (c) I = 45 pA, Bias = +1.00 V, A = 200 pm.

be interpreted that the second layer of molecules is in the Cl-down configuration maximizing the electrostatic interaction between the two molecular layers with opposite oriented dipoles. In the line profile presented in Figure 8.6(d) the apparent height difference between the first and second layer is ~ 2.5 Å. The fact that it is not possible to obtain packed 2D islands in the first layer, as being observed in the second layer, points out the reduction of the molecule-molecule electrostatic repulsion to attractive intermolecular interaction driving the assembly of the molecules of the second layer.

Comparing the surface regions with a monolayer and a bilayer of molecules, it

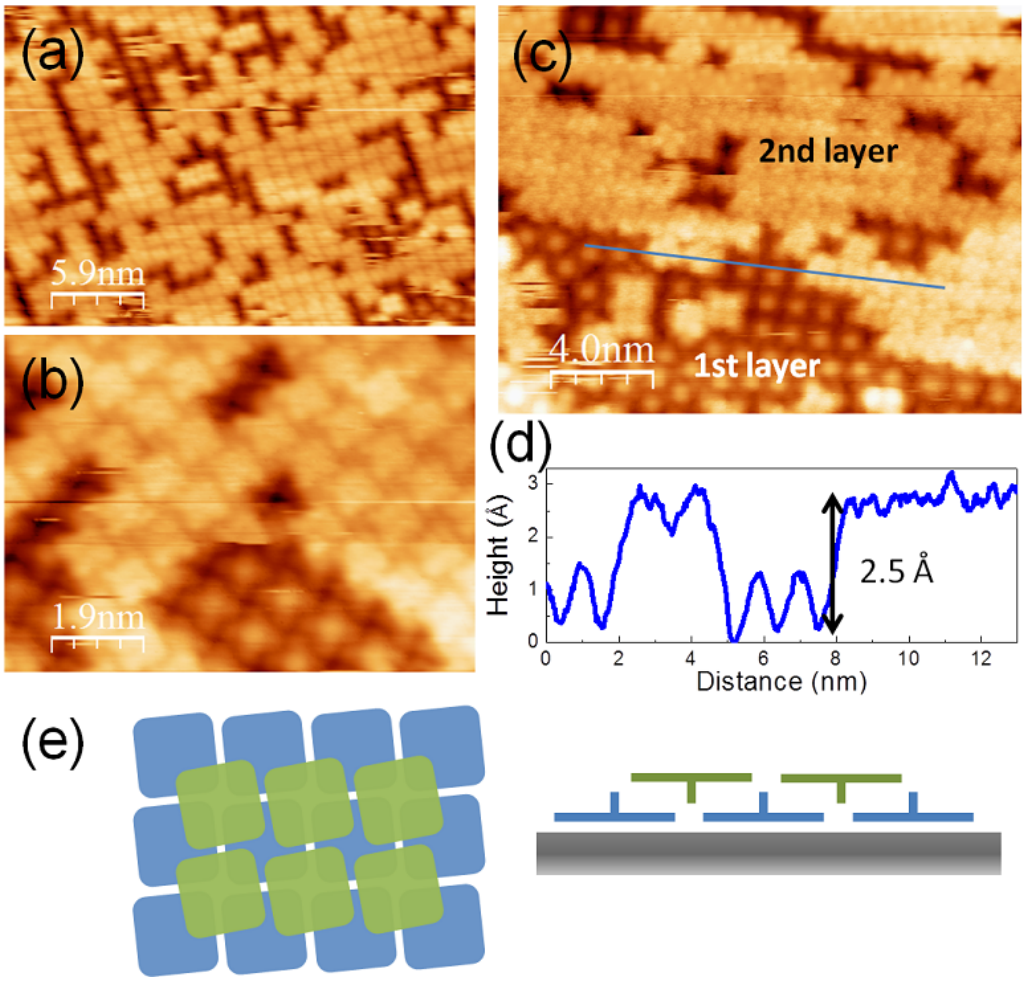

FIGURE 8.6: (a)-(c) Topographic STM images of a bilayer of ClAlPc molecules on Au(111). (d) Line profile indicated in (c) where it can be observed that the height from the fist to the second layer is $\sim$ 2Å. (e) Front and side view representation of the first (blue) and second (green) layer of molecules. In the side view is pointed out that the first layer is in the Cl-up configuration and the bilayer in the Cl-down configuration. Parameters: (a) I = 70 pA, Bias = +2.00 V, A = 200 pm, (b) I = 100 pA, Bias = +2.00 V, A = 200 pm and (c) I = 80 pA, Bias = +2.00 V, A = 200 pm.

can be extracted that molecules of the second layer are shifted half unit cell in **a** and **b** directions occupying the position between four molecules of the first layer. The front and side view of this configuration are represented schematically in Figure 8.6(e). The second layer presents the same unit cell size than the first layer as reported for the ClAlPc/HOPG system [106]. Molecules of the bilayer seem to be slightly rotated respect the first layer, $\sim 4°$. The herringbone reconstruction of the Au(111), that was observable over the monolayer of ClAlPc, is not observable over the second layer of molecules.

Consecutive scanning in the same area shows tip-induced movement of the molecules

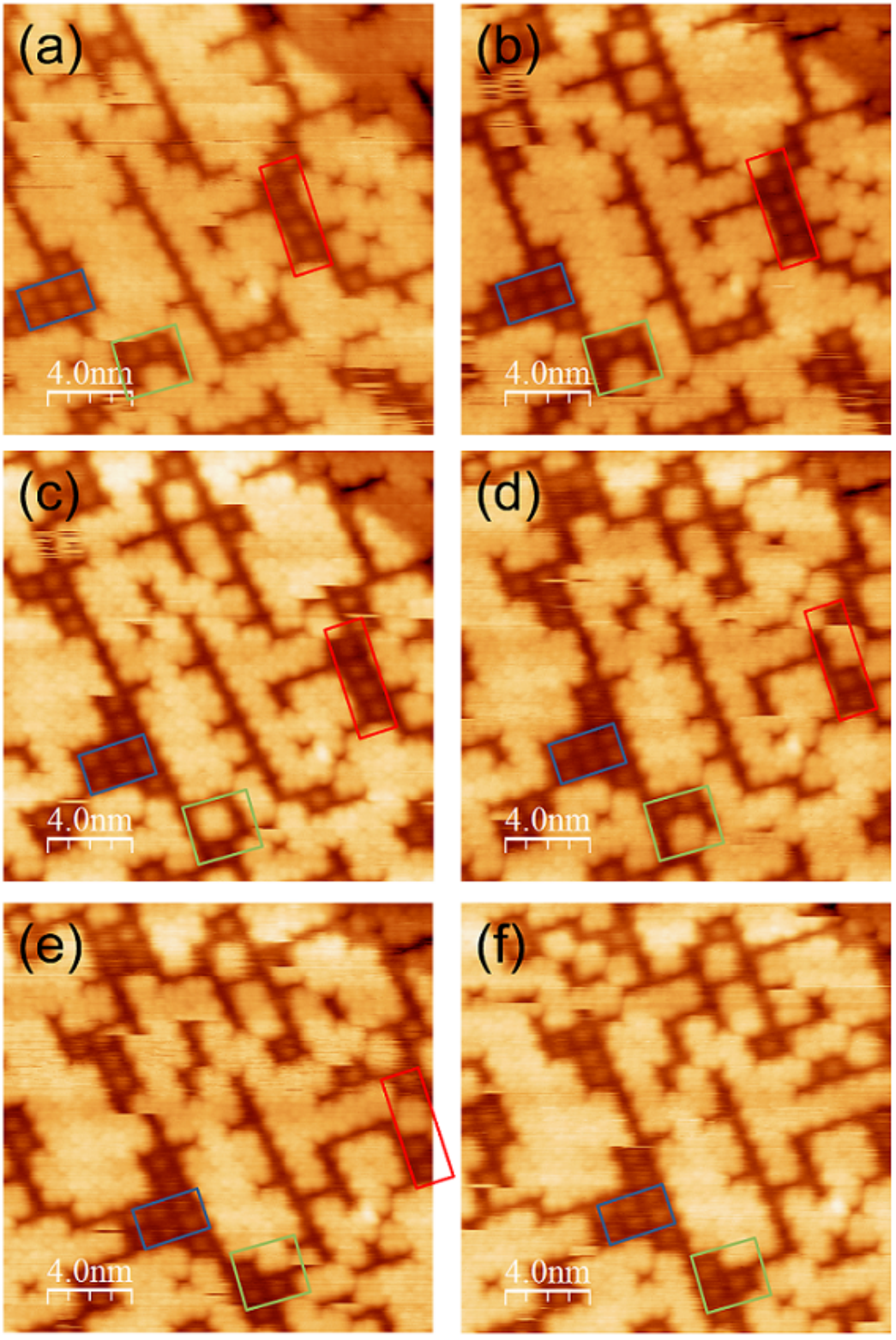

FIGURE 8.7: Consecutive topographic STM images of the same area of $\sim$ 1.7 ML of ClAlPc on Au(111). Same surface regions of the images are indicated by color boxes. Parameters: I = 105 pA, Bias = +2.00 V and A = 200 pm.

of the second layer as can be observed in the six consecutive STM images presented in Figure 8.7. Same areas are highlighted with color boxes. For example, in the area indicated in green a molecule from the bilayer is positioned between two molecules from the first layer in (a). In (b) this molecule has been slightly rotated and in (c) is positioned between four molecules of the first layer. In (d) this molecule is found in the same position than in (b) and in (e) it is incorporated to the molecular island situated above. The tip-induced movement is higher on molecules that are not surrounded by other molecules.

Figures 8.8(a) and (b) show a topographic STM images and its simultaneously acquired frequency shift image. Over surface regions with a coverage of one layer of molecules, the frequency shift reveals a more repulsive interaction whereas over regions with a bilayer the frequency shift reveals a more attractive interaction. However, due to the expected different tip-sample distance when measuring in STM constant current mode over one and two molecular layers, the simultaneous frequency shift is not easy to interpret. Since ClAlPc molecules are semiconductive, the tip-molecule distance when measuring in STM over the second layer is expected to be smaller than over the first layer. The chemical repulsion is then expected to be larger over the second layer. However this is not what is observed in the frequency image. The reduction of the surface dipole over the second molecular layer produces an increment in the attractive interaction for this STM conditions. However, this relation is different for other tip-ended materials and STM conditions as will be discussed in the following.

In the second layer, molecules are predominantly found in the Cl-down configuration but a small percentage in the opposite configuration, Cl-up, was found as observed in Figure 8.8(a). In the STM image and its simultaneously measured frequency shift channel presented in Figure 8.8(a) and (b), three molecules of the bilayer in the Cl-up configuration are imaged (blue arrows). These molecules are attributed to the Cl-up configuration due to the different appearance regarding the rest of the molecules of the second layer. In the frequency shift image the central part of these molecules appears brighter indicating a more repulsive interaction. In addition, two molecules of the second layer that are not surrounded by more molecules (green arrows), are imaged quite different and four lobes are resolved.

Distance spectroscopy has been performed over the first and second layers of ClAlPc on Au(111). The tunneling current, force and excitations versus distance are presented in Figure 8.9(a). The blue plot corresponds to the z-spectroscopy

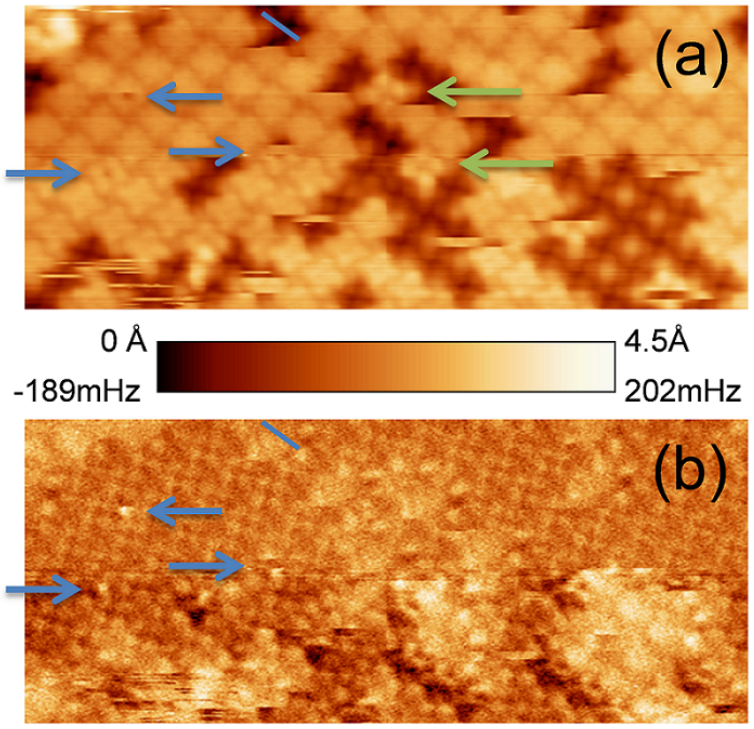

FIGURE 8.8: (a) Topographic STM image and (b) its simultaneous frequency shift channel of an area of partial second layer of molecules. Some molecules of the second layer appear with a central depression (indicated by blue arrows). Also, the molecules of the second layer that are not surrounded by more molecules look different (green arrow). The excitation image is not presented here but does not show any contrast. Parameters: I = 79 pA, Bias = +2.00 V, A = 200 pm, 20 nm x 8.4 nm.

performed over the first layer of molecules and the green plot over the second. In (b) is presented the topographic STM image where both spectroscopies were performed and in (c) the simultaneously frequency shift that we will use to compare with the z-spectroscopy. The areas where the spectroscopies were acquired are indicated with a blue (one layer) and green (two layers) circles. The force versus distance was calculated from the frequency shift versus distance employing the Sader and Jarvis formalism [167]. The spectra were acquired from the STM setpoint position then the absolute tip-sample distance is different over both surface regions as is represented by a purple dash line in Figure 8.9(d). The feedback is switched off at the setpoint position and the tip is retracted 1 nm. The spectroscopy starts by approaching the sample 1.2 nm. To use the same origin of the z-scale, the height difference from the first and second molecular layers ($\sim$ 2 Å) was used to correct the z-scale, orange line in Figure 8.9(d).

As can be observed in Figure 8.9(a), over the first molecular layer the dependence of the tunneling current with the piezo displacement is exponential. The measured

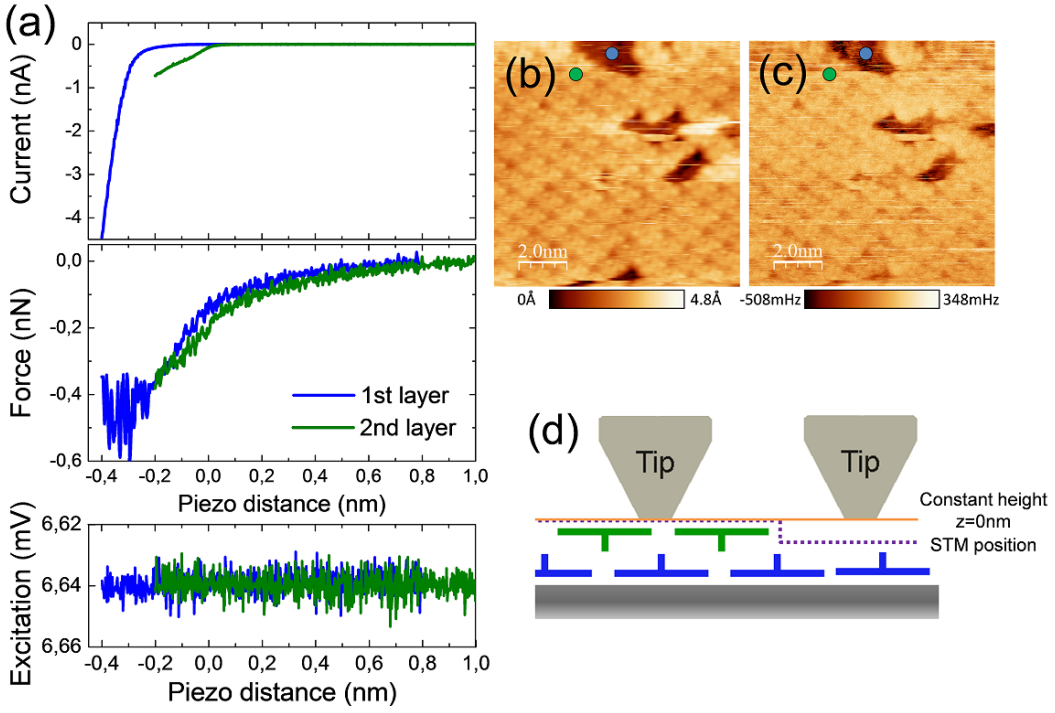

FIGURE 8.9: (a) Distance spectroscopy performed over the first (blue plot) and second layer (green plot) of ClAlPc on Au(111). The tunneling current, force and excitation versus distance are presented. Each spectrum is an average of three curves. (b)-(c) Topographic STM image and its simultaneous frequency shift where both spectroscopies were collected. (d) Schematic representation of the tip and sample in constant height (orange line) at the setpoint position in STM (purple line). Parameters of the STM image: I = 88 pA, Bias = -2.00 V, A = 200 pm. Parameters of the spectroscopy: Bias = -2.00 V and A = 200 pm.

decay length is 1.04 ± 0.02 $Å^{-1}$. Over the second layer of molecules the tunneling current does not present an exponential dependence with the piezo displacement. This is probably due to high tip-sample deformation and even a contact formation between the tip and the molecules of the second layer. The force versus distance over the monolayer and bilayer present similar behavior. As the tip approaches the surface the attractive force increases. The similar behavior over both surface regions suggests that the tip-sample interaction is dominated by the long-range interaction with the substrate. Over the monolayer it was possible to reach the maximum attractive force of -0.4 nN. From that point as the tip approaches the surface the repulsive force increases. Over the second layer this point was not reached and even when the tunneling current suggests high tip-sample interaction the net force is in the attractive regime. The excitation channel does not show apparent signature of dissipative processes.

The STM setpoint position for the first and second molecular layers corresponds

in Figure 8.9(a) to z = -0.2 nm and z = 0 nm respectively. At this tip-sample distances the tunneling current is the same, as expected since this is the z-position of the STM feedback. The force values are different and are ∼ -0.4 nN for the first layer and ∼ -0.2 nN for the second. It means the tip-sample interaction is more attractive over the first layer when scanning in STM constant current and these conditions. This relation is also observed on the simultaneous frequency shift image presented in Figure 8.9(c). The areas with one layer of molecules appear in frequency shift with a more negative value, i.e. more attractive interaction. In STM feedback the tip-molecule distance is expected to be smaller over the second layer since the two molecular layers act as a semiconductor. On one hand, a more repulsive (chemical) interaction is expected over the second layer because of the smaller tip-molecule distance. On the other hand, the long-range attractive forces (van der Waals and electrostatic) that the tip experiments due to the gold substrate are smaller for longer tip-substrate distances. The behavior observed in Figure 8.9(a) seems to be dominated by the long-range tip-substrate interaction. First because both spectra overlap perfectly showing same interaction with the first and second molecular layer and second because at the setpoint position the more repulsive interaction that would be expected because of the smaller tip-molecule distance over the second molecular layer is not observed.

It is interesting to note that the frequency shift contrast observed in Figure 8.9 is opposite to the observed in Figure 8.8 where a more repulsive interaction is measured over the first molecular layer. Molecules in Figure 8.9(b) are imaged quite different from Figure 8.8(a) suggesting a different tip-ended material causing a repulsive interaction with Cl-up molecules, i.e. a tip apex with a dipole. Additionally STM parameters also differ from the two images.

8.4.3 Contact Potential Difference Measurements

Adsorbates can strongly influence the surface work function. Firstly, the presence of adsorbates will lead to a repulsion of the negative charge cloud from the substrate due to the Pauli principle and thus to a reduction of the work function, this effect is also known as pillow effect. Secondly, in the case of a covalent adsorbate-surface interaction the involved charge redistribution in the interface can induce an interfacial dipole which will influence the work function. In addition, if the adsorbate molecule has an intrinsic dipole moment, as occurs with the ClAlPc

molecule, an additional contribution to the work function which will depend on the orientation of the molecular moments and on the relative contribution of the other mentioned effects (see for example [110]).

The effect of the electric dipole on the work function change for unidirectional ClAlPc monolayer on Au(111) was studied by UPS [104]. An extraordinarily large shift of -0.89 eV of the vacuum level was measured, which is opposite to that of +0.46 eV on graphite even though the molecular dipoles are oriented similarly [104]. The large vacuum level shift of the ClAlPc/Au(111) interface was interpreted as a strong molecule-substrate interaction compared to the physisorbed ClAlPc/HOPG system. The electronic properties of the ClAlPc/Au(111) interface are therefore not well understood. Moreover, the impact of the molecular orientation in successive layers has only been studied by UPS in the ClAlPc/HOPG system. The vacuum level shift from the substrate to the monolayer (with aligned molecules) was measured as +0.31 eV whereas for the bilayer as +0.02 eV where the effects of the molecular electric dipole were canceled [64, 122].

In order to study the influence in the electronic properties of the monolayer and bilayer of ClAlPc on Au(111), contact potential difference measurements were performed on both layers and are presented in Figure 8.10. Contrary to UPS measurements that are spatially averaged, CPD measurements allow us to perform local measurements in surface regions with one and two molecular layers. Since the first molecular layer is in the Cl-up configuration, the contribution of the permanent dipole to the work function (without considering the pillow effect) is then expected to increase its value.

On the other hand, the push back effect in the monolayer is expected to decrease the work function. For example, a monolayer of copper phthalocyanine (CuPc) physisorbed on Au(111) induces a -0.70 eV shift of the work function due to the push back effect [176, 186, 239].

The second layer of molecules in opposite configuration, i.e. with a dipole pointing toward the vacuum, will minimize the dipole effect. In an ideal situation, and only taking into account the molecular dipole, the second layer has an electrical dipole moment of equal value but opposite than that of the first layer which will nullify it. Then, in this simple representation, the work function of the first, $\Delta\phi_{1st}$, and second layer of molecules, $\Delta\phi_{2nd}$, can be expressed as:

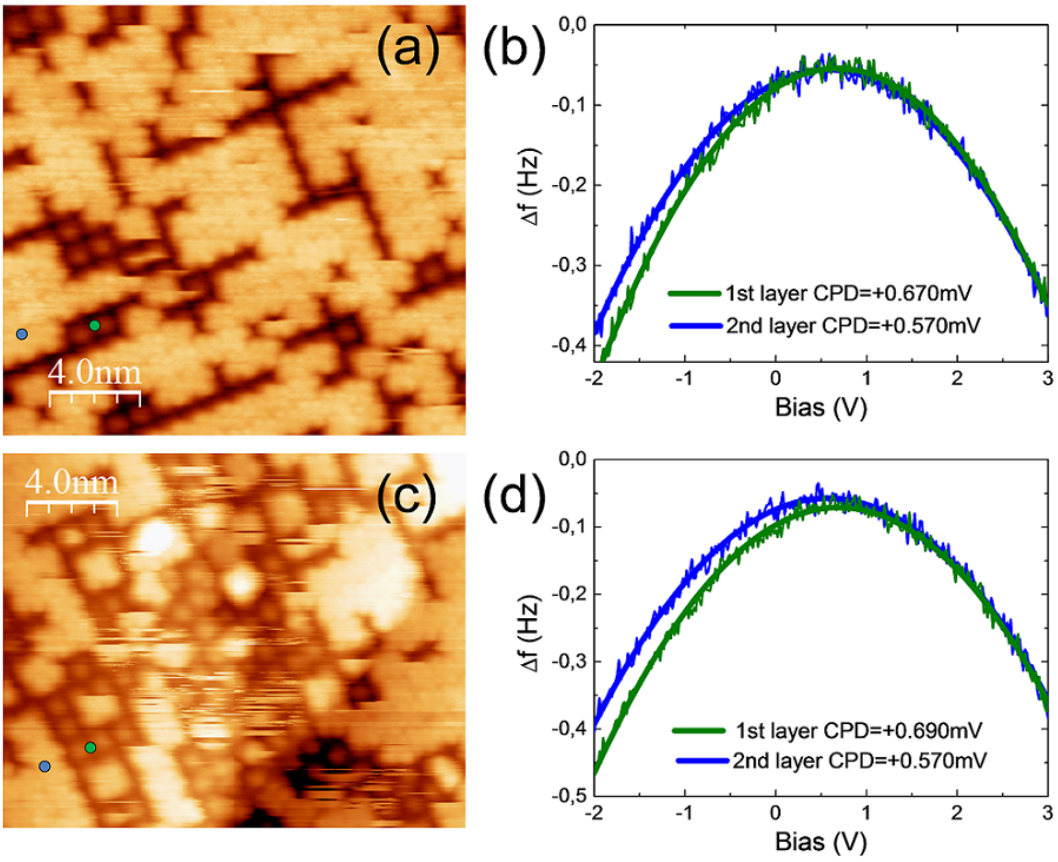

FIGURE 8.10: (a) and (c) are the topographic STM images where the CPD measurements presented in (b) and (d) are respectively performed. The frequency shift vs. bias spectroscopies performed over the monolayer are represented in green and those performed over the bilayer in blue. To perform the spectroscopy the tip was lifted from the set point position 120 pm and kept at constant height during the CPD measurements. Parameters: (a) and (c) I = 90 pA, Bias = +2.00 V, A = 200 pm.

$$\Delta\phi_{1st} = \Delta\phi_{pillow} + \Delta\phi_{down}$$
$$\Delta\phi_{2nd} = \Delta\phi_{pillow} + \Delta\phi_{down} + \Delta\phi_{up}$$
$$\Delta\phi_{2nd} - \Delta\phi_{1st} = \Delta\phi_{up}$$

where $\Delta\phi_{pillow}$ is the work function change due to the pillow effect, $\Delta\phi_{up}$ to molecules in the Cl-up configuration and $\Delta\phi_{down}$ to molecules in the Cl-down configuration. The difference between the work function of the first and second molecular layers is then produced by $\Delta\phi_{up}$. This assumes that the electrical dipole in the first layer is not appreciable changed by the deposition of the second layer.

In Figure 8.10 are represented two examples of frequency shift vs. bias voltage spectroscopies performed over the monolayer (green plot) and bilayer (blue plot). The CPD values obtained over the bilayer are (a)-(b) 100 mV and (c)-(d) 120 mV smaller than over the first monolayer. The CPD values are related with the work function difference through:

$$\Delta CPD = CPD_{2nd} - CPD_{1st} = \frac{1}{e}(\Phi_{2nd} - \Phi_{1st}) \tag{8.1}$$

Then, the maximum measured work function difference between the first and second layer is 120 meV, being the work function smaller for the bilayer. It agrees with the prediction of cancellation or at least minimization of the contribution of the permanent dipoles to the work function for the bilayer. Since there is not data in the literature about the work function value of a monolayer of ClAlPc on Au(111) and there was no clean Au(111) areas, it is only possible to give a variation of the work function from the monolayer to the bilayer but not an absolute value.

The work function change related to interface dipoles in organic layers has been analyzed using the Helmholtz equation [7, 24, 58]. The dipole of a ClAlPc molecule, p, can be estimated from the work function change measured between the first and second molecular layers, $\Delta\Phi$, through the Helmholtz equation:

$$\Delta\Phi = e\ \frac{\mu\ cos\varphi}{\varepsilon_0\ \varepsilon_r}, \tag{8.2}$$

where e is the elementary charge, μ is the dipole moment per unit area (p/A), φ is the angle between the dipole and the surface normal, ε_0 is the vacuum permittivity and ε_r is the dielectric constant of the material. The number density of dipoles is assumed to be 1 per 1.38 nm x 1.38 nm (one molecule per unit cell), the angle 0° and the dielectric constant has been experimentally determined for a monolayer of ClAlPc on HOPG as 1.30 [64]. This value was determined for one monolayer taking into account the depolarization effect. This dielectric constant is much smaller than those of other organic dipole layer systems such as SAMs, a possible reason for that is the smaller dipole density in the present system owing to the larger molecular size (smaller molecular density) [24].

With the maximum $\Delta\phi$ measured by CPD of 0.12 eV and using Equation 8.2, a dipole moment of $\sim$ 0.80 D per molecule is obtained. This value is smaller than

the experimentally calculated for the ClAlPc on HOPG system (3.70 D) [64]. The distance between dipoles in the molecular layer ($\sim$ 1.4 nm) is much larger than the distance between molecular planes ($\sim$ 2 Å) and therefore an electric field from the first layer is expected. The small dipole moment suggests that depolarization effects due to this electric field seems to important for the second layer of molecules. Additionally, it is possible a charge reorganization on the second molecular layer due to electronic coupling with the substrate since a strong molecule substrate interaction has been reported for the ClAlPc/Au(111) [64].

8.5 Conclusions

The ClAlPc/Au(111) system has been study by STM/FM-AFM in UHV and at room temperature. ClAlPc is a non-planar molecule with a Cl-atom outside the molecular plane and exhibits a permanent dipole moment perpendicular to the molecular plane. This molecule can adopt two configurations: Cl-up and Cl-down. The structure of the first and second layer of the ClAlPc molecules on Au(111) have been determined by STM measurements as well as the work function difference between them by contact potential difference measurements. Molecules in the first layer adopt a Cl-up configuration and form a square phase with a unit cell size of $\mathbf{a} = \mathbf{b} = 1.38 \pm 0.02$ nm, where $\mathbf{a}$ is oriented along the $\langle 112 \rangle$ and $\mathbf{b}$ along the $\langle 110 \rangle$ substrate directions. The molecules are slightly rotated from the $\mathbf{a}$ and $\mathbf{b}$ unit cell vectors, $\sim 5°$. Molecules in the second layer adopt a Cl-down configuration and present the same unit cell than the first layer but shifted half unit cell, i.e. each molecule of the bilayer is positioned between four molecules of the monolayer. Molecules of the bilayer seem to be slightly rotated respect the first layer, $\sim 4°$.

The tip-sample interaction over the first and second molecular layer when scanning in STM feedback mode depends on the tip-ended material as well as on the STM parameters. For certain parameters, a more repulsive interaction is measured over the first layer whereas at different conditions a more attractive interaction is measured.

In the bilayer, the dipole effect in the contribution to the work function is expected to be canceled or at least minimized. The CPD measurements reveal a smaller work function for the bilayer layer compared with the monolayer agreeing with the prediction. The maximum measured work function difference between the

first and second layers is 120 meV, being the work function smaller for the bilayer. From the work function difference, the molecular dipole can be estimated through Helmholtz equation giving a value of $\sim$ 0.8 D.

Chapter 9

Final Conclusions

In this thesis, the structural and electronic properties of selected organic and inorganic 2D systems on metallic surfaces have been investigated by a combined STM/FM-AFM in conditions of ultra high vacuum and at room temperature. In the following, the most relevant aspects are summarized.

A semilayer of copper oxide over Cu(111) was obtained by air-enriched argon sputtering plus annealing. Six different oxidic phases were observed that differ in their local oxygen content or stoichiometry. Additionally to the observation of five structures, already reported in the literature, a new open honeycomb (OHC) lattice was found. This structure has been modeled as consisting of Cu_3O units arranged in a hexagonal lattice of dimensions 13.3 Å which is labelled as $(3\sqrt{3}$ x $3\sqrt{3})$R30° in the Wood's notation. The high quality of the OHC can provide precise and confined localization of functional guest nano-objects to become a multifunctional nanostructured system.

To determine the local work function of both surface regions, copper and copper oxide, $I(z)$ spectra were collected with different tips. An anomalous $I(z)$ behavior was observed over copper oxide regions, preventing quantification of the local work function. Two models have been suggested: a resistance in series model and a tip-sample deformation. In the resistance in series model, a sample resistance is added to the tunneling junction and the $I(z)$ spectra were correctly fitted for one of the three tested tips. A sample resistance of ~ 1.4 GΩ and a reasonable kappa value were obtained. In the tip-sample deformation model a positive deviation from the z-piezo distance was calculated, i.e. the tip-sample distance is higher than the z-piezo displacement. This deformation is expected to be caused by repulsive

forces and a maximum deformation of 60 pm was calculated. Both models are able to explain the non-exponential behavior of the tunneling current with the tip-sample distance. Additionally, tip-sample instabilities have been observed in one of the data set over both surface regions. Such instability corresponds to an abrupt and reversible jump in the tunneling current and has been interpreted here as a change in the tip-sample distance. A reproducible distance change of 24 pm was observed over both surface regions and is attributed to the presence of two stable tips during the tunneling junction formation.

The PTCDA molecule has been studied on two surfaces, Si(111)—7×7 and AgSi(111), by STM/FM-AFM and kappa imaging. In the PTCDA on Si(111)—7×7 system, the high molecule-substrate interaction does not allow molecules to diffuse and form monolayers and single molecules adsorbed on the corner hole of the 7×7 are found. In this system a charge transfer from the substrate to the molecule has been reported. The STM contrast reveals five parallel stripes perpendicular to the long axis of the molecule. The FM-AFM images, with intramolecular resolution, are able to distinguish the perylene core. Kappa imaging reveals a higher kappa value on the molecule compared to the Si(111)—7×7 agreeing with an interface dipole originated from electron charge transfer from the silicon to the molecule. In the PTCDA on AgSi(111) system, molecules self-assemble in two phases: herringbone and square. In the herringbone phase, the two inequivalent molecules of the unit cell are imaged with different apparent height by STM. In FM-AFM images, both inter- and intramolecular contrast have been resolved and the two molecules of the unit cell appear with the same contrast. Then, a non topographic origin of the STM contrast is concluded. Kappa imaging reveals a contrast between these two molecules. The variation of the effective barrier height is attributed to a different charge transfer between the substrate and the two molecules of the unit cell, yielding a different surface dipole.

The DIP molecule on Cu(111) has been studied by DFT calculations and experimentally by STM/FM-AFM. The coexistence of short and long-range ordered domains are obtained from DFT calculations and observed by STM imaging contrary to previous STM studies. In addition to the oblique phase, already reported in the literature, a rectangular phase is found. Two oblique phases are observed, with molecules oriented along the $\langle 110 \rangle$ and $\langle 112 \rangle$. The relative stability of the two oblique phases has been evaluated by the influence of continuous tip scanning. It has been concluded that the ones with molecular long axis oriented along the

⟨110⟩ are metastable. Contrary, tip induces growth of the domains with molecular long axis oriented along the ⟨112⟩ as expenses of the others. The work function difference, between copper and a monolayer of DIP molecules, has been determined by contact potential measurements. The work function is lowered $\sim$ 1 eV when a monolayer of DIP is adsorbed on the Cu(111) surface, in excellent agreement with previous experimental measurements.

The ClAlPc/Au(111) system has been studied by STM/FM-AFM. ClAlPc is a non-planar molecule with the Cl-atom outside the molecular plane and exhibits a permanent dipole moment perpendicular to the molecular plane. In the first layer, ClAlPc molecules self-assemble in a square phase in the Cl-up configuration. The molecules of the second layer, in the Cl-down configuration, present the same unit cell than the first layer. The dipole effect in the work function is expected to be canceled or at least minimized in the second layer. The CPD measurements reveal a smaller work function for the bilayer layer compared with the monolayer agreeing with the prediction. The maximum measured work function difference between the first and second layer is 120 meV, being the work function smaller for the bilayer. From this difference, the molecular dipole can be estimated through Helmholtz equation giving a value of $\sim$ 0.8 D.

Chapter 10

Resumen

En los dispositivos basados en semiconductores (orgánicos o inorgánicos), las interfases entre material metálico y material semiconductor juegan un papel importante en el funcionamiento final de dichos dispositivos. Algunos ejemplos de dispositivos son las celdas solares, los diodos emisores de luz y los transistores (orgánicos o inorgánicos) de efecto campo. En las interfases metal/semiconductor se producen muchos de los procesos fundamentales para el correcto funcionamiento de éstos, como la inyección de carga o la separación de excitones. La optimización de dichos procesos requiere un sólido conocimiento a nivel atómico de las interfases desde un punto de vista estructural y electrónico. Por consiguiente, en esta tesis se han estudiado una serie de sistemas bidimensionales orgánicos e inorgánicos crecidos sobre diferentes superficies metálicas, mediante microscopía de sonda próxima, una de las técnicas más potentes en el campo de la nanotecnología. Concretamente se ha utilizado un microscopio combinado de efecto túnel (STM, por sus siglas en inglés *scanning tunneling microscope*) y de fuerzas atómicas (AFM, por sus siglas en inglés *atomic force microscope*), en condiciones de ultra alto vacío ($p \leq 10^{-9}$ mbar) y a temperatura ambiente.

Capas delgadas de óxido de cobre (Cu_2O) han sido ampliamente utilizadas por sus óptimas propiedades en catálisis y como material semiconductor en celdas solares. Con el fin de estudiar las propiedades estructurales y electrónicas, se han crecido capas ultra delgadas (un átomo de grosor) de Cu_2O sobre una superficie de cobre (111). Diferentes técnicas han sido utilizadas para la caracterización: STM, AFM y espectroscopia de fuerza y corriente. El estudio estructural ha sido presentado en el Capítulo 4 y el estudio de espectroscopia de fuerza y corriente en el Capítulo 5.

Por otro lado, otro de los materiales semiconductores utilizados en el desarrollo de futuras celdas solares son las capas finas formadas por moléculas orgánicas semiconductoras. A pesar de que se podrían utilizar muchas moléculas para la fabricación de dispositivos orgánicos, las moléculas pequeñas conjugadas son especialmente interesantes debido al bajo peso molecular, su estabilidad ante la polimerización y ante la descomposición térmica. Dichas moléculas pueden ser sublimadas en condiciones de ultra alto vacío mediante crecimiento epitaxial por haces de moléculas orgánicas (OMBE, por sus siglas en inglés *organic molecular beam epitaxy*). En el transcurso de esta tesis, varias moléculas orgánicas han sido crecidas sobre diferentes superficies metálicas: perileno tetracarboxílico dianhídrido (PTCDA), diindenoperileno (DIP) y ftalocianina de cloro y aluminio (ClAlPc). Sus estructuras pueden observarse en la Figura 10.1.

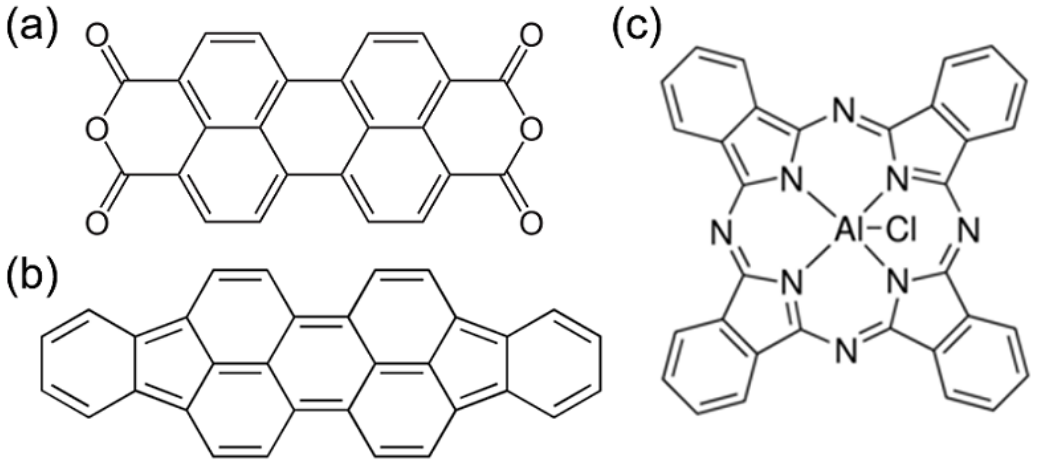

FIGURE 10.1: Representación estructural de las moléculas utilizadas en esta tesis: (a) perileno tetracarboxílico dianhídrido (PTCDA), (b) diindenoperileno (DIP) y (c) ftalocianina de cloro y aluminio (ClAlPc).

El PTCDA ha sido estudiado sobre dos superficies diferentes: Si(111)-7x7 y AgSi(111). El estudio estructural y electrónico a través de la obtención de mapas de la constante de decaimiento de la corriente túnel (mapas de kappa) de ambos sistemas (PTCDA sobre Si(111)—7x7 y PTCDA sobre AgSi(111)) se han presentado en el Capítulo 6. La molécula de DIP se ha estudiado sobre la superficie de cobre (111) y el estudio estructural y electrónico por espectroscopia de frecuencia versus voltaje, combinado con un estudio teórico llevado a cabo por un grupo de la Universidad de Paderborn se ha presentado en el Capítulo 7. Para finalizar, la ftalocianina de cloro y aluminio (ClAlPc) ha sido estudiada sobre oro (111). A diferencia de las otras moléculas utilizadas, la ClAlPc no es plana ya que tiene el átomo de cloro

fuera del plano de la molécula y por lo tanto tiene un dipolo permanente. En el Capítulo 8 se ha presentado el estudio estructural y electrónico de la primera y segunda capa de estas moléculas.

Introducción

La Interfase Molécula/Metal

La estructura y las propiedades electrónicas finales de las interfases molécula/metal son el resultado de la competición entre las interacciones intermoleculares y las interacciones con el sustrato. Dependiendo de la naturaleza de las interacciones entre las moléculas y la superficie se pueden dar, principalmente, dos procesos: fisisorción y quimisorción. La fisisorción es un proceso caracterizado por débiles interacciones de van der Waals dónde las moléculas están situadas a una distancia relativamente corta del sustrato. En cambio, la quimisorción es un proceso de interacción más fuerte y se suele definir por la formación de un enlace entre la molécula y el sustrato y/o por una transferencia de carga. En este caso las moléculas están a una distancia de la superficie menor que en el caso de la fisisorción.

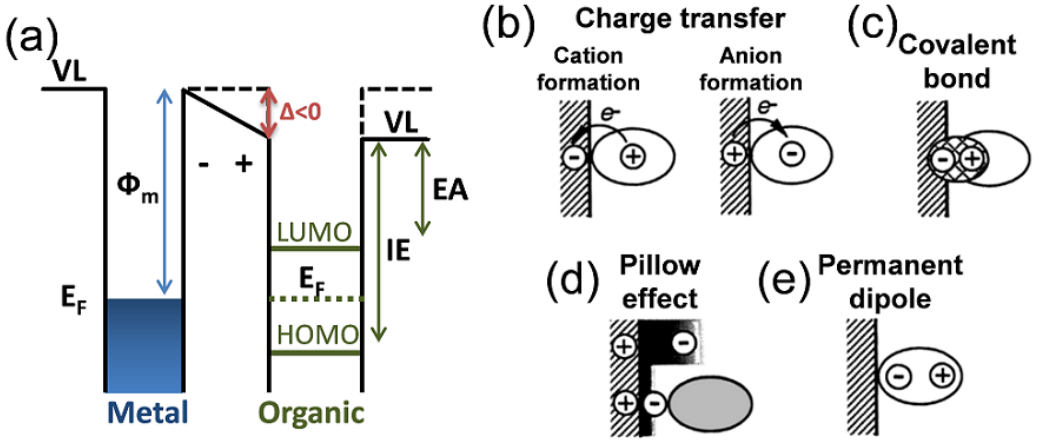

FIGURE 10.2: (a) Diagrama de energía de la interfase metal-semiconductor orgánico con un dipolo de interfase. (b)-(e) Ejemplos de posibles orígenes para la formación del dipolo: transferencia de carga desde la molécula al metal (formación de un catión) o del metal a la molécula (formación de un anión), formación de un enlace covalente, efecto *pillow* y presencia de una molécula con dipolo permanente (Figura adaptada de [110]).

Uno de los aspectos fundamentales a la hora de entender las interfases es la posición de los orbitales frontera de la molécula, orbital molecular ocupado de más energía (HOMO de sus siglas en inglés *highest occupied molecular orbital*) y orbital molecular no ocupado de más baja energía (LUMO de sus siglas en inglés *lowest unoccupied molecular orbital*) con el nivel de Fermi del metal (E_F). Varios experimentos han demostrado que el simple modelo de Schottky-Mott de la alineación de los niveles de vacio no funciona en el caso de las interfases molécula/metal [110] ya que la formación de un dipolo en la interfase (Δ) produce un desplazamiento de las posiciones relativas de los niveles de vacío (VL por sus siglas en inglés *vacuum level*) como puede verse en el diagrama presentado en la Figura 10.2(a). La formación de un dipolo de interfase provoca un desplazamiento de los niveles de vacío provocando variaciones en la función de trabajo local y por este motivo la función de trabajo local no se puede conocer solo sabiendo los niveles energéticos del metal y de la molécula por separado. En las Figuras 10.2(b)-(e) se muestran algunos ejemplos de los posibles orígenes de la formación del dipolo de interfase: transferencia de carga desde la molécula al metal (formación de un catión) o del metal a la molécula (formación de un anión), formación de un enlace covalente, efecto *pillow* y presencia de una molécula con dipolo permanente [37, 110, 116, 211].

Microscopía de Sonda de Barrido

En esta tesis se ha utilizado un microscopio combinado de efecto túnel (STM por sus siglas en inglés *scanning tunneling microscopy*) y de fuerzas atómicas de frecuencia modulada (FM-AFM por sus siglas en inglés *frequency modulation atomic force microscopy*).

El STM se basa en la medida de la corriente túnel entre una afilada punta metálica y una muestra conductora. Generalmente, se monta una punta en un escáner que permite el movimiento en x, y y z con precisión atómica y se aplica una diferencia de voltaje entre la punta y la muestra (V_{bias}). Cuando la distancia entre la punta y la superficie es de unos poco angstroms la corriente túnel fluye de la punta a la muestra o de la muestra a la punta, dependiendo de la polaridad de voltaje aplicado. La corriente túnel depende exponencialmente de la distancia entre la punta y la muestra y su magnitud se ve reducida un orden de magnitud cuando la distancia aumenta 1 Å. Además, la corriente túnel depende de la densidad

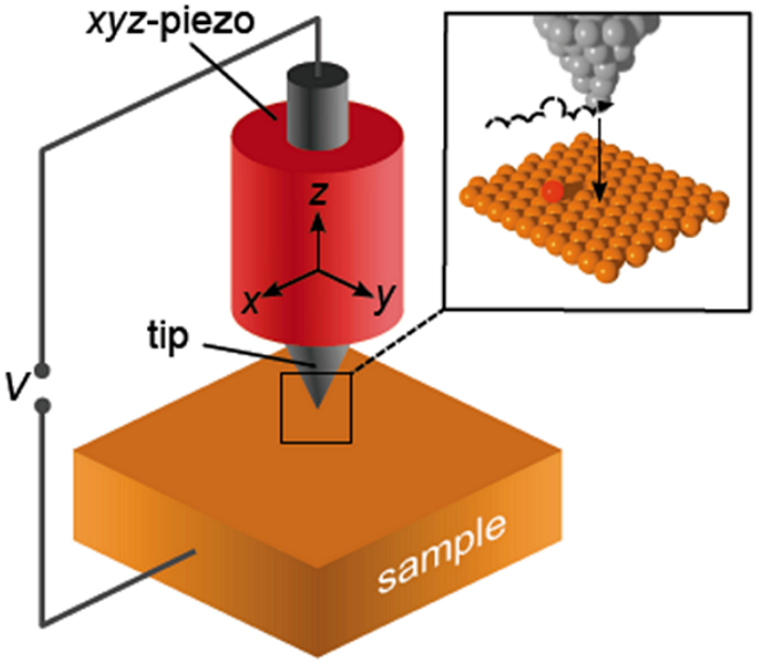

FIGURE 10.3: Representación esquemática del funcionamiento de un STM. La punta está montada en un piezo y escanea la muestra. En el zoom están representados los átomos de la punta y la muestra en el modo de corriente constante en el que un sistema de feedback corrige la distancia entre la punta y la muestra para mantener un valor constante de corriente túnel.

local de estados de la muestra (LDOS por sus siglas en inglés *local density of states*). Se puede trabajar en dos modos de medida: corriente constante o altura constante, siendo el modo de corriente constante el utilizado principalmente en la elaboración de esta tesis. La corriente túnel es la señal que utiliza un feedback (sistema de retroalimentación) que controla la distancia entre la punta y la muestra para mantener un valor de corriente túnel constante. En la Figura 10.3 está representado el funcionamiento básico de un STM operando en modo de corriente constante.

En el Capítulo 2 se ha demostrado la dependencia de la corriente túnel con la distancia punta-muestra y con la LDOS, en este resumen solo se mostrarán las ecuaciones que han sido utilizadas para el análisis de los resultados experimentales. Como ya hemos mencionado, la corriente túnel (I) depende exponencialmente de la distancia punta-muestra (z) según la expresión:

$$I = I_0 \exp\left(-2\kappa z\right), \tag{10.1}$$

siendo I_0 la corriente túnel en el punto de contacto y κ la constante de decaimiento de la corriente túnel. Una simple aproximación es asumir que la barrera de potencial entre la punta y la muestra es cuadrada, con un valor de función de trabajo aparente ϕ_{app}, y que solo los electrones del nivel de Fermi participan en la corriente túnel. En este caso:

$$\kappa = \frac{\sqrt{2\,m\,\phi_{app}}}{\hbar}, \tag{10.2}$$

siendo $\phi_{app} = \bar{\phi} - e\mathrm{V}_{bias}/2$, e la carga elemental, m la masa de un electrón y $\hbar$ la constante reducida de Planck. La función de trabajo promediada depende de la función de trabajo de la punta (ϕ_{tip}) y la muestra (ϕ_{sample}), $\bar{\phi} = (\phi_{tip} + \phi_{sample})/2$, así como del voltaje aplicado, V_{bias}.

El AFM se basa en la medida de las fuerzas que actúan entre la punta y la muestra, que suelen ser menores de 1 μN. En el FM-AFM se hace oscilar la punta a su frecuencia de resonancia (f_0) con una amplitud constante. La interacción entre la punta y la muestra provocan un cambio de la frecuencia de oscilación, de manera que $\Delta f = f - f_0$. Una interacción atractiva provoca un incremento en la frecuencia de resonancia ($\Delta f > 0$), mientras que una interacción repulsiva produce una disminución ($\Delta f < 0$).

El movimiento de la punta puede aproximarse a un oscilador armónico débilmente amortiguado con una constante de elasticidad efectiva $k' = k + k_{ts}$, siendo k la constante de elasticidad de la punta y k_{ts} la constante elástica de la interacción punta muestra ($k_{ts} = -\partial F_{ts}/\partial z$) tal y como se refleja en la Figura 10.4. La frecuencia de oscilación puede expresarse la siguiente manera [3, 70]:

$$f = f_0\sqrt{1 + \frac{k_{ts}}{k}} \approx f_0\left(1 + \frac{1}{2}\frac{k_{ts}}{k}\right). \tag{10.3}$$

El cambio en la frecuencia de oscilación, Δf, observado en FM-AFM es aproximadamente igual al gradiente de la fuerza entre la punta y la muestra ($\partial F_{ts}/\partial z$). En el caso de trabajar con pequeñas amplitudes de oscilación, más pequeñas que la constante de decaimiento de la fuerza entre la punta y la muestra, Δf se puede expresar del siguiente modo:

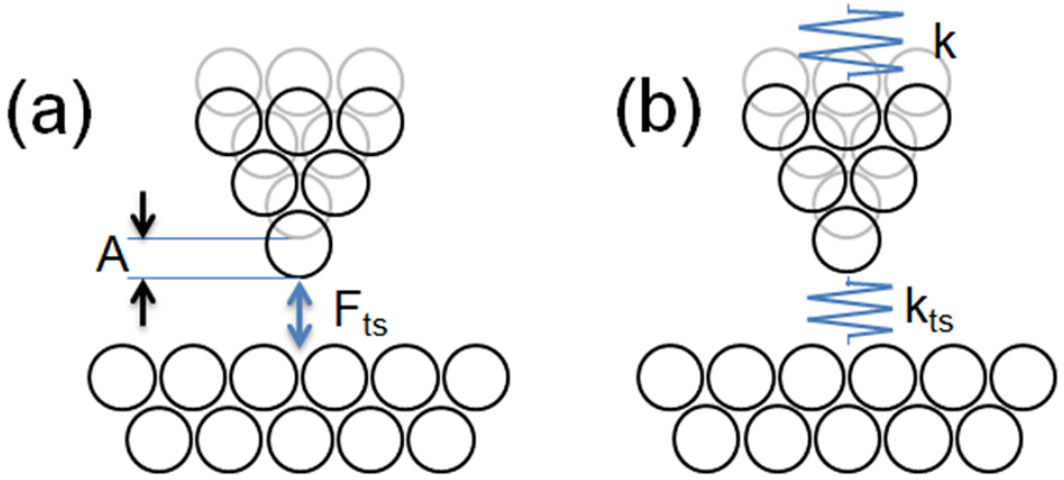

FIGURE 10.4: Representación esquemática de la punta y la muestra en un FM-AFM. La punta oscila a su frecuencia de resonancia con una amplitud constante, A. En (a) se muestra la amplitud de oscilación y la interacción punta-muestra (F_{ts}). En (b) están representadas la oscilación de la punta y la interacción entre la punta y la muestra como dos muelles. La constante de elasticidad de la punta es k y la de la interacción punta-muestra es k_{ts}.

$$\Delta f \approx -\frac{f_0}{2k}\frac{\partial F_{ts}}{\partial z}. \tag{10.4}$$

Una expresión más general de Δf, válida tanto para pequeñas como grandes amplitudes [70] es la siguiente:

$$\begin{aligned}\Delta f &= -\frac{f_0^2}{kA}\int_0^{1/f_0} F(z + A[1 + cos(2\pi f_0 t)])cos(2\pi f_0 t)dt \\ &= -\frac{f_0}{\pi k A}\int_{-1}^{1} F(z + A[1 + u])\frac{u}{\sqrt{1-u^2}}\, du.\end{aligned} \tag{10.5}$$

El problema de esta expresión es que no se conoce su solución analítica exacta. En la literatura se han propuesto varios métodos matemáticos [50, 73, 78] pero el método más utilizado, y el que se utiliza en esta tesis para la conversión de Δf a fuerzas, es el método propuesto por Sader y Jarvis [167]. El inconveniente es que es necesario alcanzar un rango de distancia entre la punta y la muestra donde no haya interacción ($F_{ts} = 0$).

En un microscopio combinado de STM y FM-AFM tanto la corriente túnel como el cambio en la frecuencia de oscilación son medidos y pueden ser utilizados como

la señal de entrada del feedback de topografía. Los sensores más utilizados en este tipo de microscopios son, a parte del cantiléver, el qPlus [71] y el Kolibri [206]. En esta tesis se ha utilizado el Kolibri a excepción de la parte experimental del Capítulo **??** que fue realizada en el grupo del Prof. F. J. Giessibl (Universidad de Regensburg). En la Figura 10.5 puede verse una representación esquemática de los feedbacks necesarios para su funcionamiento. En la parte izquierda está representado el feedback de STM y en la parte derecha los feedbacks de FM-AFM: un phase-locked loop (PLL) que mantiene la oscilación en fase, el feedback de amplitud que la mantiene la amplitud constante y el feedback que controla de la distancia entre la punta y la muestra manteniendo un valor de Δf constante.

El PLL y el feedback de amplitud están siempre activos y se puede seleccionar que el feedback de distancia utilice la señal de la corriente túnel (modo STM) o el cambio de frecuencia (modo FM-AFM). Cuando se trabaja en modo de STM, además de la imagen de topografía, se obtendrán la imagen simultánea del cambio de frecuencia y la disipación. Cuando se trabaja en modo de FM-AFM, además de la imagen de topografía y disipación, se obtendrá la imagen simultánea de corriente túnel. Además, también es posible realizar imágenes con el controlador de z desactivado, es decir, a altura constante, el canal de frecuencia aportará información sobre la interacción punta-muestra y el canal de corriente túnel aportará información sobre la densidad de estados.

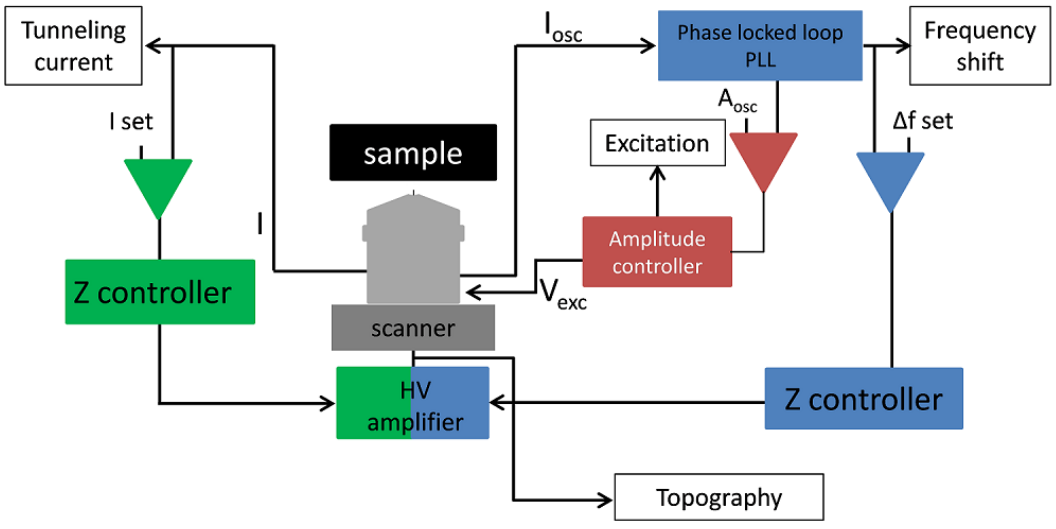

FIGURE 10.5: Representación esquemática de un Kolibri y la muestra y los feedbacks necesarios en un microscopio combinado STM/FM-AFM. Los feedbacks de STM están representados a la izquierda y los de FM-AFM a la derecha.

La fuerza total que actúa entre la punta de nuestro sistema y la muestra está formada por diferentes contribuciones que pueden ser divididas según el rango de actuación en fuerzas de corto y largo alcance. Cuando se trabaja en UHV, las fuerzas de largo alcance están compuestas por electrostática y van der Waals, mientras que las de corto alcance están compuestas por interacciones químicas. Las fuerzas de corto alcance son las que proporcionan resolución atómica, de modo que es deseable minimizar las fuerzas de largo alcance. La interacción electrostática se puede minimizar escogiendo el valor adecuado de voltaje, mientras que la fuerza de van der Waals depende del radio de la punta y no se puede eliminar. La fuerza electrostática puede expresarse como:

$$F_{elec}(z) = \frac{1}{2}\frac{\partial C}{\partial z}(V_{bias} - V_{CPD})^2, \tag{10.6}$$

siendo C la capacitancia, V_{bias} el voltaje aplicado entre la punta y la muestra y V_{CPD} la diferencia de potencial de contacto (CPD por sus siglas en inglés *contact potential difference*). De la anterior expresión se puede extraer que la fuerza electrostática depende parabólicamente con el V_{bias} y que puede ser anulada eligiendo $V_{bias} = V_{CPD}$. La diferencia de potencial de contacto está causada por la diferencia de función de trabajo entre la punta y la muestra, de modo que $eV_{CPD} = \phi_{tip} - \phi_{sample} = \Delta\phi$ siendo ϕ_{tip} la función de trabajo de la punta y ϕ_{sample} la función de trabajo de la muestra. Midiendo la dependencia de Δf con el voltaje aplicado se puede calcular el valor de CPD y por lo tanto la diferencia de función de trabajo entre la punta y la muestra. Este tipo de espectroscopia ha sido utilizada a lo largo de esta tesis para calcular la diferencia de función de trabajo entre diferentes zonas de la superficie.

Además de las fuerzas nombradas hasta ahora (electrostática, van der Waals y química) que producen un cambio en la frecuencia de oscilación, también pueden existir fuerzas no conservativas que provocan un cambio en la amplitud de oscilación. El canal de excitación, también llamado disipación en esta tesis, es el valor de energía que se tiene que proporcionar al sistema para mantener la amplitud de oscilación constante y viene regulado por el feedback de amplitud.

Oxidación de Cu(111) por Bombardeo de una Mezcla de Argón y Aire

Con el fin de poder estudiar las propiedades de una capa fina de óxido de cobre se ha utilizado un particular método de preparación basado en la oxidación de una superficie limpia de Cu(111) por bombardeo iónico de una mezcla de argón y aire y un posterior calentamiento. La superficie final está formada por zonas alternadas de óxido de cobre y cobre siendo el óxido de cobre de una capa atómica de grosor. Las estructuras de éste óxido han resultado ser muy diversas y se han podido observar hasta seis tipos de estructuras coexistiendo en la misma muestra.

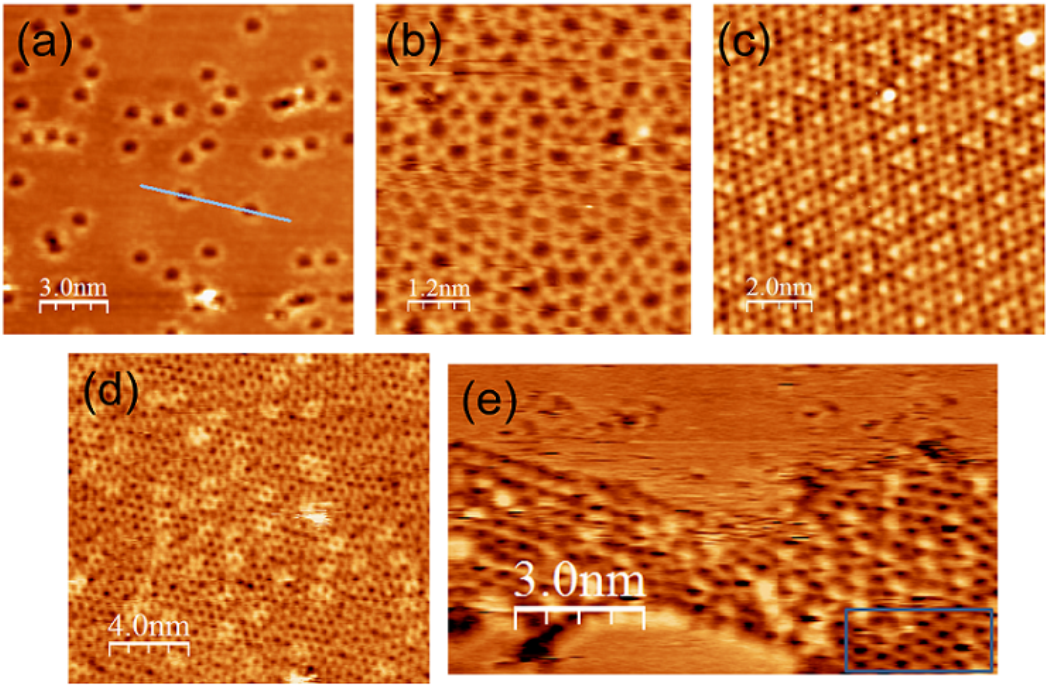

FIGURE 10.6: Ejemplos de imágenes de STM y FM-AFM de zonas con (a) oxígeno adsorbido, (b) estructura SOHC, (c) estructura "44", (d) estructura deficiente de oxígeno (OD) y (e) zona donde coexisten la estructura OD y la HC (marcado con un cuadrado azul). Parámetros: (a) I = 240 pA, Bias = -0.30 V, A = 200 pm, (b) I = 194 pA, Bias = -0.47 V, A = 200 pm, (c) I = 88 pA, Bias = +1.40 V, A = 200 pm, (d) I = 195 pA, Bias = -1.46 V, A = 200 pm y (e) Δf = -1.20 Hz, Bias = -0.22 V, A = 200 pm.

.

Dependiendo de la cantidad de oxígeno hemos observado oxígeno adsorbido sobre cobre (OA por sus siglas en inglés *oxygen adsorbed*) [226, 231], cuatro estructuras de óxido de cobre que ya habían sido previamente descritas en la literatura [137, 157, 226, 231, 232] y una nueva estructura que no había sido descrita

en la literatura y a la que hemos llamado estructura de *honeycomb* abierta (OHC por sus siglas en inglés *open honeycomb*). Un ejemplo de imágenes topográficas de oxígeno adsorbido y las cuatro estructuras del óxido de cobre previamente descritas se han presentado en la Figura 10.6. Las cuatro estructuras previamente descritas en la literatura son: honeycomb de corto alcance (SOHC por sus siglas en inglés *short order honeycomb*), honeycomb de largo alcance (HC), estructura deficiente en oxígeno (OD por sus siglas en inglés *oxygen deficient*) y la estructura "44".

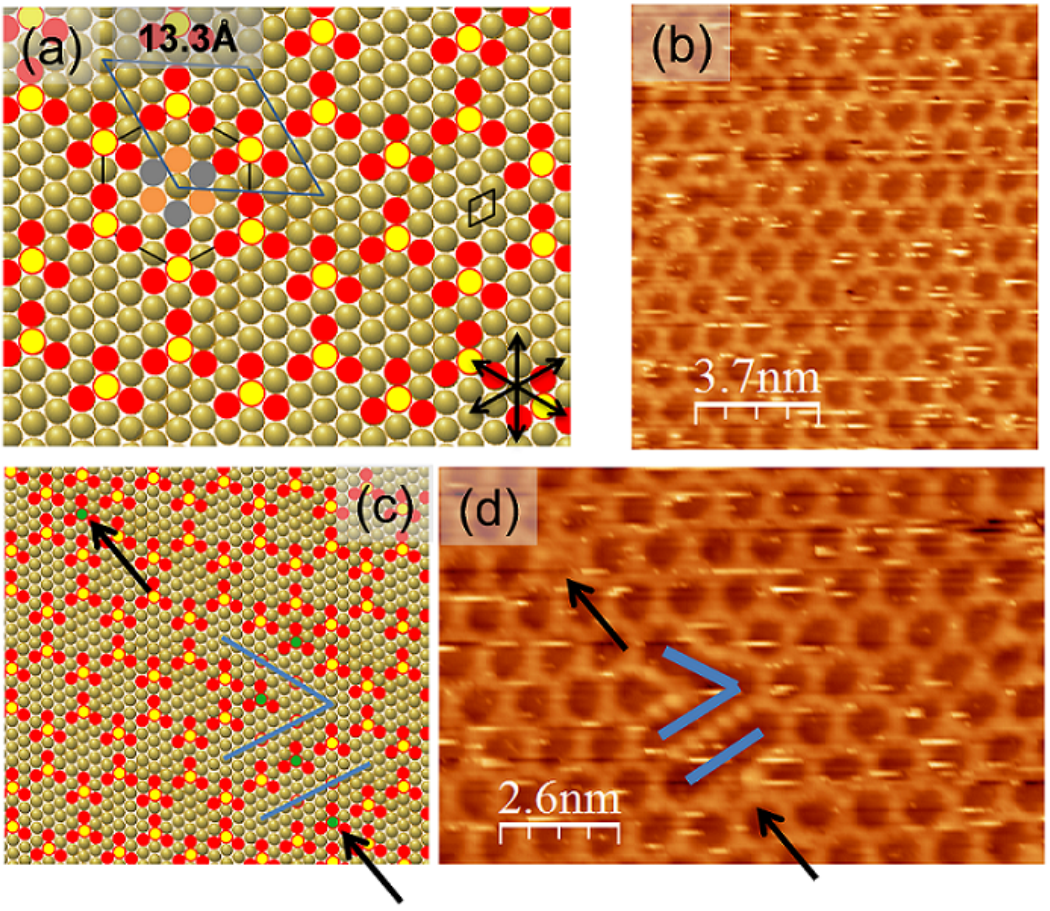

FIGURE 10.7: (a) Representación esquemática del modelo propuesto para la estructura OHC. Los átomos de oxígeno están representados por círculos amarillos y los de cobre por círculos rojos, mientras que los átomos de cobre de la superficie de Cu(111) están representados por círculos dorados. La celda unidad de la estructura de OHC y las direcciones de segundos vecinos del sustrato están indicadas en (a). (b) Imagen de topografía de STM de una región con estructura OHC. En la figura (c) está representado el modelo de la OHC adaptada a los defectos topográficos que pueden verse en la imagen topográfica presentada en (d). Parámetros: I = 110 pA, Bias = -1.56 V, A = 200 pm.

.

En la Figura 10.7 están representadas dos imágenes topográficas de la nueva estructura *honeycomb* abierta así como el modelo propuesto em esta tesis. Esta estructura tiene una gran celda unidad de $\sim$ 1.3 nm y está rotada 30° respecto la estructura *honeycomb*. El modelo propuesto consta de unidades de Cu_3O como puede verse en el modelo presentado en la Figura 10.7(a), los átomos de cobre de las unidades de Cu_3O están representados por círculos rojos y en amarillo los átomos de oxígeno. El modelo propuesto, además de representar bien el tamaño y orientación de la estructura respecto el sustrato y la estructura *honeycomb* del óxido de cobre, puede explicar los defectos que se encuentran en algunas zonas. En las Figuras 10.7(c) y (d) están representados el modelo adaptado a los defectos estructurales observados en la imagen topográfica presentada en (d). Se observan dos tipos de defectos, los producidos por las vacantes de unidades de Cu_3O (indicado con líneas azules) y los producidos por una unidad extra de Cu_3O en el centro del hexágono (indicado con flechas negras).

Caracterización Espectroscópica del Óxido de Cobre

Con el fin de completar el estudio estructural de una fina capa de óxido crecida sobre Cu(111) se han realizado medidas de diferencia de potencial de contacto (CPD) y espectroscopia de corriente túnel y fuerza. El hecho de tener una superficie heterogénea, formada por zonas de cobre y óxido de cobre, nos permite realizar espectroscopias en ambas regiones de forma alterna y poder identificar indeseados cambios de punta que son tan comunes cuando se realizan este tipo de espectroscopias a temperatura ambiente.

Las medidas de CPD realizadas en ambas regiones de la superficie muestran gran variabilidad de resultados con una diferencia máxima de CPD entre ambas regiones de $\sim$ +150 mV, siendo el valor mayor sobre óxido de cobre que sobre el cobre. La gran variabilidad de resultados podría ser atribuida a la gran variedad de estructuras que presenta el óxido de cobre. De modo que, la diferencia de función de trabajo entre ambas regiones, si existe, tiene un valor máximo de 150 meV ($\phi_{Cu_20} - \phi_{Cu} \sim +150$ meV) siendo la función de trabajo mayor sobre el óxido de cobre.

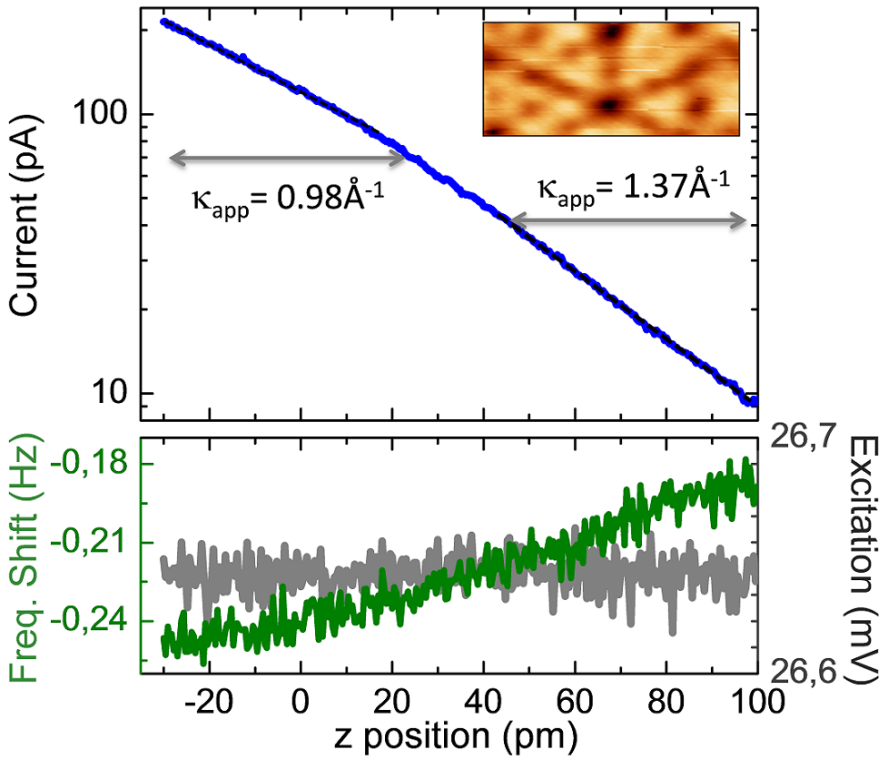

FIGURE 10.8: Corriente túnel (en escala logarítmica), cambio de frecuencia y excitación versus distancia punta-muestra. En el gráfico superior se ha insertado la imagen donde se ha realizado la espectroscopia. Parámetros: Bias = -0.89 V, A = 200 pm. Imagen de STM: I = 119 pA, Bias = -0.89 V, A = 200 pm, 2.7 nm x 1.2 nm.

Al realizar medidas de corriente túnel frente distancia para evaluar los valores de la constante de decaimiento (κ) sobre las dos regiones, se observó un comportamiento anómalo cuando la espectroscopia se realizaba sobre el óxido de cobre. La corriente túnel no dependía exponencialmente con la distancia entre la punta y la muestra, por lo que no se podía determinar un valor único de la constante de decaimiento para todo el rango de distancias como puede verse en la Figura 10.8. A mayor distancia punta-muestra se obtiene un valor de la constante de decaimiento de 1.37 Å^{-1} mientras que a menor distancia se obtiene un valor de 0.98 Å^{-1}. Con el fin de comprender el origen de esta anomalía, en esta tesis se han propuesto dos modelos. El primero está basado en una resistencia en serie que produce una disminución de la corriente a distancias punta-muestra cortas. El segundo modelo está basado en una deformación de la distancia entre los átomos de la punta y la muestra, produciendo que la distancia entre punta y muestra sea mayor de la medida por el desplazamiento del piezo.

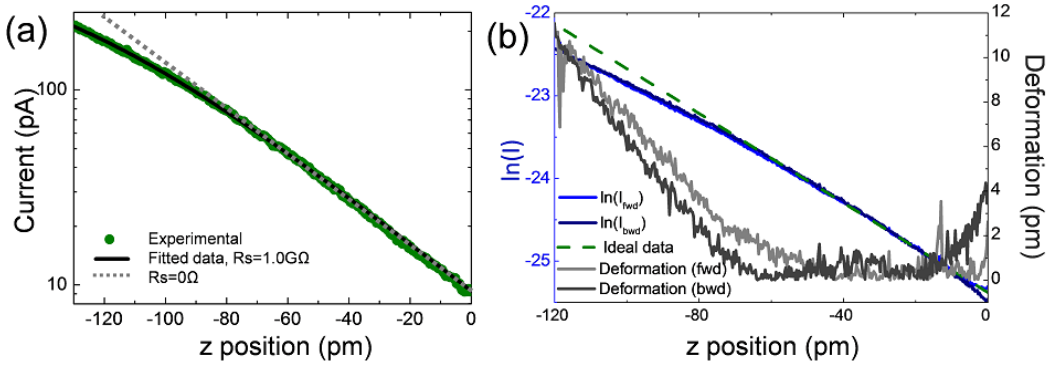

FIGURE 10.9: Ejemplos de corriente túnel versus distancia punta-muestra analizados por (a) el modelo de la resistencia en serie y (b) asumiendo una deformación de la distancia punta-muestra. En (a) el valor de la resistencia en serie obtenido es de $R_s = 1.4 \pm 0.1$ GΩ y la constante de decaimiento es $\kappa_{Cu_2O} \sim 1.23$ Å^{-1}. En (b) se ha asumido que la desviación de la dependencia exponencial de la corriente túnel con la distancia es debido a una deformación de la distancia punta-muestra, siendo el valor máximo de dicha deformación de 11 pm. Parámetros: (a) Bias = -0.89 V y A = 200 pm.

Con ambos modelos se han analizado tres sets de datos experimentales. El modelo de la resistencia en serie consigue reproducir bien uno de los tres sets de datos mientras en los otros dos los ajustes no son tan buenos. Por otro lado, el modelo de la deformación funciona siempre ya que se trata de calcular la desviación de la corriente túnel respecto lo que debería de ser en el caso de deformación cero. Aquí hemos asumido que el rango de distancia más lejana, cuando la corriente túnel empieza a fluir entre punta y muestra, es cuando la deformación es cero aunque esta suposición podría no ser cierta.

Además, en uno de los sets de datos de corriente túnel versus distancia realizados sobre el cobre y el óxido de cobre, se observó una inestabilidad en el valor de la corriente túnel. La inestabilidad corresponde a un salto abrupto en el valor de la corriente túnel a valores más pequeños que se mantiene durante unos pocos picómetros y luego recupera el valor de corriente como puede verse en la Figura 10.10(a). Aquí hemos interpretado el salto de corriente túnel como una deformación de la distancia entre la punta obteniendo un valor de 24 pm en todos las espectroscopias como puede verse en el ejemplo mostrado en la Figura 10.10(b). Una posible explicación es que existan dos estados de punta, que dieran entre en si en 24 pm en su distancia vertical. De todos modos, otros factores podrían ser la causa de estos abruptos saltos de corriente túnel como por ejemplo un incremento en el área de la punta involucrada en la corriente túnel.

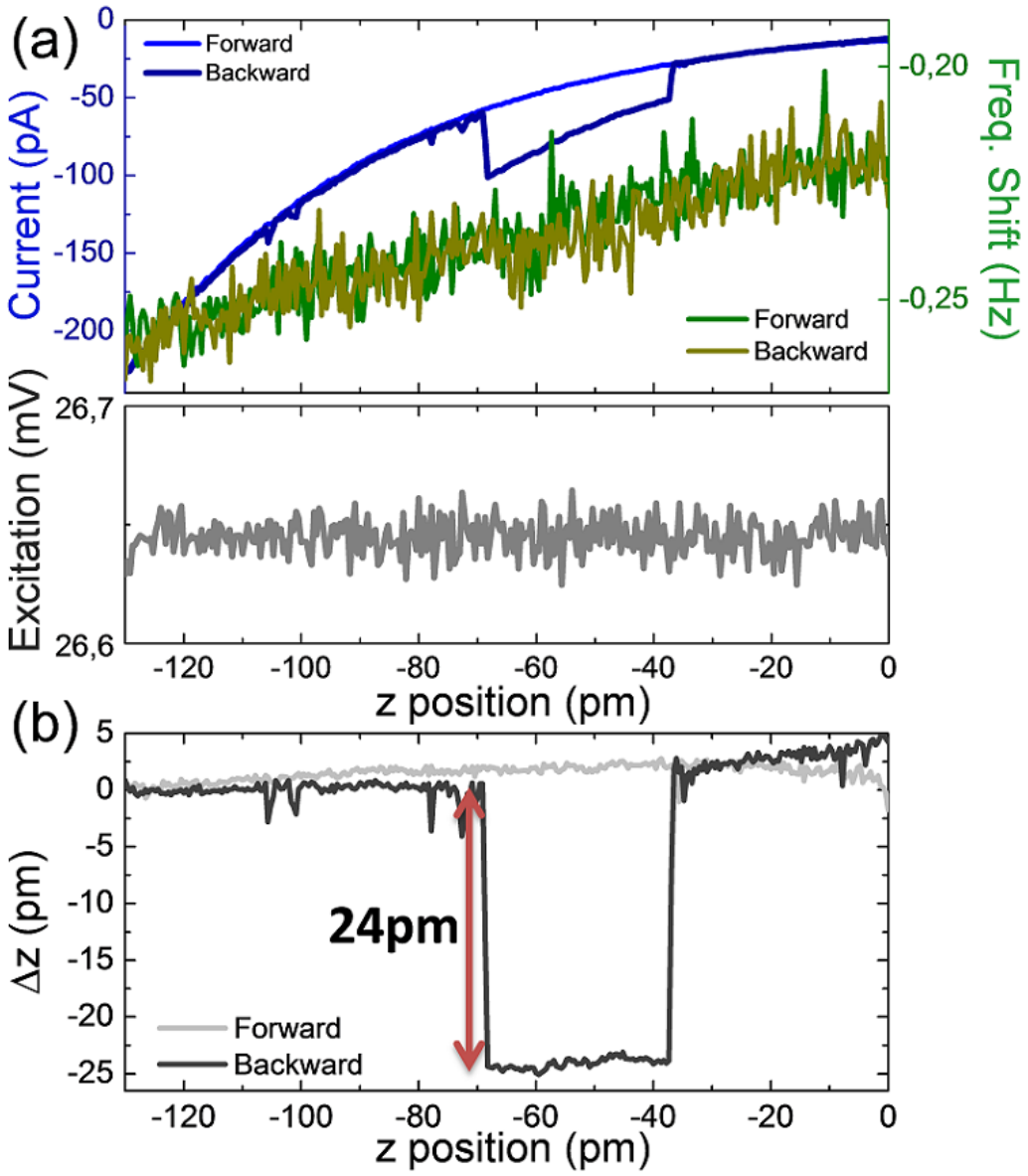

FIGURE 10.10: Ejemplo de espectroscopia de corriente túnel versus distancia realizada sobre el cobre donde puede observarse una inestabilidad. En (a) están representados los canales de corriente túnel (azul), Δf (verde) y excitación (gris). El abrupto y reversible salto solo se observa en el canal de la corriente túnel. En (b) se representa el valor del cambio de distancia en z (Δz) que explicaría el observado cambio del valor de la corriente túnel. Parámetros: Bias = -1.30 V y A = 200 pm.

Estudio de PTCDA sobre Si(111)-7x7 y AgSi(111)

En los últimos años la molécula PTCDA (perileno tetracarboxílico dianhídrido) ha sido ampliamente estudiada sobre diversas superficies. En esta tesis se ha estudiado sobre dos superficies, Si(111)–7x7 y AgSi(111) [108], observándose una interacción molécula-sustrato muy diferente. Sobre la superficie de Si(111)–7x7 la interacción es tan grande que la molécula queda fuertemente adsorbida y no puede difundir y formar monocapas ordenadas de forma que, a bajos recubrimientos, pueden encontrarse moléculas aisladas. En cambio, sobre la superficie de AgSi(111) la interacción molécula-sustrato es más débil permitiendo que las moléculas difundan y formen monocapas ordenadas. Ambos sistemas han sido estudiados por STM, FM-AFM y además se ha aplicado un método dinámico que permite obtener, de forma simultánea a las medidas de STM, mapas de la constante de decaimiento de la corriente túnel (κ). Dicha constante está relacionada con la diferencia de función de trabajo entre la muestra y la punta.

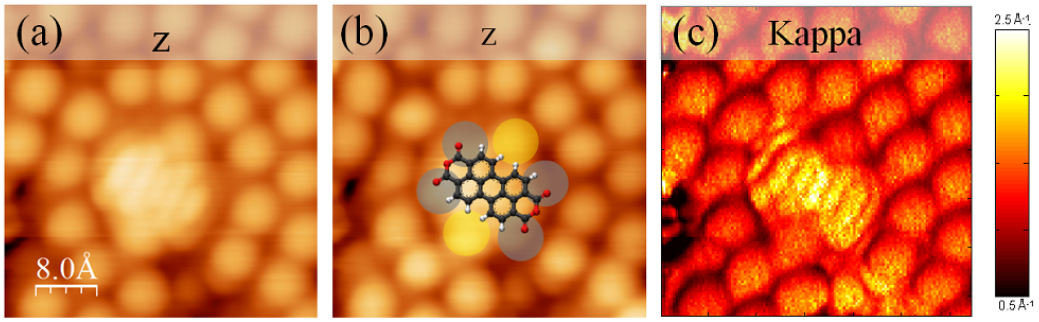

FIGURE 10.11: (a) Imagen topográfica de STM de una molécula de PTCDA adsorbida sobre el *corner hole* de la superficie Si(111)–7×7. (b) Misma imagen que (a) pero con un modelo de la molécula de PTCDA añadido y con los 6 adátomos de alrededor del *corner hole* indicados. (c) Mapa simultaneo de la constante de decaimiento de la corriente túnel en la que puede verse un valor mayor sobre la molécula. Parámetros: I = 250 pA, Bias = -1.50 V y A = 60 pm.

Cuando se subliman una pequeña cantidad de moléculas sobre la superficie de Si(111)–7x7, estas quedan adsorbidas aleatoriamente sobre la superficie. Se observan muchos adsorbatos de formas y tamaños muy diversos y solamente las moléculas adsorbidas sobre el *corner hole* de la superficie presentan un aspecto similar, por lo que el estudio realizado en este sistema se centra en estas moléculas. En las imágenes de STM de la molécula se pueden observar cinco lóbulos paralelos entre sí y perpendiculares al eje longitudinal de la molécula (Figuras 10.11(a) y

(b)), esta estructura ha sido previamente relacionada con el LUMO de la molécula libre [146]. En esta configuración, la molécula queda adsorbida plana y los cuatro oxígenos carboxilo de la molécula se sitúan sobre cuatro de los seis adátomos que hay alrededor del *corner hole* de la superficie de Si(111)–7x7 (ver Figura 10.11(b)). Estudios previos indican que se produce una transferencia de carga desde el sustrato a los cuatro oxígenos de los grupo anhidro [146] y al realizar las medidas dinámicas de la constante de decaimiento se observa un valor de κ mayor sobre la molécula que sobre el sustrato, como puede verse en la Figura 10.11(c). El mayor valor de κ sobre la molécula coincide con el dipolo de superficie que formaría una transferencia de carga del sustrato a la molécula. Los cinco lóbulos que se observaban en la imagen de STM se siguen observando pero, contrariamente a lo observado por STM, el lóbulo central no aparece con el mismo contraste que el resto. Esto se podría deber a una distribución no homogénea de la carga produciendo un dipolo de superficie mayor sobe el lóbulo central.

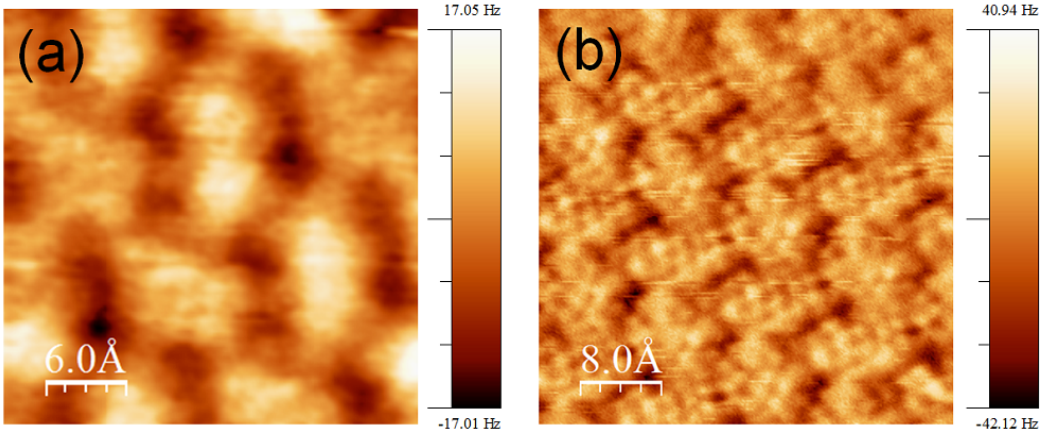

FIGURE 10.12: Imágenes de FM-AFM obtenidas a altura constante (se muestra el canal de Δf) de la fase herringbone del PTCDA sobre AgSi(111). En (a) se puede observar contraste intermolecular en las zonas en las que se esperan que estén los puentes de hidrógenos. En (b) se puede observar contraste intermolecular y la estructura del perileno central de la molécula puede ser identificado. Parámetros: (a) Bias = -0.13 V, A = 50 pm y (b) A = 40 pm, Bias = 0.10 V.

Las moléculas de PTCDA sobre AgSi(111) forman dos fases ordenadas incluso a bajos recubrimientos, una fase cuadrada y una fase *herringbone*. En este sistema, estudios previos también indican que existe una pequeña transferencia de carga desde el sustrato a la molécula [82]. En la estructura *herringbone*, las dos moléculas inequivalentes de la celda unidad presentan frecuentemente una altura

aparente diferente cuando se mide en modo STM, pudiendo ser el origen del contraste topográfico o electrónico o una combinación de ambos. Imágenes de FM-AFM (obtenidas en modo de altura constante) no revelan un contraste topográfico entre las dos moléculas inequivalentes de la celda unidad, descartando el origen topográfico de la diferencia observada por STM. Además, las imágenes de FM-AFM mostradas en la Figura 10.13 revelan resolución intermolecular en la imagen mostrada en (a) e intermolecular en la imagen mostrada en (b). El contraste intermolecular se observa en las zonas donde se esperaría encontrar los puentes de hidrógeno [195, 223], pero estudios recientes han revelado que el contraste intermolecular obtenido por FM-AFM podría ser debido a los puentes de hidrógeno pero no puede ser asociado inequívocamente [87]. El contraste intermolecular que se puede observar en la Figura 10.13(b) es de gran relevancia, ya que es uno de los primeros estudios que muestran que se puede conseguir este nivel de resolución cuando se trabaja a temperatura ambiente.

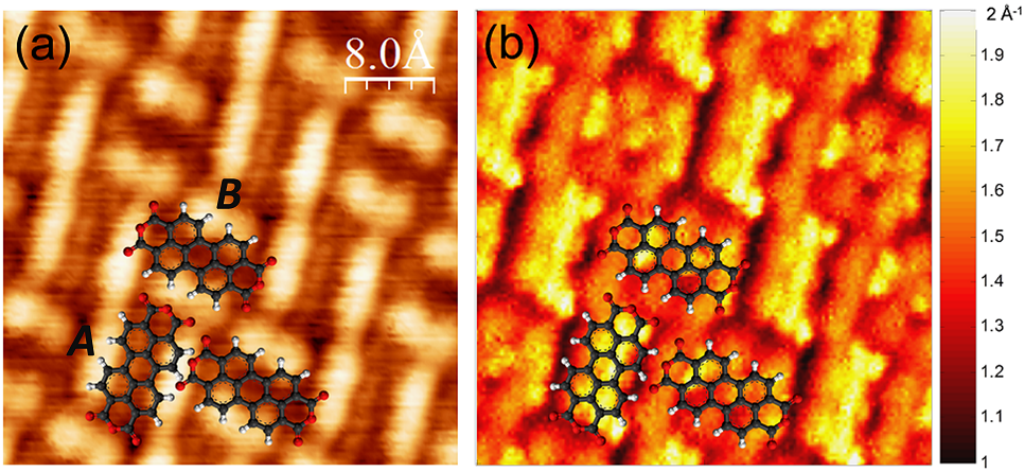

FIGURE 10.13: (a) Imagen topográfica en STM de la fase herringbone del PTCDA sobre AgSi(111) y (b) el mapa de la constante de decaimiento de la corriente túnel (κ) obtenido simultáneamente a la imagen topográfica. En la imagen de topografía no se observa contraste entre las dos moléculas inequivalentes de la celda unidad pero, en cambio, si que se puede observar en mapa de la constante de decaimiento. Parámetros: I = 200 pA, Bias = -1.20 V, A = 50 pm.

En las medidas de la constante de decaimiento de la corriente túnel podemos confirman que ambas moléculas tiene valores diferentes de κ, incluso cuando las condiciones de medida no revelan un contraste en la imagen simultánea de topografía (STM) como puede verse en la Figura 10.13. Una posible explicación para este contraste es que la interacción total (molécula-molécula y molécula-sustrato) que sufren las dos moléculas de la celda unidad no sea igual y que por lo tanto la

transferencia neta de carga no sea la misma. Además del contraste entre las dos moléculas inequivalentes de la celda unidad puede observarse un valor no constante de κ dentro de cada molécula, lo que sugiere una distribución no homogénea de la carga dentro de la molécula.

Estudio de la Monocapa de DIP sobre Cu(111)

El diindenoperileno (DIP) es una molécula aromática que, al igual que el PTCDA, es un derivado del perileno. Esta molécula también ha sido muy estudiada sobre diferentes superficies y en esta tesis se ha estudiado sobre la superficie de Cu(111) de forma experimental, mediante STM/FM-AFM, y de forma teórica mediante cálculos utilizando la teoría del funcional de la densidad (DFT por sus siglas en inglés *density functional theory*) a través de una colaboración con la Universidad de Paderborn [4].

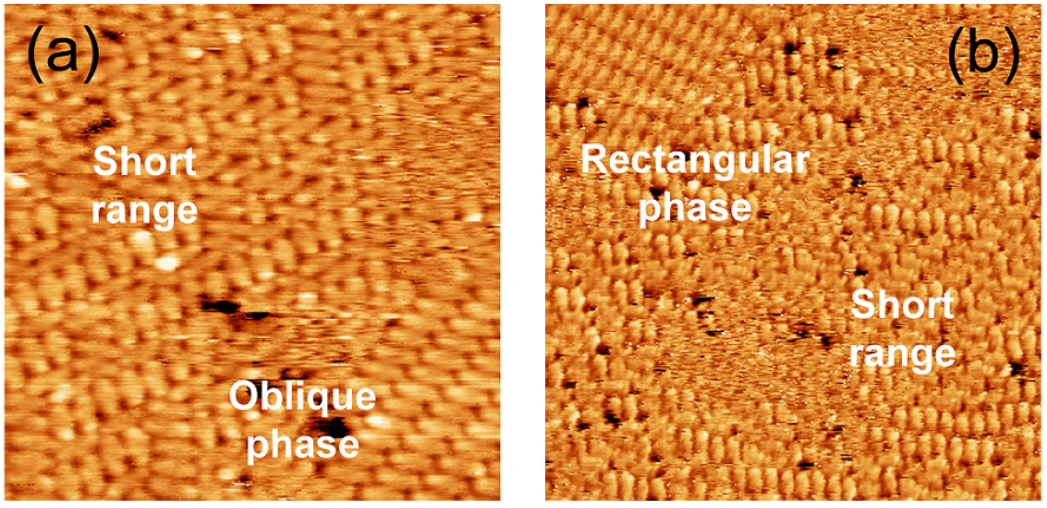

FIGURE 10.14: Imágenes topográficas de STM de $\sim$ 1 ML de DIP sobre la superficie de Cu(111). Se observa la coexistencia de fases con orden a corto (short range) y largo alcance (fase oblicua y rectangular). Parámetros: (a) 15 nm x 15 nm, I = 130 pA, Bias = -1.250 V, A = 200 pm y (b) 30 nm x 30 nm, I = 370 pA, Bias = -0.370 V, A = 200 pm.

Se han llevado a cabo cálculos de DFT de la adsorción de una molécula de DIP sobre la superficie de Cu(111) para determinar las configuraciones más favorables energéticamente. Los resultados muestran que, cuando el centro de la molécula se encuentra sobre un hueco de la estructura del Cu(111) la configuración más favorable es con el lado longitudinal de la molécula orientado a lo largo de una de

las direcciones ⟨112⟩ del sustrato. En esta configuración la molécula está paralelamente adsorbida sobre la superficie pero no completamente plana. En cambio, cuando se fija el centro de la molécula sobre un átomo de la superficie de Cu(111) la configuración que resulta ser la más favorable es la de la molécula a lo largo de una de las direcciones ⟨110⟩. El estudio de la monocapa y de las estructuras más estables también se llevó a cabo por DFT, revelando que las estructuras más favorables son dos fases oblicuas, con misma celda unidad pero diferente registro con el sustrato, en concordancia con estudios previos de STM [40]. En estas fases la molécula está desviada 10° respecto una de las direcciones ⟨112⟩ del sustrato. Además de las dos fases oblicuas se obtuvo una estructura sin orden a largo alcance en la que las moléculas están alineadas con una de las direcciones ⟨112⟩ del sustrato, a la que llamamos estructura SR (por sus siglas en inglés *short-range*). Las energías de adsorción de las fases con y sin orden a largo alcance son bastante similares por lo que sería de esperar que ambas coexistieran en la superficie.

Los resultados experimentales demuestran la coexistencia de fases de corto y largo alcance en una misma área, como puede observarse en la Figura 10.14, además de la existencia de una fase bidimensional formada por moléculas móviles. Además de la fase oblicua y la SR, que ya habían sido reportadas previamente, se observa la existencia de una estructura rectangular (Figura 10.14(b)). El tamaño de la celda unidad de la fase oblicua es del orden de la obtenida teóricamente y las moléculas de la fase de orden a corto alcance están rotadas entre sí 60° y alineadas a lo largo de las tres direcciones ⟨112⟩ de la superficie de cobre. Las moléculas de la fase oblicua están orientadas a lo largo de una de las direcciones ⟨112⟩ y las de la fase rectangular a lo largo de una de las direcciones ⟨110⟩.

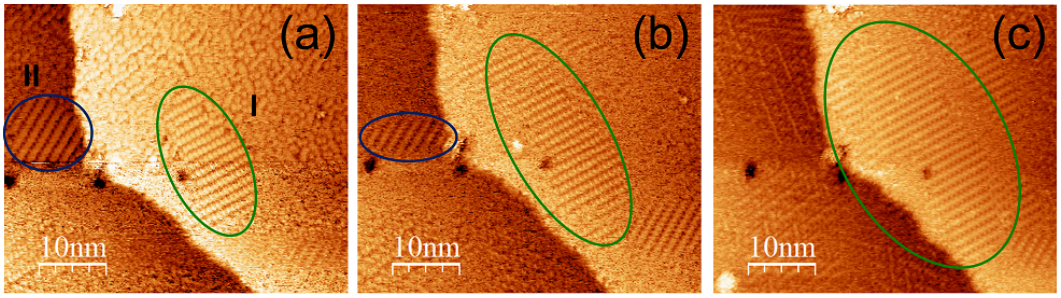

FIGURE 10.15: (a)-(c) Imágenes consecutivas de STM de la misma área de una monocapa de DIP sobre Cu(111). Hay dos dominios con orden a largo alcance indicados en verde (dominio *I*) y azul (dominio *II*). Parámetros: I = 90 pA, Bias = -0.450 V y A = 200 pm.

Se ha evaluado la estabilidad relativa de dos dominios de orden a largo alcance en función de la influencia de escaneos consecutivos de la punta para la obtención de imágenes. En la Figura 10.15 pueden observarse tres imágenes consecutivas de la misma área obtenidas por STM. Las moléculas del dominio I están orientadas a lo largo de una de las direcciones $\langle 112 \rangle$ del Cu(111) y las del dominio II a lo largo de una de las direcciones $\langle 110 \rangle$ del sustrato. Continuos escaneos de la punta sobre este área tienen un efecto diferente en ambos dominios: el aumento del área del dominio I y la desaparición del dominio ordenado II y su conversión en un dominio de moléculas con orden a corto alcance. De estos datos puede extraerse que los dominios cuyas moléculas están orientadas a lo largo de una de las direcciones $\langle 112 \rangle$ son más estables que los dominios con sus moléculas orientadas a lo largo de una de las direcciones $\langle 110 \rangle$.

Medidas de diferencia potencial de contacto (CPD) realizadas sobre la superficie limpia de Cu(111) y de la monocapa de DIP revelan que la función de trabajo de la superficie disminuye aproximadamente 1 eV con la formación de una monocapa de DIP como puede verse en la Figure 10.16. Estos valores coinciden perfectamente con valores obtenidos por técnicas de fotoemisión [42] demostrando la gran utilidad de las medidas de CPD.

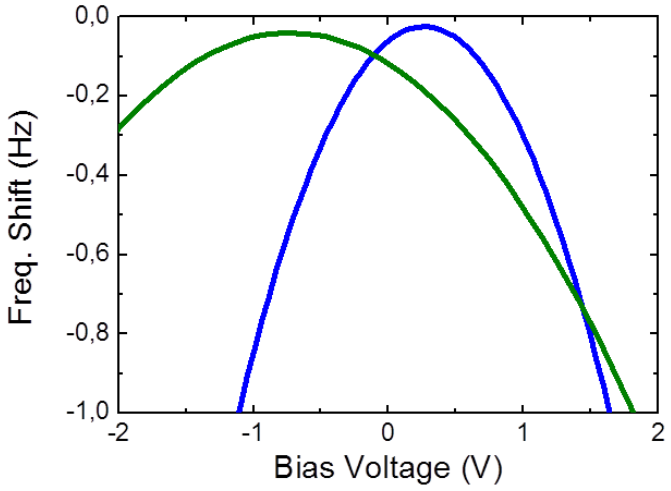

FIGURE 10.16: Espectroscopias de Δf versus voltaje aplicado realizadas sobre la superficie limpia de Cu(111) (representada en azul), CPD = +266 ±1 mV, y sobre una monocapa de DIP sobre Cu(111) (representada en verde), CPD = -725 ±2 mV.

Estudio de ClAlPc sobre Au(111)

La ftalocianina de aluminio y cloro (ClAlPc) es una molécula aromática que tiene el átomo central (cloro) perpendicular al plano de la molécula y, por lo tanto, tiene un momento dipolar. Al adsorberse sobre superficies lo puede hace en dos configuraciones posibles: con el átomo de cloro hacia el sustrato (Cl-down) o al inverso (Cl-up). Ambas configuraciones tienen un momento dipolar igual pero de signo contrario. En esta tesis, se ha estudiado el crecimiento de la primera y segunda capa de ClAlPc sobre una superficie de Au(111). La primera capa está formada por moléculas que forman una fase ordenada y cuadrada en configuración Cl-up como puede verse en la imagen de STM y la representación esquemática de la Figura 10.17. El tamaño de celda unidad es de $\mathbf{a} = \mathbf{b} = 1.38 \pm 0.02$ nm estando **a** orientado a lo largo de las direcciones ⟨110⟩ del Au(111) y **b** a lo largo de la direcciones ⟨110⟩ del sustrato. Las moléculas están débilmente rotadas, $\sim 5°$, respecto los vectores de la celda unidad.

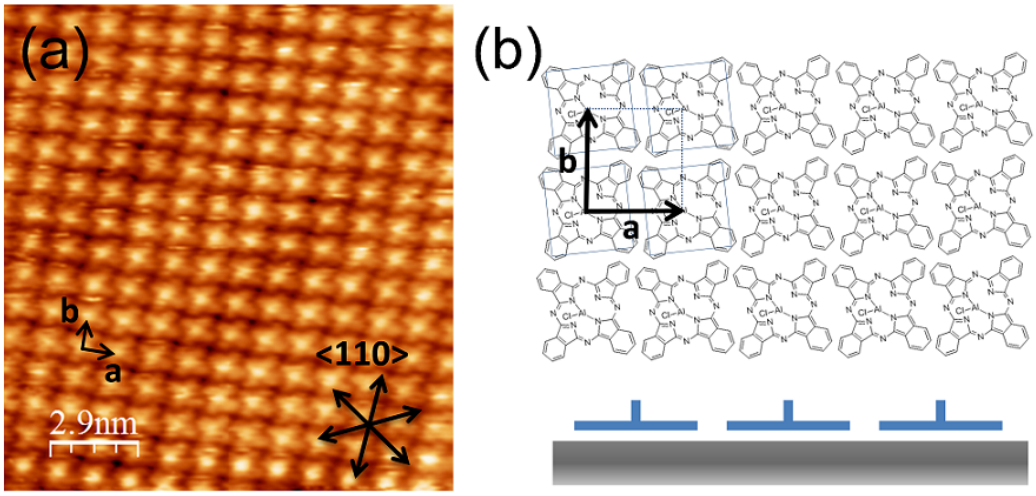

FIGURE 10.17: Imagen topográfica de una monocapa de ClAlPc sobre Au(111) y (b) representación esquemática de la configuración de la primera capa. Las moléculas se adsorbed en configuración Cl-up. En (a) están indicados los vectores de la celda unidad así como las direcciones equivalentes ⟨110⟩ del sustrato. Parámetros: (a) I = 130 pA, Bias = +1.25 V, A = 200 pm y (c) I = 45 pA, Bias = +1.00 V, A = 200 pm.

Aumentando el tiempo de deposición de ClAlPc se forma una segunda capa molecular parcial en configuración Cl-down como puede verse en las imágenes de STM presentadas en la Figura 10.18. La segunda capa forma una fase con el mismo tamaño de celda unidad que la primera pero cada molécula de la segunda capa

está colocada entre cuatro moléculas de la primera capa (ver representación esquemática de la Figura 10.18(d)). Las moléculas de la segunda capa también están ligeramente rotadas respecto los vectores de la celda unidad.

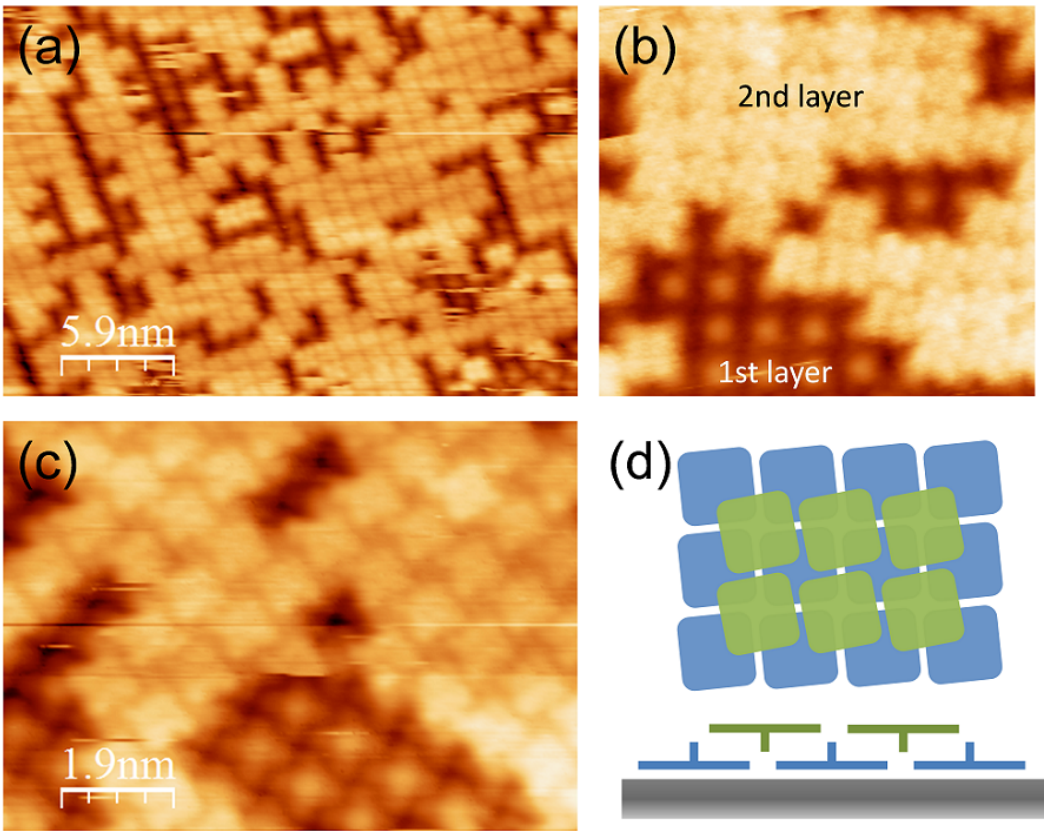

FIGURE 10.18: (a)-(c) Imágenes topográficas de una bicapa parcial de ClAlPc sobre Au(111). En (d) se ha representado la configuración de las moléculas en la primera capa (azul) y en la segunda (verde) tanto visto desde arriba como de lado. Parámetros: (a) I = 70 pA, Bias = +2.00 V, A = 200 pm, (b) I = 100 pA, Bias = +2.00 V, A = 200 pm y (c) I = 80 pA, Bias = +2.00 V, A = 200 pm.

Como se ha comentado, las moléculas en configuración Cl-down y Cl-up tienen un dipolo del mismo valor pero de signo opuesto, de modo que el cambio de función de trabajo que produce la monocapa de moléculas en configuración Cl-up se espera que se cancele, o al menos se minimice, por la capa de moléculas de la segunda capa en configuración Cl-down. Esto es solo una aproximación ya que existen más factores que afectan al cambio en la función de trabajo. Con el fin de evaluar esta influencia, se realizaron medidas de diferencia de potencial de contacto en la primera y segunda capa de moléculas como puede verse en la Figura 10.19. Los valores de CPD de ambas capas moleculares revelan una diferencia de función de trabaja entre la primera y segunda capa de 0.12 eV, siendo la función de trabajo

menor en la segunda capa. De la diferencia de función de trabajo entre ambas capas puede calcularse el valor de dipolo molecular a través de la ecuación de Helmholtz, obteniendo un valor de 0.8 D. La reducción de función de trabajo con la formación de la segunda capa sigue el sentido esperado. Sin embargo, el valor de la variación, así como el valor obtenido de dipolo molecular son menores de lo esperado. La falta de concordancia entre el valor teórico esperado y el obtenido experimentalmente refleja la importancia de otros factores influyentes, como podría ser la depolarización y el efecto *pillow*.

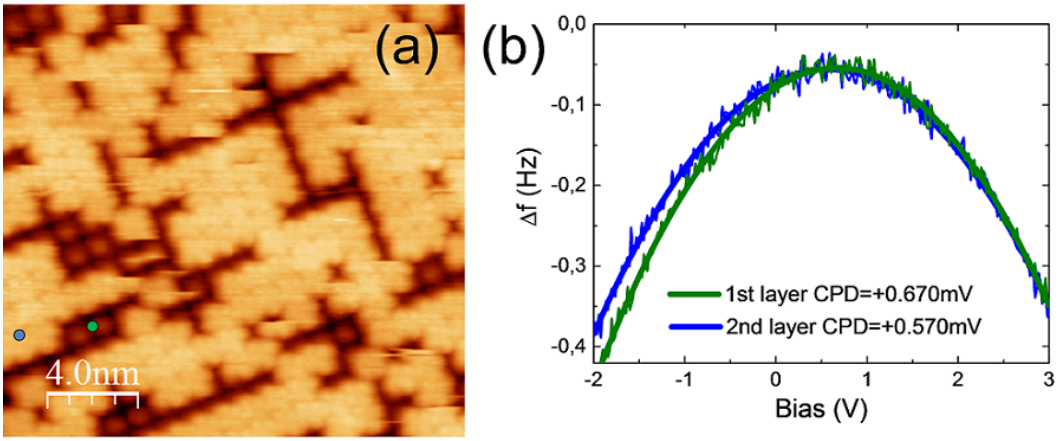

FIGURE 10.19: (a) Imagen topográfica de una bicapa parcial de ClAlPc sobre Au(111) donde se han realizado medidas de Δf vs. voltaje aplicado presentadas en (b). En verde está representada la espectroscopia medida sobre la primera capa y en azul sobre la segunda. Parámetros: I = 90 pA, Bias = +2.00 V, A = 200 pm.

Abbreviations

AFM	atomic force microscopy
AM	amplitude modulation
bcc	body-centered cubic
CITS	current imaging tunneling spectroscopy
CPD	contact potential difference
csa	coordinatively saturated
cus	coordinatively unsaturated
DAS	dimer adatom stacking
DFT	density functional theory
DIP	diindenoperylene
DL	disconmesuration lines
DOS	density of states
fcc	face centered cubic
FFT	fast Fourier transformed
FH	faulted half
FM	frequency modulation
HC	honeycomb
HCT	honeycomb chain trimer
HOMO	highest occupied molecular orbital
HOPG	highly oriented pyrolytic graphite
HV	high voltage
IET	inequivalent trimer
IFFT	inverse fast Fourier transform
KPFM	Kelvin probe force microscopy

LA	long axis
LCPD	local contact potential difference
LDOS	local density of states
LEED	low energy electron diffraction
LER	length-extension resonator
LR	long range
LT	low temperature
LUMO	lowest unoccupied molecular orbital
NEXAFS	near edge x-ray absorption fine structure
NN	nearest-neighbor
NNN	next nearest-neighbor
OA	oxygen adsorbed
OD	oxygen deficient
OFET	organic field effect transistor
OHC	open honeycomb
OLED	organic light emitting diodes
OMBE	organic molecular beam epitaxy
OSC	organic solar cell
Pc	phthalocyanine
PES	photoelectron spectroscopy
PLL	phase locked loop
PTCDA	perylene-3,4,9,10-tetracarboxylic anhydride
RT	room temperature
SCL	site coincident lattice
SEM	scanning electron microscope
SOHC	short order honeycomb
SPM	scanning probe microscopy
SR	short range
STM	scanning tunneling microscopy
STS	scanning tunneling spectroscopy
S-W	Stone-Wales

TSP	titanium sublimation pump
UF	unfaulted half
UHV	ultra-high vacuum
UPS	ultraviolet photoelectron spectroscopy
VASP	Vienna ab initio simulation package
vdW	van der Waals forces
XPS	X-ray photoelectron spectroscopy
XSW	X-ray standing wave

Acknowledgements

First of all I would like to thank my thesis supervisors Dr. Esther Barrena and Prof. Carmen Ocal and all present and former group members for their excellent support during the last four years: Ana Pérez, Dr. Markos Paradinas, Laura López, Rogger Palacios, Mahdieh Aghamohammadi, Marc Vila and Dr. Luis Eduardo Garzón. Many thanks also to Prof. Franz J. Giessibl and his group for the support during my stay there: Dr. Jay Weymouth, Ferdinand Huber, Dr. Daniel Wastl, Daniel Meuer, Dr. Thomas Hofmann, Matthias Emmrich, Dr. Florian Pielmeier, Dr. Maximilian Schneiderbauer, Dr. Angelo Peronio, Nirmalesh Kumar, Petra Wild, Anja Merkel and Florian Griesbeck.

I want to thank Dr. Elisa Vallés, Alba Synchrotron and financial support from the MINECO Grants No. BES-2011-045990, No. EEBB-I-2013-06282 and No. MAT2013-47869-C4-1-P and from the Generalitat Project 2014 SGR-501.

Bibliography

[1] A. Abdurixit, A. Baratoff, and E. Meyer. Molecular dynamics simulations of dynamic force microscopy: applications to the Si(111)-7x7 surface. *Applied Surface Science*, 157:355–360, 2000.

[2] H. Aizawa, M. Tsukada, N. Sato, and S. Hasegawa. Asymmetric structure of the Si(111)-V3xV3-Ag surface. *Surface Science*, 429:L509–L514, 1999.

[3] T. R. Albrecht, P. Grutter, D. Horne, and D. Rugar. Frequency modulation detection using high-Q cantilevers for enhanced force microscope sensitivity. *Journal of Applied Physics*, 69(2):668–673, 1991.

[4] H. Aldahhak, S. Matencio, E. Barrena, C. Ocal, W. G. Schmidt, and E. Rauls. Structure formation in diindenoperylene thin films on copper(111). *Phys. Chem. Chem. Phys.*, 17(14):8776–8783, 2015.

[5] S. J. Altenburg and R. Berndt. Local work function and STM tip-induced distortion of graphene on Ir(111). *New Journal of Physics*, 16, 2014.

[6] A. F. Armitage and D. P. Woodruff. Initial adsorption kinetics of oxygen and sulphur on copper cylindrical crystal surfaces. *Surface Science Letters*, 114(2-3):414–430, 1982.

[7] G. Ashkenasy, D. Cahen, R. Cohen, and A. Shanzer. Molecular Engineering of Semiconductor Surfaces and Devices. *Accounts of chemical research*, 35(2):121–128, 2002.

[8] H. Baek, S. Jeon, J. Seo, and Y. Kuk. Geometric and Electronic Structure of Passive CuN Monolayer on Cu(111) : A Scanning Tunneling Microscopy

and Spectroscopy Study. *Journal of the Korean Physical Society*, 56(2):620, 2010.

[9] P. Bagus, V. Staemmler, and C. Wöll. Exchangelike Effects for Closed-Shell Adsorbates: Interface Dipole and Work Function. *Physical Review Letters*, 89(9):096104, 2002.

[10] R. Baier, C. Leendertz, M. Lux-Steiner, and Sa. Sadewasser. Toward quantitative Kelvin probe force microscopy of nanoscale potential distributions. *Physical Review B*, 85(16):1–6, 2012.

[11] J. Bardeen. Tunnelling from a many-particle point of view. *Physical Review Letters*, 6(2):57–59, 1961.

[12] E. Barrena, D. G. de Oteyza, H. Dosch, and Y. Wakayama. 2D supramolecular self-assembly of binary organic monolayers. *Chemical Physical and Physical Chemistry*, 8(13):1915–8, September 2007.

[13] C. Barth, T. Hynninen, M. Bieletzki, C. R. Henry, A. S. Foster, F. Esch, and U. Heiz. AFM tip characterization by Kelvin probe force microscopy. *New Journal of Physics*, 12, 2010.

[14] J. V. Barth, H. Brune, G. Ertl, and R. J. Behm. Scanning tunneling microscopy observations on the reconstructed Au(111) surface: Atomic structure, long-range superstructure, rotational domains, and surface defects. *Physical Review B*, 42(15), 1990.

[15] N. Beaumont, I. Hancox, P. J. Sullivan, R. A. Hatton, and T. S. Jones. Increased efficiency in small molecule organic photovoltaic cells through electrode modification with self-assembled monolayers. *Energy and Environental Science*, 4:1708–1711, 2011.

[16] S. Belaidi, P. Girard, and G. Leveque. Electrostatic forces acting on the tip in atomic force microscopy: Modelization and comparison with analytic expressions. *Journal of Applied Physics*, 81(3):1023–1030, 1997.

[17] F. Besenbacher and J. K. Norskov. Oxygen chemisorption on metal surfaces: General trends for Cu, Ni and Ag. *Progress in Surface Science*, 44(1):5–66, 1993.

[18] G. Binnig, H. Rohrer, Ch. Gerber, and E. Weibel. Surface Studies by Scanning Tunneling Microscopy, 1982.

[19] G. Binnig, H. Rohrer, Ch. Gerber, and E. Weibel. Tunneling through a controllable vacuum gap. *Applied Physics Letters*, 40(2):178, 1982.

[20] G. Binnig, H. Rohrer, Ch. Gerber, and E. Weibel. 7x7 Reconstruction on Si(111) Resolved in real Space. *Physical Review Letters*, 50(2):120, 1983.

[21] J. M. Blanco, F. Flores, and R. Pérez. STM-theory: Image potential, chemistry and surface relaxation. *Progress in Surface Science*, 81(10-12):403–443, 2006.

[22] F. Bocquet, L. Nony, and C. Loppacher. Polarization effects in noncontact atomic force microscopy: A key to model the tip-sample interaction above charged adatoms. *Physical Review B*, 83(3):035411, 2011.

[23] K. Bradley, J. P. Gabriel, M. Briman, A. Star, and G. Grüner. Charge transfer from ammonia physisorbed on nanotubes. *Physical Review Letters*, 91(21):218301, 2003.

[24] M. Bruening, R. Cohen, J. F. Guillemoles, Ta. Moav, J. Libman, A. Shanzer, and D. Cahen. Simultaneous control of surface potential and wetting of solids with chemisorbed multifunctional ligands. *Journal of the American Chemical Society*, 119(24):5720–5728, 1997.

[25] S a Burke, J M LeDue, Y Miyahara, J M Topple, S Fostner, and P Grütter. Determination of the local contact potential difference of PTCDA on NaCl: a comparison of techniques. *Nanotechnology*, 20(26):264012, July 2009.

[26] C. Bürker, N. Ferri, A. Tkatchenko, A. Gerlach, J. Niederhausen, T. Hosokai, S. Duhm, J. Zegenhagen, N. Koch, and F. Schreiber. Exploring the bonding

of large hydrocarbons on noble metals: Diindoperylene on Cu(111), Ag(111), and Au(111). *Physical Review B*, 87(16):1–5, 2013.

[27] C. Julian Chen. *Introduction to scanning tunneling microscopy*. 1993.

[28] V. Caciuc, M. C. Lennartz, N. Atodiresei, S. Karthäuser, and S. Blügel. Fine tuning of the electronic structure of π-conjugated molecules for molecular electronics. *Nanotechnology*, 22(14):145701, 2011.

[29] N. M. Caffrey, K. Buchmann, N. Hauptmann, C. Lazo, P. Ferriani, S. Heinze, and R. Berndt. Competing forces during contact formation between a tip and a single molecule. *Nano Letters*, 15(111):150728113205008, 2015.

[30] A. Castellanos-Gomez, R. H. M. Smit, N. Agraït, and G. Rubio-Bollinger. Spatially resolved electronic inhomogeneities of graphene due to subsurface charges. *Carbon*, 50(3):932–938, 2012.

[31] M. B. Casu, I. Biswas, M. Nagel, P. Nagel, S. Schuppler, and T. Chassé. Photoemission electron microscopy of diindenoperylene thin films. *Physical Review B - Condensed Matter and Materials Physics*, 78(7):1–7, 2008.

[32] M. B. Casu, S. A. Savu, B. E. Schuster, I. Biswas, C. Raisch, H. Marchetto, T. Schmidt, and T. Chassé. Island shapes and aggregation steered by the geometry of the substrate lattice. *Chemical Communications*, 48(55):6957, 2012.

[33] M. B. Casu, B. E. Schuster, I. Biswas, C. Raisch, H. Marchetto, T. Schmidt, and T. Chassé. Locally resolved core-hole screening, molecular orientation, and morphology in thin films of diindenoperylene deposited on Au(111) single crystals. *Advanced Materials*, 22(33):3740–3744, 2010.

[34] I. Chizhov, A. Kahn, and G. Scoles. Initial growth of 3,4,9,10-perylenetetracarboxylic-dianhydride (PTCDA) on Au (111): a scanning tunneling microscopy study. *Journal of Crystal Growth*, 208:449–458, 2000.

[35] A. Clarke, J. Pethica, J. Nieminen, F. Besenbacher, E. Læ gsgaard, and I. Stensgaard. Quantitative Scanning Tunneling Microscopy at Atomic Resolution: Influence of Forces and Tip Configuration. *Physical Review Letters*, 76(8):1276–1279, 1996.

[36] J. P. Cleveland, B. Anczykowski, A. E. Schmid, and V. B. Elings. Energy dissipation in tapping-mode atomic force microscopy. *Applied Physics Letters*, 72(20):2613–2615, 1998.

[37] X. Crispin, V. Geskin, A. Crispin, J. Cornil, R. Lazzaroni, W. R. Salaneck, and J. Brédas. Characterization of the interface dipole at organic/ metal interfaces. *Journal of the American Chemical Society*, 124(27):8131–8141, 2002.

[38] S. Datta. *Electronic Transport in Mesoscopic Systems*. Cambridge University Press, Cambridge, 1995.

[39] D. G. de Oteyza, E. Barrena, H. Dosch, J. E. Ortega, and Y. Wakayama. Tunable symmetry and periodicity in binary supramolecular nanostructures. *Physical Chemistry Chemical Physics*, 13(10):4220–4223, 2011.

[40] D. G. de Oteyza, E. Barrena, H. Dosch, and Y. Wakayama. Nanoconfinement effects in the self-assembly of diindenoperylene (DIP) on Cu(111) surfaces. *Physical Chemistry Chemical Physics*, 11(39):8741–4, 2009.

[41] D. G. De Oteyza, A. El-Sayed, J. M. Garcia-Lastra, E. Goiri, T. N. Krauss, A. Turak, E. Barrena, H. Dosch, J. Zegenhagen, A. Rubio, Y. Wakayama, and J. E. Ortega. Copper-phthalocyanine based metal-organic interfaces: The effect of fluorination, the substrate, and its symmetry. *Journal of Chemical Physics*, 133(21), 2010.

[42] D. G. de Oteyza, J. M. García-Lastra, M. Corso, B. P. Doyle, L. Floreano, A. Morgante, Y. Wakayama, A. Rubio, and J. E. Ortega. Customized electronic coupling in self-assembled donor-acceptor nanostructures. *Advanced Functional Materials*, 19(22):3567–3573, 2009.

[43] T. A. Delchar. Oxygen chemisorption on copper single crystals. *Surface Science*, 27(1):11–20, 1971.

[44] A. Della Pia, M. Riello, A. Floris, D. Stassen, T. S. Jones, D. Bonifazi, A. De Vita, and G. Costantini. Anomalous coarsening driven by reversible charge transfer in supramolecular assembly at metal-organic interfaces. *ACS Nano*, 8(12):12356–12364, 2014.

[45] Y. Ding, C. T. Chan, and K. M. Ho. Structure of the Ag/Si(111) Surface from First-Principles Calculations. *Physical Review Letters*, 67(11):1454–1458, 1991.

[46] S. M. Driver and D. P. Woodruff. Nitrogen-induced pseudo-(100) reconstruction of the Cu(111) surface identified by STM. *Surface Science*, 442(1):1–8, 1999.

[47] L. H. Dubois. Oxygen chemisorption and cuprous oxide formation on Cu(111): A high resolution EELS study. *Surface Science*, 119(2-3):399–410, 1982.

[48] S. Duhm, A. Gerlach, I. Salzmann, B. Bröker, R.L. Johnson, F. Schreiber, and N. Koch. PTCDA on Au(111), Ag(111) and Cu(111): Correlation of interface charge transfer to bonding distance. *Organic Electronics*, 9(1):111–118, 2008.

[49] U. Dürig. Conservative and dissipative interactions in dynamic force microscopy. *Surface and Interface Analysis*, 27(56):467–473, 1999.

[50] U. Durig. Extracting interaction forces and complementary observables in dynamic probe microscopy. *Applied Physics Letters*, 76(9):1203–1205, 2000.

[51] A. Dürr, N. Koch, M. Kelsch, A. Rühm, J. Ghijsen, R. Johnson, J.-J. Pireaux, J. Schwartz, F. Schreiber, H. Dosch, and A. Kahn. Interplay between morphology, structure, and electronic properties at diindenoperylene-gold interfaces. *Physical Review B*, 68(11):1–12, 2003.

[52] A. C Dürr, F Schreiber, K. A. Ritley, V. Kruppa, J. Krug, H. Dosch, and B. Struth. Rapid roughening in thin film growth of an organic semiconductor (diindenoperylene). *Physical Review Letters*, 90(1):016104, 2003.

[53] D. Écija, J. M. Gallego, and R. Miranda. The adsorption of atomic N and the growth of copper nitrides on Cu(100). *Surface Science*, 603(15):2283–2289, 2009.

[54] K. Eguchi, Y. Takagi, T. Nakagawa, and T. Yokoyama. Molecular orientation and electronic states of vanadyl phthalocyanine on Si(111) and Ag(111) surfaces. *Journal of Physical Chemistry C*, 117(44):22843–22851, 2013.

[55] M. Eremtchenko, J. A. Schaefer, and F. S. Tautz. Understanding and tuning the epitaxy of large aromatic adsorbates by molecular design. *Nature*, 425(6958):602–5, 2003.

[56] B. Eren, L. Lichtenstein, C. Wu, H. Bluhm, G. A. Somorjai, and M. Salmeron. Reaction of CO with Preadsorbed Oxygen on Low-Index Copper Surfaces: An Ambient Pressure XPS and STM Study. *The Journal of Physical Chemistry C*, (111):150304125501007, 2015.

[57] G. Ertl. Untersuchung von oberflächenreaktionen mittels beugung langsamer elektronen (LEED): I. Wechselwirkung von O2 und N2O mit (110)-, (111)- und (100)-Kupfer-Oberflächen. *Surface Science*, 6:208–232, 1967.

[58] S. D. Evans, E. Urankar, A. Ulman, and N. Ferris. Self-Assembled Monolayers of Alkanethiols Containing a Polar Aromatic Group: Effects of the Dipole Position on Molecular Packing, Orientation, and Surface Wetting Properties. *Journal of American Chemical Society*, 113(11):4121–4131, 1991.

[59] R. M. Feenstra and J. A. Stroscio. Tunneling spectroscopy of the GaAs(110) surface. *Journal of Vacuum Science & Technology B*, 5(4):923, 1987.

[60] Richard P. Feynman. There's plenty of room at the bottom: An Invitation to Enter a New Field of Physics. In *American Physical Society Meeting*, 1959.

[61] J. C. Fisher and I. Giaever. Tunneling through thin insulating layers. *Journal of Applied Physics*, 32(1961):172–177, 1961.

[62] S. R. Forrest. Ultrathin Organic Films Grown by Organic Molecular Beam Deposition and Related Techniques. *Chemical Reviews*, 97(94):1793–1896, 1997.

[63] S. Fremy, S. Kawai, R. Pawlak, T. Glatzel, A. Baratoff, and E. Meyer. Three-dimensional dynamic force spectroscopy measurements on KBr(001): atomic deformations at small tip–sample separations. *Nanotechnology*, 23(5):055401, 2012.

[64] H. Fukagawa, S. Hosoumi, H. Yamane, S. Kera, and N. Ueno. Dielectric properties of polar-phthalocyanine monolayer systems with repulsive dipole interaction. *Physical Review B*, 83(8):085304, 2011.

[65] Ch. Gerber G. Binnig, C.F. Quate. Atomic Force Microscope. *Physical review letters*, 56(9), 1986.

[66] A. Gerlach, T. Hosokai, S. Duhm, S. Kera, O. T. Hofmann, E. Zojer, J. Zegenhagen, and F. Schreiber. Orientational ordering of nonplanar phthalocyanines on Cu(111): Strength and orientation of the electric dipole moment. *Physical Review Letters*, 106(15):1–4, 2011.

[67] M. Giesen-Seibert, R. Jentjens, M. Poensgen, and H. Ibach. Time dependence of step fluctuations on vicinal Cu(1119) surfaces investigated by tunneling microscopy. *Physical Review Letters*, 71(21):3521–3525, 1993.

[68] M. Giesen-Seibert, F. Schmitz, R. Jentjens, and H. Ibach. Time fluctuations of steps on Cu(11n) surfaces investigated by temperature variable tunneling microscopy. *Surface Science*, 329(1-2):47–60, 1995.

[69] F. J. Giessibl. Atomic resolution of the silicon (111)-(7 x 7) surface by atomic force microscopy. *Science*, 267(13):68, 1995.

[70] F. J. Giessibl. Forces and frequency shifts in atomic-resolution dynamic-force microscopy. *Physical Review B*, 56(24):16010–16015, 1997.

[71] F. J. Giessibl. High-speed force sensor for force microscopy and profilometry utilizing a quartz tuning fork. *Applied Physics Letters*, 73(26):3956–3958, 1998.

[72] F. J. Giessibl. Advances in atomic force microscopy. *Review of Modern Physics*, 75(3):949–983, 2003.

[73] F. J. Giessibl and H. Bielefeldt. Physical interpretation of frequency-modulation atomic force microscopy. *Physical Review B*, 61(15):9968–9971, 2000.

[74] T. Glatzel. Measuring atomic-scale variations of the electrostatic force. In *Kelvin Probe Force Microscopy*, volume 48, chapter 13, pages 7–24. Springer b edition, 2011.

[75] K. Glöckler, C. Seidel, A. Soukopp, M. Sokolowski, E. Umbach, M. Böhringer, R. Berndt, W. Schneider, R. Berndt, and W. Schneider. Highly ordered structures and submolecular scanning tunnelling microscopy contrast of PTCDA and DM-PBDCI monolayers on Ag (111) and Ag (110). *Surface Science*, 405:1–20, 1998.

[76] A. M. Goedken, S. L. Silva, S. M. York, and F. M. Leibsle. STM studies of the N/Cu(111) system: surface structure, electron confinement and tip-induced modification. *The European Physical Journal Applied Physics*, 19(2), 2002.

[77] J.M. Gómez-Rodríguez, J. Gómez-Herrero, and A. M. Baró. Imaging cos(s,z): A method to separate the geometric and compositional contributions on STM barrier height profiles. *Surface Science*, 220:152–164, 1989.

[78] B. Gotsmann, B. Anczykowski, C. Seidel, and H. Fuchs. Determination of tip–sample interaction forces from measured dynamic force spectroscopy curves. *Applied Surface Science*, 140(3-4):314–319, 1999.

[79] M. T. Greiner, M. G. Helander, W. M. Tang, Z. B. Wang, J. Qiu, and Z. H. Lu. Universal energy-level alignment of molecules on metal oxides. *Nature materials*, 11(11):76–81, 2011.

[80] M. Guggisberg, M. Bammerlin, Ch. Loppacher, O. Pfeiffer, A. Abdurixit, V. Barwich, R. Bennewitz, A. Baratoff, E. Meyer, and H.-J. Güntherodt. Separation of interactions by noncontact force microscopy. *Physical Review B*, 61(16):11151–11155, 2000.

[81] J. B. Gustafsson, H. M. Zhang, and L. S. O. Johansson. STM studies of thin PTCDA films on Ag/Si(111). *Physical Review B*, 75:155414, 2007.

[82] J. B. Gustafsson, H. M. Zhang, E. Moons, and L. S. O. Johansson. Electron spectroscopy studies of PTCDA on Ag/Si(111). *Physical Review B*, 75:1–10, 2007.

[83] J. Haase and H.-J. Kuhr. Reconstruction and relaxation of the oxygen-covered Cu(111) surface: A sexafs study. *Surface Science*, 203(3):L695–L699, 1988.

[84] F. H. P. M. Habraken, E. Ph. Kieffer, and G. A. Bootsma. A study of the kinetics of the interactions of O2 and N2O with a Cu(111) surface and of the reaction of CO with adsorbed oxygen using aes, LEED and ellipsometry. *Surface Science*, 83(1):45–59, 1979.

[85] H.C. Hamaker. The London—van der Waals attraction between spherical particles. *Physica*, 4(10):1058–1072, 1937.

[86] M. Häming, C. Scheuermann, A. Schöll, F. Reinert, and E. Umbach. Coverage dependent organic-metal interaction studied by high-resolution core level spectroscopy: SnPc (sub)monolayers on Ag(1 1 1). *Journal of Electron Spectroscopy and Related Phenomena*, 174(1-3):59–64, 2009.

[87] P. Hapala, G. Kichin, C. Wagner, F. S. Tautz, R. Temirov, and P. Jelínek. Mechanism of high-resolution STM/AFM imaging with functionalized tips. *Physical Review B*, 90(8):085421, 2014.

[88] M. Hara, T. Kondo, M. Komoda, S. Ikeda, K. Shinohara, and A. Tanaka. Cu2O as a photocatalyst for overall water splitting under visible light irradiation. *Chemical communications*, 2:357–358, 1998.

[89] A. Hashimoto, K. Suenaga, Al. Gloter, K. Urita, and S. Iijima. Direct evidence for atomic defects in graphene layers. *Nature*, 430(7002):870–873, 2004.

[90] N. Hauptmann and R. Berndt. Force and conductance spectroscopy of second-layer tin-phthalocyanine on Ag(111). *Physica Status Solidi (B)*, 250(11):2403–2407, 2013.

[91] N. Hauptmann, F. Mohn, L. Gross, G. Meyer, T. Frederiksen, and R. Berndt. Force and conductance during contact formation to a C60 molecule. *New Journal of Physics*, 14(7):073032, 2012.

[92] U. Heinemeyer, K. Broch, a. Hinderhofer, M. Kytka, R. Scholz, a. Gerlach, and F. Schreiber. Real-time changes in the optical spectrum of organic semiconducting films and their thickness regimes during growth. *Physical Review Letters*, 104(25):1–4, 2010.

[93] U. Heinemeyer, R. Scholz, L. Gisslén, M. I. Alonso, J. O. Ossó, M. Garriga, A. Hinderhofer, M. Kytka, S. Kowarik, A. Gerlach, and F. Schreiber. Exciton-phonon coupling in diindenoperylene thin films. *Physical Review B*, 78(8):1–10, 2008.

[94] M. A. Heinrich, J. Pflaum, A. K. Tripathi, W. Frey, M. L. Steigerwald, and T. Siegrist. Enantiotropic polymorphism in di-indenoperylene. *Journal of Physical Chemistry C*, 111(51):18878–18881, 2007.

[95] S. Hembacher, F. J. Giessibl, J. Mannhart, and C. F. Quate. Local spectroscopy and atomic imaging of tunneling current, forces, and dissipation on graphite. *Physical review letters*, 94(5):056101, 2005.

[96] M. Herz, F. J. Giessibl, and J. Mannhart. Probing the shape of atoms in real space. *Physical Review B*, 68:045301, 2003.

[97] M. Herz, Ch. Schiller, F. J. Giessibl, and J. Mannhart. Simultaneous current-, force-, and work-function measurement with atomic resolution. *Applied Physics Letters*, 86(15):153101, 2005.

[98] V. Higgs, P. Hollins, M. E. Pemble, and J. Pritchard. *Vibrations at Surfaces 1985, Proceedings of the Fourth International Conference*, volume 26 of *Studies in Surface Science and Catalysis*. Elsevier, 1986.

[99] W. A. Hofer, A. J. Fisher, R. A. Wolkow, and P. Grütter. Surface relaxations, current enhancements, and absolute distances in high resolution scanning tunneling microscopy. *Physical Review Letters*, 87(23):236104, 2001.

[100] R. Hoffmann, L. N. Kantorovich, A. Baratoff, H. J. Hug, and H. J. Güntherodt. Sublattice identification in scanning force microscopy on alkali halide surfaces. *Physical review letters*, 92(14):146103, 2004.

[101] I. Horcas, R. Fernández, J. M. Gómez-Rodríguez, J. Colchero, J. Gómez-Herrero, and A. M. Baro. WSXM: A software for scanning probe microscopy and a tool for nanotechnology. *Review of Scientific Instruments*, 78(1), 2007.

[102] A. Hoshino, S. Isoda, H. Kurata, and T. Kobayashi. Scanning tunneling microscope contrast of perylene-3,4,9,10-tetracarboxylic-dianhydride on graphite and its application to the study of epitaxy. *Journal of Applied Physics*, 76(1994):4113–4120, 1994.

[103] H. Huang, J. Sun, Y. P. Feng, W. Chen, and A. T. S. Wee. Epitaxial growth of diindenoperylene ultrathin films on Ag(111) investigated by LT-STM and LEED. *Physical Chemistry Chemical Physics*, 13(47):20933, 2011.

[104] Y. L. Huang, W. Chen, F. Bussolotti, T. C. Niu, A. T. S. Wee, N. Ueno, and S. Kera. Impact of molecule-dipole orientation on energy level alignment at the submolecular scale. *Physical Review B*, 87(8):1–6, 2013.

[105] Y. L. Huang, Y. Lu, T. C. Niu, H. Huang, S. Kera, N. Ueno, A. T. S. Wee, and W. Chen. Reversible single-molecule switching in an ordered monolayer molecular dipole array. *Small*, 8(9):1423–8, 2012.

[106] Y. L. Huang, R. Wang, T. C. Niu, S. Kera, N. Ueno, J. Pflaum, A.T. S. Wee, and W. Chen. One dimensional molecular dipole chain arrays on graphite

via nanoscale phase separation. *Chemical communications*, 46(47):9040–2, 2010.

[107] F. Huber. *Atomar aufgelöste Messung der lokalen Austrittsarbeit mit kombinierter Rasterkraft- und Rastertunnelmikroskopie*. Master thesis, University of Regensburg, 2013.

[108] F. Huber, S. Matencio, A. J. Weymouth, C. Ocal, E. Barrena, and F. J. Giessibl. Intramolecular Force Contrast and Dynamic Current-Distance Measurements at Room Temperature. *Physical Review Letters*, 115(6):066101, 2015.

[109] S Hudlet, M Saint Jean, C Guthmann, and J Berger. Evaluation of the capacitive force between an atomic force microscopy tip and a metallic surface. *The European Physical Journal B - Condensed Matter and Complex Systems*, 2(1):5–10, 1998.

[110] H. Ishii, K. Sugiyama, E. Ito, and K. Seki. Energy level alignment and interfacial electronic structures at organic metal and organic organic interfaces. *Advanced Materials*, 11(8):+, 1999.

[111] Jacob N. Israelachvili. *Intermolecular and Surface Forces*. Elsevier, third edit edition, 2011.

[112] P. Jelínek, M. Švec, P. Pou, R. Perez, and V. Cháb. Tip-Induced Reduction of the Resonant Tunneling Current on Semiconductor Surfaces. *Physical Review Letters*, 101(17):176101, 2008.

[113] F. Jensen, F. Besenbacher, E. Læ gsgaard, and I. Stensgaard. Oxidation of Cu(111): two new oxygen induced reconstructions. *Surface Science Letters*, 259(3):L774–L780, 1991.

[114] F. Jensen, F. Besenbacher, and I. Stensgaard. Two new oxygen induced reconstructions on Cu(111). *Surface Science*, 269-270(3):400–404, 1992.

[115] R. W. Judd, P. Hollins, and J. Pritchard. The interaction of oxygen with Cu(111): Adsorption, incorporation and reconstruction. *Surface Science Letters*, 171(3):A310, 1986.

[116] A. Kahn, N. Koch, and W. Gao. Electronic Structure and Electrical Properties of Interfaces between Metals and -Conjugated Molecular Films. *Journal of Polymer Science B polymer Physics*, 41(21):2529–2548, 2003.

[117] S. Kawai, T. Glatzel, H. Hug, and E. Meyer. Atomic contact potential variations of Si(111)-7 x 7 analyzed by Kelvin probe force microscopy. *Nanotechnology*, 21(24):245704, 2010.

[118] S. Kawai, T. Glatzel, S. Koch, A. Baratoff, and E. Meyer. Interaction-induced atomic displacements revealed by drift-corrected dynamic force spectroscopy. *Physical Review B*, 83(3):1–7, 2011.

[119] S. Kawai, T. Glatzel, Ba. Such, S. Koch, A. Baratoff, and E. Meyer. Energy dissipation in dynamic force microscopy on KBr(001) correlated with atomic-scale adhesion phenomena. *Physical Review B*, 86(24):245419, 2012.

[120] S. H. Ke, T. Uda, and K. Terakura. Surface topography of the Si(111)-7x7 reconstruction. *Physical Review B*, 62(23):15319–15322, 2000.

[121] S. Kera, Y. Yabuuchi, H. Yamane, H. Setoyama, K. K. Okudaira, A. Kahn, and N. Ueno. Impact of an interface dipole layer on molecular level alignment at an organic-conductor interface studied by ultraviolet photoemission spectroscopy. *Physical Review B*, 70(8):1–6, 2004.

[122] S. Kera, H. Yamane, H. Honda, H. Fukagawa, K. K. Okudaira, and N. Ueno. Photoelectron fine structures of uppermost valence band for well-characterized ClAl-phthalocyanine ultrathin film: UPS and MAES study. *Surface Science*, 566-568:571–578, 2004.

[123] M. Knupfer and G. Paasch. Origin of the interface dipole at interfaces between undoped organic semiconductors and metals. *Journal of Vacuum Science & Technology A*, 23(4):1072, 2005.

[124] N. Koch. Organic electronic devices and their functional interfaces. *ChemPhysChem*, 8(10):1438–1455, 2007.

[125] N. Koch, A. Gerlach, S. Duhm, H. Glowatzki, G. Heimel, A. Vollmer, Y. Sakamoto, T. Suzuki, J. Zegenhagen, J. P. Rabe, and F. Schreiber. Adsorption-induced intramolecular dipole: Correlating molecular conformation and interface electronic structure. *Journal of the American Chemical Society*, 130(23):7300–7304, 2008.

[126] S. Kowarik, a. Gerlach, S. Sellner, F. Schreiber, L. Cavalcanti, and O. Konovalov. Real-time observation of structural and orientational transitions during growth of organic thin films. *Physical Review Letters*, 96(12):1–4, 2006.

[127] A. Kraft, R. Temirov, S. Henze, S. Soubatch, M. Rohlfing, and F. Tautz. Lateral adsorption geometry and site-specific electronic structure of a large organic chemisorbate on a metal surface. *Physical Review B*, 74(4):041402, 2006.

[128] S. Kurokawa, M. Yuasa, A. Sakai, and Y. Hasegawa. Barrier Height Imaging of Oxygen-Adsorbed Si Surfaces. *Japanese Journal of Applied Physics*, 38:3860–3863, 1997.

[129] A. Labuda, Y. Miyahara, L. Cockins, and P. Grütter. Decoupling conservative and dissipative forces in frequency modulation atomic force microscopy. *Physical Review B*, 84(12):125433, 2011.

[130] G. Langewisch, W. Kamiński, D. A. Braun, R. Möller, H. Fuchs, A. Schirmeisen, and R. Pérez. Understanding dissipative tip-molecule interactions with submolecular resolution on an organic adsorbate. *Small*, 8(4):602–11, 2012.

[131] K. R. Lawless and A. T. Gwathmey. The structure of oxide films on different faces of a single crystal of copper. *Acta Metallurgica*, 4(2):153–163, 1956.

[132] T. J. Lawton, V. Pushkarev, E. Broitman, A. Reinicker, E. C. H. Sykes, and A. J. Gellman. Initial Oxidation of Cu(hkl) Surfaces Vicinal to Cu(111):

A High-Throughput Study of Structure Sensitivity. *The Journal of Physical Chemistry C*, 116(30):16054–16062, 2012.

[133] M. C. Lennartz, V. Caciuc, N. Atodiresei, S. Karthäuser, and S. Blügel. Electronic mapping of molecular orbitals at the molecule-metal interface. *Physical Review Letters*, 105(6):1–4, 2010.

[134] L. Limot, J. Kröger, R. Berndt, A. Garcia-Lekue, and W. A. Hofer. Atom transfer and single-adatom contacts. *Physical Review Letters*, 94(12):1–4, 2005.

[135] S. Mannsfeld, M. Toerker, T. Schmitz-Hübsch, F. Sellam, T. Fritz, and K. Leo. Combined LEED and STM study of PTCDA growth on reconstructed Au(111) and Au(100) single crystals. *Organic Electronics*, 2:121–134, 2001.

[136] B. Marchon, P. Bernhardt, M. Bussell, G. Somorjai, M. Salmeron, and W. Siekhaus. Atomic arrangement of sulfur adatoms on Mo(001) at atmospheric pressure: A scanning tunneling microscopy study. *Physical Review Letters*, 60(12):1166–1169, 1988.

[137] T. Matsumoto, R. A. Bennett, P. Stone, T. Yamada, K. Domen, and M. Bowker. Scanning tunneling microscopy studies of oxygen adsorption on Cu(111). *Surface Science*, 471(1-3):225–245, 2001.

[138] L. McDonnell, D. P. Woodruff, and K. A. R. Mitchell. Constant momentum transfer averaging in LEED; analysis of a structure of oxygen on Cu (100). *Surface Science*, 46:505–536, 1974.

[139] Gerhard Meyer and Nabil M. Amer. Simultaneous measurement of lateral and normal forces with an optical-beam-deflection atomic force microscope. *Applied Physics Letters*, 57(20):2089–2091, 1990.

[140] J. C. Meyer, C. Kisielowski, R. Erni, M. D. Rossell, M. F. Crommie, and A. Zettl. Direct imaging of lattice atoms and topological defects in graphene membranes. *Nano Letters*, 8(11):3582–3586, 2008.

[141] H. B. Michaelson. The work function of the elements and its periodicity. *Journal of Applied Physics*, 48(11):4729–4733, 1977.

[142] A. Mittiga, E. Salza, F. Sarto, M. Tucci, and R. Vasanthi. Heterojunction solar cell with 2 efficiency based on a Cu2O substrate. *Applied Physics Letters*, 88:163502, 2006.

[143] M. Möbus, N. Karl, and T. Kobayashi. Structure of perylene-tetracarboxylic-dianhydride thin films on alkali halide crystal substrates. *Journal of Crystal Growth*, 116:495–504, 1992.

[144] G. Münnich, A. Donarini, M. Wenderoth, and J. Repp. Fixing the Energy Scale in Scanning Tunneling Microscopy on Semiconductor Surfaces. *Physical Review Letters*, 111(21):216802, 2013.

[145] N. Nicoara. *Structural and Electronic Properties of PTCDA Single Molecules and Molecular Layers on Metal and Semiconductor Surfaces*. PhD thesis, 2007.

[146] N. Nicoara, Ó. Paz, J. Méndez, A. Baró, J. Soler, and J. Gómez-Rodríguez. Adsorption and electronic properties of PTCDA molecules on Si: Scanning tunneling microscopy and first-principles calculations. *Physical Review B*, 82(7):1–4, 2010.

[147] H. Niehus. Surface reconstruction of Cu(111) upon oxygen adsorption. *Surface Science*, 130:41–49, 1983.

[148] T. Niu. Low-temperature scanning tunneling microscopy study of self-assembly of molecular dipoles on surfaces. In *Thesis*. 2013.

[149] T. Niu. Surface strain mediated dipole alignment of ClAlPc on Au(111). *Applied Physics Letters*, 106(16):161601, 2015.

[150] T. Niu, C. Zhou, J. Zhang, S. Zhong, H. Cheng, and W. Chen. Substrate reconstruction mediated unidirectionally aligned molecular dipole dot arrays. *Journal of Physical Chemistry C*, 116(21):11565–11569, 2012.

[151] T. Niu, M. Zhou, J. Zhang, Y. Feng, and W. Chen. Dipole orientation dependent symmetry reduction of chloroaluminum phthalocyanine on Cu(111). *Journal of Physical Chemistry C*, 117(2):1013–1019, 2013.

[152] L. Olesen, M. Brandbyge, M. R. Sorensen, K. W. Jacobsen, E. Læ gsgaard, I. Stensgaard, and F. Besenbacher. Apparent barrier height in scanning tunneling microscopy revisited. *Physical Review Letters*, 76(9):1485–1488, 1996.

[153] L. C. Olsen, F. W. Addis, and W. Miller. Experimental and theoretical studies of Cu2O solar cells. *Solar Cells*, 7(3):247–279, 1982.

[154] F. Olsson, M. Persson, J. Repp, and G. Meyer. Scanning tunneling microscopy and spectroscopy of NaCl overlayers on the stepped Cu(311) surface: Experimental and theoretical study. *Physical Review B*, 71(7):075419, 2005.

[155] D. G. Oteyza, E. Barrena, M. Ruiz-ose, B. P. Doyle, and J. E. Ortega. Crystallographic and Electronic Structure of Self-Assembled DIP Monolayers on Au(111) Substrates. *Journal of Physical Chemistry C*, 112:7168–7172, 2008.

[156] R. Pérez, M. C. Payne, I. Stich, and K. Terakura. Role of covalent tip-surface interactions in noncontact atomic force microscopy on reactive surfaces. *Physical Review Letters*, 78(4):678, 1997.

[157] C. Pérez León, C. Sürgers, and H. V. Löhneysen. Formation of copper oxide surface structures via pulse injection of air onto Cu(111) surfaces. *Physical Review B*, 85(3):035434, 2012.

[158] L. Petersen, P. Laitenberger, E. Læ gsgaard, and F. Besenbacher. Screening waves from steps and defects on Cu(111) and Au(111) imaged with STM Contribution from bulk electrons. *Physical Review B*, 58(11):7361–7366, 1998.

[159] J. B. Pethica, J. Knall, and J. H. Wilson. Work function at a silicon surface atomically resolved by STM. *Inst. Phys. Conf. Ser.*, 134:597, 1993.

[160] O. Pfeiffer, L. Nony, R. Bennewitz, A. Baratoff, and E. Meyer. Distance dependence of force and dissipation in non-contact atomic force microscopy on Cu(100) and Al(111). *Nanotechnology*, 15(2):S101–S107, 2004.

[161] L. M. Ramaniah and M. Boero. Structural, electronic, and optical properties of the diindenoperylene molecule from first-principles density-functional theory. *Physical Review A*, 74(4):1–5, 2006.

[162] M. Rohlfing, R. Temirov, and F.S. Tautz. Adsorption structure and scanning tunneling data of a prototype organic-inorganic interface: PTCDA on Ag(111). *Physical Review B*, 76(11):115421, 2007.

[163] G. Rojas, S. Simpson, X. Chen, D. A. Kunkel, J. Nitz, J. Xiao, P. A. Dowben, E. Zurek, and A. Enders. Surface state engineering of molecule-molecule interactions. *Physical Chemistry Chemical Physics*, 14(14):4971–4976, 2011.

[164] M. S. Roy, P. Balraju, Y. S. Deol, S. K. Sharma, and G. D. Sharma. Charge-transport and photocurrent generation in bulk hetero junction based on Chloro-aluminum phthalocyanine (ClAlPc) and Rose Bengal (RB). *Journal of Materials Science*, 43(16):5551–5563, 2008.

[165] D. Rugar, H. J. Mamin, and P. Guethner. Improved fiber-optic interferometer for atomic force microscopy. *Applied Physics Letters*, 55(25):2588–2590, 1989.

[166] C. D. Ruggiero, T. Choi, and J. A. Gupta. Tunneling spectroscopy of ultrathin insulating films: CuN on Cu(100). *Applied Physics Letters*, 91(25):253106, 2007.

[167] J. E. Sader and S. P. Jarvis. Accurate formulas for interaction force and energy in frequency modulation force spectroscopy. *Applied Physics Letters*, 84(10):1801, 2004.

[168] J. E. Sader and Y. Sugimoto. Accurate formula for conversion of tunneling current in dynamic atomic force spectroscopy. *Applied Physics Letters*, 97(4):1–4, 2010.

[169] R. E. Schlier and H.E . Farnsworth. Structure and Adsorption Characteristics of Clean Surfaces of Germanium and Silicon. *The Journal of Chemical Physics*, 30(4):917, 1959.

[170] B. Schuler, W. Liu, A. Tkatchenko, N. Moll, G. Meyer, A. Mistry, D. Fox, and L. Gross. Adsorption geometry determination of single molecules by atomic force microscopy. *Physical Review Letters*, 111(10):1–5, 2013.

[171] W.M. Sears and E. Fortin. Preparation and properties of Cu2O/Cu photovoltaic cells. *Solar Energy Materials*, 10(1):93–103, 1984.

[172] G. W. Simmons, D. F. Mitchell, and R Lawless. LEED and HEED studies of the interaction of oxygen with single crystal surfaces of copper. *Surface Science*, 8:130–164, 1967.

[173] B. Sinha, T. Goswami, S. Paul, and A. Misra. The impact of surface structure and band gap on the optoelectronic properties of Cu2O nanoclusters of varying size and symmetry. *RSC Advances*, 4(10):5092, 2014.

[174] J. F. Skelly, T. Bertrams, A. W. Munz, M. J. Murphy, and A. Hodgson. Nitrogen induced restructuring of Cu(111) and explosive desorption of N2. *Surface Science*, 415(1-2):48–61, 1998.

[175] P. G. Slade. *Electrical Contacts: Principles and Applications*. CRC Press, 1999.

[176] W. H. Soe, C. Manzano, H. S. Wong, and C. Joachim. Mapping the first electronic resonances of a Cu phthalocyanine STM tunnel junction. *Journal of Physics: Condensed Matter*, 24(35):354011, 2012.

[177] Ch. Sommerhalter, Th. Glatzel, Th. W. Matthes, A. Jaeger-Waldau, and M. Ch. Lux-Steiner. Kelvin probe force microscopy in ultra high vacuum using amplitude modulation detection of the electrostatic forces. *Applied Surface Science*, 157(4):263–268, 2000.

[178] A. Soon, X. Cui, B. Delley, S. Wei, and C. Stampfl. Native defect-induced multifarious magnetism in nonstoichiometric cuprous oxide: First-principles study of bulk and surface properties of Cu2O. *Physical Review B*, 79(3):035205, 2009.

[179] A. Soon, T. Söhnel, and H. Idriss. Plane-wave pseudopotential density functional theory periodic slab calculations of CO adsorption on Cu2O(111) surface. *Surface Science*, 579(2-3):131–140, 2005.

[180] A. Soon, M. Todorova, B. Delley, and C. Stampfl. Oxygen adsorption and stability of surface oxides on Cu(111): A first-principles investigation. *Physical Review B*, 73(16):1–12, 2006.

[181] A. Soon, M. Todorova, B. Delley, and C. Stampfl. Surface oxides of the oxygen-copper system: Precursors to the bulk oxide phase? *Surface Science*, 601(24):5809–5813, 2007.

[182] A. Soon, M. Todorova, B. Delley, and C. Stampfl. Thermodynamic stability and structure of copper oxide surfaces: A first-principles investigation. *Physical Review B*, 75(12):1–9, 2007.

[183] A. Spitzer and H. Lüth. The adsorption of oxygen on copper surfaces. *Surface Science*, 118:136–144, 1982.

[184] C. Stadler, S. Hansen, I. Kröger, C. Kumpf, and E. Umbach. Tuning intermolecular interaction in long-range-ordered submonolayer organic films. *Nature Physics*, 5(2):153–158, 2009.

[185] C. Stadler, S. Hansen, F. Pollinger, C. Kumpf, E. Umbach, T. L. Lee, and J. Zegenhagen. Structural investigation of the adsorption of SnPc on Ag(111) using normal-incidence x-ray standing waves. *Physical Review B - Condensed Matter and Materials Physics*, 74(3):1–8, 2006.

[186] B. Stadtmüller, I. Kröger, F. Reinert, and C. Kumpf. Submonolayer growth of CuPc on noble metal surfaces. *Physical Review B - Condensed Matter and Materials Physics*, 83(8):1–10, 2011.

[187] C. Stampfl. Surface processes and phase transitions from ab initio atomistic thermodynamics and statistical mechanics. *Catalysis Today*, 105(1 SPEC. ISS.):17–35, 2005.

[188] C. Stampfl, M. V. Ganduglia-Pirovano, K. Reuter, and M. Scheffler. Catalysis and corrosion: The theoretical surface-science context. *Surface Science*, 500(1-3):368–394, 2002.

[189] B. Such, T. Glatzel, S. Kawai, E. Meyer, R. Turanský, J. Brndiar, and I. Štich. Interplay of the tip–sample junction stability and image contrast reversal on a Cu(111) surface revealed by the 3D force field. *Nanotechnology*, 23(4):045705, 2012.

[190] K. Suenaga, H. Wakabayashi, M. Koshino, Y. Sato, K. Urita, and S. Iijima. Imaging active topological defects in carbon nanotubes. *Nature Nanotechnology*, 2(6):358–360, 2007.

[191] Y. Sugimoto, K. Ueda, M. Abe, and S. Morita. Three-dimensional scanning force/tunneling spectroscopy at room temperature. *Journal of Physics: Condensed Matter*, 24(8):084008, 2012.

[192] J. C. Swarbrick, J. Ma, J. A. Theobald, N. S. Oxtoby, J. N. O. Shea, N. R. Champness, and P. H. Beton. Square , Hexagonal , and Row Phases of PTCDA and PTCDI on AgSi(111). *Journal of Physical Chemistry B*, 109(111):12167–12174, 2005.

[193] J. C. Swarbrick, B. L. Rogers, N. R. Champness, and P. H. Beton. Hydrogen-bonded PTCDA-melamine networks and mixed phases. *The Journal of Physical Chemistry B*, 110(12):6110–4, 2006.

[194] A. Sweetman, A. Stannard, Y. Sugimoto, M. Abe, S. Morita, and P. Moriarty. Simultaneous noncontact AFM and STM of Ag:Si(111). *Physical Review B*, 87(7):075310, 2013.

[195] A. M. Sweetman, S. P. Jarvis, H. Sang, I. Lekkas, P. Rahe, Yu Wang, J. Wang, N. R. Champness, L. Kantorovich, and P. Moriarty. Mapping

the force field of a hydrogen-bonded assembly. *Nature Communications*, 5:3931, 2014.

[196] H. Tada, H. Touda, M. Takada, and K. Matsushige. Quasi-intrinsic semiconducting state of titanyl-phthalocyanine films obtained under ultrahigh vacuum conditions. *Applied Physics Letters*, 76(7):873, 2000.

[197] K. Takayanagi. Structural analysis of Si(111)-7 7 by UHV-transmission electron diffraction and microscopy. *Journal of Vacuum Science & Technology A*, 3(3):1502, 1985.

[198] K. Takayanagi, Y. Tanishiro, S. Takahashi, and T. Masaetsu. Structure analysis of Si(111)-7x7 reconstructed surface by transmission electron diffraction. *Surface Science*, 164:367–392, 1985.

[199] K. Takeuchi, A. Suda, and S. Ushioda. Local variation of the work function of Cu(111) surface deduced from the low energy photoemission spectra. *Surface Science*, 489(1-3):100–106, 2001.

[200] F. S. Tautz. Structure and bonding of large aromatic molecules on noble metal surfaces: The example of PTCDA. *Progress in Surface Science*, 82(9-12):479–520, September 2007.

[201] A. Terentjevs, M. P. Steele, M. L. Blumenfeld, N. Ilyas, L. L. Kelly, E. Fabiano, O. L. A. Monti, and F. D. Sala. Interfacial Electronic Structure of the Dipolar Vanadyl Naphthalocyanine on Au (111): " Push-Back " vs Dipolar Effects. *The Journal of Physical Chemistry C*, 115:21128–21138, 2011.

[202] M. Ternes, C. González, C. P. Lutz, P. Hapala, F. J. Giessibl, P. Jelínek, and A. J. Heinrich. Interplay of Conductance, Force, and Structural Change in Metallic Point Contacts. *Physical Review Letters*, 106(1):016802, 2011.

[203] D. R. Tersoff, J. and Hamann. Theory of the scanning tunneling microscope. *Physical Review B*, 31(2):805—-813, 1985.

[204] M. Toader and M. Hietschold. Tuning the Energy Level Alignment at the SnPc/Ag(111) Interface Using an STM Tip. *The Journal of Physical Chemistry C*, (115):3099–3105, 2011.

[205] R. L. Toomes, D. P. Woodruff, M. Polcik, S. Bao, Ph. Hofmann, and K. M. Schindler. Is PEXAFS really PhD? *Surface Science*, 445(2-3):300–308, 2000.

[206] S. Torbrugge, O. Schaff, and J. Rychen. Application of the KolibriSensor to combined atomic-resolution scanning tunneling microscopy and noncontact atomic-force microscopy imaging. *Journal of Vacuum Science & Technology B*, 28(3):C4E12, 2010.

[207] M. Tortonese, R. C. Barrett, and C. F. Quate. Atomic resolution with an atomic force microscope using piezoresistive detection. *Applied Physics Letters*, 62(8):834–836, 1993.

[208] T. Trevethan, L. Kantorovich, J. Polesel-Maris, and S. Gauthier. Is atomic-scale dissipation in NC-AFM real? Investigation using virtual atomic force microscopy. *Nanotechnology*, 084017, 2007.

[209] A. K. Tripathi and J. Pflaum. Correlation between ambipolar transport and structural phase transition in diindenoperylene single crystals. *Applied Physics Letters*, 89(8):11–14, 2006.

[210] W. E. J. van Kooten, D. D. Kragten, O. L. J. Gijzeman, and J. W. Geus. Hydrocarbon interaction with clean and oxidised Cu(111). *Surface Science Letters*, 290(3):302–308, 1993.

[211] H. Vázquez, Y. J. Dappe, J. Ortega, and F. Flores. Energy level alignment at metal/organic semiconductor interfaces: "Pillow" effect, induced density of interface states, and charge neutrality level. *Journal of Chemical Physics*, 126(14), 2007.

[212] J. Wagner, M. Gruber, A. Hinderhofer, A. Wilke, B. Bröker, J. Frisch, P. Amsalem, A. Vollmer, A. Opitz, N. Koch, F. Schreiber, and W. Brütting. High fill factor and open circuit voltage in organic photovoltaic cells

with diindenoperylene as donor material. *Advanced Functional Materials*, 20(24):4295–4303, 2010.

[213] K. J. Wan, X. F. Lin, and J. Nogami. Reexamination of the Ag/Si(111) surface by scanning tunneling microscopy. *Physical Review B*, 45(16), 1992.

[214] K. J. Wan, X. F. Lin, and J. Nogami. Surface recosntructions Ag/Si(111) system. *Physical Review B*, 47(20):13700, 1993.

[215] K. Wandelt. The local work function: Concept and implications. *Applied Surface Science*, 111:1–10, 1997.

[216] H. Wang, D. Song, J. Yang, B. Yu, Y. Geng, and D. Yan. High mobility vanadyl-phthalocyanine polycrystalline films for organic field-effect transistors. *Applied Physics Letters*, 90(25):2005–2008, 2007.

[217] Q. H. Wang and M. C. Hersam. Room-temperature molecular-resolution characterization of self-assembled organic monolayers on epitaxial graphene. *Nature Chemistry*, 1, 2009.

[218] Y. Wang, X. Ge, G. Schull, R. Berndt, C. Bornholdt, F. Koehler, and Rainer Herges. Azo Supramolecules on Au(111) with Controlled Size and Shape. *Journal of the American Chemical Society*, (130):4218–4219, 2008.

[219] Y. Wang, X. Ge, G. Schull, R. Berndt, H. Tang, C. Bornholdt, F. Koehler, and R. Herges. Switching single azopyridine supramolecules in ordered arrays on Au(111). *Journal of the American Chemical Society*, 132(4):1196–1197, 2010.

[220] Y. Wang, J. Kröger, R. Berndt, and W. A. Hofer. Pushing and pulling a Sn ion through an adsorbed phthalocyanine molecule. *Journal of the American Chemical Society*, 131(10):3639–43, 2009.

[221] Y. Wang, J. Kröger, R. Berndt, and H. Tang. Molecular nanocrystals on ultrathin NaCl films on Au(111). *Journal of the American Chemical Society*, 132(36):12546–7, 2010.

[222] S. Watanabe, M. Aono, and M Tsukada. Theoretical calculations of the scanning-tunneling-microscopy images of the Si(111) (V3xV3)-Ag surface. *Physical Review B*, 44(15):8330–8333, 1991.

[223] C. Weiss, C. Wagner, R. Temirov, and F. S. Tautz. Direct Imaging of Intermolecular Bonds in Scanning Tunneling Microscopy. *Journal of the American Chemical Society*, pages 11864–11865, 2010.

[224] A. J. Weymouth and F. J. Giessibl. The effect of sample resistivity on Kelvin probe force microscopy. *Applied Physics Letters*, 101(21):213105, 2012.

[225] A. J. Weymouth, T. Wutscher, J. Welker, T. Hofmann, and F. J. Giessibl. Phantom Force Induced by Tunneling Current: A Characterization on Si(111). *Physical Review Letters*, 106(22):226801, 2011.

[226] F. Wiame, V. Maurice, and P. Marcus. Initial stages of oxidation of Cu(111). *Surface Science*, 601(5):1193–1204, 2007.

[227] S. S. Wilson, J. P. Bosco, Y. Tolstova, D. O. Scanlon, G. W. Watson, and H. A. Atwater. Interface stoichiometry control to improve device voltage and modify band alignment in ZnO/Cu2O heterojunction solar cells. *Energy Environ. Sci.*, 7(11):3606–3610, 2014.

[228] G. Witte, S. Lukas, P. S. Bagus, and C. Wöll. Vacuum level alignment at organic/metal junctions: "cushion" effect and the interface dipole. *Applied Physics Letters*, 87(26):1–3, 2005.

[229] Ch. Woll, S Chiang, R. J. Wilson, and P. H. Lippel. Determination of atom positions at stacking-fault dislocations on Au(111) by scanning tunneling microscopy. *Physical Review B*, 39(11):7988–7991, 1989.

[230] T. Wutscher, A. J. Weymouth, and F. J. Giessibl. Localization of the phantom force induced by the tunneling current. *Physical Review B*, 85(19):195426, 2012.

[231] F. Yang, Y. Choi, P. Liu, J. Hrbek, and J. A. Rodriguez. Autocatalytic Reduction of a Cu2O/Cu(111) Surface by CO: STM, XPS, and DFT Studies. *The Journal of Physical Chemistry C*, 114(40):17042–17050, 2010.

[232] F. Yang, Y. Choi, P. Liu, D. Stacchiola, J. Hrbek, and J. A. Rodriguez. Identification of 5 -7 Defects in a Copper Oxide Surface. *Journal of the American Chemical Society*, 133:11474–11477, 2011.

[233] H. Y. Yasuhiro Iye. *The Physics and Chemistry of Oxide Superconductors*. Springer Berlin Heidelberg, 2011.

[234] H. Ying Mao, R. Wang, Y. Wang, T. Chao Niu, J. Qiang Zhong, M. Yang Huang, D. Chen Qi, K. Ping Loh, A. Thye Shen Wee, and W. Chen. Chemical vapor deposition graphene as structural template to control interfacial molecular orientation of chloroaluminium phthalocyanine. *Applied Physics Letters*, 99(9):19–22, 2011.

[235] U. Zerweck, C. Loppacher, T. Otto, S. Grafström, and L. M. Eng. Accuracy and resolution limits of Kelvin probe force microscopy. *Physical Review B*, 71(12):1–9, 2005.

[236] H. M. Zhang, J. B. Gustafsson, and L.S.O. Johansson. STM study of the electronic structure of PTCDA on Ag/Si(111). *Chemical Physics Letters*, 485(1-3):69–76, 2010.

[237] X. N. Zhang, E. Barrena, D. G. de Oteyza, and H. Dosch. Transition from layer-by-layer to rapid roughening in the growth of DIP on SiO2. *Surface Science*, 601(12):2420–2425, 2007.

[238] X. N. Zhang, D. G. de Oteyza, Y. Wakayama, and H. Dosch. STM study of di-indenoperylene molecules on Cu(100) surfaces: Mobility, stability and epitaxy. *Surface Science*, 603(21):3179–3183, 2009.

[239] Y. Zhang, S. Du, and H.-J. Gao. Binding configuration, electronic structure, and magnetic properties of metal phthalocyanines on a Au(111) surface studied with ab initio calculations. *Physical Review B*, 84(12):1–8, 2011.

[240] Y. Zhang, P. Wahl, and K. Kern. Quantum point contact microscopy. *Nano Letters*, 11(9):3838–43, 2011.

[241] Y. Zou, L. Kilian, A. Schöll, Th. Schmidt, R. Fink, and E. Umbach. Chemical bonding of PTCDA on Ag surfaces and the formation of interface states. *Surface Science*, 600(6):1240–1251, 2006.